Contribution of Anthropogenic Climate Change to the Magnitude of Extreme Rainfall Events and Associated Synoptic Conditions during Recent Flooding in Kenya

By

Joyce Kimutai

Supervisors: Prof. Mark New & Dr. Piotr Wolski

Dissertation Submitted to the Faculty of Science in Partial Fulfilment for the Requirements of Doctor of Philosophy in Climate Science: Attribution of Climate Extremes

Environmental and Geographical Sciences Department, African Climate and Development Initiative University of Cape Town, Cape Town

Submitted: February 2023

Plagiarism Declaration

I understand the meaning of plagiarism and I am fully aware of the University of Cape Town's policy on the same. I certify that this dissertation reports original work done by me during my university project and that all the work that is not mine has been properly referenced in line with the university's guidelines. Parts of the work of this thesis were published as a journal article in 2022. The journal article includes material in Chapter 1, 3, 4 and 5 (event description, data, model evaluation, attribution of human influence on rainfall magnitude).

Name: Joyce Jepngetich Kimutai

Signed by candidate

Date: 12 February 2023

Acknowledgements

I would like to express my heartfelt gratitude to my supervisors Prof. Mark New and Dr. Piotr Wolski for their commitment to the best supervision possible for my research. Their input and guidance were extremely key to the successful completion of my research work as well as laying a solid foundation for my research career. Special thanks to Dr. Friederike Otto for inspiring me to join the fascinating and fast evolving field of attribution science and her continuous commitment to making me a great attribution researcher. Heartfelt gratitude to the climate risk team at ACDI; Dr. Romaric Odoulami, Dr. Petra Holden, Dr. Chris Trisos, Dr. Lawal Kamoru, Dr. Nick Simpson, Tiro Nkemelang, Sylvia Dorbor, Lavinia Perumal and Andrew Hall, and the whole ACDI team for their support throughout my studies at UCT. Thanks to the climate lab team of 2019 at the Environmental Change Institute (ECI) Oxford University (Prof. Myles Allen, Dr. Karsten Hausten, Dr. Sihan Li, and Dr. Sarah Sparrow) for their informative research sessions at the lab. I would also like to appreciate the late Prof. Geert van Oldenborgh for his advice during my visit at ECI and beyond, and his zealous contribution to the field. Special thanks to the PNB Paribas and the AXA Chair programme on African climate risk for funds provided for my studies. Special mention of my family and friends who have always been there for me. Special thanks to Kenya Meteorological Department for the meteorological data used in this work. Finally, I would like to thank the Kenya Meteorological Department and Ministry of Environment for granting leave of absence to pursue my studies.

This work is dedicated to my supportive family, my husband Adolphus Lwova and my daughter Layla Lwova, and all the people putting an effort to protect the planet!

Abstract

The changing probabilities of extreme climate and weather events, in terms of frequency, intensity, spatial extent, duration and timing, are one of the most noticeable and damaging manifestations of human-induced climate change. The Greater Horn of Africa has experienced a number of extreme weather and seasonal climate events over the past two decades. While droughts have predominated, several heavy precipitation events with devastating impacts have also been recorded. During the March-April-May (MAM) rainfall seasons of 2012, 2016 and 2018, Kenya experienced high rainfall that caused both widespread and localised flooding, resulting in human and livestock deaths, destruction of infrastructure and property, bursting of riverbanks, submerging of farmlands and emergence of isolated cases of water-borne diseases.

This research aimed to assess whether human influence on climate played a role in modifying the rainfall intensity and associated synoptic conditions of extreme rainfall in these years. The work had three specific objectives: (i) Characterise the rainfall magnitude and associated synoptic conditions at the time of the flooding events; (ii) Evaluate the role of human influence on the magnitude of heavy rainfall; (iii) Evaluate the role of human influence on the synoptic conditions associated with heavy rainfall. By using three different attribution approaches, and utilising two observational datasets, one reanalysis data and two independent climate model experiment setups, the study was able to quantify how the local thermodynamic and regional dynamic conditions driving the flood-inducing rainfall in these seasons may have been altered by human-induced climate change. The rainfall magnitudes and associated atmospheric states were first characterised and then differences in the rainfall magnitudes and frequency of the atmospheric states in MAM 2012, 2016 and 2018 were compared to those in pre-industrial climate. Three different seasonal heavy rainfall indices were analysed; seasonal maximum consecutive 5-day, 10-day, and 20-day rainfall. The atmospheric states were based on Self Organizing Maps analysis of specific humidity, air temperature, and zonal and meridional wind at 850hPa on surface level pressure and zonal moisture flux.

Results from the three approaches used in attribution of rainfall intensity showed intensification of extreme rainfall in the current climate (MAM 2012, 2012, 2018) compared to the pre-industrial period climate (1850-1900), but without statistical significance. Analysis of synoptic atmospheric conditions during the heavy rainfall seasons detected above average frequencies in nodes associated with wet weather conditions (wet clusters), corresponding increases in rainfall across the three event-years in the current climate. Analysis of differences in climate model simulations between today's climate[1] and a pre-industrial climate

[1] The terms "current climate" and "today's climate" are used interchangeably.

did not find consistent differences across models. These results could suggest that it is more likely than not that anthropogenic climate change increased the magnitude of heavy rainfall in these years, but this influence is yet not formally (statistically significant) attributable to human influence on the climate system. These findings provide new insights on drivers of extreme MAM rainfall in Kenya and the potential influence of anthropogenic climate change. This work shows that even in the drying trend experienced over region, flood-inducing extreme rainfall can and does occur, and is associated with a higher frequency of certain synoptic conditions. As this study provide tentative evidence that a human influence might be emerging, it highlights the need for ongoing monitoring of extremes and attribution studies to track how climate change signals emerges and modify extremes, so that society can prepare for changing climate risks.

Table of Contents

List of Figures

List of Tables

1 Introduction

1.1 Background

The Greater Horn of Africa has experienced several extreme weather and seasonal climate events over the past two decades (2000-2020) (Funk et al., 2018; Kilavi et al., 2018; Hoell et al., 2017; Uhe et al., 2018; Liebmann et al., 2014; Philippon et al., 2015). While droughts have predominated, several heavy precipitation events with devastating impacts on agricultural systems, infrastructure, settlements, property, and life have also been recorded (Kimutai et al. 2022). During the March-April-May (hereafter, MAM) seasons of 2012, 2016, and 2018, many areas of Kenya experienced extremely high rainfall causing widespread flooding. Many meteorological stations recorded seasonal rainfall above their long-term means, especially in the central and western parts of the country. Among the impacts reported were loss of lives, submerged farmlands, bursting of riverbanks, destruction of roads and property, and isolated cases of waterborne diseases. In MAM 2018 all meteorological stations in the country recorded rainfall exceeding the long-term mean, and at many stations, that season has turned out to be the wettest MAM on record so far. By 7 May 2018, at least 311,164 people had been displaced by floods across the country, at least 132 had died, and a further 33 were injured (OCHA, 2018; Kenya Govt, 2018). Additionally, 47 deaths were reported after Solai Dam in Nakuru County could not withstand the floods and burst on 9 May. Very heavy rainfall was also recorded over several periods during the MAM seasons in 2016 and 2012 across the country, but the severity of rainfall, flooding and associated impacts were not as large as in 2018. Many stations recorded seasonal rainfall above their long-term means, especially in the central and western parts of the country. In 2012, at least 8,450 acres of farmland were submerged following bank bursting along the Tana, Ewaso Nyiro, Yala, and Nyando rivers, and some bridges were swept away, rendering roads impassable (OCHA, 2012). In 2016, an estimated total of 34,129 people were affected by the floods, with informal settlements in the Nairobi metropolitan area being the worst impacted, including the collapse of a residential building on 29 April 2016 that caused 16 fatalities (IFRC, 2016). A detailed description of these flooding events is provided in section 3.1.

Global mean surface temperature (GMST) has increased since the 19th century (IPCC, 2007; IPCC, 2013; Zorita et al., 2008; Drost et al, 2010; Stott & Jones, 2012; Gillert et al., 2012). Human activity through emission of greenhouse gases has already warmed the planet by over 1°C since pre-industrial times (IPCC 2021; IPCC, 2018). Present-day global concentrations of atmospheric well-mixed greenhouse gases are at higher levels than at any time in at least the past 800,000 years (Gulev et al., 2021). The warming has triggered changes in processes, behaviour and associations in the climate system (e.g Mondal and

Mujumdar, 2015). Extreme weather and climate events are among the most pertinent perils of the warming of the climate and robust evidence of widespread impacts resulting from changes in the intensity and likelihood of extreme events exist (Trisos et al., 2022; Seneviratne et al., 2021). Impacts have been felt at different magnitudes in different parts of the world with additional warming expected to significantly amplify existing risks and associated impacts, especially in the most vulnerable parts of the world, including Sub-Saharan Africa (Trisos et al., 2022). In the aftermath of an extreme event, the question mostly posed by the general public, media and policymakers is whether climate change played a role, especially if the event resulted in significant impacts. This interest demonstrates that extreme weather and climate events with measurable impacts provide a crucial opportunity to raise awareness of how global warming is playing a role in modifying risks associated with extreme events and preparing better for future risks.

The fast-evolving field of climate science, climate change attribution science, seeks to understand how anthropogenic climate change influences the climate system. Over the last decade (2010- 2020), the field has made significant advances, not only in proving the human contribution to global and regional climate change, but also in attributing human influence on changing likelihoods (and associated risks) of weather and climate events such as heatwaves, droughts, extreme rainfall, floods, and tropical cyclones/hurricanes (IPCC, 2021). While many aspects of the climate system are deterministic in nature, the system's complexity and the multitude of interacting processes introduce elements of stochasticity. Therefore, in principle, every extreme event is unique and usually results from a combination of external drivers, natural and anthropogenic, as well as climate system internal (random or unresolved) variability (Stott et al., 2016). The presence of an external driver like human-induced climate change can alter the likelihood of occurrence (including frequency and magnitude) of an extreme weather or climate event. The specific way in which human influence on global climate contributes to a particular weather event is not important when considering the impacts. Therefore, understanding the overall changes in risks of extreme events in a warming climate requires both a thermodynamic and dynamic perspective (Otto, 2016, 2017; Shepherd, 2016). Dynamic contributions constitute the changes in atmospheric conditions while thermodynamic contributions constitute changes in atmospheric physical properties. While more extreme precipitation is expected in a warmer atmosphere that can hold more water vapour (Boer,1993; Allen and Ingram, 2002; Trenberth 2011; O'Gorman 2015) from thermodynamic considerations, the increasing greenhouse gas concentration in the atmosphere and higher ocean temperatures also affect the atmospheric circulation, which either amplify or attenuate the effects of thermodynamic changes. The synoptic situation of a heavy rainfall event can be characterised by the extremeness of certain dynamic and thermodynamic meteorological variables which are distinctly correlated with the extremity of the rainfall event (Müller et

al., 2009). In most extreme events, the role of intensifying dynamical conditions is generally a critical causal factor (Cheng et al. 2018; Yiou and Cattiaux, 2013). For instance, changing dynamics or behavior of the atmosphere can play a pivotal role in either triggering or intensifying those events. This is particularly likely in regions where the initiation and evolution of weather systems are influenced by an interaction between synoptic and mesoscale systems (Nicholson, 2017; Sun et al., 2015; Segele et al., 2015), such as East Africa (Hession & Moore, 2011; Hastenrath et al., 2011; Pohl and Camberlin, 2011).

Only a handful studies have investigated the possible role of human influence on the processes, dynamics, and drivers of rainfall in Kenya. All the attribution work so far has been on drought and the observed long-term drying trend of the MAM rains (Funk et al., 2013; Lott et al., 2013; Hoell and Funk, 2014; Liebmann et al., 2014; Marthews et al., 2015; Uhe et al., 2018; Funk et al., 2018) with some mixed results, at least partly due of the different approaches and framings used (Otto, 2016). There have not been any heavy rainfall attribution studies in the region. Attribution analysis of wet extremes in Kenya is crucial for informing policy and planning e.g., in infrastructure and urban planning, agriculture, disaster preparedness and water resource management. This thesis sought to investigate the role and contribution of human-induced climate change on both the local thermodynamic and wider synoptic atmospheric conditions in driving 2012, 2016, and 2018 MAM flood-inducing extreme rainfall in Kenya. The study focussed on a region (study domain) that received highest positive rainfall anomalies and experienced huge impacts. Focusing on three different MAM seasons allows for the investigation of a wider set of cases in the possible responses to anthropogenic forcing and natural variability, thus enhancing confidence in the attribution results. Based on peer-reviewed methods (Odoulami et al., 2021; Trenberth et al., 2015; Vautard et al., 2016; NAS, 2016), a combination of observational data and climate model outputs is used to evaluate changes in the rainfall intensity and atmospheric states of the three extreme rainfall events between a world with and without anthropogenic influence on the climate system. The study utilizes a multi-method, multi-model approach, designed to enhance confidence in the results by accounting for uncertainties in attribution statements beyond just sampling uncertainty. This thesis is structured as follows: introduction to the thesis is presented in chapter 1, along with the objectives of the study. Chapter 2 presents a review of the literature on general climate change, the climate of Kenya, detection and attribution of climate change, history of attribution, precipitation extremes under climate change and extreme event attribution. Chapter 3 presents a description of the data and the methods used. Results with discussions on model evaluation, characterisation of rainfall magnitude and synoptic conditions, attribution of rainfall magnitude, and attribution of synoptic conditions are provided in chapters 4, 5 and 6, respectively. Chapter 7 presents the conclusions and recommendations. The thesis argument map is presented in table 1.1.

1.2 Objectives of the study and Research Questions

The aim of this study was to evaluate the extent to which human forcing on the climate system influenced the severity of the 2018, 2016 and 2012 March-April-May extreme rainfall events in a defined region in Kenya. This overall objective is split into three specific objectives outlined as follows.

(i) Characterisation of rainfall magnitude and associated synoptic atmospheric conditions during recent flooding events

(ii) Attribution of human influence on the magnitude of rainfall

(iii) Attribution of human influence on synoptic atmospheric conditions

Table 1.1 Thesis Argument map

<table>
<tr><td colspan="7">Research aim/question: Evaluate the extent to which human forcing on the climate system influenced the severity of the 2018, 2016 and 2012 March-April-May extreme rainfall events in a defined region in Kenya.</td></tr>
<tr><td rowspan="6">Chapter 1: Introduction

Broad purpose: Introduces the topic, provides a brief overview of the research, and states the research question.</td><td>Chapter 2: Literature review
Broad purpose: Reviews existing literature and provides an analysis of the existing body of research on the topic</td><td>Chapter 3: Data and Methods

Broad purpose: Describes the research methods used, including data and models, and analysis techniques</td><td colspan="4">Results and Discussions
Broad purpose: Documents the findings of the research and presents evidence that supports the research question.</td><td rowspan="6">Chapter8: Conclusions and recommendations
Broad purpose: Summarises the research and its findings, and explores the implications of the research</td></tr>
<tr><td>Section 1: Kenyan Climate</td><td rowspan="3">Section 1: Event description and study area</td><td rowspan="5">Chapter 4: Model Evaluation</td><td rowspan="5">Chapter 5: Characterisation of Rainfall Magnitude and Associated Synoptic Conditions</td><td rowspan="5">Chapter 6: Attribution of Human Influence on Magnitude of Rainfall</td><td rowspan="5">Chapter 7: Attribution of Human Influence on Synoptic conditions</td></tr>
<tr><td>Section 2: General Climate Change</td></tr>
<tr><td>Section 3: Precipitation Extremes under Climate Change</td></tr>
<tr><td>Section 4: Reasons for Concern</td><td rowspan="2">Section 2: Data; Observational and model data</td></tr>
<tr><td>Section 1: Background Information</td><td>Section 5: Attribution of</td></tr>
</table>

	Climate Change	**Section 3:** Methods					
Section 2: Overall objective and the specific objectives	**Section 6:** Extreme Event Attribution						
	Section 7: Attribution of Extreme Rainfall						
	Section 8: Role and importance of Event Attribution Studies						
	Section 9: Summary of the literature review and research gap						

2 Literature Review

Attribution of causes of climate change is an evolving field which aims to evaluate the relative contributions of multiple possible driving factors to a detected climate change with an assignment of statistical confidence. Detection of climate change is done by demonstrating that the climate or a system affected by climate has changed in some defined statistical sense (Hegerl et al., 2010). Attribution then aims to understand the cause or causes of the detected changes. Attribution of extreme events, on the other hand, is the evaluation and quantification of the role of anthropogenic climate change in the changing likelihoods of frequency, magnitude and/or occurrence of extreme weather and climate events.

This section presents an overview of climate change science relevant to the thesis, including how it influences precipitation extremes; the concept of attribution science and the philosophy of factual/counterfactual; the history of climate change attribution; and finally previous research on extreme event attribution with a focus on extreme rainfall. The climate of Kenya is first presented as a preamble.

2.1 Kenyan Climate

East Africa is one of the most meteorologically complex regions on the African continent (Nicholson, 2017; Cook & Vizy, 2013; Rowell et al., 2015). The high seasonal and interannual variability of rainfall experienced in the region is a result of the complex interaction between local factors, regional circulation patterns and remote forcings/teleconnections. Topographic heterogeneity, large latitudinal extent, large inland water bodies and extensive coastal lowlands are some of the local factors that characterise the region. Regional circulation factors include the Inter-tropical Convergence Zone (ITCZ), Madden-Julian Oscillation (MJO), Quasi-Biennial Oscillation (QBO) and East African Low-Level Jet (EALLJ). Remote teleconnections include the Indian Ocean Dipole (IOD), El Nino Southern Oscillation (ENSO) and variations in the position and strength of the subtropical high-pressure cells (Mascarene, St. Helena, Azores and Arabian highs). Kenya lies astride the equator and is situated between longitudes 34°E to 42°E and latitudes 5.5°N to 5°S. Uganda borders it to the west, Tanzania to the south, Indian Ocean to the southeast, Somali to the east, and Ethiopia and Sudan to the north (see, Figure 2.1.) Rainfall in Kenya is modulated from one season to the other by the interaction between the ITCZ and perturbations in the global and regional circulation as well as with changes in mesoscale systems initiated by land surface heterogeneity induced by variable vegetation characteristics, large lakes and topography. The Great Rift Valley is a dominant geographical feature of the region, whose eastern and western branches run meridionally through Kenya and

Tanzania and lie between highland areas comprising mountains e.g. Mt Kenya. At the heart of the eastern branch are Lake Victoria, the world's largest tropical lake, and other lakes. The valley is flanked by the Indian Ocean coastline and the large dense Congo rainforest to the east and west, respectively.

The three main moisture sources for rainfall in the region are therefore Lake Victoria, the Indian Ocean, and the humid layer of the Congo airmass. The contrasted topographical settings induce widespread dynamic effects and sub-synoptic disturbances through mesoscale circulation systems. For instance, the highlands perturb uniform flow and create lee rain shadows as they block the flow of moist airmass either from the Congo basin or the Indian Ocean (Ogwang et al. 2014; Camberlin et al., 2014). Mesoscale flows form a coupling between Lake Victoria and the surrounding mountains leading to storm formation on highland regions during the afternoon, and over the lake at night, as a result of lake-land thermal contrast (land and sea breezes) (Anyah, et al., 2006; Thiery et al., 2016). The topography also modulates the speed of the East African low-level jet due to orographic channelling (Bernoulli effect; Indeje et al., 2001; Nicholson, 2016). To the east is the low-lying coastline and semi-arid regions which have a drier climate than that of Lake Victoria basin and Mt Kenya. Nevertheless, the region experiences occasional flooding such as that experienced in Mombasa in April 2018 and Garissa and Moyale in October 2019 (Author analysis; KMD, 2018; KMD, 2019).

Kenya experiences a bimodal rainfall distribution. The main rainfall season, 'long rains' occurs in March-April-May (MAM) while the 'short rains' season occurs in October-November-December (OND) (e.g. Nicholson, 1996). The zonal arm of ITCZ, which lags the overhead sun by about 3-4 weeks, delineates the regional seasonal characteristics. Intra-seasonal characteristics (onset, cessation, number, and intensity of dry and wet spells) influence the seasonal distribution of rainfall. Several attempts have been made to delineate climatological zones in Kenya for the purpose of agriculture, risk mapping, prediction, analysis of interannual variability and general planning and management of all rainfall dependent activities (Camberlin & Planchon, 1997; Indeje & Semazzi, 2000; Muhindi, et al., 2001; Nicholson et al., 2012; Ogallo, 1989). Most of these studies employed principal component analysis including clustering techniques and linear correlation. The climatological zones that are commonly used and identified in most regionalization schemes are shown in Figure 2.1. The spatial distribution of seasonal rainfall has been found to delineate these zones.

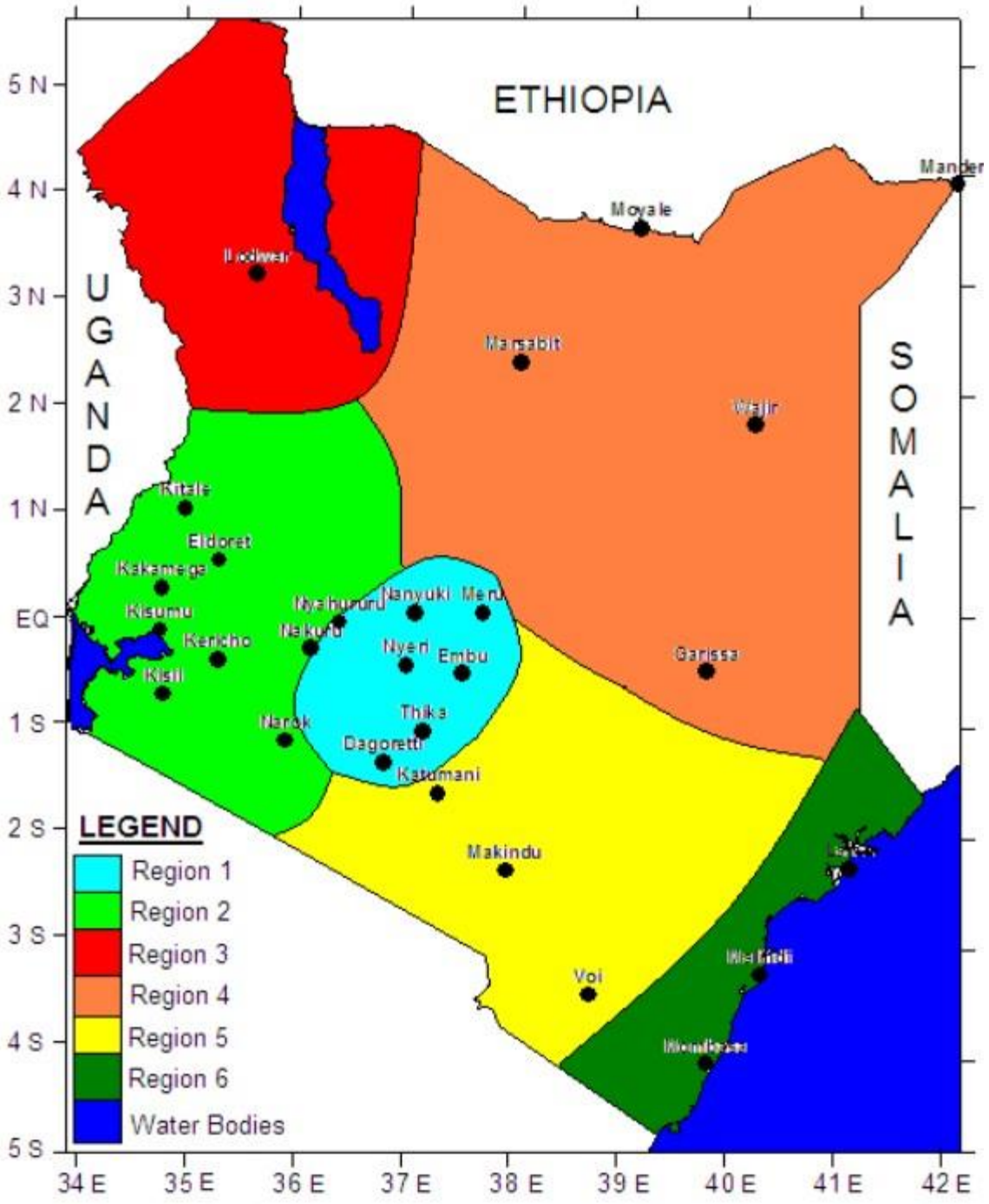

Figure 2.1 Map showing the six climatic zones in Kenya: Central Highlands (Region1), Lake Victoria Basin and Highlands west of the Rift Valley (Region 2), North-western (Region 3), Northeastern (Region 4), South-eastern (Region 5), the Coastal strip (Region 6). The water bodies shown are Lake Victoria to the west and the Indian Ocean to the east. Source: Muita et al., 2016.

Region I: Central Highlands including Nairobi area

The region encompasses the counties of Nairobi, Nyandarua, Laikipia, Nyeri, Kirinyaga, Murang'a, Kiambu, Meru, Embu and Tharaka Nithi.

Region II: Lake Victoria Basin and Highlands west of the Rift Valley

It comprises the counties of Siaya, Kisumu, Homabay, Migori, Kisii, Nyamira, Trans Nzoia, Baringo, Uasin Gishu, Elgeyo-Marakwet, Nandi, Nakuru, Narok, Kericho, Bomet, Kakamega, Vihiga, Bungoma and Busia.

Region III: North-western

It includes counties of Turkana, West Pokot, and Samburu

Region IV: North-eastern

It encompasses counties of Marsabit, Mandera, Wajir, Garissa and Isiolo.

Region V: South-eastern

It includes the counties of Kitui, Makueni, Machakos, Kajiado and Taita Taveta.

Region VI: The Coastal strip

It comprises the counties of Mombasa, Tana River, Kilifi, Lamu and Kwale.

The above climatological zoning is based on commonality in climate drivers and homogeneity in climate characteristics. The Lake Victoria Basin, highlands west of the Rift Valley, central and south Rift Valley and central highlands including Nairobi area are climatologically wetter than the rest of the regions in the country, which are mainly arid and semi-arid lands (ASALs). ASAL regions like North-eastern, North-western, and South-eastern lowlands experience a dry period of about 6 or more months in a year. For the coastal strip, the peak rainfall month is May with very little rainfall received in March. In addition, the coastal strip receives rainfall between June and August (JJA) in third rainfall season with less overall precipitation compared with MAM and OND.

The MAM season coincides with a transition from equatorial northeast monsoons of December-January-February (boreal winter) and southeast monsoons of June-July-August (boreal summer) (e.g., Anyamba, 1983; Okoola, 1999). In MAM, the average flow across the troposphere is easterly. The temporal distribution of rainfall comprises several 5-day to 10-day wet spells, punctuated by dry spells (e.g., Camberlin & Okoola, 2003). The main drivers of MAM intraseasonal and inter-annual rainfall variability are relatively well studied and are related to zonal wind anomalies, advection of moisture and zonal propagation of convection (Camberlin and Wairoto, 1997; Okoola, 1999; Camberlin & Okoola, 2003; Pohl & Camberlin, 2006a; Hastenrath et al., 2010; Pohl & Camberlin, 2011; Omondi et al., 2012; Hogan et al., 2015; Nicholson, 2017; Vellinga & Milton, 2018).

Teleconnections or modes of inter-annual tropical SST variability and large-scale circulation anomalies have been found to have a strong influence on MAM rainfall. SST modulation is largely due to oceanic processes, mainly vertical and horizontal advection, and upwelling. Each individual mode may have a modest effect on the season, however, when combined, they could account for 30-60% of the variability in yearly rainfall in the region (Vellinga & Milton, 2018). These modes can modify the large-scale subsidence over the region during MAM season whereby SSTs in the western Indian Ocean induce an anomalous boundary-layer heating of the lower troposphere (Funk, 2018). For instance, Hoell et al. (2017) and Funk et al. (2018) have connected the rise in the number of drier MAM seasons from 1981 to 2016 with warming of the Indo-Pacific SSTs, which is associated with the strengthening of the Indian Ocean branch of the Walker Circulation. Similarly, Liebmann et al. (2014) have linked the observed drying trend in the season from 1979 to 2012 to the sensitivity of weather systems to the increased zonal SST gradient between Indonesia and the central Pacific. Lyon (2014) has related the MAM rainfall decline after 1998 to natural multi-decadal variability in the tropical Pacific. Ogallo et al. (1988) found variability influence from Indian Ocean Dipole (IOD) to be weak for MAM compared to OND season while Vellinga and Milton (2018) found significant correlations of MAM rains to SST conditions in the western Indian Ocean but weaker correlations in other parts of the tropical oceans.

The MJO is responsible for most of the seasonal weather variability in the global tropics (Madden and Julian, 1994). It is characterised as an eastward moving 'pulse' of cloud and rainfall near the equator that typically recurs every 30 to 60 days. Most studies link MJO to intra-seasonal spells of enhanced or suppressed MAM rainfall in East Africa, depending on the MJO phase (e.g., Pohl & Camberlin, 2006a; Hogan et al., 2015). Years of high MJO amplitude (phases 2–4) are characterised by earlier onsets and higher seasonal amounts (Pohl & Camberlin, 2006a). MJO was found to be in an active phase (with the main centre of enhanced convection concentrated over the western Indian Ocean) during the high rainfall events of 1981, 1990, 1997, 2010, 2013, 2016 and 2018 (Camberlin, 2006a; Kilavi et al., 2018).

The QBO is a quasi-periodic oscillation of the equatorial zonal wind between easterlies and westerlies in the tropical stratosphere. It moves in sympathy with stratospheric wind oscillations, being westerly at one phase, and reversing to easterly at the other phase with an average period of 23-33 months. Ogallo et al. (1994); Indeje & Semazzi (2000) and Hogan et al. (2015) found the westerly phase of the QBO to be associated with enhanced rainfall over East Africa in the MAM season.

The influence of tropical cyclones on East Africa weather depends on their relative position and intensity. Tropical cyclones occurring in the Indian Ocean are known to interfere with the normal low-level flow of

winds. For instance, during 2018 MAM rainfall season, an anomalous low-level westerly wind pattern across the equatorial western Indian Ocean created by tropical cyclone Dumazile and tropical storm Eliakim and Fakir was linked to enhanced rainfall activities over most parts of Kenya (Kilavi et al., 2018). The position, strength, and orientation of the subtropical high-pressure systems in the Southwest Indian Ocean (Mascarene High), southeast Atlantic Ocean (St Helena High), North Atlantic Ocean (Azores/Saharan High), and the Arabian High to the northeast influence East Africa weather. The differential strength of the sub-tropical high-pressure systems determines the relative positions of the ITCZ and the associated weather systems. The inter-hemispheric meridional pressure gradient favours advection of warm moist maritime air from Indian Ocean and aid in the propagation of weather systems. The northeast trades bring relatively dry air (low relative humidity) and favour low-level subsidence.

Few studies have explored the dynamical drivers of flood-inducing MAM rainfall events in Kenya. Camberlin and Wairoto (1997) examined the relationship between intra-seasonal wind anomalies and wet spells over Western Kenya. They found an association with the slow-down of the easterlies, or even, in extreme wet spells, its reversal i.e westerly flow, and anomalous convergence. Pohl and Camberlin (2006) established that 80% of wettest episodes in the Kenyan highlands result from deep atmospheric convection associated with high Madden-Julian Oscillation (MJO) amplitude. Kilavi et al., (2018) and Finney et al., (2019) investigated the interacting influence of low-level westerlies, the MJO and tropical cyclones on the 2018 MAM extreme rainfall. They found that days characterised by westerly moisture flux with active MJO in the Indian Ocean (phase 2-4) are linked to a higher frequency of wet spells with an increased likelihood of one or more tropical cyclones in the southwest Indian Ocean. These studies agree that the establishment of anomalous westerly flow over equatorial Africa corresponds to a large scale zonal gradient in lower-level pressure between the Atlantic (high) and Indian (low) Oceans.

Most global climate models have been found to misrepresent the East African rainfall variability — especially the seasonal cycle by overestimating the OND rains and underestimating the MAM rains (Li & Xie, 2014). The 'East African climate paradox' (Rowell et al., 2015) where an increased frequency of droughts and a general drying trend has been observed since early 1990s (e.g., Funk et al., 2008; Liebmann et al., 2014; Maidment et al., 2015; Nicholson, 2016a; Ongoma & Chen, 2016) while global climate model projections show increases in rainfall (Meehl et al., 2007; Otieno & Anyah, 2012;) has spawned scientific interest. Few hypotheses have been presented to explain this paradox. Giannini et al., (2018), argued that confidence and reliance in projections of future increase in rainfall in East Africa is limited due to substantial biases in simulations of the regional climate, and discrepancy in the modelled versus observed tropical

Pacific and Indian SST trends. They pointed out the role and effect of the complex East African topography in advection of moisture from the Indian Ocean and Congo Basin, and on whether the current cooling of the tropical eastern Pacific is due to internal variability alone or partly attributable to evolving La Niña-like conditions due to increasing GHGs in the atmosphere. Tierney et al., (2015) demonstrated how simulated El-Niño-like shifts tend to unrealistically increase annual rainfall through the effects of overestimated short rains. According to Batté & Déqué, (2011), the paradox can partly be explained by a limited understanding of the complexity of the interactions between local, regional, and large-scale processes in the tropics making model simulations less robust compared to other regions.

Nonetheless, few studies have attempted to evaluate the possible role of human influence in the increased frequency of droughts in the MAM season. Hoell and Funk (2014) and Funk et al. (2018) linked the increasing frequency of drier MAM seasons in the period 1981-2016 to warming Indo-West Pacific Sea surface temperatures (SST), with strong anthropogenic influence on the north-western Pacific associated with intensification of Indian Ocean branch of the Walker Circulation. Similarly, Liebmann et al. (2014) linked the observed MAM 1979-2012 drying trend to the sensitivity of weather systems to increased zonal SST gradient between Indonesia and the central Pacific, attributable to anthropogenic climate change. Lott et al. (2013) concluded that human influence on climate enhanced the probability of rainfall anomalies at least as dry as that of the MAM 2011 drought in East Africa by a small factor. On the other hand, Marthews et al. (2015) and Uhe et al. (2017) found no anthropogenic influence on the likelihood of low rainfall observed during the 2014 MAM and 2016 October-November-December (hereafter, OND) 'short rains' respectively, although they could not rule out the influence on other variables like surface air temperature and net incoming radiation at the surface. Kew et al. (2021) repeated several of the previous studies with multiple models and concluded that there was an absence of a statistically significant human-influenced climate signal in the periods of lower rainfall.

2.2 General Climate Change

The climate system comprises five interacting components: the atmosphere, hydrosphere, cryosphere, biosphere, and lithosphere (Chen et al., 2021). The main factors affecting the global climate system are forcings, feedbacks and internal variability. Forcings are factors imposed externally onto the climate system while feedbacks are a result of interaction between different processes in the system whereby one process triggers change in the other. Climate feedback can amplify (positive feedback) or dampen (negative feedback) the response of the climate to a given forcing or internal variation. The climate system shows

internal variability (a natural process that result from complex interactions between components, such as the coupling between the atmosphere and ocean) both in the presence and absence of forcings imposed on it. An ongoing and accelerating increase in global and regional surface temperature has been observed since the mid-20th century (e.g., IPCC 2021; IPCC, 2013; Hegerl et al., 2007; Drost et al., 2010; Gillett et al., 2012; Fischer & Knutti, 2015; Jones et al., 2013). Possible causes of this warming could be changes in solar irradiance (e.g., sunspot numbers), the composition of the earth's atmosphere (e.g. presence of greenhouse gases, aerosols and dust), properties of the earth's surface (albedo, vegetation, permeability and water storage) and oceanic oscillation (quasi-periodic change of processes of ocean heat intake and release). Orbital parameters have also been considered as a possible cause although they occur at very slow timescales.

The dominant mechanism to which this change has been attributed is human activity through the emission of greenhouse gases and aerosols in the atmosphere and emissions from land (e.g., IPCC 2021; IPCC, 2013; Bindoff et al., 2013a; Mirle et al., 2013). Multiple lines of evidence supporting the attribution of recent climate change to human activities have been established. The basic understanding of the climate system shows that the levels of greenhouse gases in the atmosphere have risen, and their warming properties (well established with historical estimates) suggests that the recent warming trend is unusual and cannot be solely attributed to natural forces. The natural range of carbon dioxide in the atmosphere over the last 650,000 years (determined from ice cores) is 180-300 ppm (parts per million) (Zorita et al., 2000). The current concentrations stand at 410 ppm (IPCC, 2021) which is far beyond the upper limit of the historical range.
The observed clustering of global warm years would be very unlikely to occur by chance in a stationary climate. In its extensive assessment of literature, the six successive IPCC assessment reports (AR) have assigned increasing levels of certainty to anthropogenic influence on the climate system. AR5 (IPCC, 2013) concluded that "warming of the climate system is unequivocal, and since the 1950s, many of the observed changes are unprecedented over decades to millennia. The atmosphere and ocean have warmed, the amounts of snow and ice have diminished, sea level has risen, and the concentrations of greenhouse gases have increased" (IPCC, 2013: SPM, p4). Since AR5, improvements in observational estimates and paleoclimate information provide a comprehensive view of each component of the climate system and its changes to date. New climate model simulations, new analyses, and methods combining multiple lines of evidence led to improved understanding of human influence on a wider range of climate variables, including weather and climate extremes. Methodological advances and new datasets contributed approximately 0.1°C to the updated estimate of warming in AR6 (IPCC, 2021). AR6 concluded that "it is unequivocal that human

influence has warmed the atmosphere, ocean and land and that widespread and rapid changes in the atmosphere, ocean, cryosphere, and biosphere have occurred" (IPCC, 2021: SPM, p5).

Figure 2.2 illustrates observed warming associated with increase in GHGs and all other forcings since the industrial revolution in the 1850s. Evidence shows that most of the warming is due to well-mixed greenhouse gases in which their emissions and concentrations are on the rise. Figure 2.3 (a) shows that the climate system has warmed at unprecedented rate in at least the last 2000 years, and this is attributable to human influence (b).

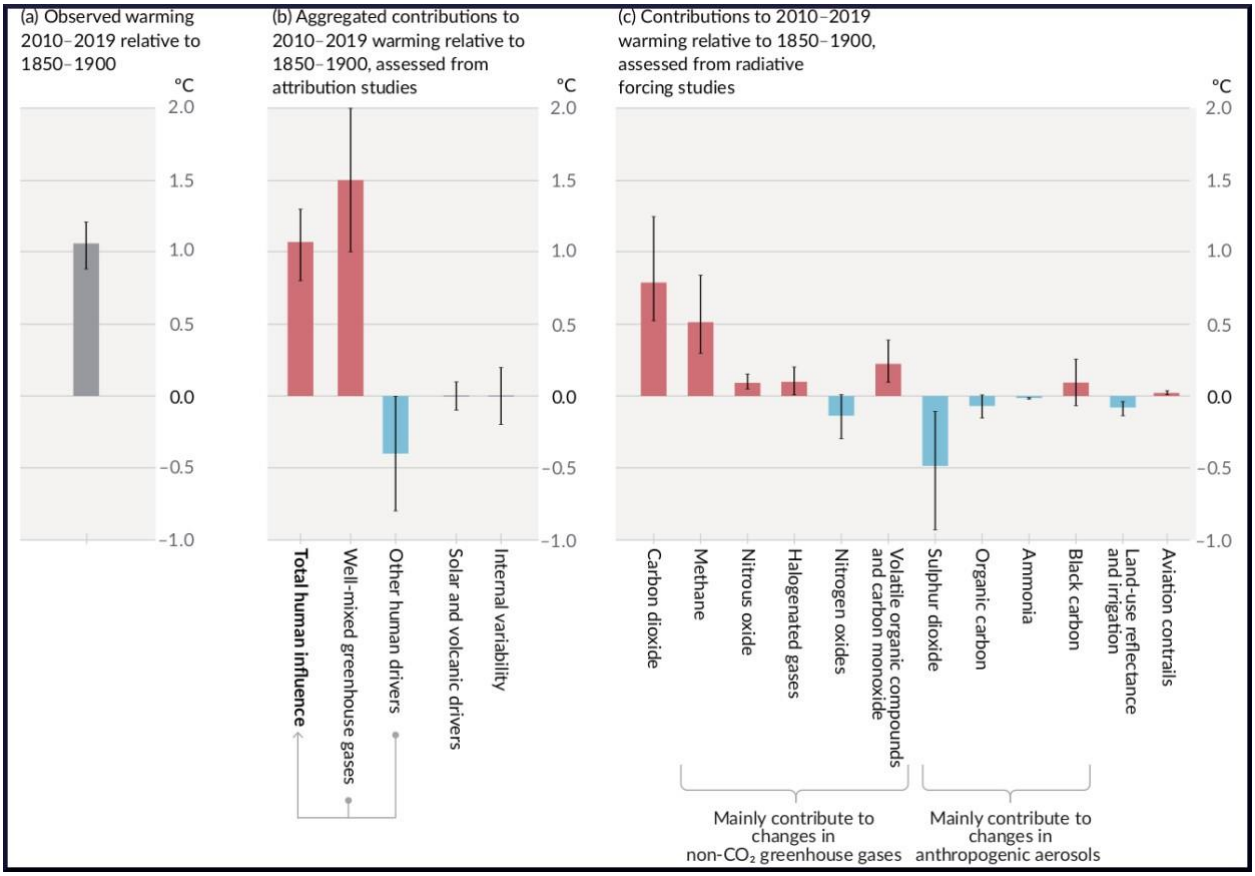

Figure 2.2 Observed warming in the decade 2010-2019 relative 1850-1900 period, (b) Contributions to warming in the decade 2010-2019 relative 1850-1900 period based on attribution studies and, (c) Contributions to warming in the decade 2010-2019 relative 1850-1900 period based on radiative forcing studies. The whiskers show the assessed likely ranges, and the mid-points show the warming level. Global surface temperature was 1.09°C higher in 2011–2019 than 1850– 1900. The observed warming is mainly driven by human activities with greenhouse gas warming partly masked by aerosol cooling. Source: IPCC (2021; Figure SPM.2; page 8).

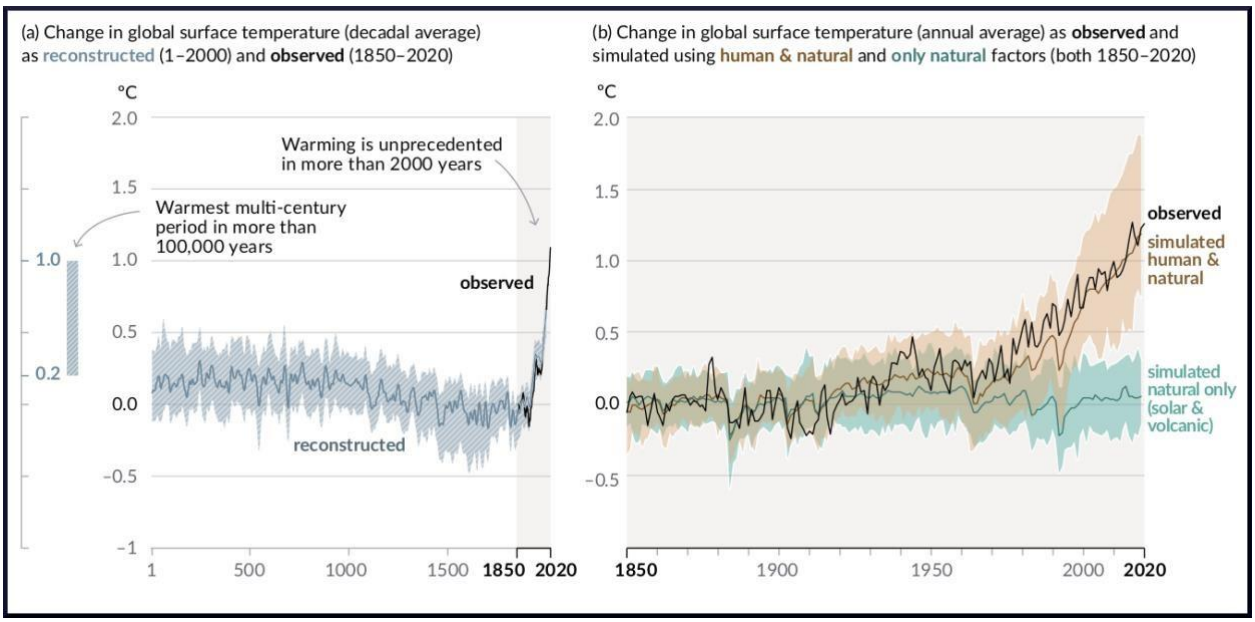

Figure 2.3 Changes in observed global surface temperature. (a) Changes in global surface temperature reconstructed from paleoclimate archives (solid grey line, years 1–2000) and from direct observations (solid black line, 1850–2020). (b) Changes in annual average global surface temperature (GST) from 1850–1900 (black line); Coupled Model Intercomparison Project Phase 6 (CMIP6) climate model simulations of the temperature response to both human and natural drivers (brown) and the temperature response to only natural drivers (solar and volcanic activity, green). Solid coloured lines show the multi-model average, and coloured shades show the very likely range of simulations. Source: IPCC (2021; Figure SPM.1; page 7).

A few key findings from AR6 WGI (IPCC, 2021) are outlined as follows.

- The last four decades (1981-2020) have been successively warmer than any decade that preceded it since 1850. In the first two decades of the 21st century (2001–2010 and 2011–2020), GST was 0.99°C and 1.09°C higher relative to 1850–1900 average, respectively. Larger increases are seen over land than over the ocean. The likely range of total human caused GST increase from 1850–1900 to 2010–2019 is 0.8°C to 1.3°C, with a best estimate of 1.07°C.
- Well-mixed GHGs contributed a warming of 1.0°C to 2.0°C while aerosols contributed a cooling of 0.0°C to 0.8°C. The changes on GST by natural drivers and internal variability are –0.1°C to +0.1°C and –0.2°C to +0.2°C, respectively. Well-mixed GHGs and human caused stratospheric ozone depletion are the main drivers of tropospheric warming since 1979 and lower stratosphere cooling between 1979 and the mid-1990s, respectively.
- With every additional 0.5°C of global warming (from 2021 levels), there will be clear discernible increases in the intensity and frequency of heavy precipitation events.
- Globally averaged precipitation over land has increased at a faster rate since the 1980s. The pattern of observed precipitation changes and near-surface ocean salinity since the mid-20th century, global retreat of glaciers since the 1990s and the decrease in Arctic Sea ice area

between 1979–1988 and 2010–2019 are attributable to human influence. Human-induced climate change is also the main driver of decrease in Northern Hemisphere spring snow cover since 1950 and surface melting of the Greenland Ice Sheet over the past two decades.

- No significant trend has been found in change in Antarctic Sea ice area from 1979 to 2020 due to regionally opposing trends (has experienced both increases and decreases), and large internal variability.

2.3 Precipitation Extremes under Climate Change

Precipitation extremes are expected to respond to radiative forcing of climate, and the associated changes in the climate system. The atmospheric and surface energy budget plays a critical role in the hydrological cycle. The overall intensity of the hydrological cycle and hence global-mean rainfall is primarily constrained by the availability of energy, not moisture. But it is indisputable that lower-tropospheric water vapour will increase as the climate warms through Clausius Clapeyron (C-C) relationship (Boer,1993; Allen and Ingram, 2002; Trenberth, 2011). The C-C equation gives the relationship between saturation vapor pressure and temperature for a unit parcel of air. The C-C equation is given by:

$de_s / e_s = LdT/RT^2$

Where e_s is the saturation vapour pressure at temperature T, L is the latent heat of vaporization and R is the gas constant

According to the equation, the change in the water-holding capacity of the atmosphere with local atmospheric temperature is about 7% K^{-1}. The importance of understanding changes in the amount of water vapour in the atmosphere is its role in energy transfer by latent heat fluxes, precipitation patterns/evaporation and freshwater exchanges in the ocean (O'Gorman & Muller, 2010). Otto (2016) illustrates how a shift in GMST can correlate with a large change in the frequency and magnitude of extremes, as shown in Figure 2.4: — (b) illustrates less light precipitation and more extreme precipitation events are expected. With this, warm days will become more frequent with warm spells lasting longer and warmer and more intense rainfall events becoming more frequent.

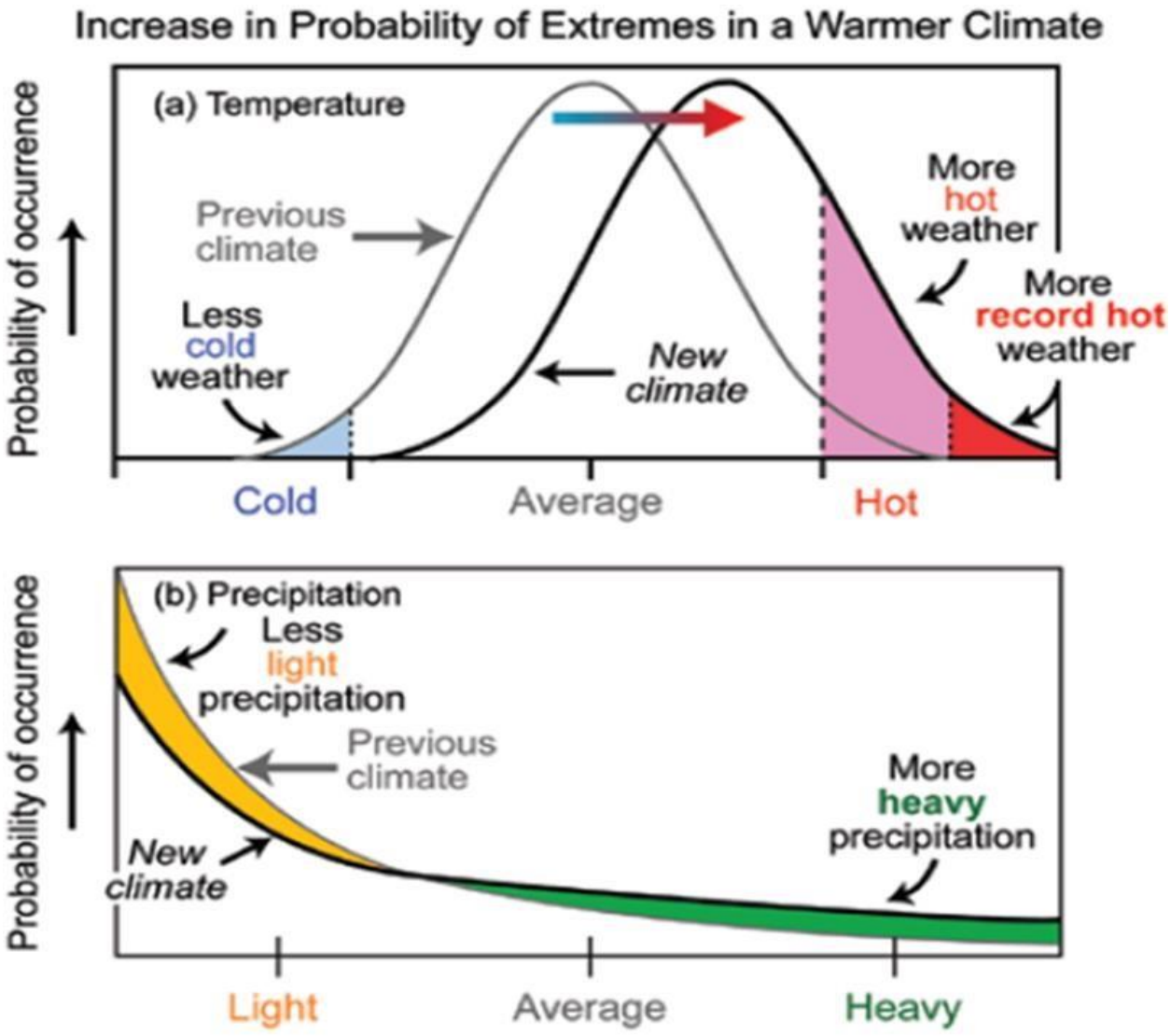

Figure 2.4 Changes in probabilities of temperature and precipitation extremes in a warmer climate resulting from a shift in the mean global surface temperature. Source: Otto (2016).

In Figure 2.5, O'Gorman (2015) illustrates how annual maximum daily precipitation has intensified in 15° latitude bands with GMST and with local mean temperature rise since the mid-20th century. O'Gorman (2015) notes, however, that precipitation extremes seem to be more sensitive to regional land temperature changes in the tropics than mid-latitudes. In the tropics, for example, precipitation extremes are highly sensitive to complex small-scale processes like moist convection/upward velocities and to interannual variability (e.g., warm anomalies associated with ENSO events etc.). Changes in relative humidity with GMST are however not well understood yet, although changes in rainfall intensity are expected to increase proportionately with moisture increase. Characteristics of rain seem to be more apt to change and thus

prospects are greater for changes in the extremes of floods and droughts than in total precipitation amount (Trenberth et al., 2003). A strong relationship exists between total column water vapour (precipitable water) and sea surface temperatures (SSTs) over global oceans. Largest average precipitable water values occur over the Tropical Pacific Warm Pool where highest large-scale values of SST typically reside. Subsequently, precipitation patterns in the Tropics mimic changes in precipitable water and SSTs. In higher latitudes in both hemispheres, the mean precipitable water falls off along with SSTs although precipitation has a secondary maximum over the ocean regions associated with storm tracks (Trenberth, 2011).

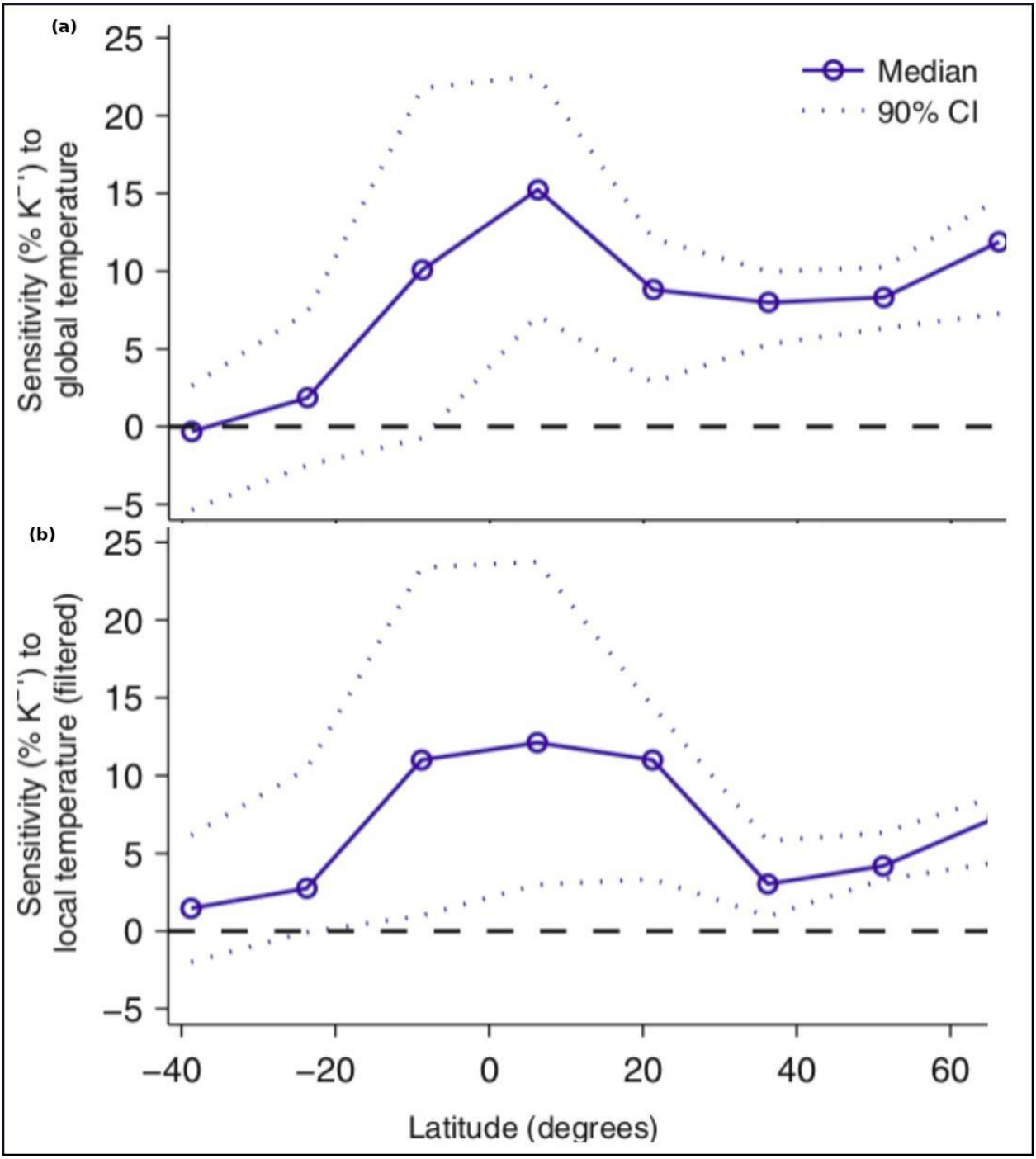

Figure 2.5 Sensitivities of observed annual-maximum daily precipitation over land (solid lines with circles; dotted lines show the 90 % confidence interval) in 15° latitude bands relative to (a) global mean surface temperature and (b) mean local surface temperature. The median sensitivity is plotted for each 15° latitude band. Source: O'Gorman (2015)

2.4 Reasons for Concern

"Reasons for Concern" (RFCs) communicate the scientific understanding of risks in varying levels of climate change as a function of GMST (O'Neill et al., 2017). RFCs have been illustrated using the "Burning Embers Diagram" (Figures 2.6 and 2.7) in IPCC reports. Figure 2.6 is the embers diagram adopted from (IPCC, 2018) illustrating risks and impacts at different levels of warming. Changing likelihoods and intensities of extreme weather events and their impacts are one of the RFCs. Risks associated with extreme weather events (RFC2) encompass risks to human health, livelihoods, assets, and ecosystems resulting from heat waves, floods, droughts (and associated wildfires) and tropical cyclones/coastal flooding. Based on detection and attribution of impacts of extreme events on coral reefs and human health, the transition from undetectable to moderate risk is located at the recent and current temperatures (Skirving et al., 2019). Bleaching of coral reefs is due to increase in near-surface ocean temperatures whereas impacts on human health is through the loss of life and/or property from extreme heat and heavy precipitation events confounded by high levels of vulnerability and exposure (IPCC, 2018). The transition from moderate to high risk associated with extreme events is expected to occur at 1.5 °C above the pre-industrial level where duration, intensity and spatial extent of heatwaves and warm spells are expected to increase as a result of 25–30% increase in daily maximum temperatures above the historical period (1961-1990) by 2035. Frequency and intensity of heavy precipitation events over land is expected to increase with a reduction in return period for historical 1-in-20-year precipitation events globally to about 1-in-14-year or less by 2046–2065 (IPCC, 2018).

Improving the adaptive capacity of societies is key in mitigating the impacts of extreme events. In some regions like Asia and Africa, risks are expected to increase even when temperature change remains moderate or constant, since exposure and vulnerability to climate-related hazards are increasing significantly due to other human factors like population growth, urbanisation, and migration (e.g., Thornton & Gerber, 2010)

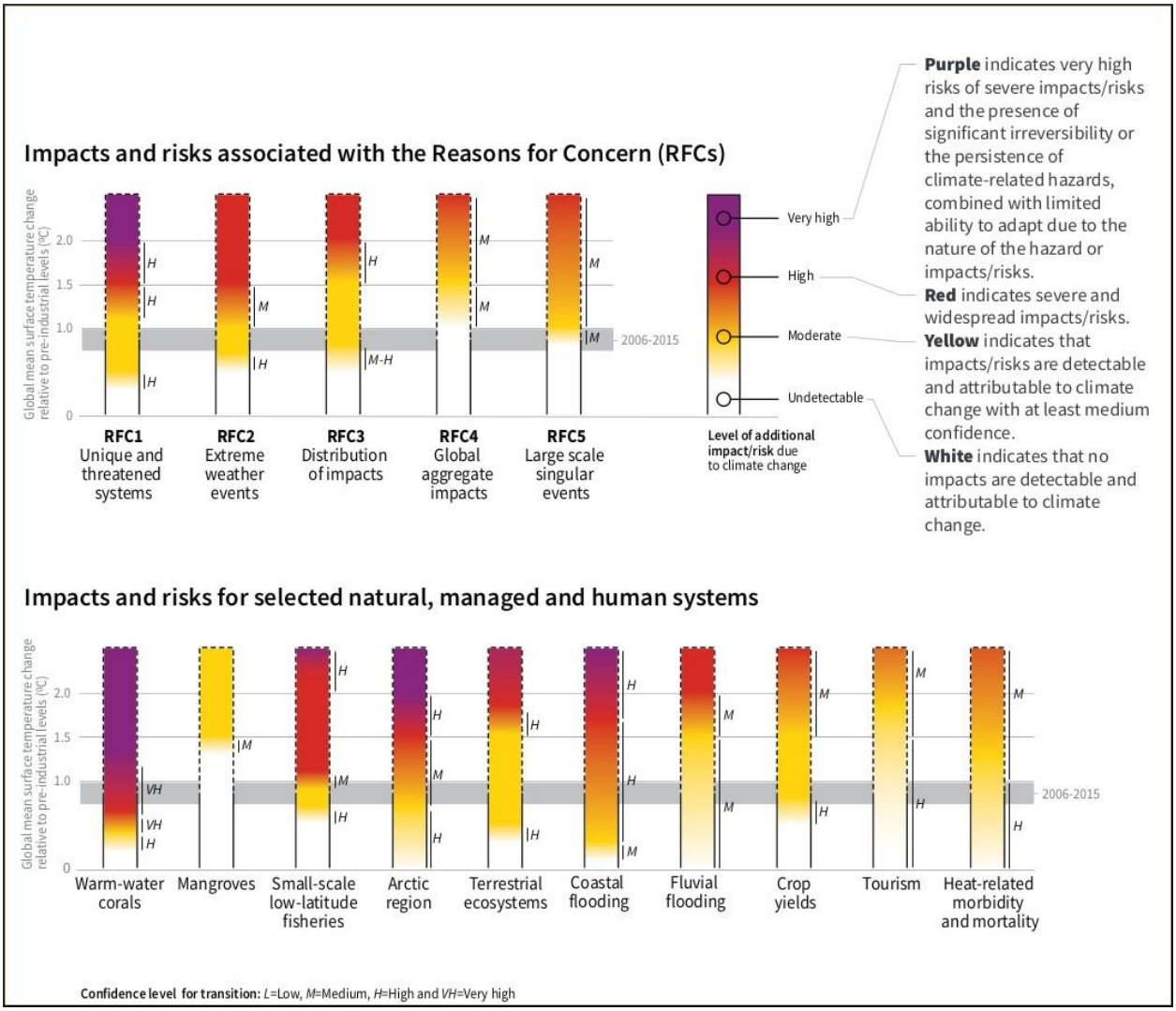

Figure 2.6 Burning Embers Diagram illustrates the five reasons for concern for different levels of additional impact or risk resulting from 0 up to 2 degrees of warming for people, economies and ecosystems across sectors and regions. RFC2 for extreme events shows hat at the current temperature conditions, impacts are detectable and attributable to climate change with medium confidence. At 1.5°C to 2°C, impacts and risks are expected to be severe and widespread. Source: IPCC (2018; Figure SPM.2; page 11).

Figure 2.7 is the embers diagram for Africa adopted from (Trisos et al., 2022) illustrating risks and impacts at different levels of warming. In Africa, mean and extreme temperatures are rising. The rate of surface temperature increase has generally been more rapid in the continent than the global average, with human-induced climate change being the dominant driver (IPCC, 2021). Above 1.5°C there is a high risk of large regional crop losses, increasing poverty and inequality, increasing disease exposure, increasing drought, and increasing heat mortality. Above 2°C, the risks are even higher: high risk of widespread crop yield loss, widespread heat-related mortality risk, 7 to 18% of species at risk of extinction, and over 30% decline in

fisheries catch, and potential and severe risks of malnutrition (Trisos et al., 2022). In scenarios with low adaptation, transition to high risk i.e., widespread, and severe impacts have already begun for biodiversity loss.

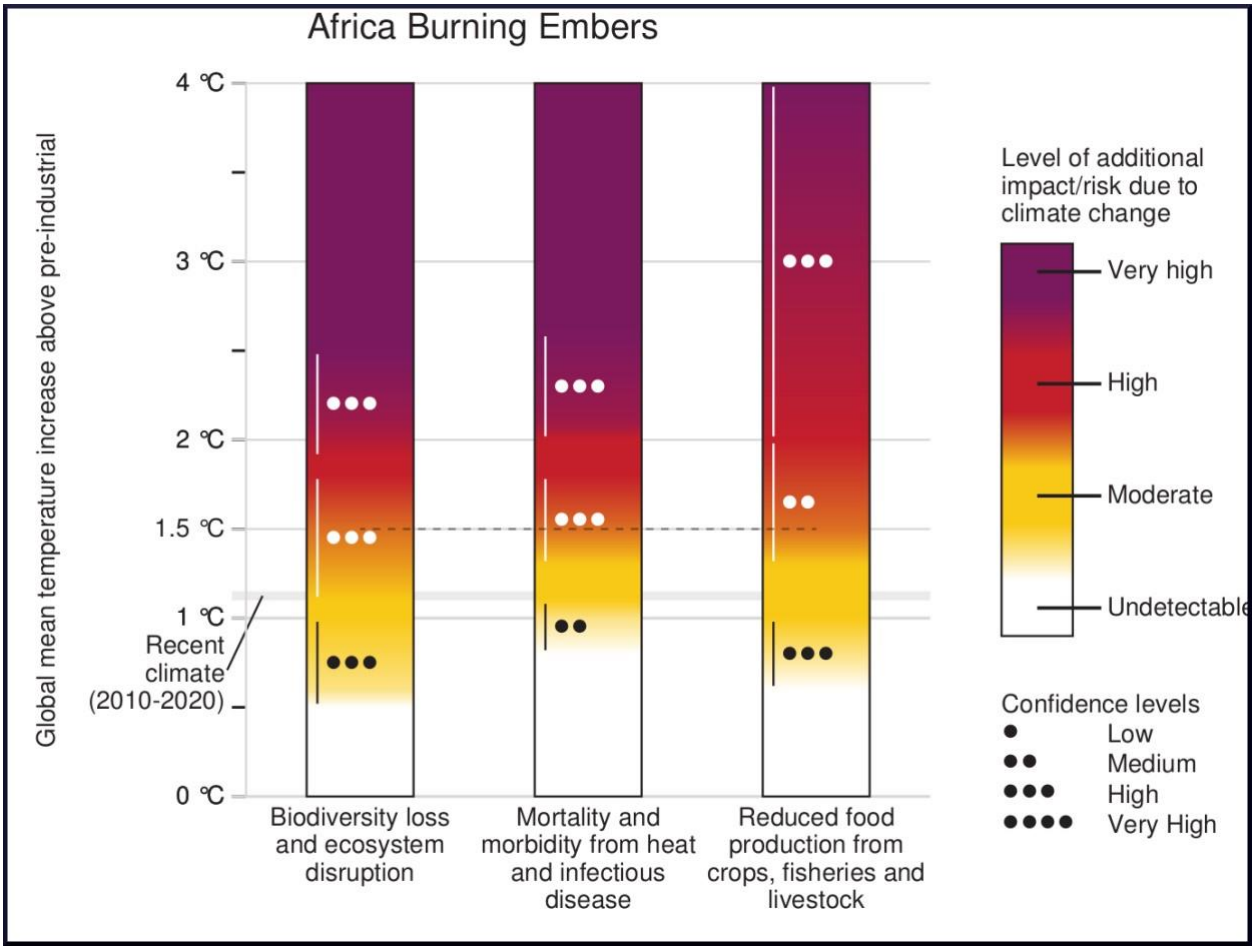

Figure 2.7 Burning Embers Diagram showing increasing risk due to climate change for selected key risks in Africa. All the risks have transitioned to moderate-high risk by the recent level of global warming 2010-2020 (1.09°C). Source: Trisos et al., 2022.

Figure 2.8 shows the location of people affected by climate hazards and the number of people affected by floods in Africa between 2010 and 2020. An estimated 337 million people were affected by natural disasters in Africa between 2000-2019, in which floods accounted for 80% and droughts for 16% (Trisos et al., 2022). Between 2018 and 2019, 6 million people were displaced by weather-related disasters in Sub-Saharan Africa and 46,078 deaths from natural disasters were reported between 2000 and 2019 (CRED, 2019). Globally, Sub-Saharan Africa reported the largest number of mortalities associated with floods since 1990 (Tellman et al., 2021).

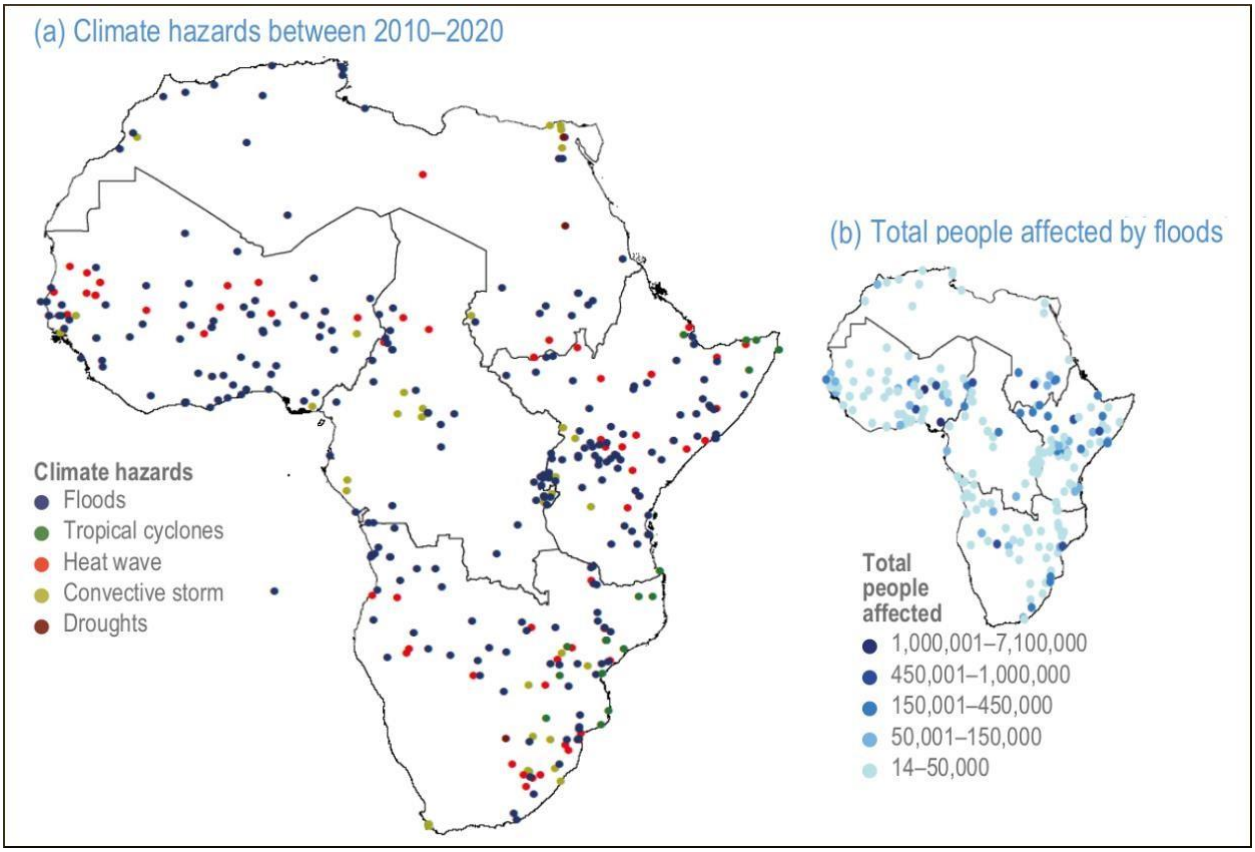

Figure 2.8 Map showing the location of all reported climate hazards (a) and people affected by floods (b) in Africa. Over 166 million people were reported to be affected by climate hazards from 2010–2020. Source: EMDAT and CRED (2020).

2.5 Attribution of Climate Change

Climate change is the change in the state of the climate that can be identified (e.g., by using statistical tests) by changes in the mean and/or the variability of its properties and that persists for an extended period, typically decades or longer. For instance, in comparing an average (e.g., regionally or globally) characteristic of a variable (e.g., temperature or rainfall) for different periods long enough (e.g., 30-year climatological periods), detecting a significant difference between the two periods implies the system has changed. The trend of the change could either be a deterministic underlying mechanism or simply a tendency in the statistical properties of the process. This inspired the concept of attribution.

"Detection of change is defined as the process of demonstrating that climate or a system affected by climate has changed in some statistical sense without providing a reason for that change" (Hegerl et al., 2010; IPCC, 2013). "Detection of climate change in a time series is done by demonstrating that the change is significantly

different from what can be explained by natural internal variability (i.e., occurrence chance due to internal variability is less than 10%)" (Hegerl et al., 2010). The ability to detect change depends on the signal-to-noise ratio and the relative size of the trend, in terms of amplitude and duration of the change.

Attribution is defined as the process of evaluating the relative contributions of multiple causal factors to a change in climate or the likelihood-magnitude of a specific event, with an assignment of statistical confidence (IPCC, 2013). Attribution of climate change involves both statistical analysis and careful assessment of multiple lines of evidence to demonstrate, within a specified margin of error, that the observed changes are unlikely to be entirely due to internal variability and are consistent with the estimated responses to a given combination of anthropogenic and natural forcings. Consistency of an estimated response to a hypothesised forcing with an observed change is often determined by estimating the amplitude of the hypothesised pattern of change from observations and then assessing whether this estimate is statistically consistent with the expected amplitude of the pattern (IPCC, 2007). It is establishing a cause-effect relationship by separating internal and external drivers/forcings of the climate system responsible for the observed changes.

2.5.1 Factual and Counterfactual Concept

Unequivocal attribution would require controlled experimentation with the climate system, which is not practical. In practice, two climate worlds are compared: the factual, which is the current climatic conditions in which the event to be analysed occurred; and the counterfactual, "the world that might have been", which is the climate system with no influences from anthropogenic forcings. These two-climate worlds are compared by running numerous model simulations using the same climate model with and without anthropogenic forcings. Statistics of these large ensemble runs are analysed and compared. The significant differences in the statistics are attributed to anthropogenic forcings (e.g., Otto, 2015; Uhe et al., 2018; Vautard, 2016; Allen, 2003; Harrington & Otto, 2018).

A strong relationship exists between total column water vapour (precipitable water) and sea surface temperatures (SSTs) over global oceans. Largest average precipitable water values occur over the Tropical Pacific Warm Pool where highest large-scale values of SST typically reside. Subsequently, precipitation patterns in the Tropics mimic changes in precipitable water and SSTs. In higher latitudes in both hemispheres, the mean precipitable water falls off along with SSTs although precipitation has a secondary maximum over the ocean regions associated with storm tracks (Trenberth, 2011). Studies suggest that

anthropogenic influence has changed the spatial distribution of precipitation over global land areas, increased atmospheric water content and high-latitude precipitation (Polson et al., 2013; Lintner et al., 2012).

2.5.2 History of Attribution

Most early formal detection and attribution studies concentrated on variables with high climate change signal-to-noise ratios, good observational data coverage, and consistent signals from different model simulations, mainly using mean surface air temperatures or zonal mean upper air temperatures. To enhance signal-to-noise ratio, the studies generally considered variations on large spatial scales and timescales of several decades or longer. All early studies were on a global scale and focused on "has a human influence on climate been detected? And "how large is anthropogenic change?" The concern was whether the magnitude of the response to greenhouse gas forcing as estimated in the observed record is consistent with the response simulated by climate models. The IPCC's First Assessment Report (IPCC, 1990) concluded that the global mean surface temperature had increased by 0.3 to 0.6°C over the previous 100 years and the magnitude of the warming was broadly consistent with the predictions of climate models forced by increasing concentrations of greenhouse gases. However, there was a limited agreement between model predictions and observations. Back then, climate models were still in the early stages of development. Inadequate knowledge of natural variability and other possible anthropogenic effects on climate and scarcity of suitable observational data, particularly long, reliable time-series, was a huge hindrance. More effort focused on changes observed during the period of the instrumental temperature record, particularly in the last 50 years when human activity increased through rapid industrialization and when observations of the atmosphere above the surface became available.

By the time of the Second Assessment Report (SAR; IPCC, 1996), considerable progress had been made in identifying an anthropogenic effect on global climate. The first area of significant advance was climate models beginning to incorporate the possible climatic effects of human-induced changes in sulphate aerosols and stratospheric ozone. Second is a better definition of background variability of the climate system through multi-century model experiments that assume no changes in forcing. The third is the application of pattern-based methods that attempt to attribute some part of the observed changes in climate to human activities. After assessing literature published mainly between 1990 and 1995, the SAR concluded that "Our ability to quantify the human influence on global climate is currently limited because the expected signal is still emerging from the noise of natural variability, and because there are uncertainties in key factors. Nevertheless, the balance of evidence suggests that there is a discernible human influence on global climate" (IPCC, 1996: SPM).

Detection and attribution studies published before the Third Assessment Report (TAR; IPCC, 2001) were largely still limited to a global scale. Only a handful looked at the continental scale and regional scales and over shorter periods (less than 50 years). The main reason is that averaging over larger regions reduces natural variability "noise", making detection and attribution easier. However, most studies looked at both fixed and temporally varying response patterns unlike studies before SAR which used fixed signal patterns that did not evolve with time. Estimation of internal natural variability using paleoclimatic data and influence of natural climate forcing (volcanic eruptions and solar luminosity) indicated that both could not fully explain 20th-century warming. Many models began to include individual greenhouse gases (as opposed to a carbon dioxide equivalent) and an interactive Sulphur cycle. An explicit treatment of scattering by aerosols (as opposed to using prescribed changes in surface albedo) and inclusion of the effect of increases in tropospheric ozone and a representation of the indirect effect of sulphate aerosols on cloud albedo were also incorporated.

Attribution in the 21st century heralded the rise of "fingerprint" studies, which evaluated the extent to which *patterns* of response (fingerprints) to external forcing from climate model simulations explain observed climate change in observations. These studies enabled detailed comparisons of modelled and observed climate change patterns. Findings of warming in subsurface land temperatures measured in boreholes, warming in ice cores, and corresponding boreholes, warming in subsurface ocean temperatures, the retreat of glaciers, and reductions in Arctic sea-ice extent and snow cover studies were all found to be consistent with the observed warming in surface air temperatures and with model projections of the response to increasing greenhouse gases. However, discrepancies were found between the vertical profile of temperature change in the troposphere in observations and models. The observed lower tropospheric trends could not be resolved by models. There was less confidence in observed variations in the hydrological indicator. General consistency between the changes in mean precipitation in the tropics and changes in ENSO were found. But no consistency was found between observed changes in mean tropical precipitation and model simulations. In the middle and high latitudes of the Northern Hemisphere, the observed increase in precipitation was found to be consistent with most model simulations. The TAR concluded that "Most of the observed warming over the last 50 years is likely to have been due to increases in greenhouse gas concentrations" (IPCC, 2001: SPM page 3).

Studies published from the end of the first decade of the 21st century have substantially stronger evidence. Most are based on analyses of widespread temperature increases throughout the climate system and changes

in other climate variables. The Fourth Assessment Report AR4(IPCC, 2007) concluded that "Most of the observed increase in global average temperatures since the mid-20th century is very likely due to the observed increase in anthropogenic greenhouse gas concentrations". Further improvements in models and analysis techniques led to increased confidence in the understanding of the influence of external forcing on climate. Human fingerprints were found in the increased levels of atmospheric moisture (both close to the surface and over the full extent of the atmosphere). The decline of Arctic Sea ice extent and the patterns of changes in the Arctic and Antarctic surface temperatures were also observed (Barnett et al 2008; Wilson et al., 2010). Increase in the height of the tropopause was associated with tropospheric warming and stratospheric cooling due to an increase in greenhouse gas concentrations (Santer et al., 2009). Indicators of climate extremes and variability, including the annual numbers of frost days, warm and cold days, and warm and cold nights, showed changes that were consistent with the warming (Stott et al., 2011; Christidis et al., 2012a, 2012b). More attention shifted to attribution of climate changes at continental and regional scales, and on variables that could have large impacts on societies. Evidence of human influence on climate grew stronger overtime with a wider range of observational data. A greater variety of more sophisticated climate models including improved representations of forcings, and processes and a wider variety of analysis techniques were used. AR5 (IPCC, 2013), concluded that 'It is extremely likely that more than half of the observed increase in global average surface temperature from 1951 to 2010 was caused by the anthropogenic increase in greenhouse gas concentrations and other anthropogenic forcings together. AR6 (IPCC, 2021) concluded that "It is unequivocal that human influence has warmed the atmosphere, ocean and land and that widespread and rapid changes in the atmosphere, ocean, cryosphere and biosphere have occurred".

Apart from the detection and attribution of long-term trends in extremes, new methodologies/approaches have been developed to answer the question of whether and to what extent external drivers on the climate system have altered the intensity and probability of occurrence of individual extreme weather and climate events (NAS, 2016) (see, section 2.7). Table 2.1 gives a sample of detection and attribution studies of long-term trends in observed records of various climate variables carried out since FAR (1990) on global, continental, and regional scales.

Table 2.1 A sample of studies of Attribution of observed long-term changes (Author's Analysis).

Variable	Observed changes	Attribution of observed changes	Paper citation
Surface temperature change	The period 1981-2020 has been successively warmer than any decade that preceded it since 1850. In the first two decades of the 21st century (2001–2010 and 2011– 2020), GST was 0.99°C and 1.09°C higher relative to the 1850–1900 average, respectively. Larger increases are seen over land than over the ocean. The likely range of total human-caused GST increase from 1850–1900 to 2010– 2019 is 0.8°C to 1.3°C, with a best estimate of 1.07°C	Well-mixed GHGs contributed a warming of 1.0°C to 2.0°C while aerosols contributed a cooling of 0.0°C to 0.8°C. The changes on GST by natural drivers and internal variability are –0.1°C to +0.1°C and –0.2°C to +0.2°C, respectively. Well-mixed GHGs and human-caused stratospheric ozone depletion are the main drivers of tropospheric warming since 1979 and lower stratosphere cooling between 1979 and the mid-1990s, respectively.	IPCC, 2021; IPCC, 2018; Hegerl et al., 2007b; Drost et al., 2010; Gillett et al., 2012; Stott & Jones, 2012
Tropospheric temperature change	There is medium confidence that temperatures in the tropical upper troposphere have warmed faster than those at the surface since 2001, but low confidence in changes prior to 2001 The global troposphere has warmed since the mid-20th century, medium confidence in the northern hemisphere and low confidence in tropics and mid latitudes	Well-mixed GHGs are the main drivers of tropospheric warming Very unlikely that the natural forcing alone could have caused the observed warming	Gulev et al., 2021 Hegerl et al., 2007a
Stratospheric temperature change	The global lower stratosphere has cooled since 1979 It is likely that middle and upper stratospheric temperatures have decreased since 1980, but there is low confidence in the magnitude	Well-mixed GHGs and human-caused stratospheric ozone depletion are the main drivers of lower stratosphere cooling between 1979 and the mid1990s, respectively.	IPCC, 2021; Gillert et al., 2011 Gulev et al., 2021

		The cooling is highly explained by stratospheric ozone depletion due to the presence of ozone-depleting substances in the stratosphere.	
Atmospheric water vapour change	Increase in atmospheric water vapour over oceans consistent with the warming of sea surface temperatures Significant increase in surface-specific humidity since the 1970s over both land and oceans. A very likely decrease in relative humidity over much of the global land area since 2000, particularly over mid-latitude regions of the NH, with increases at northern high latitudes	Anthropogenic warming of sea surface temperatures Anthropogenic warming of surface temperatures over land	Gulev et al., 2021; Willett et al., 2020; Stott et al., 2010; Trenterth 2011b; Sabter et al. 2007
Precipitation changes	Globally averaged precipitation over land has increased at a faster rate since the 1980s High latitudes of the northern hemisphere showed increasing trends in the 20th century. Decreasing trends in parts of the tropics Decline in austral summer precipitation around 45°S and increased around 60°S since 1957 Strong regional to sub-regional variation in trends Low confidence in precipitation trends over the global ocean, linked to uncertainties in satellite retrievals, and limited in situ observations.	Anthropogenic warming especially over land	Min et al., 2008a. Gulev et al., 2021; Douville et al., 2021; al., 2007
Changes in moisture evapotranspiration and stream flow	Regional trends towards drier soils Trends towards earlier timing of snowmelt stream flow in North America since 1950 Regional varying trends in snow flow consistent with changes in temperature in Scandinavian, Europe, and USA	Anthropogenic warming of surface temperatures	Gulev et al., 2021; Douville et al., 2021; Jung et al., 2010. Hidalgo et al., 2001. Wilson et al., 2010. Stahl et al., 2010; Kraukauer & Fung, 2008

	Increases in Arctic River discharge		
Atmospheric circulation	Expansion of tropical cell i.e., pole ward expansion of Hadley cell since 1979 Pole ward expansion of southern Hadley cell during austral summer due to the depletion of Antarctic tropospheric ozone The width of tropical belt has widened since 1979 Trends since 1980 are better characterised and consistent Very likely strengthening of La-Niña-like Walker circulation and a westward shift of the Walker circulation Positive trend in Southern Annular Mode since 1950 Medium confidence in trends toward more frequent central equatorial Pacific El Niño-Southern Oscillation (ENSO) events	Increase in ozone-depleting substances Likely anthropogenic influence for SAM than ENSO	Gulev et al., 2021; Douville et al., 2021; Johanson & Fu 2009; Hu et al., 2013. Fu et al., 2006; Hu & Fu, 2007
Change in global sea level pressure pattern	No clear signal for trends in the strength and position of the permanent and quasi-permanent pressure centres of action since the 1950s Large-scale SLP strongly associated with the changes in modes of natural and internal variability Altered patterns of zonal mean sea level pressure	Anthropogenic influence on sea surface temperatures	Gillert et al., 2003; Gillert & Stott 2009
Ocean salinity and freshwater fluxes	Very likely Atlantic Ocean has become saltier, and the Pacific and Southern oceans have freshened Tendency to increased salinity in subtropical regions of high salinity and regions of low salinity (mostly in the tropics and high latitudes) become saltier	Intensification of the hydrological cycle linked to human influence Increase in greenhouse gases and tropospheric aerosols	Gulev et al., 2021; Boyer et al., 2005; Hosoda et al., 2009; Roemmich & Gilson, 2009
Change in sea level	Rise due to thermal expansion and glacier melting with additional contributions from Greenland and Antarctic ice sheets since the 1970s	Warming highly likely from anthropogenic forcing	Gulev et al., 2021; IPCC, 2019; Domingues et al., 2008; Palmer et al., 2009; Church et al., 2013

Oxygen and ocean acidity	Very high confidence that open ocean surface pH is now the lowest it has been for at least 26 kyr Strong decrease observed in midlatitudes Increased acidification of surface waters since 1980s between 0.0015-0.0024pH units per year High confidence in open-ocean de-oxygenation over most regions of the open ocean during the mid-20th to early 21st centuries, and medium confidence due decadal variability	Increased ocean uptake of carbon dioxide (20–30% of total CO_2 emissions since the 1980s) Increase in CO2 concentrations in the atmosphere and loss of oxygen from the ocean	Gulev et al., 2021; IPCC, 2019; Andrews et al., 2013
Sea ice extent	Decreases in Arctic Sea ice area and thickness. Extent declined considerably in the 21st century The amount decreased by 50% between 2005-2012 Shrinking in Greenland and Antarctic ice sheets	Anthropogenic warming manifested in Arctic amplification	IPCC 2021; IPCC; 2019; Maslanik et al., 2007; Nghiem et al., 2007; Comiso & Nishio, 2008
Change in Glacier mass	Loss of glacier mass since the 1960s. Global glacier mass loss of 278 ± 113 Gt yr^{-1} between 2006 and 2015	Anthropogenic warming of surface temperatures	IPCC, 2019; Hugonnet et al., 2021; Oerlemans, 2005; Yamaguchi et al., 2008; Huss & Bauder, 2009
Snow cover	Decrease in spring snow cover in the northern hemisphere since the 1970s Increased thawing of permafrost	Anthropogenic warming of the surface temperatures	Gulev et al., 2021; Ruppert et al., 2013; Pierce et al., 2008
Change in frequency/occurrence and magnitude of temperature extremes	Decrease in the number of unusually cold days and nights Increase in the number of unusually hot days and nights	Anthropogenic influence of surface and lower tropospheric temperatures	Seneviratne et al., 2021; Stott et al., 2011; Christidis et al., 2012

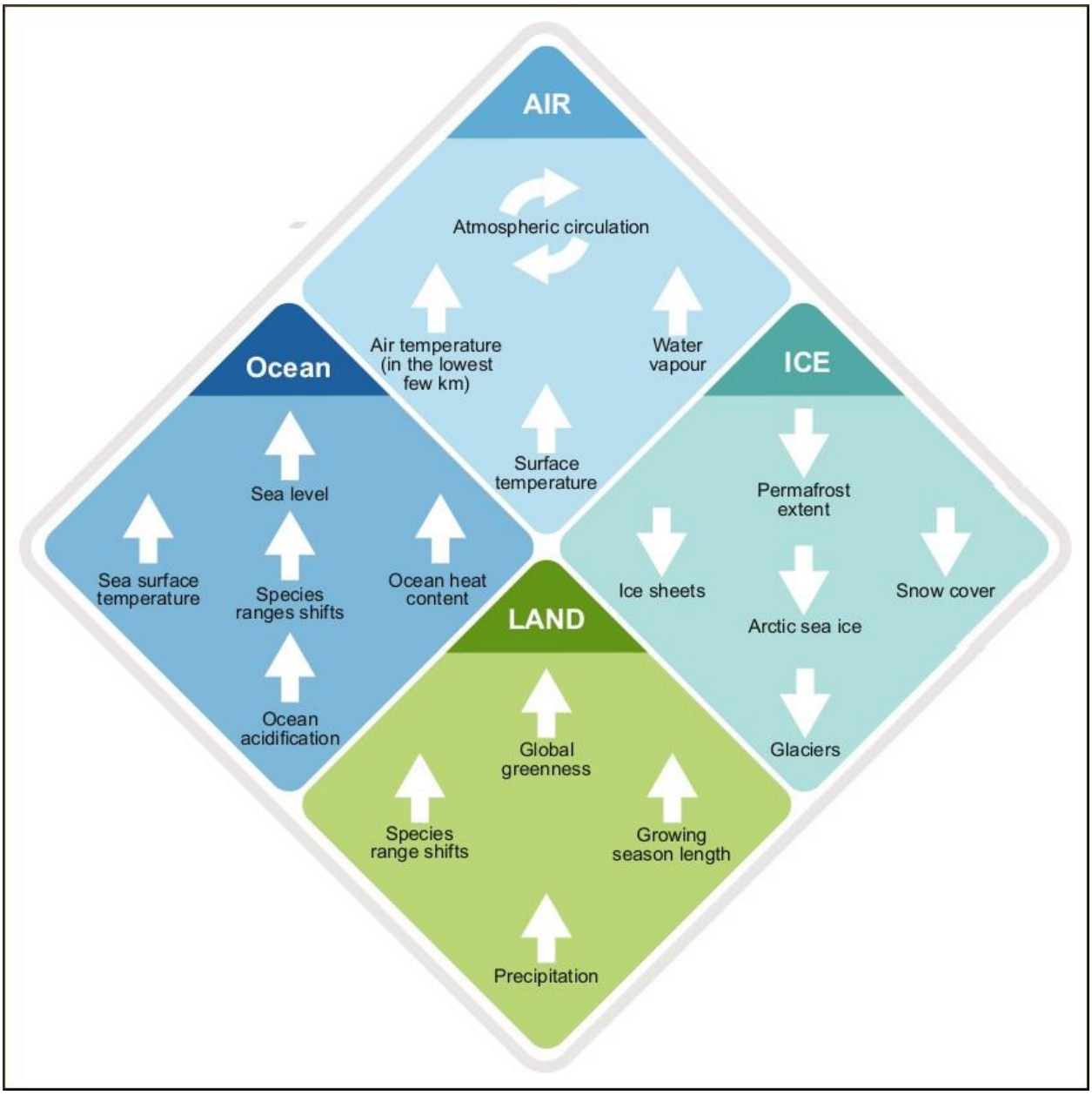

Figure 2.9 Synthesis of the observed changes in the climate system over the past several decades. Upwards, downwards, and circling arrows indicate increases, decreases and changes, respectively. Taken together, the changes reveal an unequivocally warming world. Source: Gulev et al., 2021.

2.6 Extreme Event Attribution

Trend detection using optimal fingerprinting methods is now a well-established field of climate science (Bindoff et al., 2013). And with climate change being indisputable, focus has recently shifted to extreme event attribution (EEA) which provides best estimates of the contribution of the change to the current climate conditions. EEA is the investigation of changes in the frequency and/or magnitude of individual and local- and regional-scale extreme weather events due to various drivers (Seneviratne et al., 2021). An attribution analysis has four possible outcomes: (i) the event was made more likely due to the anthropogenic influence on the climate system, (ii) the event was made less likely due to the anthropogenic influence on the climate system, (iii) no discernible influence of anthropogenic climate change, (iv) with the current understanding and available tools (observations, models, expertise) the role of external factors on the events could not be analysed. This includes change in intensity, duration of the event, spatial extent, etc. The science of event attribution is rapidly advancing through improved understanding of the mechanisms that produce extreme events and the marked progress in the development of methods used. The first attempt at attributing an extreme weather event to human influence on the climate system was made in 2004, analysing the 2003 European summer heat wave that killed tens of thousands of people in France and Germany (Stott et al., 2004). A number of attribution studies followed that. They include England and Wales autumn 2000 floods that destroyed over 10,000 properties (Pall et al., 2011) and 2010 Russian heat wave that resulted in several deaths (Dole et al., 2011) among others. By AR5, consensus had emerged that in principle the contribution and the role of external drivers of climate change in specific extreme weather events could be estimated and quantified, but that the assessments were still confined to high-impact events with a clear attributable signal. Nonetheless, the possibility of linking a single extreme event with a specific external driver was still contested.

Over the past 11 years, post-AR5 studies on extremes have been proceeding at a fast pace, with important outcomes springing up. This emerging area of science has drawn the interest of the public due to the frequently devastating impacts of the events on societies and ecosystems. This is reflected in the strong media interest of the connection between climate change and extreme events. Since 2012, the American Meteorological Society (AMS) has published a special annual issue of their Bulletin, synthesising articles on extreme weather events of the previous year. Between 2012 and 2015, the number of research groups submitting studies to this issue grew by more than a factor of five. A National Academy of Sciences report (NAS, 2016), a committee on extreme weather events and climate change attribution, provided a snapshot of the then state of the science of attribution of extreme weather events and recommendations for what might be useful future avenues of both research and applications within the field. The report also gave a synopsis

of the attribution of nine specific types of extreme events that had occurred by 2016. Since 2015, World Weather Attribution (WWA) initiative comprising different institutions including Grantham Institute, Imperial College London, Environmental Change Institute, University of Oxford, Red Cross Red Crescent Climate Centre, and Royal Netherlands Meteorological Institute has been conducting real-time attribution analysis of extreme weather events as they happen around the world and have been published extensively. The initiative actively conducts research and develops scientific tools and methodologies to perform timely and robust assessments of the role of human-induced climate change on extreme weather events.

2.6.1 Approaches for Extreme Event Attribution

A variety of approaches have been used in extreme event attribution, dependent on the framing of the attribution questions, and their use of observations and models in answering the questions. This section describes the main approaches currently used in attribution studies.

2.6.1.1 Risk-based Approach

Risk-based approach is a probabilistic assessment of change in the current and future risks associated with extreme weather and climate events. The risk ratio (RR) or probability ratio (PR) is a measure used to determine the change in the likelihood of occurrence of an extreme weather/climate event between the current climate and the pre-industrial or counterfactual climate (e.g., Allen, 2003; Stott et al., 2004; Stone and Allen, 2005). It involves event definition i.e., setting spatial and temporal resolutions, and construction of the factual and counterfactual likelihood distribution mainly using climate models. In principle, every extreme event is unique and always the result of a combination of external drivers, natural and anthropogenic, as well as internal climate variability and noise; therefore, it is impossible to say that an event could not have occurred without anthropogenic influence (Otto, 2017). However, the presence of an external driver like anthropogenic climate change can alter the likelihood of occurrence of an extreme weather event (just like loading a dice would increase a chance of rolling a six). Estimating RR is undertaken either based on observed or reanalysis data or model simulations of possible weather. Atmosphere-only models are used to generate large ensembles, thus allowing for the statistics of rare events to be assessed without assumptions about the statistical properties of the distribution of the event(s) (e.g., Guillod et al. 2017; Stone et al. 2019). Model evaluation is a critical first step since in many cases extremes involve mesoscale processes that are not adequately resolved by models. Observational data provide better estimation of role climate influence than climate models, obviously because observations represent the real

world unlike the models. However, short observational records often require assumptions about the properties of the underlying distribution.

The risk ratio is evaluated as the ratio of the probability of the event in the current climate (p_1) to the probability in the counterfactual climate or pre-industrial climate (p_0)

RR= p1/ p0

An RR value of 1 would mean that the likelihood has not changed. This implies anthropogenic climate change did not alter the frequency of occurrence of the event. An RR value more than 1 would mean that the likelihood has increased implying the event has been made more likely due to anthropogenic climate change. An RR value less than 1 would mean that the likelihood has decreased indicating that the event has been made less likely due to anthropogenic climate change. Conceptual framework for risk-based approach is illustrated in Figure 2.10.

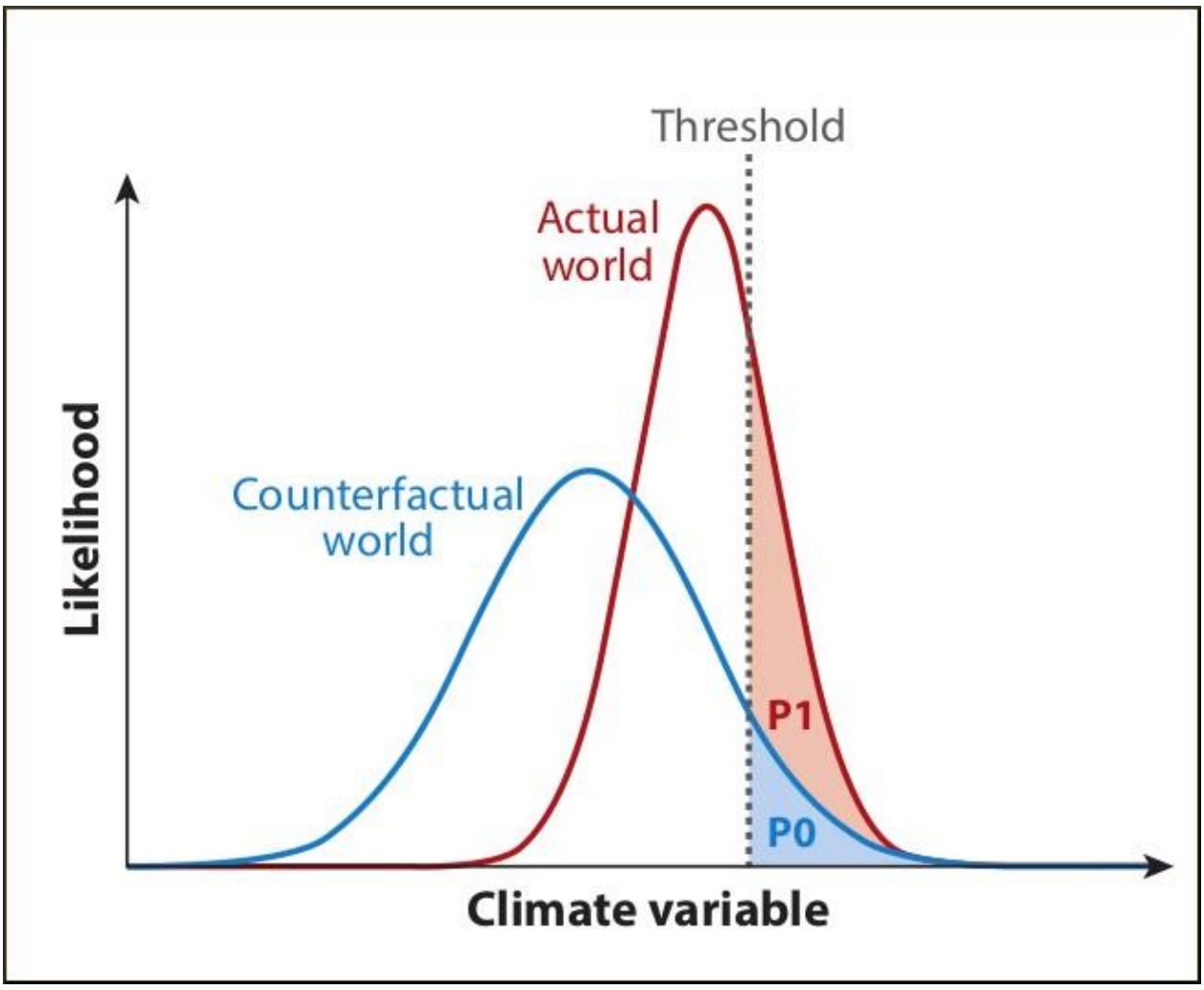

Figure 2.10 Schematic of probability distribution functions (PDFs) a climatic variable under a factual (P1) and a counterfactual (P0) world. The event is defined by a threshold (vertical dashed line). Source: Otto et al., 2017

To make an attribution statement, the entire confidence interval of the RR should be greater than 1.0 (or less than 1.0 in the case of decreasing risk). If the one- or two-sided confidence interval on the RR excludes one (no change), the change is statistically significant i.e., the distribution is significantly different between the two climates. In most cases, a non-parametric bootstrap procedure is used to estimate uncertainty of RR, such as the 95 % confidence interval (e.g., van der Wiel et al. 2017).

2.6.1.2 Circulation-based Approach (es)

Using a risk-based approach, a strong attribution statement can be made if the extreme event resulted from a purely thermodynamic process. If the event was partly caused by extreme dynamical conditions, then the credibility of the model in simulating change in the likelihood or severity of the event needs to be thoroughly

assessed (Shepherd et al., 2018). Circulation-based approaches involve understanding the relative role of both dynamical and thermodynamic contributions to changes in the probability of extreme events. Dynamic contributions constitute the changes in atmospheric circulation (e.g., in wind and pressure patterns) while thermodynamics constitute changes in atmospheric physical properties (e.g., water content, temperature, upper-ocean heat content). Otto et al. (2016b) agrees that understanding how the overall risks of extreme events are changing in a warming world requires both a thermodynamic perspective and an understanding of changes in the atmospheric circulation. Thermodynamic aspects of the climate system which mainly include global or continental averages of quantities exhibit changes that are generally robust in observations and in models while dynamic aspects are not. For dynamically related quantities, the signal-to-noise ratio of forced changes is comparatively small and the sensitivity of model behaviour to parameterized processes remains poorly understood (Trenberth et al. 2015; Zappa et al., 2015). Although from the thermodynamic considerations alone more extreme rainfall is expected in a warmer atmosphere that can hold more water vapour (see Clausius Clapeyron relationship; section 2.3), increasing concentrations of greenhouse gases in the atmosphere and the higher SSTs influence atmospheric circulation, either in the same direction as the thermodynamics or in the opposite direction. Models can exhibit variations in their simulations of atmospheric circulation in response to global warming. If there are plausible uncertainties in the changes being studied, it is likely that the result will be that "no effect is detected". This tends to be the attribution statement for studies of dynamically driven extremes, for example (Uhe et al., 2018). Indeed, lack of general non-robustness of the circulation response in models should not be the basis for absence of evidence (Mcgrath, 2015).

Some studies have attempted to disentangle the thermodynamic aspects from dynamics in explaining changes in likelihoods of extremes. In many cases, these approaches are highly conditional. The conditions that have been imposed limit assessment of the full extent of human influence on the event, so it is only possible to make a conditional statement (e.g Patricola & Wehner, 2018). In some cases, the extreme event is defined by its circulation state based on regime classification and then reanalysis or model data is used to identify and calculate analog states of that state. An increase in the number of analog states in the recent years is taken to indicate the potential influence of anthropogenic climate change on the probability of the analogs occurring. For example, Cattiaux et al., (2010) examined the cold European winter of 2010 and argued that once one accounted for the anomalous circulation regime, including the record-long persistence of a negative North Atlantic Oscillation (NAO) index, the winter was anomalously warm, in line with a warming climate. Diffenbaugh et al., (2015) on the other hand, found that although there was no significant change in observed precipitation during the 2012 California drought, systematic warming over the past

century has made dry years almost always also warm years (hence increasing the propensity to drought). In the past, the combination of the two conditions was less likely to occur.

The storyline approach proposed by Trenberth et al., (2015) and Shepherd, (2016) aims to provide physically based unfoldings of past or future climate/weather events that give a conditional explanation which can be represented in casual links (Doblas-Reyes et al., 2021.). Here, emphasis is placed on understanding the driving/causal factors involved, their plausibility and how climate change might have contributed to those causal factors (Shepherd et al., 2018) with no probability of storylines assessed. This approach can be useful in attribution of low-likelihood events, which are often associated with the highest impacts e.g., short-lived convective storms. Figure 2.8 shows two ways in which storylines can be defined depending on which elements (dark blue) are specified. Variable elements (light blue) are simulated conditional on the specified elements while the white elements are 'blocked' since their state does not need to be known to determine the variable elements.

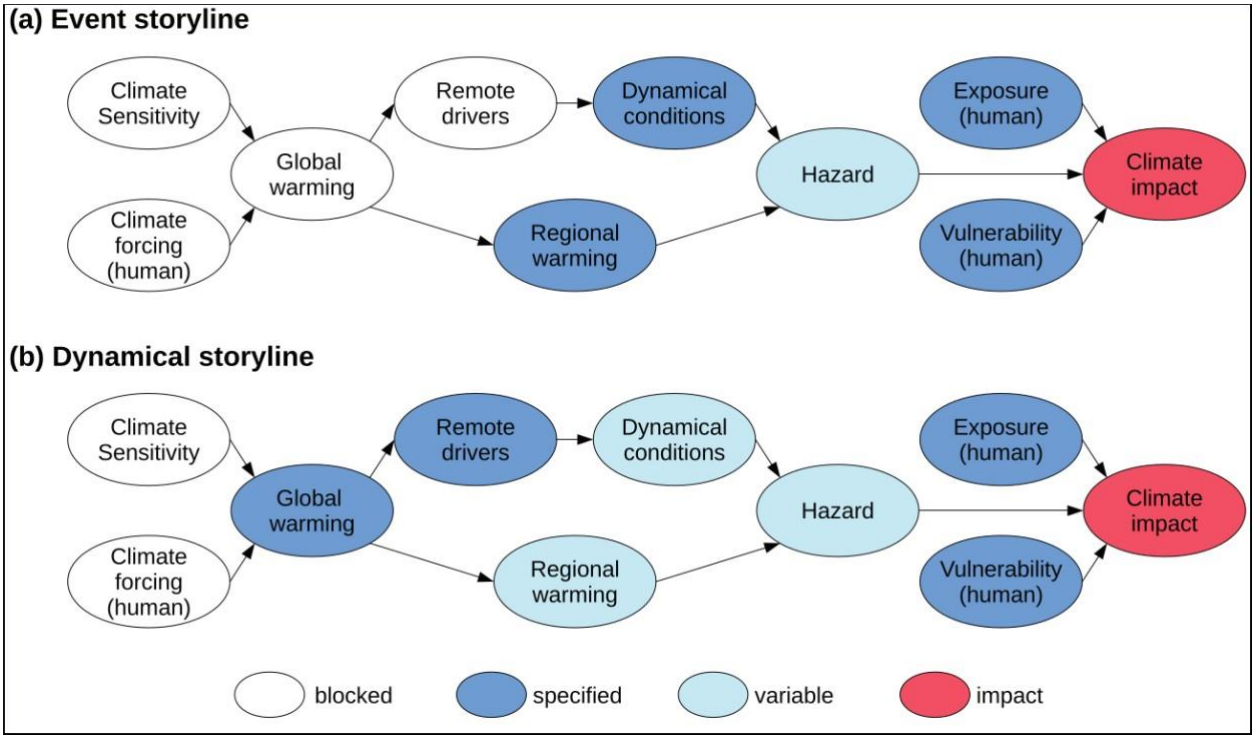

Figure 2.11 Schematic diagram showing the two types of physical climate storylines. In event storyline (a) the particular dynamical conditions during the event and the regional warming patterns are specified and control the hazard arising from the event. For dynamical storyline (b), the global warming level and remote drivers are specified and control the long-term changes in atmospheric dynamics and regional warming. In both cases the impact is also conditioned on specified exposure and vulnerability. Source: Shepherd, 2019

The results of event attribution studies are influenced by various factors; the way in which the event is defined and framed (Jézéquel et al., 2018; Leach et al., 2021; Otto et al., 2016), the context in which the event is being analysed, the uncertainties in the observations and modelling frameworks that are used, and the specific climate variables (Wehner et al., 2016) that are being considered. Additionally, the outcome of these studies can be sensitive to the spatial and temporal definitions (Harrington, 2017) of the event being analysed. Certainly, there is need for continued development of methodological approaches to increase reliability of attribution results. The two key challenges are disentangling the thermodynamic and dynamic effects, and model simulation of localised events like tropical cyclones. Confidence in attribution findings can be enhanced when independent approaches lead to similar results.

2.6.2 Methodologies of Event Attribution

Attribution of extreme weather/climate events involve the use of both observational data and climate models to assess the probability of occurrence of the events. Observational approaches cannot prove causality; however, they can assess the extent to which a correlated hypothesised predictor affects the likelihood of the distribution. Model approach uses climate models to determine the role of different external forcings in the changing characteristics of extreme events. The type of methodology used is often dictated by the attribution question being answered, on epistemological leanings and data availability (observed and model). For model approach, factual and counterfactual model simulations representing present-day climatic conditions and those of a 'world that might have been' (climate conditions without anthropogenic influence) are assessed and compared. Counterfactual simulations are achieved by running the same climate model but with anthropogenic forcings removed or using pre-industrial levels (commonly 1850). The difference in statistics of these model simulations is taken to represent the human influence on the climate.

2.6.2.1 Observational

In many attribution studies, observations are mainly used to define and determine the rarity of the event in a historical context. Statistical analysis of an observed long-term time series is used to characterise the distribution of a parameter or event. The observational data needs to be of high quality, that is, free from non-climatic heterogeneities and a record long enough to allow reliable comparison of extremes between two sub-periods. Observation method of attribution seeks to determine whether observed data indicate that the climate is changing or are simply consistent with possible fluctuations from natural internal variability of the climate system (Stott et al., 2010). Gaussian, Generalised Pareto Distribution (GPD), Gumbel and

Gamma functions have been used to define trends, calculate return periods and probability of threshold exceedance. Andreas et al. (2008) and Oldenborgh et al. (2015) used Generalised Extreme Value (GEV) distribution to determine return times of temperature extremes. The observational method has also been used to understand the circulation patterns and other aspects of the synoptic processes observed during meteorological events. For instance, Cattiaux et al. (2010) demonstrated that the 2010 European winter mainly caused by persistence of the negative phase of NAO was quasi-systematically warmer than the analogue flows of the past two decades. Similarly, Marshall et al. (2004) demonstrated that recent trends in annual and austral summer southern hemisphere annular mode (SAM) are unlikely due to internal variability but anthropogenic forcings. Some studies have used observations to separate signal and noise based on timescales indicating that changes in external drivers, particularly greenhouse gas increases, lead to patterns that are statistically distinct from shorter-term patterns recorded due to internal variability (Hegerl & Zwiers, 2011).

2.6.2.2 Model

Climate models are based on the integration of equations governing atmospheric motions; the gas law, the equation of continuity (mass), the first law of thermodynamics (heat) and the conservation equation of momentum, energy, water, and carbon. For event attribution studies, they incorporate knowledge of the physics of the climate system to quantify how human or natural factors have influenced the frequency or magnitude of the climate events relative to baseline forcing scenarios (NAS, 2016).

To be used in attribution studies, models should be able to replicate the event under study. This includes reproducing the statistics of the events correctly, reproducing the specific weather situation leading to the event and the local feedbacks that may strengthen such events. The advantage of using climate models is the ability to utilise specific input conditions and obtain ensemble simulations to estimate uncertainties/sensitivities involved. Unlike observation-only methods, models are well suited for making comparisons between factual and counterfactual worlds. For this reason, climate models are used for fingerprint studies which evaluate the extent to which external forcing (fingerprints) have contributed to the observed climate change. Attribution studies make use of both atmosphere-only and coupled models.

2.6.2.2.1 Global Atmospheric models

These models are mainly used for conditional attribution studies where observed historical evolution of sea surface temperatures and sea ice extent are specified. Several ensembles are generated using different types

of perturbations depending on the nature of the event being investigated. It could be by initial conditions perturbations (e.g., using next day differences) or sea surface temperature perturbations or perturbed physics. Counterfactual SSTs are obtained in two ways. One is from SST difference patterns in coupled model simulations (mainly from CMIP5 archive) of historical and historical natural simulations with the same coupled model.

The patterns are then subtracted from the observed SSTs to obtain an estimate of counterfactual SSTs (e.g., Otto, 2017). In most cases, more than one pattern is used to estimate the spread in possible warming patterns. The other way is to use scaling factors from optimal fingerprinting analysis of coupled simulations where a signal in SSTs is detected (e.g., Pall et al., 2011). While atmosphere-only models, rather than coupled atmosphere-ocean ones, are meant to reduce ocean biases, and permit greater computational efficiency (hence more simulations with higher spatial resolutions), the lack of dynamically interacting ocean implies a number of assumptions. (i) Anthropogenic climate change does not influence ocean variability; (ii) short-term coupled atmosphere-ocean interactions are unimportant in the production of extreme weather, and (iii) anthropogenic climate change is identical for all forms of extreme weather (Stone et al., 2019). See Table 2.2 for a detailed comparison of observational, atmosphere-only and coupled attribution methodological approaches, including their advantages and disadvantages.

2.6.2.2.2 Coupled Climate models

These models incorporate the interactive representations of the atmosphere, ocean, sea ice, land surface and some, the carbon cycle. A holistic simulation of the historical global climate change is obtained from the estimates of both natural and external forcings (e.g CMIP6-ALL[2]). Preindustrial control runs, or sometimes natural forcing estimates runs are used to define the counterfactual world (e.g., CMIP6-NAT)[3]. In coupled models, however, the timing of individual unforced climate events does not match the observations, unless only by coincidence. For example, the El Nino years in a historical climate period in the model will rarely coincide with years when El Nino occurred in the observational period, and if so, only by chance. As explained in Taylor et al. (2012), the reason is that historical runs are initiated from an arbitrary point of a quasi-equilibrium control run, so internal unforced variations would not be expected to occur at the same time as those found on the observational record. In contrast, for atmosphere-only models in which sea

[2] Refers Coupled Model Inter Comparison Project (CMIP) model simulations that incorporate all forcings i.e., natural and external.
[3] Refers Coupled Model Inter Comparison Project (CMIP) model simulations that incorporate only natural forcings.

surface temperatures are specified based on observations, the occurrences of simulated historical internal variations e.g., ENSO events coincide with observations.

Since extreme event attribution began early this century, most studies use at least two or three approaches, that is, observation, atmosphere-only and coupled models. Table 2.2 gives a summary of some of the main advantages and disadvantages of each approach. Multi-method multi-model approaches are highly recommended to improve and enhance robustness and confidence in results. A sample of such studies are presented in Table 2.4 showing the methodology used, the attribution results and their impacts on human and natural systems are also provided. Figure 2.7 shows the estimated number of studies for each type of extreme event that have been attributed to human influence, according to Carbon Brief (2022).

Table 2.2 Some Advantages and Disadvantages of observational, atmosphere-only and coupled attribution methodological approaches

Approach	**Advantages**	**Disadvantages**
Observational analysis	Observations are less biased compared to necessarily imperfect model simulations i.e., they represent the reality (assuming homogeneity and completeness). Results obtained from do not hinge or depend on model suitability, therefore, confidence in attribution results are improved especially where the trend is detectable.	Requires long observation record and high quality Prone to the influence of unforced natural variability in trend detection especially low frequency e.g., decadal to multi-decadal (which reduces signal-to-noise ratio) Prone to the influence of circulation changes which can amplify or attenuate the effects of human influence Can only use a non-stationary statistical model with a covariate (CO2 or GMST) which must have a well-established causal link to human influences Only favours attribution of temperature change or variables closely related to temperature which human influences have been well detected.
Atmosphere only models	Use of large ensembles enables averaging that removes much of internal variability Ocean biases are reduced by prescribing SSTs instead of incorporating the ocean component in the model (as in coupled) Allow for greater computational efficiency hence more simulations at a higher spatial resolution	Lack of dynamically interacting ocean implies assumptions that anthropogenic climate change does not influence ocean variability i.e., short-term coupled ocean interactions are unimportant in the production of extreme events Assumes that anthropogenic climate change influence is identical for all forms of extreme weather
Ocean atmosphere models	Incorporates the ocean component hence the influence of ocean-atmosphere coupling is factored	Limited to unconditional studies Externally forced signals are prominent. Not designed to, and not very good at simulating weather events.

Table 2.3 A sample of key attribution studies of extreme events using different methods.

Event	**Methodology/Models used**	**Result**	**Impacts**	**Citation**
England and Wales autumn 2000 Floods	Models; HadAM3	Human influence on the climate increased the flood risk by 20% in 9 out 10 cases and by 90% in 2 out of 3 cases	Estimated 10,000 properties damaged Estimated £1.3 billion insured losses	Pall et al., 2011
2003 European heat wave	Generalised Pareto distribution -HadCM3	Human influence on the climate doubled the heat wave risk by exceeding threshold magnitude	Heat-related deaths in Italy, Germany, and France	Stott et al., 2004
2010 Russian heat wave	Model 22 CMIP3 models GFDL AM2.1 atmospheric general circulation model ECHAM5	No human influence detected Attributed to natural internal atmospheric variability	Deaths in Moscow and parts of western Russia	Dole et al., 2011
2010 European winter	Observation and models	Extreme persistence of the negative the phase of the NAO Temperatures anomalies attributed to climate change	Several severe cold spells over Northern and Western Europe	Cattiaux et al., 2010
2011 Texas drought/heat wave	20 CMIP5 models CCSM4 CFSv2	Human-induced climate change increased the probability of a new temperature record from 3% (1981-2010) to 6% in 2011. Human influence responsible for 0.6 warming relative to 1981-2010	Agricultural losses of $7.62 billion (USD) Wildfires burned 3 993 716 acres Commercial timber losses of	Hoerling et al., 2013

			$755 million	
2013 Australia record summer temperatures	9 CMIP5 models	Human influences increased the risk by at least 2.5 times (more likely,>90%)	Bush fires in south-eastern Australia in Victoria and Tasmania Severe flooding in north-eastern Australia in Queensland and New South Wale	Lewis & Karoly, 2013
2011 rainfall deficits in Eastern Kenya and Southern Somalia	AMIP models	Anthropogenic influence associated with western pacific warming and stronger western-to-central Pacific SST gradients Non-ENSO SSTs variations substantially increased the risk of failed rains in 2012	Crop failures Poor pasture conditions Famine and Malnutrition	Funk et al., 2014
2011 rainfall deficits in Eastern Kenya and Southern Somalia	AMIP models	Anthropogenic influence associated with western pacific warming and stronger western-to-central Pacific SST gradients Non-ENSO SSTs variations substantially increased the risk of failed rains in 2012	Crop failures Poor pasture conditions Famine and Malnutrition	Funk et al., 2014
2013/2014 California drought	Pareto III-type parametric distribution CMIP5 models	Human influence increased the probability of extreme North Pacific geopotential heights (enhanced North pacific ridging) attributable to increased drought risk	Water shortages	

2015 European heat wave	HadGEM3-A	Anthropogenic influence accounted for 2/3 of the warming (1.6°C) -Internal variability responsible 1/3 of the warming (0.8°C)	Precipitation deficit	Dong et al., 2015
2014 Horn of Africa drought	HadRM3P embedded in HadAM3P	No detected anthropogenic signal in the reduced precipitation Detected anthropogenic influence in increase of temperatures and incoming solar radiation	Crop failures. Increased food insecurity	Marthews et al., 2014

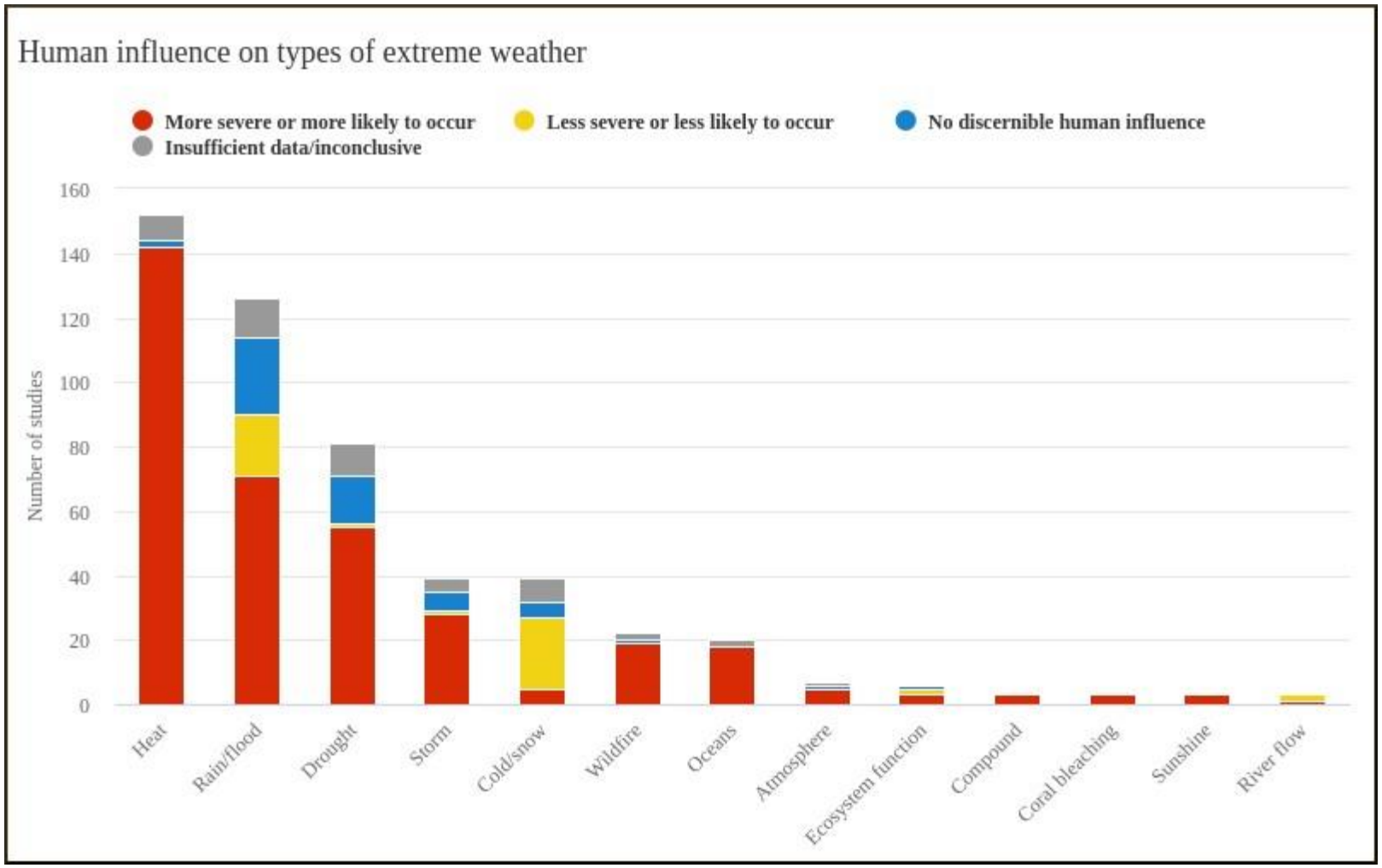

Figure 2.12 Number of attributed studies for each type of extreme event: More severe/likely (red), less severe/likely (yellow), no influence (blue) and inconclusive (grey).

Source: Carbon Brief 2022 report

2.7 Attribution of Extreme Rainfall

Attribution of precipitation extremes has gained huge prominence within the climate science community. This could partly be motivated by increasing public/policy interest in the role of climate change in modifying current and future risks associated with precipitation extremes, and as the leading cause of extreme-weather related disasters across the globe. In general, warming of the climate system increases the atmospheric water-holding capacity, according to the Clausius-Clapeyron (C-C) scaling. This thermodynamic effect results in increases in extreme precipitation at a similar rate at a global scale. At regional and local scales, increases are further modulated by dynamic effects. For a fact, changes in dynamics can increase rainfall intensity more than that expected of the C-C scaling rate. These increases vary greatly across regions and seasons (e.g. IPCC, 2021). Figure 2.13 shows the observed change in heavy precipitation and confidence in human contribution to the changes in the AR6 land-regions. It is worth noting that increases are seen across all regions on the globe with no strongly decreased likelihoods anywhere. Regions in Africa where data is available show increases in heavy precipitation. Limited data and literature over most regions in Africa including East Africa is depicted by the grey hexagons on the map that dominate the continent. For Southern Africa, increases in heavy precipitation events have been observed (Kruger et al. 2019) and a general shift towards intensification of extreme rainfall over East Africa (Omondi et al., 2014; Kimutai et al., 2022). By 2015, at 0.85°C warmer than pre-industrial period, human induced climate change increased the likelihood of daily precipitation extremes exceeding the 99.9th percentile of pre-industrial events by 18%, on average across land regions (Fischer and Knutti 2015).

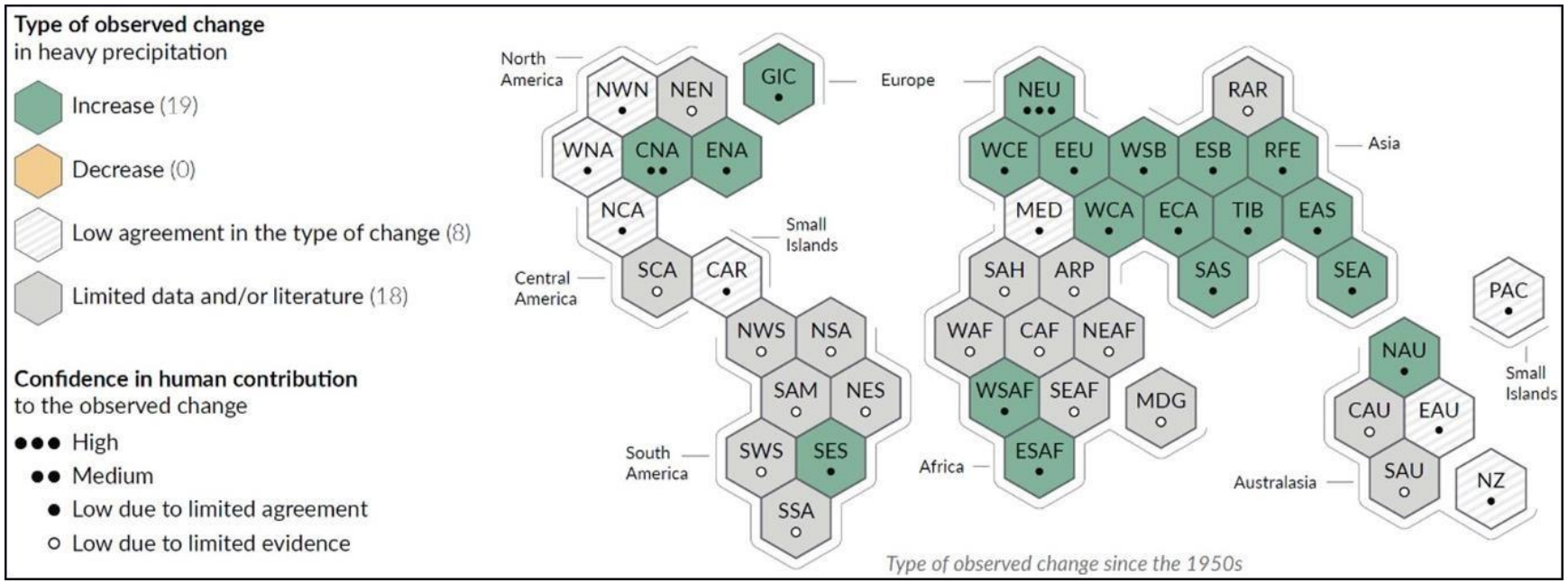

Figure 2.13 Synthesis of assessment of observed change in heavy precipitation and confidence in human contribution to the observed changes in land-regions, excluding Antarctica. The evidence is mostly drawn from changes in indices based on one-day or five-day precipitation amounts using global and regional studies. Source IPCC (2021; Figure SPM.3; Page 10).

Table 2.4 A sample of attribution studies of extreme rainfall events

Rainfall event	Description/Definition	Results	Citation
2022 Pakistan floods	Annual maximum of the mean 60-day precipitation during June-September over the Indus River basin Annual maximum of the mean 5-day precipitation in June-September over the worst hit provinces Sindh and Balochistan	The intensity of 5-day rainfall has increase by about 50% due anthropogenic climate change No clear anthropogenic signal on changes in 60-day mean rainfall High uncertainties in the estimates exist due to high variability of rainfall in Pakistan.	Otto et al., 2022
2022 Eastern South Africa	Changing likelihood and intensity of maximum 2day rainfall in KwaZulu Natal and Eastern Cape provinces of South Africa	The probability of occurrence of the event double while the intensity increased by 4-8% due to human-induced climate change	Pinto et al., 2022
2017 Bangladesh floods	Changing frequency in 10-day precipitation in the Brahmaputra basin	A significant positive influence is shown by one climate model ensemble No overall change in risk in precipitation and discharge All models project an increase in the probability of precipitation and discharge at 1.5 and 2deg	Oldenborgh al., et 2016
U.S. Daily Rainfall Extremes	2015 high impact daily rainfall over the U. S	The increase in magnitude and frequency of extreme daily precipitation of 2015 and recent decades linked to an increase in global mean temperatures	Wolter et 2016 al.,
Heavy precipitation in Chennai India	Daily precipitation in Chennai city on 1 Dec 2015	A small but clear increase in the probability of daily precipitation extremes in SST-forced regional models, associated with El Nino and other SST anomalies Both greenhouse gases and aerosols are contributing human influence factors; have opposing effects	Oldenborgh al., et 2016

Late-onset of the 2015 wet season in Nigeria	Delayed seasonal rainfall onset and latitudinal position of ITD	Little or no evidence of anthropogenic emissions or anomalous SSTs on the delay in the onset of the 2015 wet season in Nigeria	Lawal et al., 2016
Extreme Rainfall in Yangtze–Huia, China, June–July 2016	Changes in characteristics of June-July rainfall period; daily precipitation above 20mm(R20mm) and maximum 5-day precipitation (RX5day)	The increase in the risk of the event attributed to anthropogenic climate change and El Nino conditions	Sun & Miao, 2018
Extreme September 2016 Rainfall Across South-eastern Australia	Widespread flooding and extreme rainfall in September 2016 in Eastern Australia	Increasing levels of CO2 over the past 5 decades have already led to circulation and stability changes that promoted drier than normal conditions	Hope et al., 2018
2011 Thailand floods	Widespread flooding in monsoon season of July-September	Climate change was not found to have played a role in the floods	Urk et al., 2012
Severe precipitation in Northern India in June 2013	Changes in precipitation characteristics; 4-day heavy precipitation events in June 2013	Anthropogenic climate change increased the likelihood of the event	Singh et al., 2014
Contribution of atmospheric circulation change to the 2012 heavy rainfall in south-western Japan	Extraordinary heavy rainfall from 11 to 14 July 2012 in SW Japan	Extremity of the event linked to oceanic natural variability and probabilistic atmospheric natural variability rather than by anthropogenic climate change	Imada et al., 2013
Contribution of atmospheric circulation to wet North European summer precipitation of 2012	Anomalous high precipitation during 2012 summer in Northern Europe (France, Scandinavia, Netherlands, Germany, UK)	Event linked to climate change Increased moisture levels due to increased temperature depicted in the cyclonic patterns	Yiou & Cattiaux, 2013
Diagnosing human Induced dynamic and thermodynamic	Interplay between El Nino dynamics and human induced climate change in May rainfall	The intensity of the event made more by human-induced thermodynamic drivers	Cheng et al., 2018

drivers of Extreme Rainfall in Oklahoma and Texas in 2015			

2.8 Role and Importance of Event Attribution Studies

Attribution science has the potential value of informing choices about assessing and managing risk and in guiding climate adaptation strategies both in private and government spaces. It provides the public, scientists, and decision-makers with the means to make clear connections between human influence on the climate system, for example, emission of GHGs and high-impact extreme weather events, such as storms, floods, heatwaves, and droughts, and appreciate the need to curb the emissions (James et al., 2014; Stott et al., 2014). Climate change being a key determinant for sustainable development and with the growing concerns about its impacts on societies, there is a need to understand and manage the current risks and prepare for future ones. The impacts of climate change are felt at different magnitudes in various parts of the world. Africa is bearing disproportionately the worst consequences of the impacts of climate change, while contributing the least GHG emissions. This study, for instance, seeks to contribute to the science-based evidence for this. The rate of surface temperature increase has generally been more rapid in Africa than the global average, with human-induced climate change being the dominant driver (IPCC, 2021). Extreme weather and climate events attributable to human-induced climate change include marine heatwaves (2 times more likely) (Frölicher et al., 2018; Laufkötter et al., 2020; Oliver et al., 2018; Seneviratne et al., 2021), multi-year droughts in West Africa (Biao, 2017) and East Africa (Funk et al. 2018; Hoell and Funk; Liebmann et al. 2014) and Cape Town drought (3 times more likely) (Otto et al., 2018), Eastern South Africa floods (2 times more likely) (Pinto et al. 2022). Africa has already experienced widespread losses and damages attributed to human-caused climate change. These include reduced food production, reduced water security, reduced economic output, loss of biodiversity, and increased human morbidity and mortality (Trisos et al., 2022). Some of these impacts will become more severe with increased warming. An estimated 337 million people were affected by natural disasters in Africa between 2000-2019, in which floods accounted for 80% and droughts for 16%. Between 2018 and 2019, 6 million people were displaced by weather-related disasters in Sub-Saharan Africa and 46, 078 deaths from natural disasters were reported between 2000 and 2019 (CRED, 2019). Globally, only Sub-Saharan Africa has reported the largest number of mortalities associated with floods since 1990 (Tallman, et al., 2021).

Three key areas in which attribution science play a role are discussed: (i) loss and damage debate, (ii) climate-related index-based insurance and (iii) as a catalyst to adaptation. The progress and challenges of applying attribution science in these areas are also highlighted.

AR6 WGI (IPCC, 2021) and WGII (IPCC, 2022) report and findings in other relevant recent scientific reports have highlighted the increasing urgency of enhancing efforts to avert, minimise and address loss and damage associated with the adverse effects of climate change in the light of continued global warming and its significant impacts on vulnerable populations and the ecosystems on which they depend. The gravity, scope and frequency of loss and damage will continue to increase with every additional fraction of a degree of temperature increase. The United Nations Framework Convention on Climate Change (UNFCCC) has been at the centre stage in convening and facilitating the debate on loss and damage at the international arena. The debate began in 1991 when Vanuatu proposed to be compensated by developed countries for emitting GHGs responsible for sea-level rise which was bound to disrupt their lives and livelihoods. Although the proposition was rejected, it opened doors for further discussion.

Alliance of Small Island States, (AOSIS, 2008) proposed a mechanism to address loss and damage, consisting of three interdependent tracks: an insurance element to address climate related extreme events and risks to food security and livelihoods; rehabilitation and compensation to address the progressive negative impacts of climate change such as sea-level rise; and a risk management component. The UNFCCC Conference of Parties (COP) established the Warsaw International Mechanism for Loss and Damage associated with Climate Change Impacts (WIM), to address loss and damage associated with impacts of climate change, including extreme events and slow onset events, in developing countries that are particularly vulnerable to the adverse effects of climate change at COP19 in Warsaw, Poland (UNFCCC, 2013). Parties later established the Santiago network on loss and damage (SNLD) as part of the WIM mechanism to contribute to the effective implementation of the WIM functions. SNLD's main purpose was to catalyse technical assistance of relevant organisations, bodies, networks, and experts, for the implementation of relevant approaches for averting, minimising, and addressing loss and damage at the local, national, and regional level, in developing countries that are particularly vulnerable to the adverse effects of climate change. The idea of loss and damage is underpinned by an understanding of liability, and that compensation is one part of an appropriate policy response. Allen (2003) proposed Probabilistic Event Attribution methodology to possibly determine the liability of climate change if the likelihood that the external drivers of the change have altered the risk of an extreme event. It might prove difficult to determine exactly how and by how much the external driver has altered extreme events, but likelihoods can be determined by averaging over all possibilities consistent with currently available information and state of knowledge/tools. Fraction of Attributable Risk (FAR) is used as a measure to quantify the contribution of anthropogenic climate change to the increased risk of an observed extreme event. In a conceptional way, an increase in the probability or risk of an extreme event occurring in the externally forced climate, as

compared to the baseline climate (e.g., pre-industrial), can be attributed to the change in external forcing as $\Delta q = q_1 - q_0$ where q_1 is the probability or risk in the externally forced climate and q_0 is probability or risk in the baseline climate. This is obtained by taking the fraction of the new risk that cannot be attributed to the random probability (p_0) of the event occurring in the baseline climate, as follows; FAR= $(p_1/p_0)/ (p_1)$ FAR=$1-p_1/p_0$. Figure 2.14 shows how anthropogenic forcings in the climate system can change the fraction of attributable risk of extreme events.

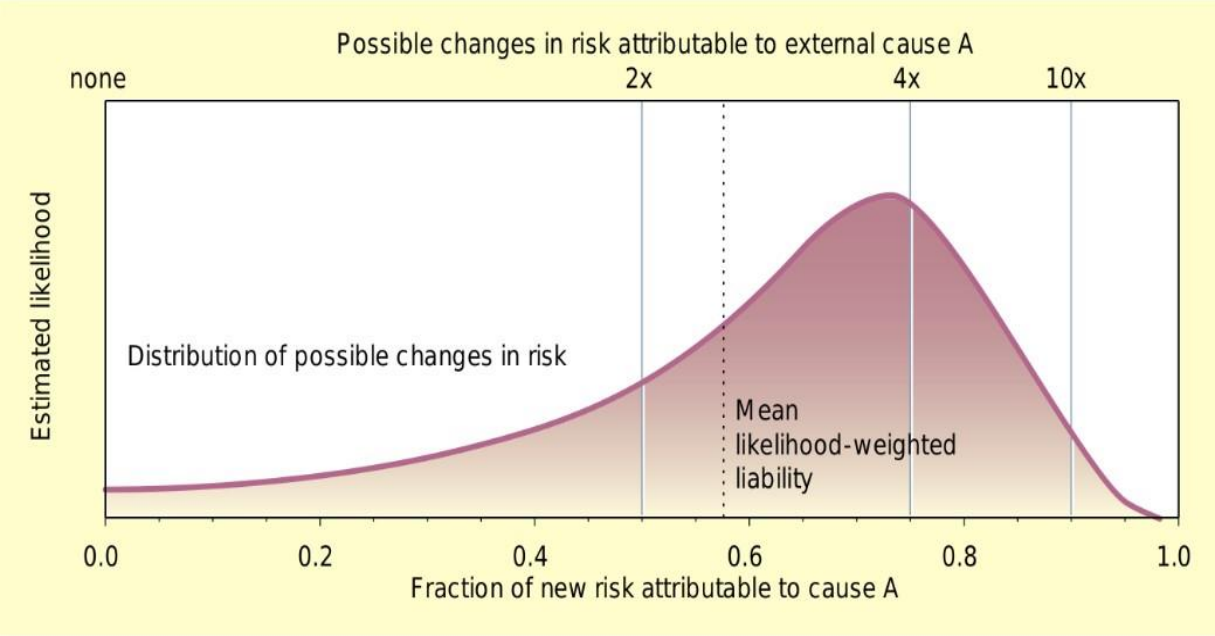

Figure 2.14 Distribution of possible changes in the fraction of attributable risk due to an external forcing A (e.g., greenhouse gases) on the climate system. 2x, 4x and 10x represent the possible changes in risk as a result of external forcing A which brings about changes in the fraction of attributable risk. Determining exactly how an external forcing alters the risk of an extreme event may not be possible but working out 'mean likelihood-weighted liability' by averaging all possibilities consistent with the currently available information and state of knowledge is feasible. Source: Allen (2003).

A landmark outcome of COP27 negotiations in Sharm El Sheikh Egypt is a funding arrangement for loss and damage. The cover decision stated: "The Conference of the Parties welcomes the consideration, for the first time, of matters relating to funding arrangements responding to loss and damage associated with the adverse effects of climate change, including a focus on addressing loss and damage, under the Conference of the Parties and the Conference of the Parties serving as the meeting of the Parties to the Paris Agreement" (UNFCCC, 2022). A transitional committee on the operationalization of the funding arrangements was established for consideration and adoption by parties at COP28 in Dubai. As the transitional committee gathers suggestions and recommendations to operationalize the Loss & Damage Fund, several critical questions require insights from the scientific community. Here, some potentials and boundaries of

attribution science in informing the operationalization, are outlined — particularly pertaining to the size and eligibility of different regions and event classes to the fund. There are still uncertainties associated with attribution studies. Uncertainties are larger for short-lived events than slow onset ones, for some extreme events than others, and some regions than others (Otto, 2015). Lower attributability of extreme events in most vulnerable countries, mainly due to unavailability of good quality historical observations and underperformance of climate models also remain key concerns. There is unwillingness by high emitters to take responsibility for losses and damages from events not attributable to anthropogenic climate change, apportionment of responsibility for those who failed to mitigate and those who failed to adapt and the risk of only dealing with the attributable part of an event. It is important to note, however, that there are serious ethical concerns if compensation for loss and damage is increasingly pursued through EEA. As mentioned above, attributability of events are highly dependent on tools available (mainly good quality data and reliable models). In developing countries, often most vulnerable to climate change, the adequacy of such tools remains quite low. If compensation is not provided for losses and damages [in the case of] events that cannot directly be attributed to climate change or where the signal is not good enough, the most vulnerable and highly impacted communities will be greatly disadvantaged. With scientific strictness i.e. looking at statistical significance and the level of confidence in the attribution statement, many extremes in developing countries are likely to be considered unattributable. Basis for non-compensation in this case will be merely a data issue rather than a scientific one. There is also the risk that many, if not most, problems associated with climate change will not remain unattributed (Olsson et al., 2022). The collective work of the field of attribution science in attributing climate-related events to human-induced climate change has provided compelling evidence for the urgent need to address the impacts of a warming climate. The science can provide information on the class of hazards and the type of damages that fund can support. The science should inform the level of funding required and the funding should be based on vulnerability to extreme events, not attributability (Hulme et al., 2011; Hulme, 2014).

There is also the potential role of EEA in insurance, which can be considered both a mechanism for financing of recovery from loss and damage, but also as a broader climate risk management mechanism. Allen (2003) argued that premiums for flood risk cover, for instance, could be determined by the risk of flooding and greenhouse-gas emitters held liable for the actual impacts of their emissions. In vulnerable countries, the use of climate related index-based insurance is on the rise in enabling rapid pay-outs to support disaster recovery in the aftermath of extreme events. Currently, the full cost of the cover is borne by those who take the insurance. But as evidence of anthropogenic climate change becomes unequivocal and in pursuit for climate justice in the face of sustainable development, the added cost of insurance

resulting from increased climate risks from extreme events modified by climate change should be borne by the emitters. It is only just that the insurance premiums be split between the policy holder and international climate funds (e.g., ActionAid, 2010; New et al., 2020). Insurance related action has been proposed on several UNFCCC forums. The challenge is that these policies are yet to be applicable in most existing business processes. To most insurers what really matters is the risk and how it evolves, not so much about the causal explanation.

EEA can also act as a catalyst for adaptation (Stott et al. 2003). Robust information and awareness of how climate risks are changing and how climate change is modifying such risks can improve decision-making. Since attribution findings act as harbinger for the future, type I or type II errors in attribution can misguide investment, e.g., reconstruction of community infrastructure that is not resilient to future extremes (i.e., maladaptation) and failure to identify the non-climate factors (e.g., components of vulnerability and exposure) that contribute to the scale and nature of the hazard. Hazards evolve into disasters when they interact with vulnerability and exposure. While there is significant methodological progress in quantifying the hazard aspect of evolving risks from extreme weather, vulnerability and exposure often receive minimal attention, if addressed at all, in the context of disasters. This inadvertently deflects responsibility of human-induced factors that create vulnerabilities and increase exposure. For vulnerable and data sparse regions such as Africa that do not allow for robust attribution analysis, taking a more integrated approach on interacting human and environmental systems allows for a consistent and robust assessment of complex climate change risks (Schipper, 2020; Simpson et al., 2021), that can guide disaster risk reduction and improve adaptation.

2.9 Summary of the literature review and research gap

As climate change is unequivocal, scientific and policy discussions have shifted from whether anthropogenic climate change is real to the evaluation of potential impacts and risks, and response options. There is already robust evidence that impacts from changes in likelihood and intensity of extreme weather/climate events are widespread (Seneviratne et al., 2021). The societally relevant question now is: what is the impact of certain human actions, in regards to adaptation and mitigation, under uncertain regional/local climate change? Every extreme event is unique and the uniqueness matters for impacts (Otto, 2017). Attribution science has improved significantly over the last two decades through methodological advances and new datasets. Advances in methods have led to better understanding of how climate change

is modifying risks associated with extreme weather and climate events by linking the physical and human aspects of change. And even as the methods continue to evolve, they should provide a physical basis for partitioning uncertainty and exploring boundaries of plausibility. The framing of events and risk should correspond more directly to how people perceive and respond to them. This way, it allows societies to work backward from a particular vulnerability or decision point, combining climate change information with other relevant factors to address risk and develop appropriate response options and/or adaptation measures. In most cases, extreme weather events become disasters due to interactions between the given hazard and existing conditions of exposure and vulnerability of the affected communities. For instance, there is not always a one-to-one correspondence between changes in extreme precipitation and changes in floods, because floods are affected by many factors in addition to heavy precipitation. While the methodological development in quantifying the hazard component of changing risks from extreme weather has greatly improved, the issues of vulnerability and exposure, if mentioned at all, are barely treated as components of disasters. For vulnerable and data sparse regions such as East Africa (that do not allow for robust attribution analysis) taking a more integrated perspective on interacting human and environmental systems allows for a consistent and robust assessment of complex climate change risks, allowing for immediate and appropriate actions (Simpson et al., 2022; Harington et al., 2021).

Previous attribution studies in East Africa have only focused on attribution of drought (Hoell & Funk, 2014; Funk, et al., 2018; Funk et al., 2013; Funk et al., 2016; Uhe et al., 2018; Marthews et., 2015; Lott et al., 2013). In at least 500+ studies tracked by Carbon Brief (Carbon Brief, 2023) no attribution study on extreme rainfall and/or floods for East Africa at the time of writing this thesis. Attribution studies of flood-inducing extreme rainfall are particularly important in vulnerable regions of the world, such as East Africa, where the impacts of these events can be severe and far-reaching. For the past two decades, the Greater Horn of Africa has experienced a sequence of droughts and floods. Droughts have dominated with punctuations of flood-inducing extreme rainfall. Currently, for instance, the region experiencing the worst drought in 70years, characterised by four failed consecutive rainy seasons (OCHA, 2022). Remarkably, in the months of October and November, flooding due to extreme rainfall was reported in several parts regions hardest hit by the ongoing drought (Author analysis, KMD 2022). The vagaries and swings of extremes has led to devastating impacts on livelihoods, food prices, water availability, nutrition, insecurity, and human-wildlife conflict. Lack of recovery of both human and environmental systems from the shocks exacerbates levels of exposure and vulnerability, pushes adaptive limits, and lowers resilience (e.g., Pal et al., 2016). As the climate continues to warm, assessing the role of and contribution of climate change to extreme rainfall amid

the drying trend in East Africa is of critical importance to the broader goal of building a more resilient and sustainable society.

3 Data and Methods

This chapter provides a detailed description of the data utilised and the method(s) used to achieve the objectives of the study. A description of the studied rainfall events and the study region are first presented in section 3.1.

3.1 Event Description and Study Area

This section provides a descriptive review of both the rainfall anomalies and reported impacts across the country, and the choice of study area(s). During the March-April-May (MAM) seasons of 2012, 2016, and 2018, several parts of Kenya experienced extremely high rainfall that caused both widespread and localised flooding which resulted in human and livestock deaths, destruction of infrastructure and property, bursting of riverbanks, submerging of farmlands and emergence of isolated cases of water-borne diseases. Based on Kenya Meteorological Department (KMD) station data, a description of the rainfall events showing the stations that received above normal rainfall with the corresponding climatological zones, and onset and cessation dates is provided in Table 3.1. MAM 2018 was the wettest season on record. All the meteorological stations in the country recorded above-normal rainfall i.e., above 100% of the long-term mean (LTM). Some stations recorded the highest in their operational record: Narok station (highest since 1950), Eldoret (highest since 1972), Kitale (highest since 1979), Kericho (highest since 1974), Laikipia (highest since 1957), Makindu (highest since 1950), Kakamega (highest since 1958), Nakuru (highest since 1964), Embu (highest since 1976) and Nyeri (highest since 1968). For MAM 2016, much of the rainfall was received during the second half of April through the month of May. In that season, most stations recorded between 75% and 125% of their LTMs. Although most stations received close to seasonal average rainfall (75% and 125% of their LTMs), the second half of the season was much wetter than average, while the first half was drier. For MAM 2012, several rainfall storms were recorded during the season. The heaviest storm of 105.mm was recorded at Embu station (central highlands) on 16 May and 104.5mm on 15 May at Malindi station (coastal strip). Kericho station (western highlands) recorded the highest seasonal rainfall amount of 892.4mm (132% of its LTM). Other stations that recorded above 80mm include Kakamega and Kisii (western highlands), Moi Airbase and Wilson Airport (Nairobi area), Nyeri (central highlands), Machakos (southeast) and Msabaha (Coastal strip). As a rationale for the choice of events: at the time of analysis and the writing of this thesis, the three MAM events were the most recent and with the highest impacts. Reported impacts are summarised in Table 3.2. A spatial distribution of the seasonal rainfall anomalies and the recorded impacts is presented in Figure 3.1.

Table 3.1 Description of MAM 2018, 2016 & 2012 rainfall events in Kenya. Highlights the climatological zones and synoptic weather stations that recorded above-normal rainfall (more that 100% of the LTM) and the onset and cessation dates/periods. Source: Author analysis (KMD, 2018; KMD, 2016; KMD, 2012).

Rainfall Event	**Climatological zones that recorded above normal rainfall**	**Stations that recorded above normal rainfall**	**MAM Onset date/period**	**MAM Cessation date/period**
MAM 2018	Highlands West of the Rift Valley, including Lake Victoria region; North-western; Central highlands including Nairobi Area; North-eastern; South-eastern; Coastal strip	Makindu, Dagoretti, Garissa, Lodwar, Marsabit, Moyale, Mandera, Laikipia, Narok, Meru, Wajir, Eldoret, Nakuru, Embu, Nyeri, Narok, Nyahururu, Kakamega, Kitale, Kericho, Kisumu, Kisii, Malindi, Lamu, Lodwar, MAB, Voi, JKIA, Thika, Msabaha, Mtwapa, Mombasa, Machakos	4th week of March	4th week of May
MAM 2016	Highlands West of the Rift Valley, including Lake Victoria region; Nairobi area and few stations in Central highlands; Few parts of North-eastern Kenya	Kakamega, Kisii, Eldoret, Kericho, Kitale,Nakuru, Nyahururu, Thika, Wilson, Dagoretti, MAB, Marsabit, Moyale, Lodwar	2nd week of April	4th week of May
MAM 2012	Highlands West of the Rift Valley, including Lake Victoria region; Central Highlands including Nairobi Area; North-western Kenya	Dagoretti, Eldoret, Embu, JKIA, Kakamega, Kericho, Kisii, Kisumu, Kitale, Lodwar, MAB, Makindu, Nakuru, Narok, Nyahururu, Nyeri, Wilson, Laikipia, Machakos, Malindi	3rd week of April	4th week of May

Table 3.2 Reported impacts of 2018, 2016 & 2012 heavy rainfall events in Kenya Source: Kenya Red Cross Society (KRC, 2018), Kenya National Disaster Management Unit (NDMU) and Office for the Coordination of Humanitarian Affairs (OCHA, 2012; OCHA, 2016; OCHA, 2018).

Rainfall event	**Reported Impacts**
MAM 2018	● Estimated 186 flood-related human deaths (47 deaths from Solai Dam collapse in Nakuru County) and 6,000 livestock deaths ● Displacement of 225,360 people ● Land and mudslides on the steep slopes of Kangema, Elgeyo-Marakwet and Mai Mahiu escarpments ● Destruction of infrastructure reported countrywide e.g., road cut-off in Moyale. ● At least 8450 acres of farmlands submerged ● The burst of riverbanks e.g., Rivers Tana, Ewaso Nyiro, Yala and Nyando ● Isolated cases of water-borne diseases like cholera and malaria reported
MAM 2016	• Flooding of Tana River • Collapse of a residential building in Nairobi — 16 deaths confirmed. • Outbreak of water-borne diseases, like cholera in some parts of the country • Land and Mudslides on the steep slopes of Kangema escarpment • Several roads rendered impassable, and some bridges swept away. • Total of 34,129 people affected in Nairobi Area
MAM 2012	• 84 deaths and approximately 30, 000 displaced, especially in western and central highlands including Nairobi area. • Landslides rendered several families homeless in Murang'a county. • Submerged farmlands in parts of western highlands

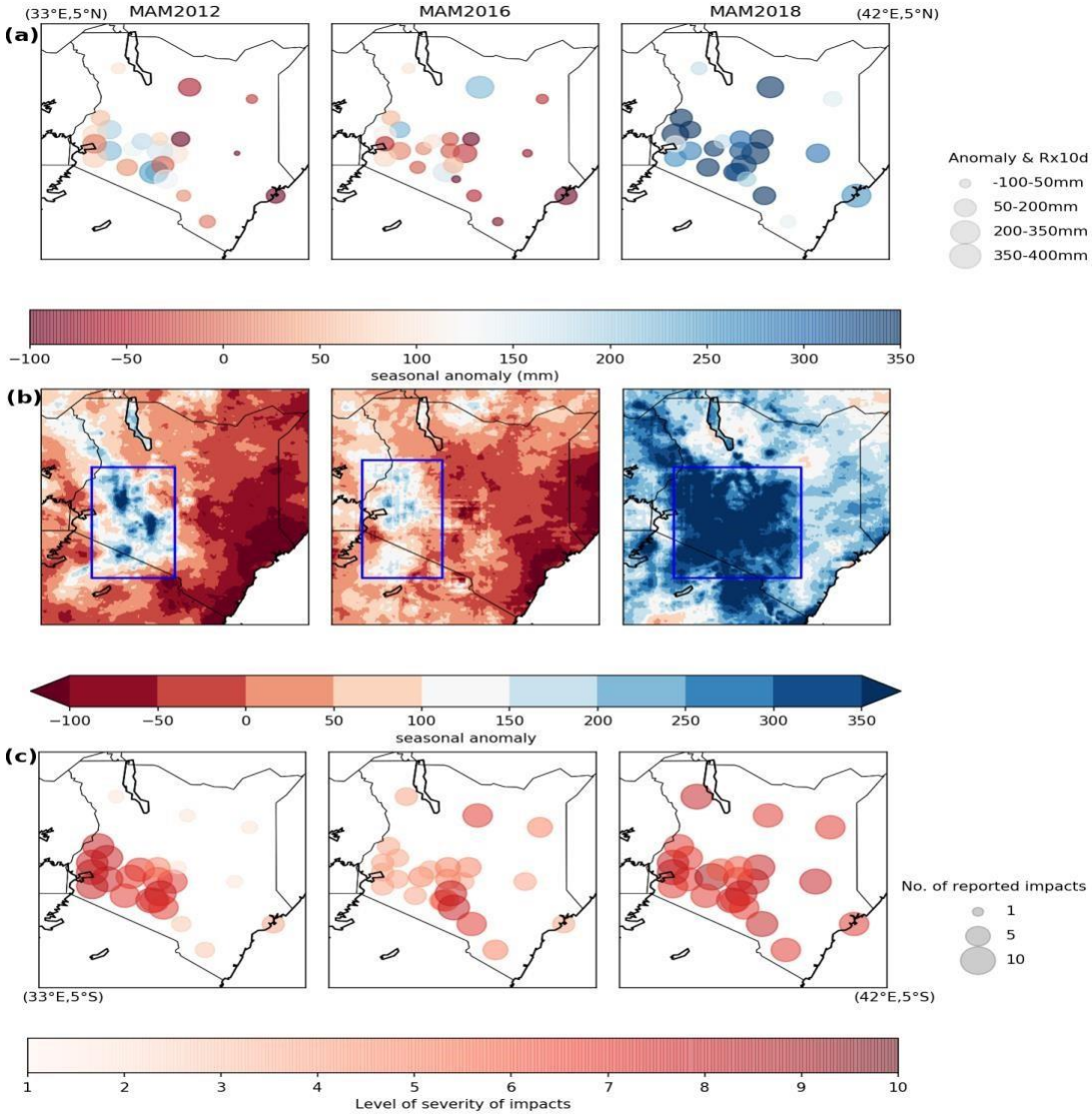

Figure 3.1 Spatial distribution of season total rainfall anomalies during the MAM 2018, 2016, and 2012 seasons and the recorded impacts of associated flood events in Kenya. Anomalies in seasonal mean rainfall based on Kenya Meteorological Department (KMD) station data (a), CHIRPS gridded dataset (b) (see description, section 3.2.1) in reference to the 1981-2016 climatological period and their associated impacts (c). In (a), the size of the circle corresponds to the maximum 10-day consecutive rainfall (Rx10d) amount, while the colour shows the seasonal anomaly. For (c), the circle size corresponds to the number of reported cases of flood impacts while the colour saturation shows the level of severity. The reported impacts (third panel) are obtained from the Kenya National Disaster Management Unit website, and Kenya Red Cross Society and Office for the Coordination of Humanitarian Affairs seasonal hazard reports. Due to an unavailability of monetary values of impact losses, the impacts are rated on a scale of 1 to 10 based on the following criteria: reported deaths, landslides, river/dam bursts and displacement of people are considered most severe with a rating of 7- 10; isolated cases of water-borne diseases and submerged farmlands as of moderate severity with a rating of 4- 6; and impassable roads as of minimal severity with a rating of 1-3. Boxes in (b) show the region(s) of study for each year — (3⁰S, 1.7⁰N, 34.7⁰E, 37⁰E), (3⁰S, 2.0⁰N, 34⁰E, 36.7⁰E) and (3⁰S, 1.7⁰N, 34.7⁰E, 39⁰E) for 2012, 2016 & 2018 respectively).

3.2 Data

3.2.1 Observational and Reanalysis data

Observational data are the basis for determining the spatial and temporal definitions of the study events, as well magnitude-likelihood characteristics. The results of the attribution analyses are strongly conditional on data quality and particularly on the duration of the available time series. The study utilised two observational datasets: (i) Kenya Meteorological Department (KMD) meteorological station data; and (ii) the Climate Infrared Precipitation with Stations (CHIRPS) satellite-based gridded data. For KMD data, daily rainfall records from 17 synoptic weather stations within the study area(s) for the period 1981-2018 are utilised (see Table 3.3 for station details and Figure 3.1 for climatological zones). Since the interest is on a regional constrained exceedance of flood-relevant amounts of rainfall at scales suitable for analysis by climate models, area-average of the station data was obtained over the analysis domain (Figure 3.1) using the Thiessen polygon approach (Thiessen, 1911). CHIRPS is a high resolution (0.05°) daily precipitation dataset (available from 1981-present) that uses the Tropical Rainfall Measuring Mission Multi-Satellite Precipitation Analysis version 7 (TMPA 3B42 v7) to calibrate global Cold Cloud Duration (CCD) rainfall estimates (Funk et al., 2015). It includes monthly precipitation climatology, and atmospheric model rainfall fields from the NOAA Climate Forecast System, version 2 (CFSv2). It is blended with station data to produce a gridded rainfall time series suitable for trend analysis, and seasonal flood and drought monitoring. CHIRPS has been found to have low bias and better gauge coverage over East Africa (Dezfuli et al. 2017) and agrees well with station-based interpolated rainfall over Kenya as it incorporates data from most synoptic stations. For reanalysis data, the study utilised the European Centre for Medium-Range Weather Forecasts (ECMWF) ERA-Interim (ERAINT) (Dee et al., 2011) and ERA5 datasets available on the grid size of 0.75 × 0.75 from the 1979 onwards. For all the four datasets, daily data for the period 1981-2018 is utilised.

Table 3.3 List of the 17 synoptic weather stations in the study area run by the Kenya Meteorological Department utilized in the observational analysis. The data period is March-April-May (MAM) 1981-2018

Station name	Station ID	Longitude	Latitude
Dagoretti	9136164	36.8	-1.3
Eldoret	8935181	35.3	0.5
Embu	9037202	37.5	-0.5
Kakamega	8934096	34.8	0.3
Kericho	9035279	35.3	-0.4
Kisii	9034088	34.8	-0.7
Kisumu	9034025	34.8	-0.1
Kitale	8834098	35.0	1.0
M.A.B	9136087	36.9	-1.3
Meru	8937065	37.7	0.1
Nakuru	9036021	36.1	-0.3
Narok	9135001	35.9	-1.1
Nyahururu	9036135	36.4	0.0
Nyeri	9036288	37.0	-0.4
Thika	9137048	37.1	-1.0
Laikipia	8937022	37.0	0.1
Machakos	9137089	37.2	-1.6

3.2.2 Climate models and experiments

3.2.2.1 Atmospheric General Circulation Models (AGCMs)

Atmospheric General Circulation Models (AGCMs) are primarily designed to isolate the component of atmospheric variability driven by oceanic boundary forcing. AGCMs are less computationally demanding hence more simulations at higher spatial resolution aimed at improving signal-to-noise ratio can be obtained. This study employs ensemble simulations from four attribution-dedicated experiments: weather@home2, ECHAM5.4, CAM5.1, HadGEM3-A. Simulations for weather@home2 (Guillod et al., 2017) are produced by the www.climateprediction.net distributed system based at the University of Oxford. ECHAM5.4, and CAM5.1 participated in the Climate of the 20th Century Plus (C20C+) Detection and Attribution project (Stone et al., 2019) while HadGEM3-A contributed to both C20C+ and the Weather Events Interpretation and Attribution (EUCLEIA) (Christidis et al., 2013; Ciavarella et al., 2018; Vautard et al., 2019) event attribution projects. For each model, two sets of simulations are utilised: historical and natural, which serve as factual and counterfactual runs respectively for the attribution analysis. Historical runs are simulations representing possible states of the atmosphere and land surface for all years of 20th and 21st century under observed SST, land surface and sea ice boundary conditions, along with historical radiative forcing. Thus, they contain both natural and anthropogenic forcings. For observed SST and Sea Ice (SIC) extent, version 2 of the National Oceanic and Atmospheric Administration (NOAA) weekly optimum interpolation (NOAA OI.v2) SST dataset is used (Hurrell et al., 2008). For this study, outputs for MAM 2012, 2016, and 2018 are analysed. Natural simulations represent possible states of the atmosphere under an estimate of what the observed boundary conditions might have been in the absence of anthropogenic interference with the climate system. They have only natural historical forcings with all other held fixed at 1850 levels. For instance, SST and SIC fields are equal to those provided for historical runs but from which an estimate of the changes due to anthropogenic influence, ΔSST and ΔSIC, have been removed (Christidis et al., 2013). ΔSST is calculated as the difference between estimates using coupled model simulations of the historical and natural scenarios. Detailed experiment descriptions are laid out in Table 3.4 and further documentation and outputs from the CAM5.1, ECHAM5.4 simulations can be found online (https://portal.nersc.gov/c20c/data), (https://www.esrl.noaa.gov/psd/repository/alias/facts), and respectively. Outputs from weather@home2 and HadGEM3-A data are archived at (https://jasmin.ac.uk/).

Table 3.4 A description of Atmosphere-only model experiments used in the study

Model	**Experiment**	**Description**	**Citation**
CAM5.1	Historical All-Hist/est1 300 simulations	2012, 2016, and 2018 observationally derived SSTs and sea ice, GHG concentrations, sulphate aerosol burden, organic aerosol burden, black carbon aerosol burden, dust aerosol burden, sea salt aerosol burden, ozone concentrations, solar insolation, volcanic aerosol, land surface cover/use. Prescribed model aerosol values are used for the non-volcanic aerosols; volcanic aerosols are not included	Neale et al., 2012; Stone et al., 2018
	Natural Nat-Hist/ CMIP5-est1 300 simulations	1855 GHG concentrations, aerosol burdens, SST and Sea Ice extent, and ozone concentrations. Solar and volcanic forcing is identical to All-Hist/est1 SSTs generated by subtracting a CMIP5 multi-model mean estimate of the historical warming attributable to human influence, with sea ice adjusted for consistency	
ECHAM 5.4	Historical AMIP with observed Radiative Forcing 50 simulations	2012, 2016 & 2018 AMIP conditions with specified historical time varying GHG and ozone. The GHG evolution is based on observed estimates from 1979-2005, and then an RCP6 scenario thereafter. The time-varying ozone is based on data from the AC&C/SPARC ozone database	Roeckner et al., 2003; Roeckner et al., 2006
	Natural AMIP with 1880s Radiative Forcing 50 simulations	AMIP conditions in which the SST has been detrended and adjusted to 1880 equivalent mean conditions (the SST otherwise retain identical interannual and decadal variability as in the other experiments). Sea ice is set to a repeating seasonal cycle of roughly 1979-1990 (pre-emergence of the melt out). The GHG and ozone concentrations are adjusted to their 1880 values.	

weather@home2	Historical Actual 1131 simulations for 2012, 933 for 2016, and 1610 for 2018	2012, 2016, and 2018 SSTs and sea ice as observed, other forcings as RCP4.5	Guillod et al., 2017
	Natural Counterfactual 1131 simulations for 2012, 933 for 2016, and 1610 for 2018	2012, 2016, and 2018 SSTs reconstructed for preindustrial conditions, all other forcing set to preindustrial. The maximum observed sea-ice extent is used	
HadGEM3-A	Historical Historical 15 simulations for 2012, 140 for 2016, and 61 for 2018	2012, 2016, and 2018 observationally derived SSTs and sea ice, GHG concentrations, sulphate aerosol burden, organic aerosol burden, black carbon aerosol burden, dust aerosol burden, sea salt aerosol burden, ozone concentrations, solar insolation, volcanic aerosol, land surface cover/use	Christidis et al. 2013; Ciavarella et al. 2018; Vautard et al., 2019
	Natural Historical-NAT 15 simulations for 2012, 210 for 2016, and 66 for 2018	1850 GHG concentrations, aerosol burdens, SST and Sea Ice extent, and ozone concentration	

3.2.2.2 General Circulation Models (CGCMs)

Comprehensive coupled climate models allow a dynamically interacting ocean. Therefore, assumptions on the influence of anthropogenic climate change on ocean variability and on the effects of short-term coupled atmosphere-ocean interactions on the production of extreme weather and climate events are minimised. However, the simulated SSTs do not track those observed, so daily to decadal internal variability, and the timing of specific events, are not captured in these experiments. 7 models (see asterisked; Table 3.5) from the sixth phase of Coupled Model Intercomparison Project (CMIP6; Eyring et al., 2016) selected after evaluation (see section 3.4.1) of 15 (Table 3.5) for which daily rainfall data were available are employed. For models with more than one simulation, only the first member of the ensemble is utilised. Thus, the choice of the first member is arbitrary as ensemble members only differ by initial conditions.

For attribution, two climate worlds are considered: historical and natural. For the historical climate, the period 2000–2030 centred on 2015 is used. The study utilises historical simulations covering the period 1850–2014, and then extends the data to 2030 using simulations driven by the SSP1-2.6 (shared socio-economic pathway) scenario, which is closest to the current forcing for the averaging period (2000–2030). For all the SSP scenarios, climate conditions in the next 15–20 years are not projected to be significantly different from each other nor depart significantly from the current climate conditions. Therefore, it is assumed that the average forcing over the averaging period is roughly equal to the forcing during the period 2012–2018. The period 1850–1900 is taken to represent the natural climate, representative of the period prior to the onset of large-scale industrialization and human influence on the climate. This approach has been used in several studies (e.g., Van Oldenborgh et al., 2016; Uhe et al., 2017) to understand the pre-industrial climate in assessing changes in weather/climate extremes. While cognizant of alternative approaches used in other studies e.g., use of historicaNat runs, not all the coupled models used in this analysis have such data available. Further documentation and outputs from the CMIP6 experiments can be found online (https://esgf-node.llnl.gov/projects/cmip6/). Table 3.6 provides a summary of all the data used in the study.

Table 3.5 List of CMIP6 models evaluated. Those utilized are asterisked. (Expansions of acronyms are available online at https://www.ametsoc.org/ams/list-of-acronyms-and-abbreviations/)

Model	**Resolution**	**Institution**	**Citation**
CNRM-CM6-1-HR*	0.5° in the atmosphere, 0.25° in the ocean, 12 vertical levels	Centre National de Recherches Météorologiques, France	Voldoire et al., 2019
IPSL-CM6A-LR*	2.0°×2.0°, 39 layers in the vertical in both the atmosphere and ocean	Institute Pierre-Simon Laplace Climate Modelling Centre, France	Boucher et al., 2020; Lurton et al., 2020
INM-CM5*	2×1.5°, 73 vertical levels in the atmosphere; 0.5×0.25°, 40 levels in the ocean	Institute for Numerical Mathematics, Russian Academy of Science, Russia	Volodin & Gritsun, 2018; Volodin et al., 2017
NorESM2-MM*	1°×1° in both atmosphere and ocean, 32 vertical layers	NorESM Climate modelling Consortium, Norway	Seland et al., 2020
UKESM1-0-LL*	1.25°×1.875°, 85 vertical levels in the atmosphere and 1°, 75 vertical levels in the ocean	Met Office Hadley Centre, UK	Sellar et al., 2019
NESM3*	1.9°, 47 vertical levels in the atmosphere; 1°, 46 vertical levels in the ocean	Nanjing University of Information Science and Technology, China	Cao et al., 2018
MRI-ESM2-0*	1°×1° in both atmosphere and ocean, 80 vertical layers	Meteorological Research Institute (MRI) of the Japan Meteorological Agency	Yukimoto et al., 2019
CanESM5	2.8° in the atmosphere, 1° in the ocean, 49 vertical layers	Canadian Centre for Climate Modelling and Analysis	Swart et al., 2019
CESM2-FV2	1.25° × 0.96°, 32 vertical levels in the atmosphere and 1.25°× 0.27°,60 vertical levels in the ocean	National Centre for Atmospheric research, Climate and Dynamics Laboratory	Danabasoglu et al., 2020
EC-EARTH3	1° in both atmosphere and ocean, 91 vertical levels in the atmosphere, 75 levels in the ocean	European Research Consortium (EC-EARTH)	Döscher et al., 2021

MIROC6	2.5° in the atmosphere, 81 levels and 2.5°, 63 levels in the ocean	JAMSTEC, Japan	Tatebe et al., 2019
SAMO-UNICON	1.25°×0.94 in both atmosphere and ocean, 30 vertical levels in the atmosphere, 60 levels in the ocean	Seoul National University, South Korea	Park & Shin, 2019
TaiESM1	0.9× 1.25°, 30 vertical levels in the atmosphere and 1°, 60 levels in the ocean	Research Centre for Environmental Changes, Taiwan	Lee et al., 2020
HadGEM3-GC31-MM	1°, 85 vertical levels in the atmosphere and 0.25°, 75 levels in the ocean	Met Office Hadley Centre, UK	Andrews et al., 2020
MPI-ESM1-2-HR	T255,95 vertical levels in the atmosphere and 0.4°, 40 levels in the ocean	Max Planck Institute for Meteorology	Gutjahr et al., 2019

Table 3.6 A Summary of data used to achieve the objectives of the study

Characterisation of rainfall magnitude and associated synoptic conditions	**Attribution of human influence on rainfall magnitude**	**Attribution of human influence on synoptic conditions**
KMD station data	CHIRPS	Atmosphere-only run (AGCMs)
CHIRPS gridded data	Atmosphere-only runs (AGCMs)	Coupled model runs (CGCMs)
ERA5 reanalysis data	Coupled model runs (CGCMs)	
ERAINT reanalysis data		

3.3 Methods

3.3.1 Overall approach

This study seeks to understand and quantify human-induced thermodynamic and dynamic contributions to extreme rainfall in a defined region(s) in Kenya. The focus is on the role of anthropogenic climate change in the magnitude of flood-inducing rainfall and the synoptic atmospheric conditions associated with the heavy rainfall events of 2012, 2016 and 2018 March-April-May (MAM) seasons. The aim is to answer three questions: (i) what were the dominant synoptic atmospheric conditions present during heavy rainfall events of MAM 2012, 2016 and 2018 over the study region? (ii) Has the intensity of rainfall anomalies MAM 2012, 2016 and 2018 that resulted in both localised and widespread flooding in the study region been altered by anthropogenic climate change? (iii) Have the synoptic atmospheric conditions present during the 2012, 2016 and 2018 MAM extreme rainfall events been influenced by anthropogenic climate change? To answer these research questions, the study seeks to utilise existing well-established modelling frameworks and peer-reviewed methods, based on a wide range of observational, reanalysis and model data (see section 3.2). This approach is implemented in four steps outlined below.

Step 1: Model evaluation

The models are first evaluated to ensure that they reliably represent the observed rainfall in the study region. The focus is on the ability of both the AGCMs and CGCMs to realistically simulate MAM spatio-temporal patterns of seasonal and heavy rainfall over the study region. The methodology is detailed in section 3.3.1, and the results with discussions are presented in chapter 4.

Step 2: Characterise rainfall magnitude and synoptic atmospheric conditions associated with extreme rainfall of MAM 2012, 2016 and 2018 over the study region.

The heavy rainfall events are characterised and defined in a way that best reflects the extremity of the meteorological event and represents the cause of the impacts. For rainfall magnitude, three heavy rainfall indices are analysed: maximum consecutive 5-day (Rx5d), 10-day (Rx10d), and 20-day (Rx20d) precipitation over the study region. For synoptic atmospheric conditions, four atmospheric variables: specific humidity (q), air temperature (t), zonal (u) and meridional (v) wind at 850hPa (qtuv at 850hPa) are used to characterise the synoptic states. The methodology is detailed in section 3.3.2, and the results with discussions are presented in chapter 5.

Step 3: Quantify the role and contribution of human influence on changes in the magnitude of 2012, 2016, & 2018 MAM rainfall anomalies.

A multi-method multi-model event-attribution approach (Hegerl and Zwiers, 2011; Otto et al., 2016; NAS, 2016; Hannart et al., 2016) applied routinely to attribution studies (e.g., Van Oldenborgh et al., 2016; Haustein et al., 2016; Uhe et al., 2018; Sun and Miao, 2018; Herring et al., 2018; Philip et al., 2019) is used to estimate changes in magnitudes of Rx5d, Rx10d, and Rx20d attributable to human-induced climate change. Independent experiment-specific attribution methodology is applied to two different observational datasets and mul-tiple climate model simulations of varied experimental setups (see section 3.2). To obtain a general attribution statement(s), the results of each experiment type are first synthesised independently and then combined into an overall synthesis result. The methodology is detailed in section 3.3.3, and the results with discussions are presented in chapter 6.

Step 4: Quantify the contribution of human influence on changes in synoptic atmospheric conditions driving the intensity of extreme rainfall of 2012, 2016 and 2018 MAM season over the study region. The synoptic conditions associated with flood-inducing rainfall events of 2012, 2016 and 2018 MAM season over the study region in the current climate are analysed and compared to those in the pre-industrial climate to understand changes attributable to human influence. In this analysis, only climate models with the four atmospheric variables (qtuv at 850 hPa) available on daily timescales are utilised: one atmospheric model — HadGEM3-A, and four coupled models — CanESM, INM-CM5-0, MPI-ESM-2-HR and IPSL-CM6A-LR. The methodology is detailed in section 3.3.4, and the results with discussions are presented in chapter 7.

3.3.2 Model evaluation

Models have the advantage of a larger number of data points (many realisations of the climate), as they can simulate the climate many times over. However, for extreme event studies climate models are required, in terms of resolution and other properties, to capture the statistics of the events in a realistic manner (Shepherd, 2016; Van Der Wiel et al., 2017). Therefore, model evaluation is an integral part of every attribution study. Precipitation extremes in Eastern Africa are influenced by a complex interaction of changes in local weather systems and perturbations in the global and regional circulation (Nicholson 2017; Vellinga & Milton, 2018; Ongoma et al., 2018). In the region, there is limited understanding of the influence of regionally important forcings such as aerosols and land-use changes on weather and climate (Rowell et al., 2016) and remote forcing control, and inadequate simulation of the regional climate by many climate models (Giannini et al. 2018). These important factors pose a challenge in application of models to understanding changes in extremes over the region (Otto et al., 2015; Nicholson 2017; Otto et al., 2020). In this study, therefore, particular attention is paid on reliable

representation of observed rainfall by models for their application. Model evaluation focuses on the ability of the models to replicate the spatio-temporal patterns of seasonal and heavy rainfall over the study region. Four metrics are used to test the models' reproducibility of the patterns over the period 1987-2016: (a) Mean Absolute Error (MAE), (b) Pearson correlation coefficient (R), (c) Root Mean Squared Error (RMSE) and (d) Kolmogorov Smirnov Test (K-S test). The metrics are described in Table 3.7. The evaluation is undertaken over a region that encompasses the study domains of three events (3ºS, 3ºN, 34ºE, 39ºE; hereafter evaluation domain; see, section 3.1). The following patterns are assessed:

- The **spatial patterns** (hereafter, SS) of long term mean MAM rainfall over the domain which encompass study regions of the three events. Pattern correlations, deviations and absolute difference using R, RMSE and MAE, respectively between model outputs and observations are assessed. Good representation provides confidence that the larger scale atmospheric factors that control rainfall climatology are reasonably simulated in the model.
- ii) The **seasonal cycle** (hereafter, SC) of area-averaged rainfall over the evaluation domain. Pattern correlations, deviations and absolute differences using R, RMSE and MAE, respectively between model outputs and observations are assessed. Good representation provides confidence that the drivers of the seasonal cycle of rainfall are reasonably represented in the model.

- For the AGCMs, the **temporal (interannual) patterns** (hereafter, TS) of area-averaged rainfall over the evaluation domain. Pattern correlations, deviations and absolute differences using R, RMSE and MAE, respectively between model outputs and observations are assessed. Good representation increases confidence that a model is capturing the sea surface forced variability in rainfall. This evaluation is not undertaken for CGCMs as they are not forced by SST, and so interannual variability is not expected to correlate with observed rainfall.

- The **distribution of the seasonal rainfall maxima** (Rx5day, Rx10day and Rx20day) on which the attribution analysis is undertaken, derived from area-averaged daily rainfall over the evaluation domain. To evaluate the distributions of seasonal rainfall maxima, Quantile-Quantile (Q-Q) plots are generated for model outputs against observations and Kolmogorov- Smirnov (K-S) test is used to quantify the agreement. Good simulation of the distribution pattern increases confidence that the models can replicate the heavy rainfall events.

Table 3.7 Model performance metrics employed.

Metric	Description
$R = \frac{\sum_{t=1}^{n}(\hat{y}_t - \overline{\hat{y}_t})(y - \overline{y})}{\{[\sum_{t=1}^{n}(\hat{y}_t - \overline{\hat{y}_t})^2 \sum_{t=1}^{n}(y - \overline{y})^2]\}^2}$ Obtained by dividing the covariance of the model output and the observed data by the product of their standard deviations	Evaluates the strength of linear association between the anomalies of the model output and observations. It is constrained at -1 and 1. Positive values denote direct linear association; negatives denote inverse linear association; a value of 0 denotes no linear association. The closer the value is to 1 or –1, the stronger the linear association. A perfect relationship is denoted by 1. It is not sensitive to the bias but sensitive to outliers that might be present in the model.
$RMSE = \sqrt{\sum_{t=1}^{n}(\hat{y}_t - y)/n}$ The square root of the average of the squares of the errors.	It evaluates the deviation between the model output and observations. RMSE gives a relatively high weight to large errors since the errors are squared before they are averaged which makes this metric more useful when large errors are particularly undesirable.
$\mathrm{MAE} = \frac{1}{n}\sum_{j=1}^{n}\lvert y_j - \hat{y}_j\rvert$ It measures the average magnitude of the errors in a set of model simulations, without considering their direction	It gives the average of the absolute differences between model output and observations over the test sample where all individual differences have equal weight
K-S test	It compares the cumulative distribution function for the model outputs with that of the observations.
D= Maximum$\lvert F_o(X) - F_r(X)\rvert$ Fo(X): Observed cumulative frequency distribution i.e. (No. of observations ≤ X)/(Total no. of observations) Fr(X): The model frequency distribution	The null hypothesis assumes no difference between the observed and model distribution

The model performance is compared against the CHIRPS rainfall dataset, but also ERA5 is compared against CHIRPS, and then the performance statistics of the models are compared to those for ERA5. As an atmospheric reanalysis product, ERA5 can be considered as a benchmark for the models since data assimilation in the reanalysis process arguably makes ERA5 (or other reanalysis) “as good as it gets” for a model representation in a region. ERA5 combines vast amounts of historical observations into global estimates using stateof-the-science

modelling and data assimilation systems. It covers the earth on a 30 km horizontal resolution and resolves the atmosphere using 137 levels from the surface to a height of 80km (Hersbach et al., 2020). ERA5 has been found to exhibit similarity with gridded datasets like CHIRPS and CenTrends (Centennial Trends; Funk et al., 2015a) which incorporate most observations in Kenya (Nicholson & Wotter, 2021) with considerable improvements over ERA-interim through better representation of spatial distribution of precipitation during extreme years and reduction in climatological biases (Gleixner et al. 2020).

For every model, each performance metric is rated on a scale of 1 to 3 based on how close the metrics of its performance against CHIRPS are to those of ERA5. For each metric, a range of values is defined based on performance statistics of ERA5: 1 being on the low performing range, 2 medium performing range and 3 on the good performing range. The range of values and thresholds are set based on a much generalised understanding of what constitutes a bad and a good model. A model is rated based on the score of each metric after which the scores are averaged to give an overall score i.e., scores 1, 2, and 3 are averaged to give a mean performance of each parameter for every model. The cut-off score for AGCMs models is 2.5 while that of CGCMs models is 2.4 — the former exhibits better replicability than the latter. As such, model selection is based on mean performance (MP) i.e., those found to deviate substantially (persistent low average performance) from ERA5, and consequently CHIRPS, are disregarded for the analysis. For MAE, RMSE and the K-S test, small values indicate better model performance compared to big values. For R, positive values (preferably closer to 1) indicate better model performance than zero or negative values. Results for model evaluation are discussed in chapter 4. To note is that HadGEM3-A is not evaluated as the model runs were accessed later in the analysis as it was found that the necessary data from the other atmospheric models were not available for synoptic analysis.

3.3.3 Characterisation of Rainfall Magnitude and Associated Synoptic Atmospheric Conditions during MAM 2012, 2016 and 2018 Flooding Events

The extreme rainfall events of 2012, 2016 and 2018 MAM were characterised by heavy storms that caused localised and widespread flooding. Flood events can arise from different forms of rainfall extremes; short intense events or longer events resulting from multi-day accumulations. In the case of flood events considered here, there is no clear definition of what aspects of the observed rainfall events (e.g., duration and intensity) caused any single flood. Therefore, to guide the statistical analysis of the observations and the model experiments (NAS, 2016; Otto, 2017), the three MAM events are characterised and defined in a way that best reflects the extremity of the meteorological event and represents the causes of impacts i.e., spatial, and temporal definitions are based on the extremity of the anomalies and severity of impacts (see section 3.1). Spatially, index region(s): (3ºS, 1.7ºN, 34.7ºE, 37ºE), (3ºS, 2.0ºN, 34ºE, 36.7ºE) and (3ºS, 1.7ºN, 34.7ºE, 39ºE) for 2012, 2016 and 2018 events,

respectively covering the central highlands, western highlands and few parts of the arid and semi-arid central region of Kenya are selected as study regions. The domains are also large enough to accommodate GCM-scale data. Temporally, three different heavy rainfall indices: maximum consecutive 5-day, 10-day, and 20day precipitation (Rx5d, Rx10d, and Rx20d) (Zhang et al., 2011; Sillmann et al., 2013) are assessed.

To characterise the synoptic atmospheric conditions that underlied the extreme rainfall events, Self-Organizing Maps (SOMs), an unsupervised machine learning technique, is used to cluster multi-dimensional linked lower-level air variables into distinct dynamical states. SOM is an artificial neural net method for topologically sensitive clustering (Kohonen, 2001) and is visualised as an array of data archetypes or nodes, representing a nonlinear two-dimensional mapping of atmospheric states. Several studies have employed this method in deriving synoptic circulation types (e.g., Lennard & Hegerl, 2014; Wolski et al., 2017; Odoulami et al., 2020). In this study, SOM-based classification of atmospheric states and associated rainfall are characterised and analysed to evaluate changes in frequency of the synoptic conditions associated with the MAM rainfall anomalies. The clustering is carried out on four variables commonly used to define the synoptic state: specific humidity (q), air temperature (t), zonal (u) and meridional (v) wind at 850hPa. For simplicity hereafter, this set of variables are referred as qtuv. The suitability of the four variables (qtuv) is based on their ability to delineate wet and dry archetypes in the MAM season over the rainfall region.

The suitability assessment was carried out on several lower-level air variables, in combination and in isolation. The pressure level used (850 hPa) is close to the surface in highlands; near-surface conditions have the most explanatory power in these regions (Ogwang et al., 2014; Nicholson, 2016; Monday et al., 2021). The analysis is applied to ERAINT qtuv 850 hPa over a domain extending from 22° to 42°E and 4°S to 4°N (hereafter, SOM domain; Figure 3.2a) to characterise synoptic conditions associated with MAM rainfall over a region covering 3°S to 3°N and 34° to 39°E (hereafter, rainfall region; box in Figure 3.2b). The SOM domain captures the main synoptic features such as zonal and meridional wind and pressure patterns that influence MAM rainfall variability over Kenya. For instance, at the low levels, the Congo basin to the west exhibits substantial influence through the westerly humid air mass and the Indian Ocean to the east with easterlies/south easterlies. The positioning/location of the SOM domain (in reference to the rainfall/study region) is such that the synoptic features are well characterised and situated, to enable a proper evaluation of their influence in the season. The rainfall region encompasses the study areas for the three rainfall events i.e a common region that received high positive rainfall anomalies and reported widespread impacts in 2012, 2016 & 2018 MAM seasons. Also to note is that the rainfall region is the same domain used in model evaluation. First, the SOM classification is performed over the period 1981-2018, then nodes associated with wet, intermediate, and dry conditions are identified and assessed to determine whether those associated with wet conditions were more prevalent during the three MAM seasons.

To assess the contribution of different synoptic conditions to the extreme rainfall, mean (composite) climatological synoptic conditions of two circulation-related variables for each archetype (SOM node) are plotted: (i) geopotential heights (z) with moisture flux (Q): Q =q × V, and (ii) zonal wind (u), as well as their event-year anomalies, and rainfall characteristics of area average climatological and event-years total rainfall, all based on nodes obtained from the SOM analysis of qtuv at 850hPa. A 20-node 4 × 5 SOM is used. As clustering is carried out only on MAM data, a single SOM node represents conditions occurring approximately 4 days per MAM season (92 days/20 nodes) or 152 days over the analysed period of 1981-2018.

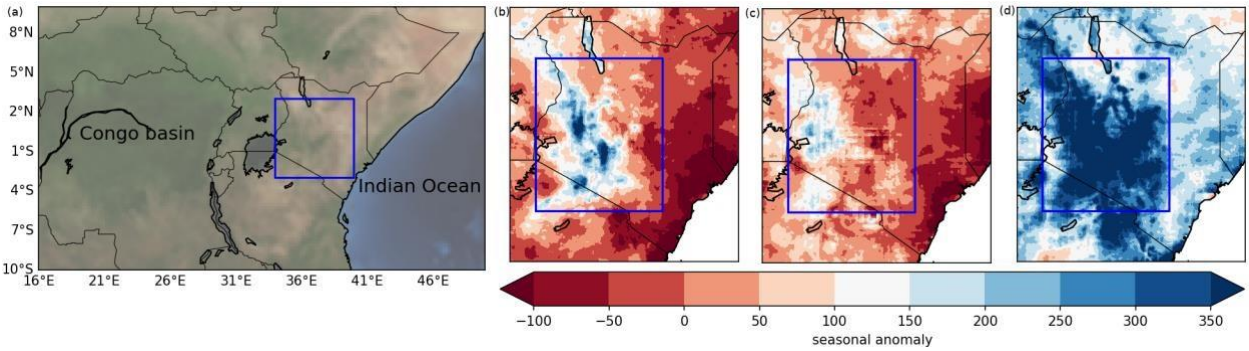

Figure 3.2 The SOM domain showing the dominant relief features for the region. Spatial distribution of seasonal total rainfall anomalies during MAM 2012(b), 2016(c), and 2018(d) in Kenya based on CHIRPS gridded dataset in reference to the 1981-2018 climatological period. The box shows the rainfall region over which area-average seasonal rainfall was calculated. SOM domain showing the dominant relief features for the region. Spatial distribution of seasonal total rainfall anomalies during MAM 2012(b), 2016(c), and 2018(d) in Kenya based on CHIRPS gridded dataset in reference to the 1981-2018 climatological

To evaluate frequencies of synoptic conditions responsible for the rainfall anomalies in the event years, nodes are grouped based on similarity in climatological synoptic conditions and rainfall characteristics. First, the nodes are grouped into wet and dry, then re-grouped into 6 different clusters of SOM nodes based on similarity in synoptic conditions. Here, the aim is to have separate groups of wet and dry nodes with distinct atmospheric states (synoptic clusters). A node is considered wet when the total rainfall associated with that node is above the 10th percentile of seasonal total rainfall across all nodes in the climatological period, with those below the 10th percentile classified as dry. Grouping into synoptic clusters is done based on similarity in patterns of pressure gradient, zonal wind shear and direction of moisture flux from the composite fields of z, Q and u over the SOM domain. It is carried out through visual interpretation of the node-specific composites for the atmospheric variables rather than a strict clustering procedure. The clusters are then ranked from wettest to driest. This process is a crucial step in this analysis as the resulting clusters form the basis for evaluating changes in node frequency associated with anomalous rainfall in the event years. The results with discussions are provided in chapter 5.

3.3.4 Attribution of Human Influence on Magnitude of Rainfall

In principle, every extreme event is unique and usually results from a combination of external drivers, natural and anthropogenic, as well as climate system internal (random or unresolved) variability (Stott et al., 2016). The presence of an external driver like human-induced climate change can alter the probability of occurrence or magnitude of an extreme weather or climate event. Therefore, the principle approach behind the probabilistic event attribution methodology employed in this study is to assess possible weather event(s) under current and preindustrial (counterfactual) climate conditions to estimate the occurrence magnitude of the event(s) under two conditions. The scientific question posed here is: Has the intensity of rainfall anomalies MAM 2012, 2016 and 2018 that resulted in widespread flooding in the study region been altered by anthropogenic climate change? To identify whether and to what extent the magnitude has changed, possible weather under 2012, 2016 and 2018 (current) climate conditions is simulated to identify the magnitude(s) of the event(s) in current climates and compares this with the magnitudes of the same kind of event(s) in a counterfactual climate with the human-induced drivers removed. The focus is on three heavy rainfall indices, the 5-day, 10-day and 20-day seasonal maxima, which capture a range of possible flood-inducing rainfall processes, from shorter intense events to longer more persistent rainfall that leads to flooding through saturation of the soil. Two different observational data sets and multiple climate model simulations of varied experimental setups are used, in each case independently applying an experiment-specific attribution methodology. This multi-method and multi-model approach is geared to-wards enhancing confidence in the findings and in the final overall attribution statement(s) (Philip et al., 2020).

Given its importance for the impacts, the attribution analysis focuses on the change in intensity or magnitude rather than probability of occurrence. Thus, magnitude ratio (MR) and the fraction of attributable magnitude (FAM) are evaluated to understand the role of human influence on the heavy rainfall events. MR is the measure of how the magnitude of n-day maximum rainfall during the season has changed in the present day versus the pre-industrial period. A MR >1.0 indicates that anthropogenic climate change has increased the magnitude of the event and vice versa for MR < 1.0. Following Stone & Allen's (2005) definition of FAR (Fraction of Attributable Risk) for likelihood-based event attribution, Fraction of Attributable Magnitude (FAM; expressed as $1 - 1/MR$) is defined here as the proportion of Rx5d, Rx10d, and Rx20d that can be ascribed to anthropogenic climate change. FAM is expressed as percentage increase (positive values) and percentage decrease (negative values) in interpreting the changes in attributable magnitude. For instance, FAM of 100% indicates that the event or class of events of the given magnitude would never occur in the preindustrial climate and thus is entirely attributable to anthropogenic climate change, while zero indicates that there is no influence of anthropogenic climate change on the magnitude of the event. FAM greater than zero implies human influence, with the amount of human influence

increasing for larger values. Negative values indicate that human influence has resulted in decrease in the given magnitude by that given proportion. The approaches are detailed in sections 3.4.4.1, 3.4.4.2 and 3.4.4.3.

3.3.4.1 Attribution analysis using observations

For observations, the study adopts an approach used in several recent attribution studies (e.g., van Oldenborgh et al., 2016; Van Der Wiel et al., 2017; Philip et al. 2019). That is Generalised extreme value (GEV) distribution, an approach to extreme value analysis that allows for characterization of intensity, duration, as well as the frequency of extreme events by defining extremes as block maxima (Coles, 2001). Since Rx5d, Rx10d, and Rx20d (for convenience hereafter, RxNds) are seasonal maxima, GEV analysis is well suited for the study. Following Katz (2013), a GEV is fitted to each of the RxNds, with 4-year smoothed global mean surface temperature (GMST) as a covariate to account for possible changes due to anthropogenic climate change over time, from which the return period and magnitude of each event in 2012, 2016 and 2018 (hereafter, event-years) with respect to preindustrial conditions (specifically, the year 1880) are estimated. MR is then calculated as the ratio of event-year magnitude versus preindustrial magnitude for the same return period as that observed.

For an extreme value x, GEV function is represented by

$$F(x) = \exp\left[-\left(1+\xi\frac{x-\mu}{\sigma}\right)^{1/\xi}\right]$$

$$\mu = \mu_0 \exp\left(\frac{\alpha T'}{\mu_0}\right),$$

$$\sigma = \sigma_0 \exp\left(\frac{\alpha T'}{\mu_0}\right),$$

Where **μ** is the location parameter, **σ** is the scale parameter, and **ξ** represents the shape parameter of the curve. The location parameter specifies the centre of the distribution while the scale parameter determines the size of deviations around the location parameter. The shape parameter determines the tail's behaviour (negative indicates light tail while positive indicates heavy tail). T′ is the smoothed GMST, a measure of the uniform global climate response to external forcing used to scale the GEV fit. In the case of precipitation, it is assumed that σ scales with μ (Hanel et al, 2009). The scaling is taken to be an exponential function of GMST resembling Clausius–Clapeyron (CC) scaling expected of daily precipitation extremes with local daily temperature in regions with enough

moisture availability (Allen & Ingram, 2002; Trenberth et al., 2003; Trenberth, 2011; O'Gorman, 2015). The fit parameters are estimated using the maximum likelihood estimation (MLE) method where σ, μ 0 and σ 0 are varied while ξ is assumed to be constant. For each event i, therefore, the return period is estimated in the event-year then the magnitude of the event with the same return period in 1880. MR and FAM are then calculated as described earlier. To sample the uncertainty of MR, 95% confidence intervals are estimated using a non-parametric bootstrap approach, by repeating the GEV fitting and magnitude estimation through 1000 random samples, with replication, of the observed data.

3.3.4.2 Attribution analysis using AGCMs

For the AGCMs, a non-parametric approach is applied since the high number of simulations do not require making distributional assumptions on the data. The simulations are initial-condition ensembles, so the variation between each simulation captures the stochastic nature of RxNd, while the ensemble mean represents the common (forced) signal. Therefore, in order to estimate the distribution of MR, RxNd is bootstrapped for each set of attribution runs to obtain a 1000member resample of the mean. To do this, 1000 pairs of historical and natural RxNd values are selected with replacement from which 1000 MRs are calculated. Basically, the ensemble mean of each RxNd is taken from the historical and the natural simulations as the forced and the unforced signal, respectively. Thus, for each event i, M_i , magnitudes in the event year, and M_0 , magnitudes are obtained in the natural climate for every RxNd. MR and FAM are then calculated, as described earlier, and calculate a median MR and FAM across the 1000 resamples. To sample the uncertainty of MR from the distribution, the 95% sampling interval for MR and FAM are calculated from the 1000 resamples.

3.3.4.3 Attribution analysis using CGCMs

For each CGCM, the return periods estimated in the observational analysis are used to evaluate changes in the event magnitudes between the current and the past climate. For this, GEV is fitted to RxNd (1851-1900 and 2001-2030), without a covariate, to evaluate magnitudes for a given return period. Present-day return periods based on CHIRPS analysis are used rather than KMD data, although results do not vary significantly (not shown). For every event i, therefore, M_i and M_0 for each RxNd are obtained. Then MR and FAM are calculated as described earlier and a bootstrapping approach is adopted to estimate the median and the 95% confidence intervals.

3.3.4.4 Synthesis of results

Since different approaches are used to evaluate MR and FAM for each experiment type, the results are first synthesised independently for each experiment type, and then combined into an overall synthesis result. The results are combining in the synthesis step to give quantitative summary statement for the attribution analysis. This, however, does not suggest that the best guess of that summary range is indeed any closer to the real answer to the question than the results from the individual experiments. But since none of the three experiment types provides the whole uncertainty, synthesis is used as a numerical aid to summarise the results. This has become a common practice, for example as described Philip et al., 2020. To calculate the median for each experiment, the mean of the individual medians is taken assuming equal weighting, and likewise for the overall synthesis result.

To estimate confidence intervals for the synthesis, the approach follows (Paciorek et al., 2018) in assuming that the experiment MRs (each with a median and 95% CI) distributions are not normally distributed, but that the right and left tails can be approximated as parts of two different normal distributions, with standard deviations (SD) equal to (mean – 2.5th percentile)/1.96 and (97.5th percentile – mean)/1.96, respectively. First, a pooled variance (S^2) is calculated using the estimated upper and the lower SD for each attribution result:

$$S^2 = (S_1^2(n_1-1) + S_2^2(n_2-1))/n_1 + n_2 - 2, \ldots\ldots\ldots\ldots\ldots\ldots \quad (1)$$

where n is the sample size, S^2 is the pooled variance. For equal sample size (as in our case), equation (4) reduces to $S^2=(S_1^2+S_2^2)/2$.

This can be extended for more than two samples (experiments)

$$S^2= (S_1^2+S_2^2+S_3^2+\ldots\ldots+S_m^2)/m\ldots\ldots\ldots \quad (2)$$

Where m is the number of experiments.

For each experiment type, lower pooled variance and upper pooled variance is calculated — from which the square root gives the pooled lower (pSD_l) and upper (pSD_u) standard deviation, respectively.

$$S_l^2 = (S_l1^2+ S_l2^2+ S_l3^2+\ldots\ldots+ S_lm^2)/m \ldots\ldots\ldots\ldots\ldots\ldots\ldots\ldots\ldots\ldots\ldots\ldots\ldots\ldots\ldots\ldots\ldots\ldots\ldots\ldots(3)$$

$$S_u^2 = (S_u1^2+ S_u2^2+ S_u3^2+\ldots\ldots+ S_um^2)/m \ldots\ldots\ldots\ldots\ldots\ldots\ldots\ldots\ldots\ldots\ldots\ldots\ldots\ldots\ldots\ldots\ldots\ldots\ldots\ldots(4)$$

Where S_l^2 and S_u^2 are the lower and upper pooled variances, respectively. The value of m is 2 for observations, 3[4] for atmospheric and 7 for coupled experiments.

Therefore, synthesis mean - ($1.96pSD_l$) and synthesis mean +($1.96pSD_u$) is taken to obtain lower and upper bound synthesis, respectively. To calculate the confidence interval for the overall synthesis mean, the above procedure is repeated using the pooled variances from each experiment. The results with discussions on the three approaches as well the synthesis are provided in chapter 6.

---

[4] The 4th atmospheric model (HadGEM3-A) was not used for this part of the study as the model runs were accessed later in the analysis as it was found that the necessary data from the other atmospheric models were not available for synoptic analysis.

3.3.5 Attribution of Human Influence on synoptic conditions

To understand changes in synoptic atmospheric states attributable to human influence, atmospheric circulation states associated with rainfall over the study region in the current climate are compared to those in the pre-industrial climate. SOM analysis is applied to natural and historical runs of both coupled (CanESM, INM-CM5-0, MPI-ESM-2-HR and IPSL-CM6A-LR) and atmospheric (HadGEM3-A) global model simulations (see description, section 3.2.2). These were the only models in which daily qtuv at 850 hPa required for the identification of atmospheric states were available. SOM clustering is applied on daily qtuv 850 hPa independently for each model after which it is linked to the model rainfall.

For each synoptic cluster (see section 3.4.3), changes in SOM characteristics (node frequency and associated rainfall) between the current and the natural climates are assessed. The statistical significance of changes in node frequencies and rainfall are tested using nonparametric Chi-square and Mann-Whitey U (Mann and D.R. Whitney, 1947; Shier, 2004; Fay and Proschan, 2010) tests, respectively. A confidence level of 90% is required to reject the null hypothesis in favour of the alternative that the change in node frequency and/or associated rainfall is statistically significant. The results with discussions are provided in chapter 7

4 Results: Model Evaluation

This chapter presents the results of the model evaluation (see section 3.3, step 1 & sub-section 3.3.1). The results are presented for spatial statistics, temporal statistics, seasonal cycle and Quantile-Quantile plots for AGCMs and CGCMs, in Section 4.1 and section 4.2, respectively. For each metric, a range of values is defined based on performance statistics of ERA5: 1 being on the low performing range, 2 medium performing range and 3 on the good performing range. As a summary, Figure 4.9 provides the average scores on a scale of 1-3 for each performance parameter for every model, and the mean of the average scores i.e. the overall performance of each model. A summary of findings is presented at the end of the chapter.

4.1 Atmospheric General Circulation Models (AGCMs)

For AGCMs, the evaluation is carried out on the spatial (SS), temporal (TS) and seasonal cycle (SC) patterns, and the distributions of the seasonal maxima (RxNds) using Q-Q plots. Statistics of MAE, RMSE and R for SS, TS and SC of the models are compared with those of ERA5 in which a range of values is defined to evaluate the performance of each model. For each parameter, every model is rated based on the score of each metric (relative to ERA5) after which the scores are averaged to give an overall score (see section 3.3.1). A separate table showing the range of values for each scoring category is given below the score table.

4.1.1 Spatial Statistics (SS)

Here, the results of the AGCMs' evaluation to reproduce spatial patterns of long term mean MAM rainfall over the study region(s) are presented. A separate table showing the range of values for each scoring category is given below the score table. From Table 4.1, ECHAM5 and ESRL_CAM5 perform best (score 3) in simulating the spatial characteristics of MAM rainfall over the study region. Both weather@home, HadGEM3-A and CAM5 show medium performance while MIROC show lowest performance.

Table 4.1 Scores of AGCM performance based on the statistics of the spatial characteristics. The table below this provides the range of values for each scoring category.

Model	MAE	score	RMSE	score	R	score	Overall score
ERA5	1.05		1.49		0.76		
ECHAM5	0.83	3	1.13	3	0.81	3	3
ESRL_CAM5	1.16	3	1.50	3	0.73	3	3
weather@home	1.41	2	1.86	2	0.73	3	2
MIROC	1.57	1	2	1	0.41	2	1
CAM5	1.25	2	1.58	2	0.46	2	2

Metric	Best performance range	Medium performance range	Low performance range
MAE	0.1-1.2	1.21-1.42	1.42-1.6
RMSE	1.0-1.5	1.51-1.9	2.0-2.5
R	0.5-1.0	0.3-0.49	-0.1- 0.29

4.1.2 Temporal Statistics (TS)

In simulating the temporal patterns (Table 4.2), ECHAM5 and CAM5 (score 3) exhibit highest reproducibility compared to the other models. ESRL_CAM5, HadGEM3-A and weather@home (score 2) show medium performance. Like spatial patterns, MIROC (score 1) show least performance in simulating temporal rainfall patterns over the region. A separate table showing the range of values for each scoring category is given below the score table.

Table 4.2 Scores of AGCM performance based on the statistics of the temporal characteristics. The table below this provides the range of values for each scoring category.

Model	MAE	score	RMSE	score	R	score	Overall score
ERA5	1.08		1.35		0.9		
ECHAM5.4	1.18	3	1.49	3	0.5	3	3
ESRL_CAM5	1.20	3	1.53	2	0.02	1	2
weather@home	0.87	2	1.51	2	0.44	2	2
MIROC	1.87	1	2.16	1	-0.13	1	1
CAM5.1	1.13	3	1.39	3	0.57	3	3

Metric	Good performance range	Medium performance range	Low performance range
MAE	0-1.2	1.21-1.3	1.31-1.9
RMSE	1.2-1.5	1.51-1.8	1.81-2.2
R	0.5-1.0	0.3-0.49	-0.1- 0.29

4.1.3 Seasonal cycle (SC)

Figure 4.1 shows the seasonal cycle patterns for the models together with that of CHIRPS and ERA5 in the region. Performance results are presented in Table 4.3. A separate table showing the range of values for each scoring category is given below the score table. Most models reliably reproduce the bimodal rainfall regime over the region — two rainy seasons (MAM and OND). However, all the models tend to under-estimate monthly rainfall in MAM (the wettest season) and over-estimate OND rainfall. Similarly, all but weather@home, HadGEM3-A and ECHAM5 tend to over-estimate rainfall in the relatively dry month of February. Looking at the overall performance, least reproducibility is shown by MIROC — wet biases in January, December and May, and less agreement in the bimodal pattern in comparison with that of CHIRPS and/or ERA5.

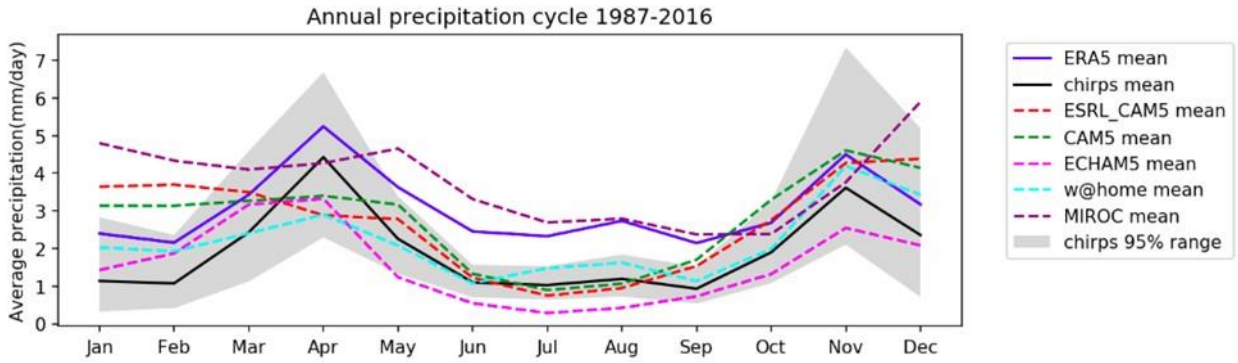

Figure 4.1 The mean annual cycle of rainfall (mm/day) during the period 1987–2016, averaged over (3ºS, 3ºN, 34ºE, 40ºE) for AGCMs, the reference datasets CHIRPs (thick black line) and ERA5 (thick purple line).

Table 4.3 Scores of AGCM performance based on the statistics of the monthly values of SC pattern shown in Figure 4.1. The table below this provides the range of values for each scoring category.

Model	MAE	score	RMSE	score	R	score	Overall score
ERA5	1.12		1.15		0.98		
ECHAM5	0.68	3	0.74	3	0.81	3	3
ESRL_CAM5	1.09	3	1.38	3	0.71	3	3

weather@home	0.53	3	0.69	3	0.80	3	3
MIROC	1.20	3	2.19	1	0.35	2	2
CAM5	1.02	3	1.21	3	0.71	3	3

Metric	**Good performance range**	**Medium performance range**	**Low performance range**
MAE	0-1.2	1.21-1.3	1.31-1.4
RMSE	0.1-1.5	1.51-1.8	1.81-2.2
R	0.7-1.0	0.3-0.69	-0.1- 0.29

4.1.4 Quantile-Quantile (Q-Q) plots

Figures 4.2, 4.3 and 4.4 show Q-Q plots used to assess the modelled distributions of Rx5d, Rx10d and Rx20d, respectively. The performance scores are presented in tables 4.4, 4.5 and 4.6, respectively. A separate table showing the range of values for each scoring category is given below the score table. The scores are based on the K-S statistic test. Despite all the models showing a dry bias, the relationship in the distribution is somewhat linear. Albeit not perfect, the linear relationship indicates that the models can be used reliably to assess the modelled changes in rainfall maxima. For Rx5d, ECHAM5, HadGEM3-A and weather@home exhibit relatively better performance (score 3) compared to ESRL_CAM5, MIROC and CAM5 (score 2). For Rx10d, weather@home (score 3) performs better than the rest while both weather@home and CAM5 simulate Rx20d the distribution relatively well.

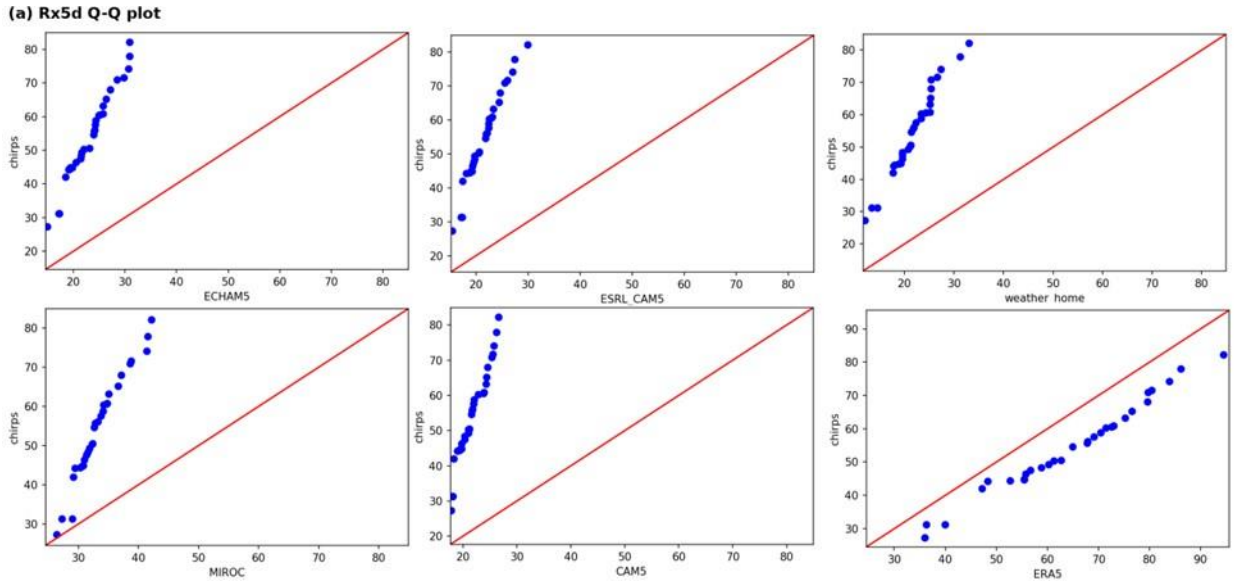

Figure 4.2 Quantile-Quantile plots comparing the distribution of observed versus modelled Rx5d rainfall over the evaluation region. The red line shows the function that would represent identical distributions between observations and model; while the blue the blue dots show the observed quantiles as a function of the model quantiles.

Table 4.4 Scores of AGCM performance based on the K-S statistics of Rx5d rainfall distribution as shown by the Q-Q plots on Figure 4.2. The table below this provides the range of values for each scoring category.

Rx5d	**k-s statistic**	**score**
ERA5	0.33	
ECHAM5	0.57	3
ESRL_CAM5	0.87	2
weather@home	0.53	3
MIROC	0.87	2
CAM5	0.89	2

Metric	**Good performance range**	**Medium performance range**	**Worst performance range**
K-S	0.1-0.6	0.61-0.9	0.91-1.0

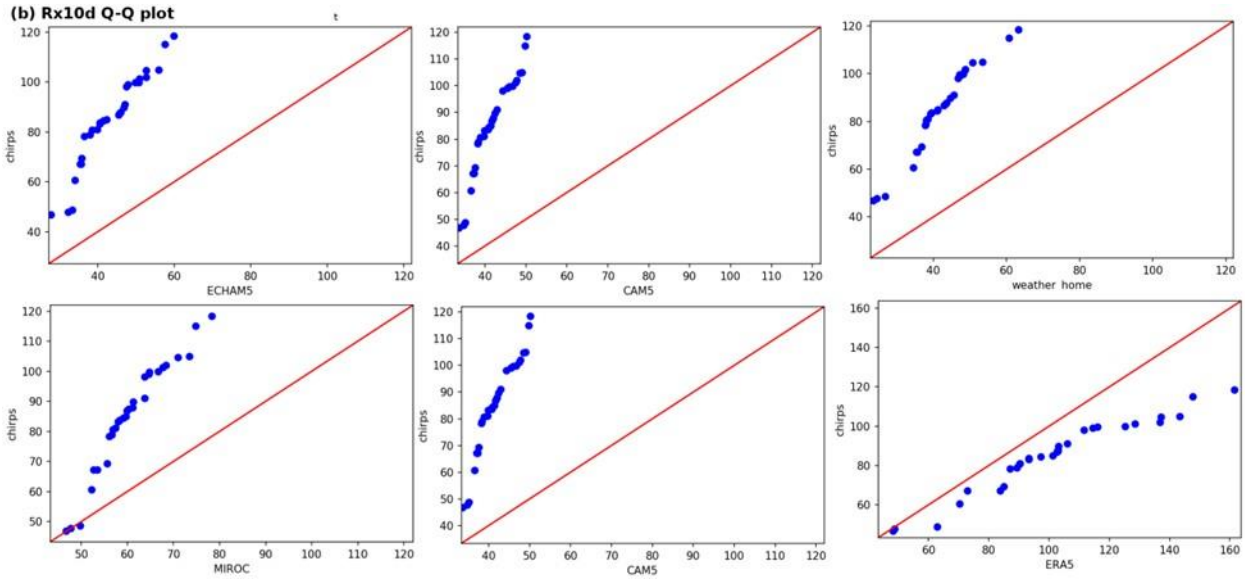

Figure 4.3 Quantile-Quantile plots comparing the distribution of observed versus modelled Rx10d rainfall over the evaluation region. The red line shows the function that would represent identical distributions between observations and model; while the blue dots show the observed quantiles as a function of the model quantiles.

Table 4.5 Scores of AGCM performance based on the K-S statistics of Rx10d rainfall distribution as shown by the Q-Q plots on Figure 4.3. The table below this provides the range of values for each scoring category.

Rx10d	**k-s statistic**	**score**
ERA5	0.37	
ECHAM5	0.90	2
ESRL_CAM5	0.90	2
weather@home	0.59	3
MIROC	0.77	2
CAM5	0.90	2

Metric	**Good performance range**	**Medium performance range**	**Low performance range**
K-S	0.1-0.6	0.61-0.9	0.91-1.0

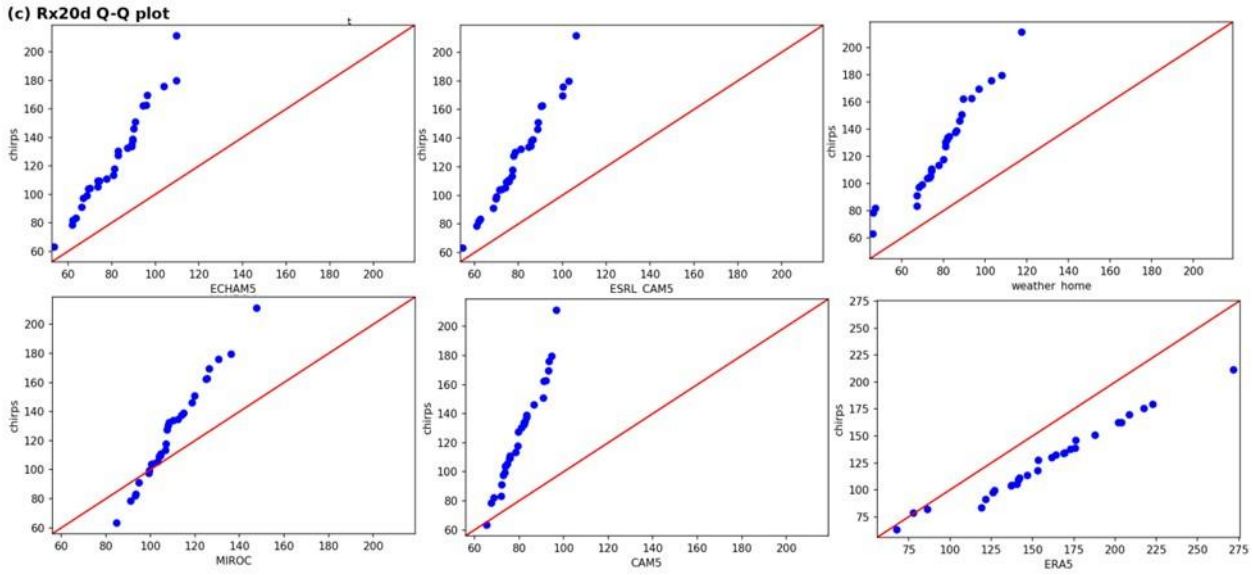

Figure 4.4 Quantile-Quantile plots comparing the distribution of observed versus modelled Rx20d rainfall over the evaluation region. The red line shows the function that would represent identical distributions between observations and model; while the blue dots show the observed quantiles as a function of the model quantiles.

Table 4.6 . Scores of AGCM performance based on the K-S statistics of Rx20d rainfall distribution as shown by the Q-Q plots on Figure 4.4. The table below this provides the range of values for each scoring category.

Rx20d	**k-s statistic**	**score**
ERA5	0.43	
ECHAM5	0.73	2
ESRL_CAM5	0.73	2
weather@home	0.60	3
MIROC	0.64	2
CAM5	0.59	3

Metric	**Good performance range**	**Medium performance range**	**Low performance range**
K-S	0.1-0.6	0.61-0.9	0.91-1.0

4.2 General Circulation Models (CGCMs)

For CGCMs, the spatial (SS) and seasonal cycle (SC) patterns, and Q-Q plots are used to evaluate the models. Statistics of MAE, RMSE and R for SS and SC, and K-S test for Q-Q plots for the models are analysed and compared with that of ERA5. A range of values is defined to evaluate the performance of each model. For each

parameter, every model is rated based on the score of each metric after which the scores are averaged to give an overall score (see section 3.3.1). A separate Table showing the range of values for each scoring category is given below the score table.

4.2.1 Spatial Statistics (SS)

Table 4.7 shows the spatial statistics evaluated for 15 coupled models that participated in the sixth model intercomparison project (CMIP6). CNRM-CM6, IPSL-CM6A, INM-CM5, NESM3, NorESM2_MM, TaiESM1 and UKESM1 (score 3) were found to perform relatively well in simulating the spatial patterns of rainfall over the region. The rest of the models registered an overall score of 2.

Table 4.7 Scores of CGCMs performance based on the statistics of the spatial characteristics. The table below this provides the range of values for each scoring category.

Model	**MAE**	**Score**	**RMSE**	**score**	**R**	**score**	**Overall score**
ERA5	1.15		1.49		0.76		
CanESM5	1.20	2	1.54	2	0.67	2	2
CESM2-FV2	1.23	2	1.72	2	0.33	2	2
CNRM-CM6	1.18	3	1.34	3	0.57	2	3
EC-EARTH	1.49	1	1.42	3	0.67	2	2
IPSL-CM6A	1.14	3	1.50	3	0.70	3	3
MPI-ESM1	1.30	2	1.76	2	0.73	3	2
MRI-ESM2	1.20	3	1.42	3	0.70	3	3
HadGEM3-GC31	0.97	3	1.39	1	0.78	3	2
INM-CM5	1.14	3	1.41	3	0.70	3	3
MIROC6	1.29	2	1.57	2	0.68	2	2
NESM3	1.08	3	1.48	3	0.71	3	3
NorESM2_MM	0.82	3	1.36	3	0.76	3	3
SAMO-UNICON	1.42	1	1.30	3	0.33	2	2
TaiESM1	1.17	3	1.47	3	0.70	2	3
UKESM1	1.19	3	1.14	3	0.73	3	3

Metric	**Good performance range**	**Medium performance range**	**Low performance range**
MAE	0-1.19	1.20-1.3	1.31-1.5
RMSE	1.2-1.5	1.51-1.8	1.81-2.2

R	0.7-1.0	0.3-0.69	-0.1- 0.29

4.2.2 Seasonal cycle (SC)

The season cycle patterns for the CGCMs, as well as CHIRPS and ERA5 are shown in Figure 4.5. The performance scores are shown in Table 4.8. A separate table showing the range of values for each scoring category is given below the score table. Most models reliably simulate the bimodal regime with the rainfall peaks in April and November for MAM and OND, respectively. However, for MIROC6, IPSL_CM6A, EC-EARTH and SAMO_UNICON the rainfall peak in the MAM season occurs in May. In general, the models underestimate (overestimate) rainfall in MAM (OND) seasons. Relatively good performance is exhibited by CESM2-FV2, CNRM_CM6, MPI-ESM1, MPIESM1, INM-CM5, NESM3 and NorESM2_MM (score 3).

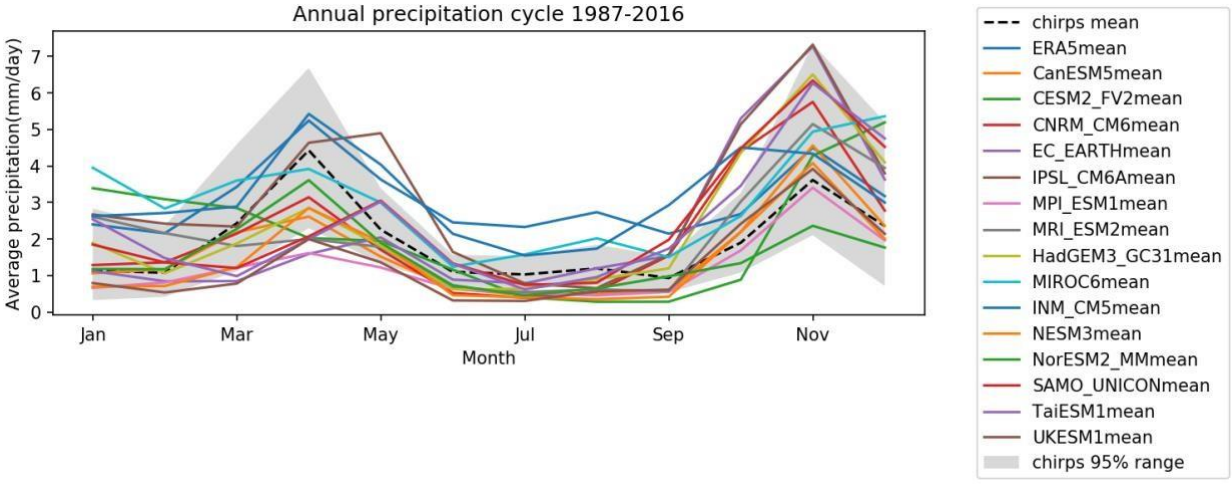

Figure 4.5 The mean annual cycle of rainfall (mm/day) during the period 1987–2016, averaged over (3ºS, 3ºN, 34ºE, 40ºE) for CGCMs, the reference datasets CHIRPs (thick black line) and ERA5 (thick purple line).

Table 4.8 Scores of CGCM performance based on the statistics of the monthly values of SC pattern shown in Figure 4.5. The table below this provides the range of values for each scoring category.

Model	MAE	Score	RMSE	Score	R	score	Overall score
ERA5	1.12		1.15		0.98		
CanESM5	1.32	1	1.71	2	0.81	3	2
CESM2-FV2	1.18	3	1.48	3	0.73	3	3
CNRM_CM6	0.84	3	1.11	3	0.72	3	3
EC-EARTH	1.19	3	1.77	2	0.29	1	2

IPSL-CM6A	1.35	1	1.79	2	0.76	3	2
MPI-ESM1	0.73	3	1.01	3	0.76	3	3
MRI-ESM2	1.01	3	1.81	1	0.56	2	2
HadGEM3 -GC31	1.25	2	1.64	2	0.67	2	2
INM-CM5	0.20	3	1.37	3	0.82	3	3
MIROC6	1.28	2	1.57	2	0.67	2	2
NESM3	0.64	3	0.74	3	0.88	3	3
NorESM2_MM	0.45	3	0.57	3	0.95	3	3
SAMO-UNICON	1.23	2	1.54	2	0.53	2	2
TaiESM1	1.33	1	1.85	1	0.28	1	1
UKESM1	1.28	2	1.23	2	0.65	2	2

Metric	**Good performance range**	**Medium performance range**	**Low performance range**
MAE	0-1.2	1.21-1.3	1.31-1.4
RMSE	0.1-1.5	1.51-1.8	1.81-2.2
R	0.7-1.0	0.3-0.69	-0.1- 0.29

4.2.3 Quantile-Quantile (Q-Q) plots

The Q-Q plots for Rx5d, Rx10d and Rx20d are shown in Figures 4.6, 4.7 and 4.8 respectively. The performance scores are presented in tables 4.9, 4.10 and 4.11, respectively. A separate table showing the range of values for each scoring category is given below the score table. A separate table showing the range of values for each scoring category is given below the score table. For the three seasonal maxima, the distribution of ERA5, which is the benchmark for the models, exhibits a linear relationship although with a rather wet bias. For Rx5d, the models exhibit both non-linear (combined wet and dry bias) and linear (with dry bias) relationships. Substantial non-linear relationships are depicted by CanESM5, CESM2-FV2 and MIROC6. Linear relationship in the distribution (with dry bias) is shown by EC-EARTH, HadGEM3-GC31, UKESM1 and SAMOUNICON. Best performance is exhibited by CNRM-CM6, IPSL-CM6A and MRI-ESM2. For Rx10d, substantial non-linear relationships are

shown by CESM2-FV2 and MIROC6. IPSL-CM6A, NESM3 and UKESM1 are the best performing models. For Rx20d, all the models simulate the distribution relatively well. Linear relationships are shown by all models with a minimal wet and dry bias, except for CESM2-FV2 which show a substantial non-linear relationship. MRI-ESM2 and NorESM2_MM perform best in simulating the distribution of Rx20d.

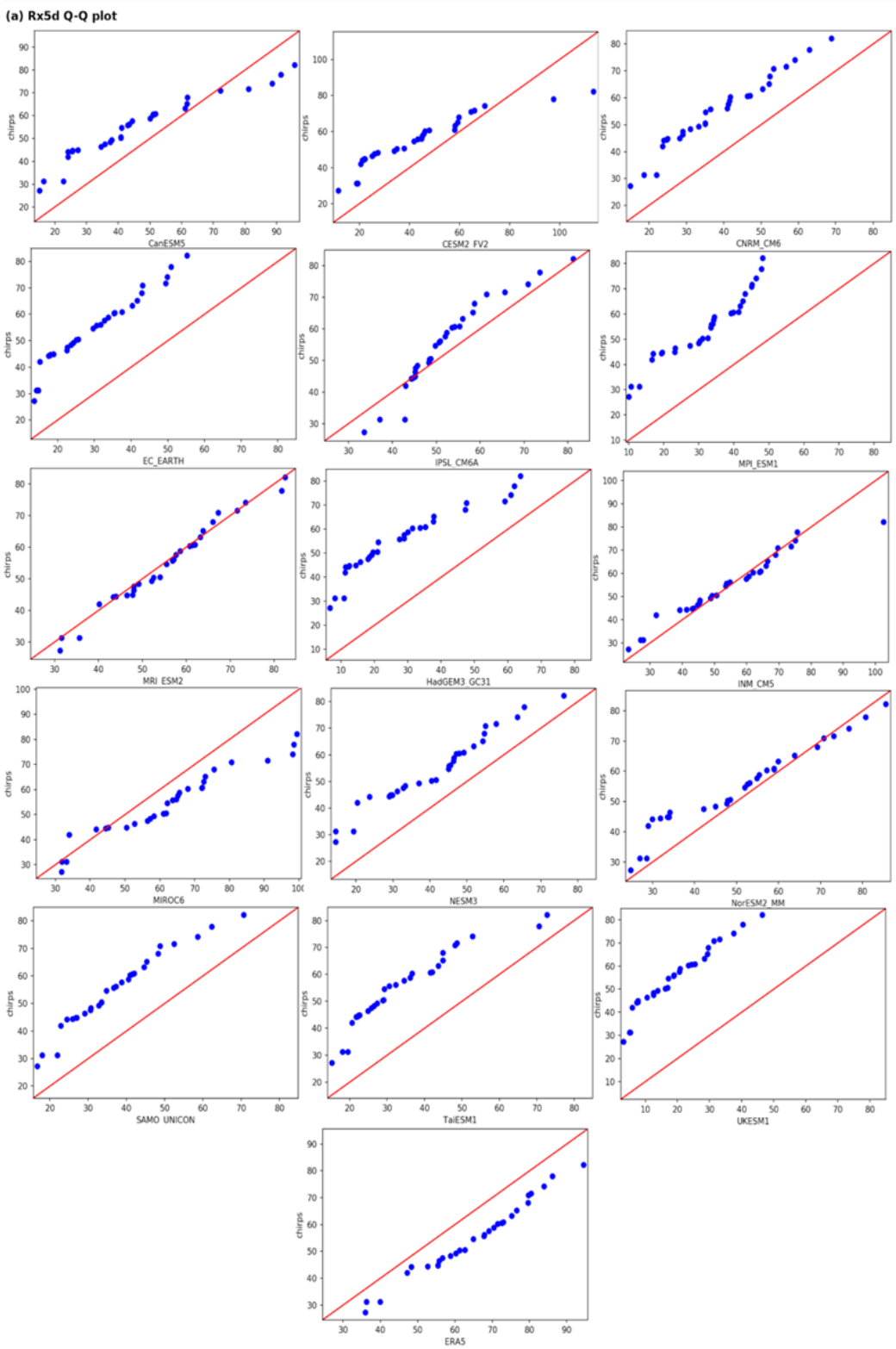

Figure 4.6 Quantile-Quantile plots comparing the distribution of observed versus modelled Rx5d rainfall over the evaluation region. The red line shows the function that would represent identical distributions between observations and model; while the blue dots show the observed quantiles as a function of the model quantiles.

-

Table 4.9 Scores of CGCMs performance based on the statistics of Rx5d rainfall distribution as shown by the Q-Q plots on Figure 4.6. The table below this provides the range of values for each scoring category

Rx5d	**k-s statistic**	**score**
ERA5	0.33	
CanESM5	0.63	2
CESM2-FV2	0.70	2
CNRM-CM6	0.57	3
EC-EARTH	0.93	1
IPSL-CM6A	0.23	3
MPI-ESM1	0.70	2
MRI-ESM2	0.10	3
HadGEM3-GC31	0.70	2
INM-CM5	0.63	2
MIROC6	0.93	1
NESM3	0.67	2
NorESM2_MM	0.72	2
SAMO-UNICON	0.63	2
TaiESM1	0.53	1
UKESM1	0.87	2

Metric	**Good performance range**	**Medium performance range**	**Low performance range**
K-S	0.1-0.6	0.61-0.9	0.91-1.0

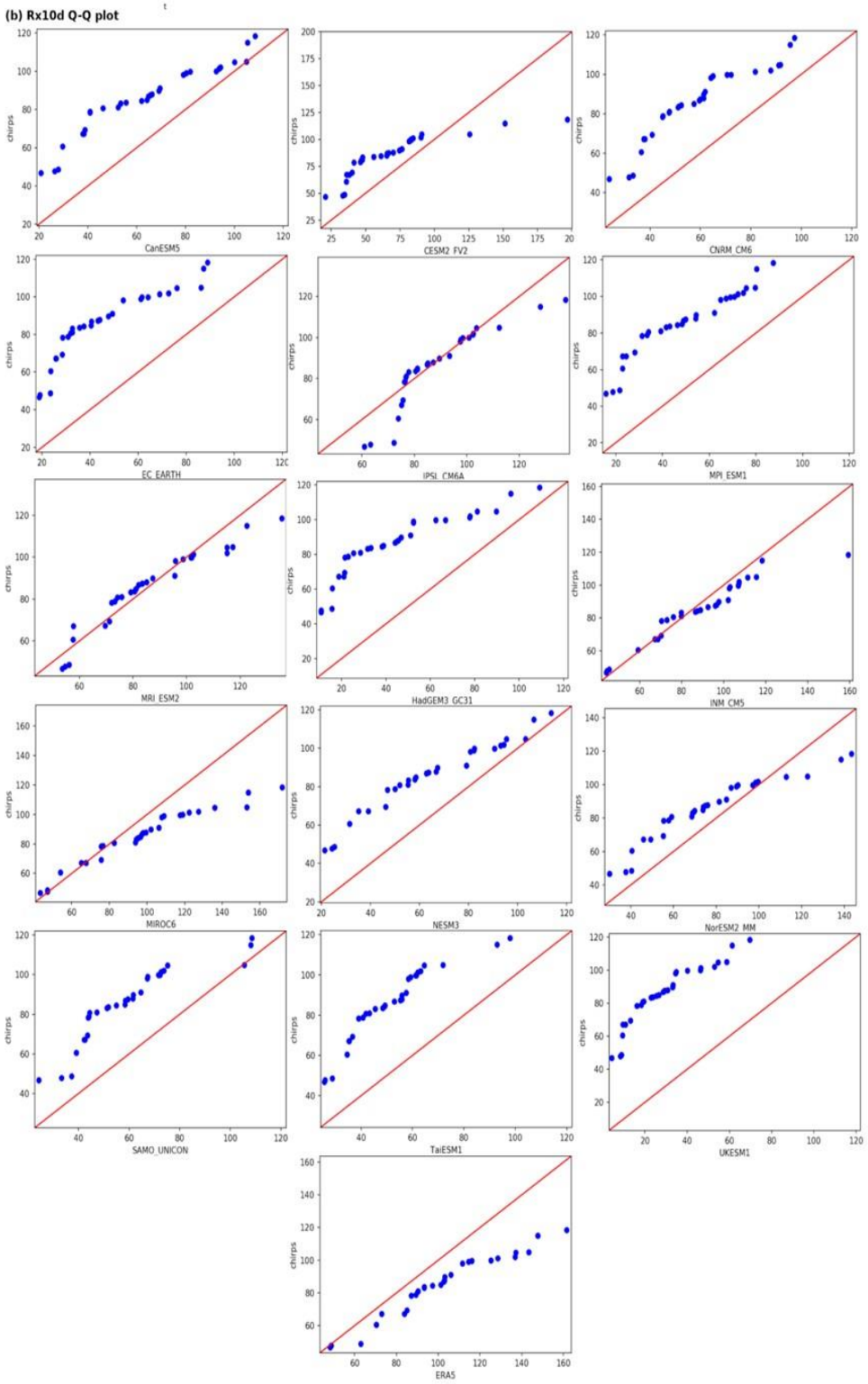

Figure 4.7 Quantile-Quantile plots comparing the distribution of observed versus modelled Rx10d rainfall over the evaluation region. The red line shows the function that would represent identical distributions between observations and model; while the blue dots show the observed quantiles as a function of the model quantiles.

-

Table 4.10 Scores of CGCMs performance based on the statistics of Rx10d rainfall distribution as shown by the Q-Q plots on Figure 4.7. The table below this provides the range of values for each scoring category

Rx10d	k-s statistic	score
ERA5	0.37	
CanESM5	0.70	2
CESM2-FV2	0.63	2
CNRM-CM6	0.61	2
EC-EARTH	0.92	1
IPSL-CM6A	0.17	3
MPI-ESM1	0.92	1
MRI-ESM2	0.67	2
HadGEM3-GC31	0.67	2
INM-CM5	0.63	2
MIROC6	0.73	2
NESM3	0.47	3
NorESM2_MM	0.67	2
SAMO-UNICON	0.67	2
TaiESM1	0.57	1
UKESM1	0.53	3

Metric	Good performance range	Medium performance range	Low performance range
K-S	0.1-0.6	0.61-0.9	0.91-1.0

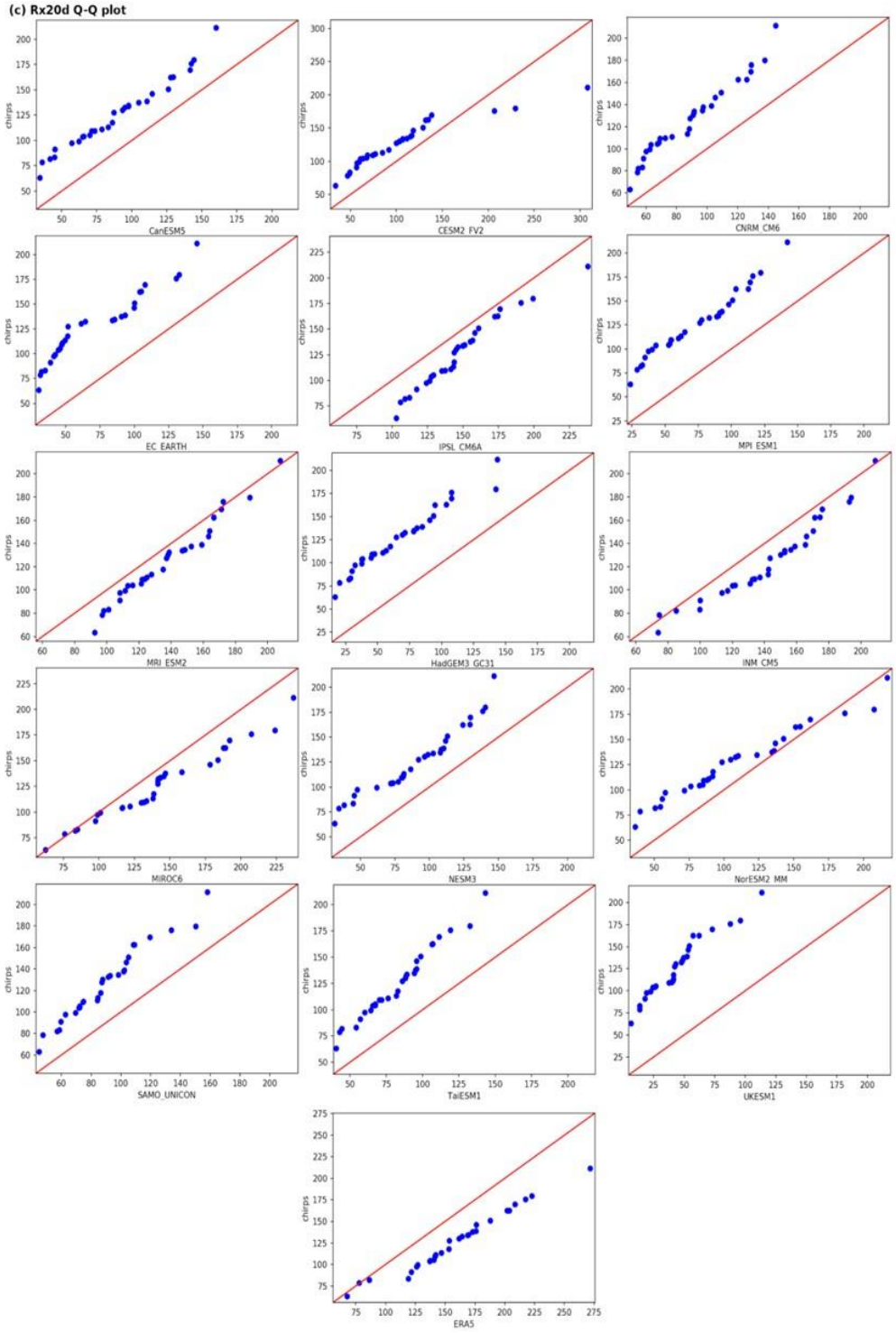

Figure 4.8 Quantile-Quantile plots comparing the distribution of observed versus modelled Rx10d rainfall over the evaluation region. The red line shows the function that would represent identical distributions between observations and model; while the blue dots show the observed quantiles as a function of a function of the model quantiles.

-

Table 4.11 . Scores of CGCMs performance based on the statistics of Rx10d rainfall distribution as shown by the Q-Q plots on Figure 4.8. The table below this provides the range of values for each scoring category.

Rx20d	**k-s statistic**	**score**	
ERA5	0.43		
CanESM5	0.92	1	
CESM2-FV2	0.61	2	
CNRM-CM6	0.63	2	
EC-EARTH	0.67	2	
IPSL-CM6A	0.73	2	
MPI-ESM1	0.60	1	
MRI-ESM2	0.23	3	
HadGEM3-GC31	0.67	2	
INM-CM5	0.63	2	
MIROC6	0.93	1	
NESM3	0.70	2	
NorESM2_MM	0.33	3	
SAMO-UNICON	0.63	2	
TaiESM1	0.70	2	
UKESM1	0.87	2	

Metric	**Good performance range**	**Medium performance range**	**Low performance range**
K-S	0.1-0.6	0.61-0.9	0.91-1.0

4.3 Summary of findings

Figure 4.9 provides a summary of AGCM and CGCM evaluation results based on temporal patterns (TS) and spatial patterns (SS), Rx5d Q-Q plot (QQ5), Rx10d Q-Q plot (QQ10) and Rx20d Q-Q plot (QQ20), and seasonal cycle pattern (SC). For every model, each rainfall characteristic (TS, SS, QQ5, QQ10, QQ20, and SC) is rated on a scale of 1-3 based on how close the statistics of its metrics are to that of CHIRPS and ERA5 data (see Section 3.3.1). Models with an average score below 2.5 are marked with an X over the MP boxes and were excluded in the analysis. For AGCMs, ESRL_CAM5 and MIROC were excluded while weather@home, CAM5 and ECHAM5 were utilised in the analysis. For CGCMs, CanESM5, CESM2-FV2,

EC-EARTH, MPI-ESM1, HadGEM3GC31, MIROC6, SAMO-UNICON, TaiESM1 were excluded while CNRM-CM6, IPSL-CM6A, MRIESM2, INM-CM5, NESM3, NorESM2_MM and UKESM1_LL were used in study.

The models generally reproduce the expected rainfall characteristics over the study region. All models simulate reliably well the expected bimodal rainfall regime, associated with north-south migration of the inter-tropical convergence zone (ITCZ). However, they all underestimate MAM rainfall intensities, while overestimating OND. This misrepresentation is larger in the coupled models. The same weakness has been found in CMIP5 (Tierney et al., 2015; Ongoma et al., 2018; King et al., 2020), CMIP3 (Anyah & Qiu, 2012a) and weather@home2 (Uhe et al. 2017). However, Ayugi et al. (2021) found substantial performance improvement in CMIP6 over CMIP5 in representation of East African rainfall, notably, simulation of mean annual cycle and extreme indices although biases remain. The coupled models systematically produce larger extremes than the atmospheric models. Nonetheless, coupled models capture the distribution of RxNds, and spatial and temporal patterns of MAM rainfall season reasonably well compared to the atmospheric models. Higher resolution models like the atmosphere-only models are generally considered to capture extreme rainfall better, but this does not appear to be the case here; why this is the case is unclear, and worthy of further research, but is out of scope for this thesis. However, in general, AGCMs show better performance than the coupled models in this evaluation.

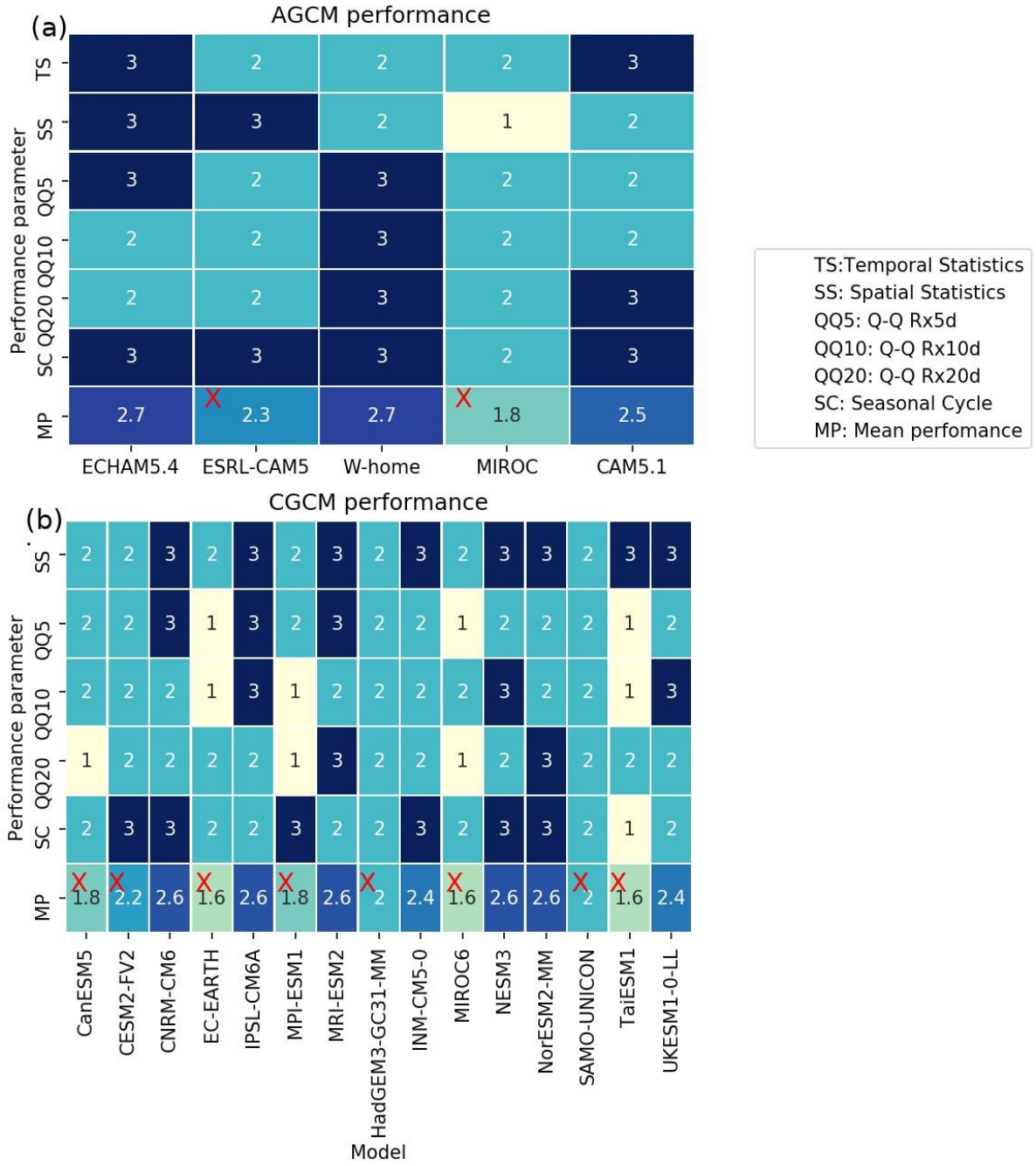

Figure 4.9 Summary of model performance for (a) C20C+ and weather@home and (b) CMIP6 models based on different statistics of spatio-temporal characteristics of MAM rainfall in the study region. The numbers in the heat map represent the average score on a scale of 1-3 (with 3 representing good and 1 bad performance), based on MAE, R, and RMSE for TS, SS, SC, QQ5, QQ10, and QQ20. MP is the mean of the average scores which gives the overall performance of each model. Models with an average score below 2.5 are marked with a red X over the MP boxes and were excluded in the analysis.

5 Results: Characterisation of Rainfall Magnitude and Associated Synoptic Conditions during Recent Flooding Events

This chapter provides and discusses the results of the characterization of the rainfall intensity and the associated atmospheric states during the MAM 2012, 2016 and 2018 seasons (see Objective 1, Section 1.2; Step 2, Section 3.3). Section 5.1 presents and discusses the results on SOM classification of synoptic conditions in the MAM season (1981-2018) and the associated rainfall characteristics. Section 5.2 provides results and discussions on the changes in atmospheric conditions associated with anomalies in rainfall and node frequencies during the flood events of 2012, 2016 and 2018 MAM season. A summary of findings is presented at the end of the chapter.

5.1 Climatology of synoptic conditions and associations with rainfall

This section provides a description of the archetypal synoptic climatological conditions classified by the SOM process and their association with the climatological rainfall characteristics over the rainfall region. Figures 5.1, 5.2, and 5.3 show the characterised states of moisture flux and geopotential heights at 850 hPa, zonal wind at 850 hPa, total observed rainfall in the MAM season and daily distribution of rainfall, respectively for the period 1981-2018, for each SOM node. From the node-grouping analysis (see methodology, section 3.4.3), nodes 1, 2, 3, 4, 5, 6, 7, 8, 9, 10, 11, 12 were identified as wet, and 13, 14, 15, 16, 17, 18, 19, 20 as dry (Figures 5.3 and 5.4). Three distinct categories of synoptic clusters were identified for each set of wet and dry nodes resulting in six clusters. Based on total rainfall amounts, the clusters are named/numbered in descending order of wetness (1 being wettest and 6 driest) as follows: cluster 1 — nodes 3, 4, 8, 12; cluster 2 — nodes 1, 2, 5, 9; cluster 3 — nodes 6, 7, 10, 11; cluster 4 — nodes 15,16,19, 20 ; cluster 5 — 13,17 and cluster 6 — 14, 18. Generally, in the MAM season, the atmospheric pressure over the SOM domain is relatively high over the Indian Ocean (east) compared to the western half of the SOM domain while the moisture flux mostly is easterly to south-easterly (Figure 5.1). The zonal wind flow is predominantly easterly with relatively weak easterly to weak westerly at lower levels compared to mid and upper levels (Figure 5.2). However, a relatively strong pressure gradient between the east and the west of the SOM domain and vertical wind shear between low and high tropospheric levels are seen for nodes on the right half of the panel compared to those on the left (Fig. 5.2). Table 5.1 gives the cluster total rainfall, percentage of total seasonal rainfall and a summary of the synoptic conditions in each cluster.

Table 5.1 Total mean seasonal rainfall, percentage of total mean rainfall and summary of synoptic conditions in each cluster

Cluster	**Nodes**	**Total mean Rainfall (mm. season^{-1})**	**% Of total mean seasonal**	**Summary of synoptic conditions**
1	3, 4, 8, 12	107.3	34.7	Widespread convergent flow at the surface. Strong vertical wind shear
2	1, 2, 5, 9	83.7	27.1	Localised convergent flow at the surface. Relatively less strong zonal surface pressure gradients over the SOM domain compared to cluster 1. Strong vertical wind shear
3	6,7,10,11	73	23.6	Localised convergent flow at the surface. Confined upper easterly flow. Weak vertical wind shear.
4	15, 16, 19, 20	34.2	11.1	Localised convergent flow at the surface. Confined and weak vertical wind shear.
5	13, 17	6.9	2.2	Divergent flow at the surface. No vertical wind shear i.e. easterlies at tropospheric levels.
6	4, 18	3.7	1.2	Divergent flow at the surface No vertical wind shear i.e. easterlies at all tropospheric levels.

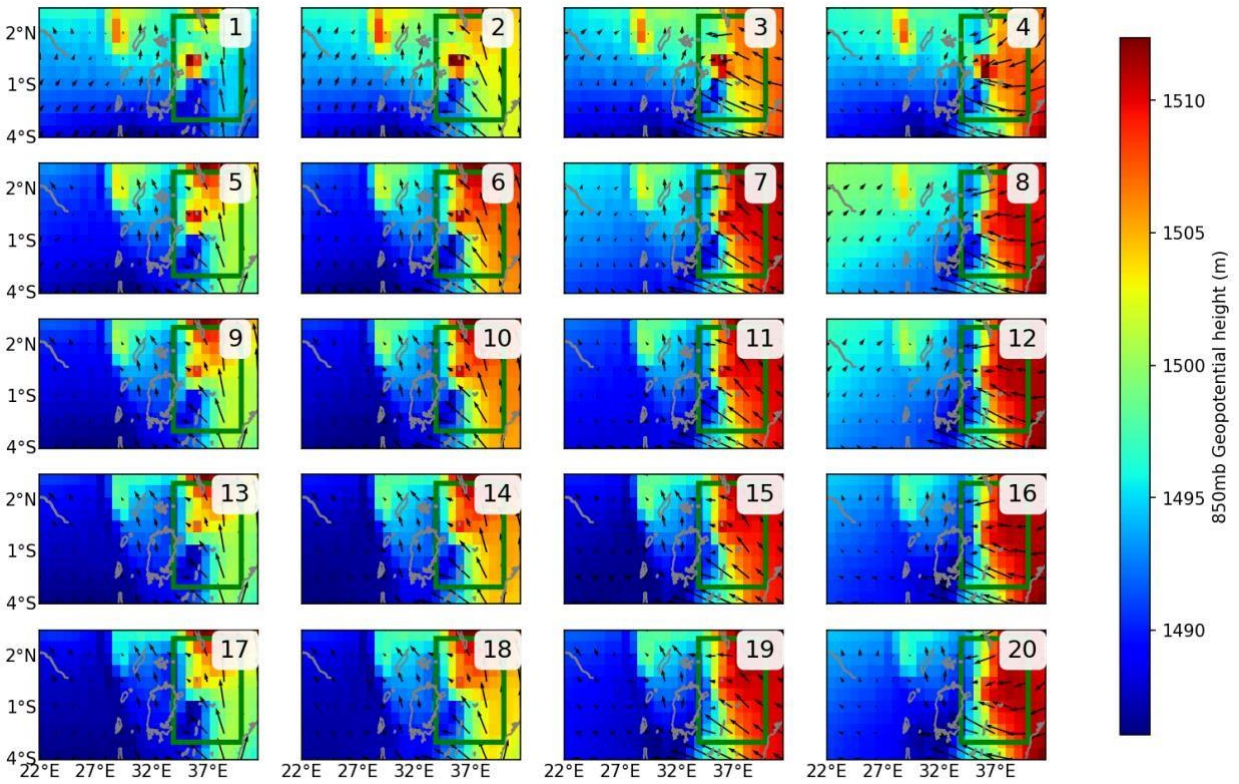

Figure 5.1 Mean MAM geopotential heights(shaded) and moisture flux (arrows) at 850hPa for each node over the SOM domain on days in the climatological period that are characterised by synoptic conditions identified by SOM analysis of qtuv at 850 hPa. The box shows the rainfall region analysed.

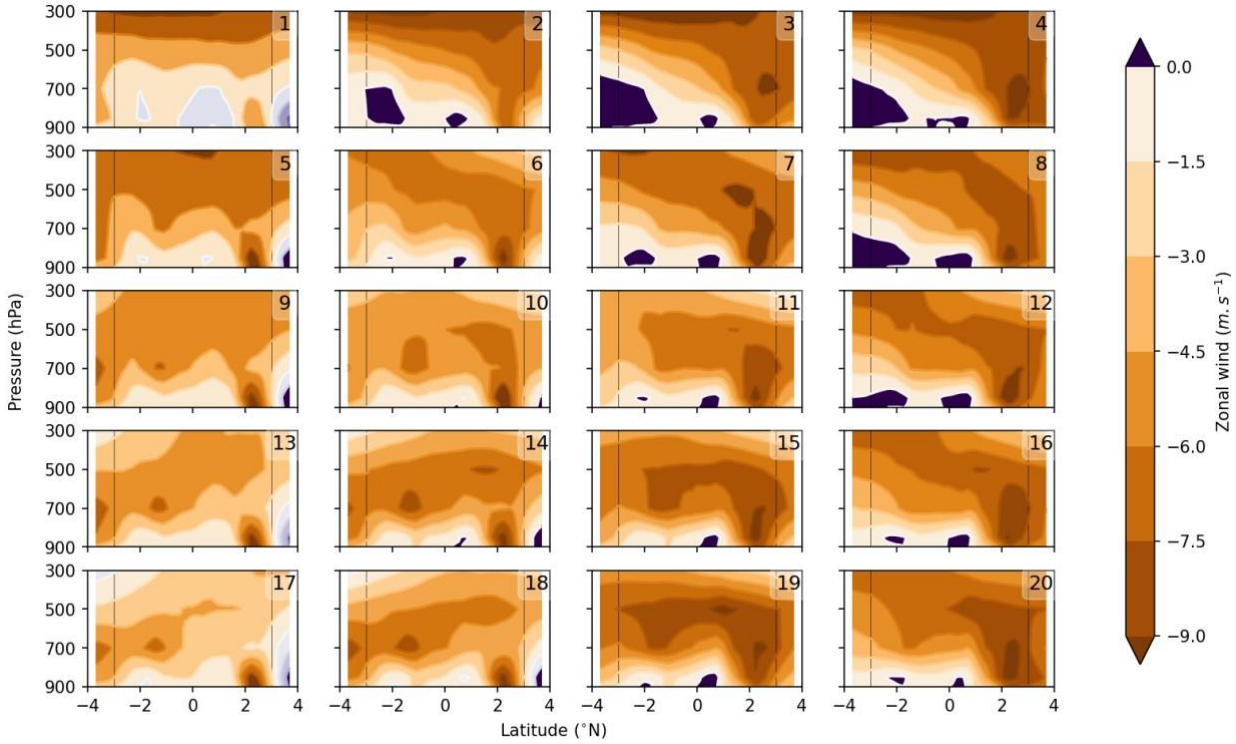

Figure 5.2 Latitude-height cross-section of mean zonal wind at 850hPa over SOM domain on days in the climatological period characterised by circulation types identified by SOM analysis of qtuv at 850 hPa. The wind is plotted for values at a particular longitude. The box shows the rainfall region. Numbers in the top right of each plot indicate the SOM node. The negative values of zonal wind indicate flow is generally easterly

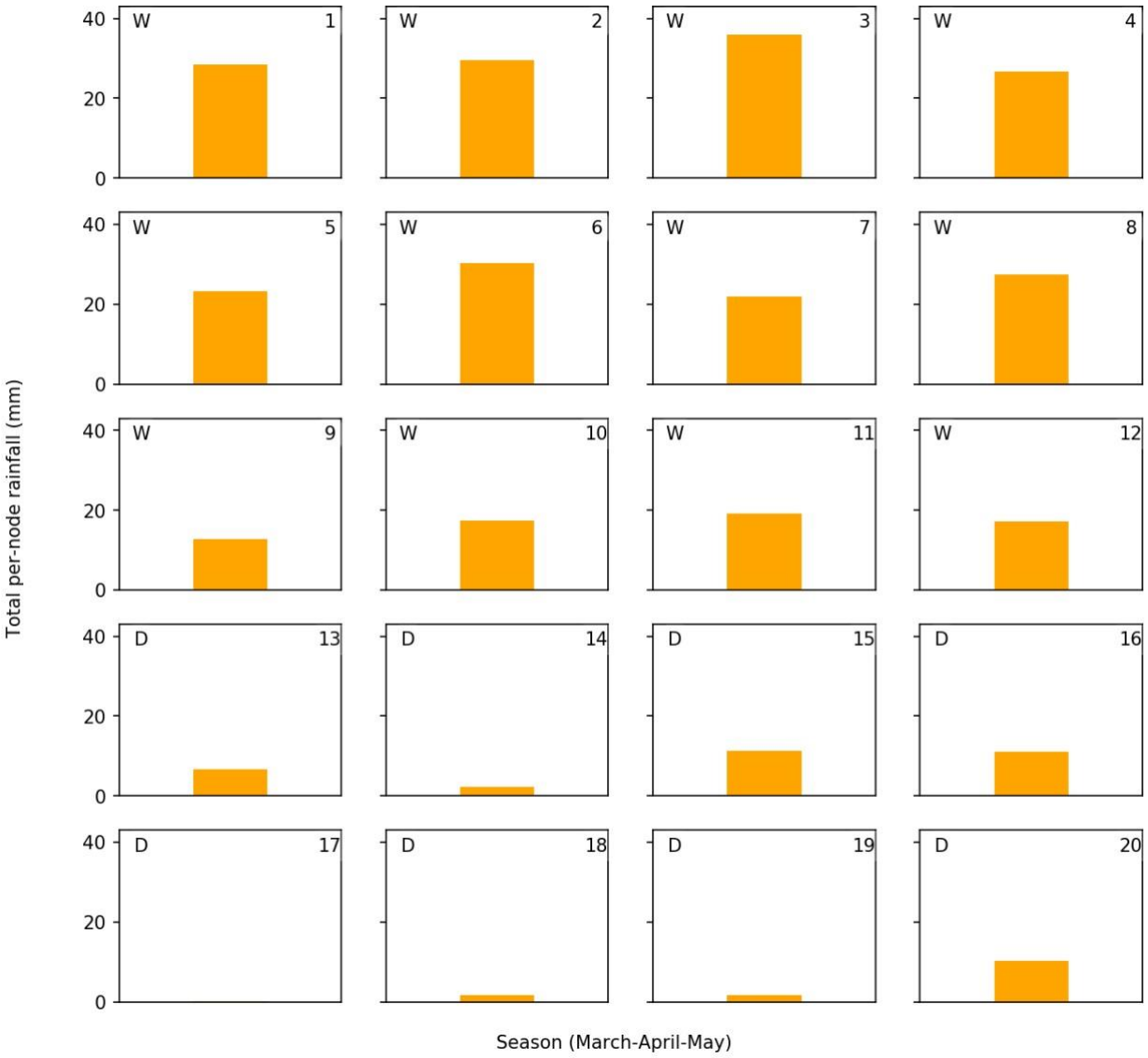

Figure 5.3 Total mean seasonal rainfall (mm.season-1) on days characterised by the atmospheric states represented in Figures 5.1 and 5.2, during the climatological period (1981–2018). Numbers in the top right of each plot indicate the SOM node. The letter in the top left represents the rainfall characteristic for that node: 'W' for wet nodes and 'D' for dry nodes.

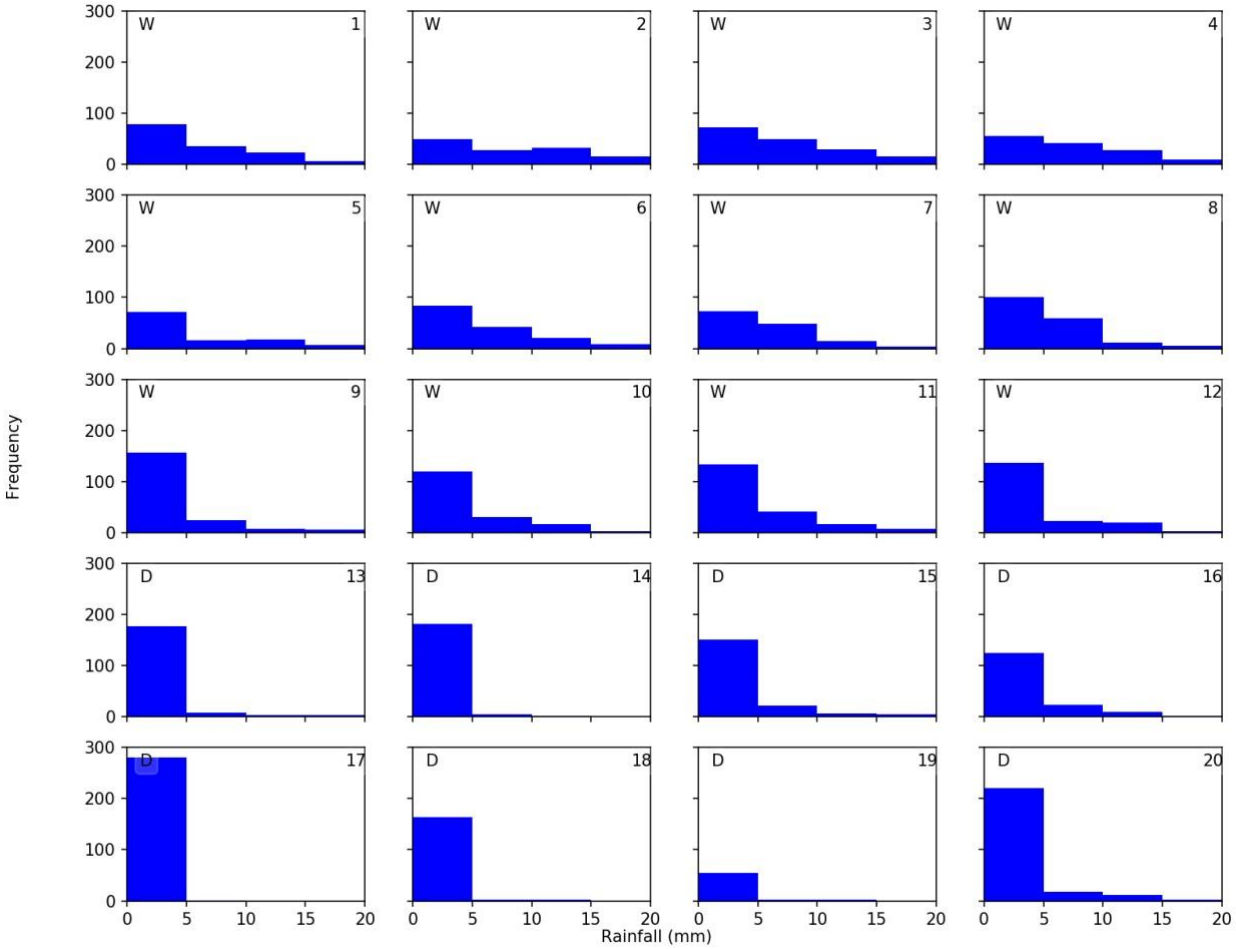

Figure 5.4 Distribution of daily rainfall (mm.day-1) on days characterised by the atmospheric states represented in Figures 5.1 and 5.2, during the climatological period (1981–2018). Numbers in the top right of each plot indicate the SOM node. The letter in the top left represents the rainfall characteristic for that node: 'W' for wet nodes and 'D' for dry nodes.

Cluster 1 nodes (3, 4, 8, 12) are characterised by high pressure to the east and the eastern half of the rainfall region and low pressure over the western side, i.e., over the Congo basin. The flow is predominantly easterly to south-easterly over the Indian Ocean and westerly to south-westerly over the Congo basin. This favours large-scale and localised convergence over the rainfall region and moisture flux from the Ocean and the Congo basin (Figure 5.1). These nodes also exhibit considerable vertical wind shear; relatively strong easterlies dominate mid-upper levels as weak easterly to westerly flow characterises the low levels (Figure 3). These conditions favour atmospheric instability i.e., conditional instability of the second kind, and are conducive to the generation and development of convective rainfall activities.

Cluster 2 nodes (1, 2, 5, 9) are characterised by relatively less strong zonal surface pressure gradients over the SOM domain. The low-level flow over the rainfall region is southerly to south-westerly (1, 2) and

southerly to south-easterly (5, 9) over the Congo basin in the SOM domain. The surface pressure gradient coupled with a weak easterly flow at low levels allows for an incursion of westerlies from the Congo basin which combines with relatively strong easterlies at upper levels to trigger vertical wind shear. Days characterised by cluster 2 conditions are extremely rare in March, relatively frequent in April, and are the dominant rainfall-producing cluster in late April and May (dekad 4 to 9).

Cluster 3 (6, 7, 10, 11) nodes are characterised by south-easterly flow and relatively high pressure that prevails over the eastern half of the study region compared to the western parts and over the Congo basin. Over the Congo basin, the flow is southerly to south-easterly. The synoptic conditions that characterise cluster 3 nodes seem to act as a transition between wet and dry clusters. For instance, the dominant features (e.g zonal flow patterns; Figure 5.2) of nodes 6 & 7 appear to depart slightly from those of nodes 2 & 3 while those of 10 & 11 exhibit resemblance to nodes 14 & 15. They are also dominant in mid-season (Figure 5.5) as cessation of rainfall commences.

Cluster 4 nodes (15, 16, 19, 20), on the other hand, are relatively dry. The upper air easterly flow is less extensive across the whole region and weak, suggesting little or no vertical shear (Figure 5.2). Localised zones of low tropospheric convergence are however seen in nodes 16 and 20 with the westerly flow at the surface. These nodes occur at the first 4 dekads of the season.

Days characterised by cluster 5 nodes (13 and 17) and 6 (nodes 14 & 18) are generally dry. There are no regions of convergence nor atmospheric vertical wind shear as the flow is unidirectional at all levels i.e wind is south-easterly over the entire SOM region at the surface (Figure 2) and easterly at all levels (Figure 3). These nodes prevail mostly in May as they signal the end of the MAM season and the start of the SE monsoon season during boreal summer (Okoola, 1999) and the development/intensification of the East African low-level jet (Vizy and Cook, 2019).

Figure 5.5 shows how different SOM clusters are distributed, on average, through the MAM season and their relative temporal evolution of rainfall across the season. There is a consistent increase in total rainfall in the first three dekads, peaking at dekad 3, before a gradual decline towards cessation in dekad 9 (see also Table 5.1). Dekads 3, 4, 5 and 6 (last week of March through second week of April) are the wettest in the season. Cluster 1 conditions dominate the first 5 dekads, prevailing over at least half the days in dekads 1, 2 & 3, and are completely absent in the month of May (dekads 7, 8 & 9). Cluster 2 nodes are present in every dekad, more so in the last four. Cluster 3 nodes dominate the mid-season, marking the transition

between the wet and dry phases of the season. Cluster 4 nodes are present during the first four dekads while 5 & 6 dominate in the last four.

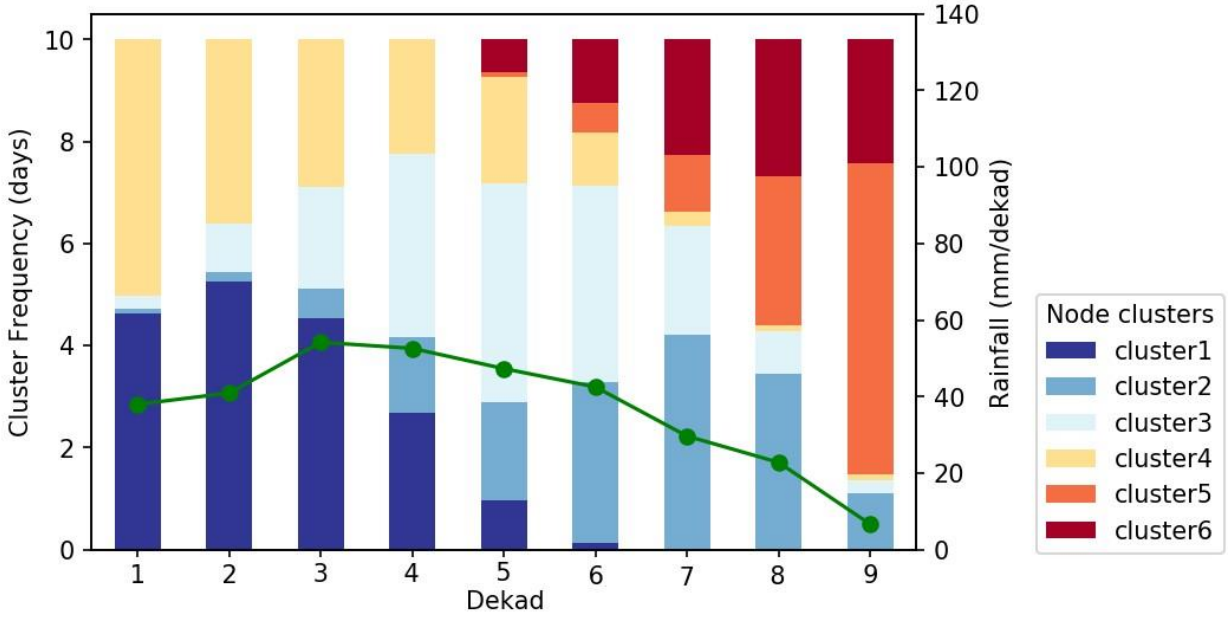

Figure 5.5 Dekadal analysis of node clusters showing total rainfall (mm.dekad-1) and node frequencies (no. of days/dekad) for the MAM climatological period (1981-2018). The green line shows the evolution of mean dekad rainfall throughout the season. The clusters are ordered from wettest (1) to driest (6).

5.2 Changes in atmospheric conditions associated with anomalies in Rainfall and Node frequency

This section describes the changes in atmospheric conditions associated with rainfall anomalies and change in node frequencies in the event years. This is to determine whether atmospheric states conducive to wet weather conditions were more prevalent during the extreme rainfall seasons of 2012, 2016 and 2018. Figure 5.6 shows per-node total rainfall and node frequencies in the event-years as well as the climatological period. A dekadal analysis of total rainfall and node frequencies in each cluster is presented in Figure 5.8. To understand the changes in circulation conditions associated with the extreme rainfall events, the anomalies in surface pressure and moisture flux (see, Figure 5.9), and zonal wind (Figure 5.10) are assessed.

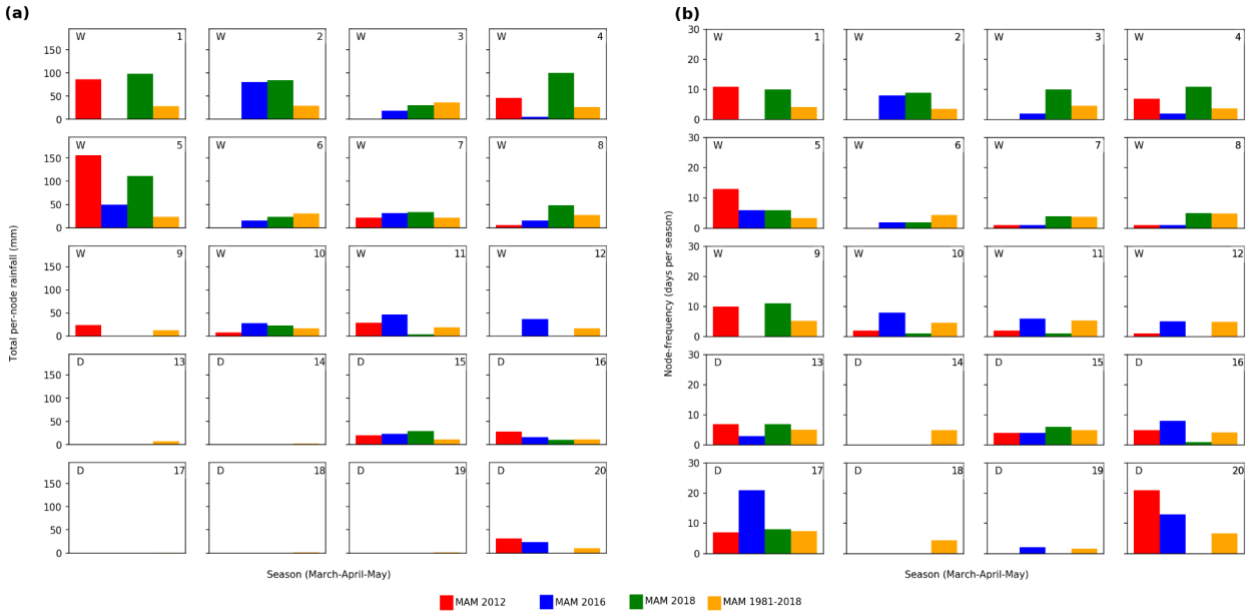

Figure 5.6 Seasonal rainfall characteristics (a) and node frequencies (b) in the MAM season on days characterised by SOM archetypes of qtuv at 850hPa for the climatological reference period (1981–2018; orange) and event-years (2012; red, 2016; blue & 2018; green) over the rainfall region. Numbers in the top right of each plot indicate the SOM node. The letter in the top left represents the rainfall characteristic for that node: 'W' for wet nodes and 'D' for dry nodes.

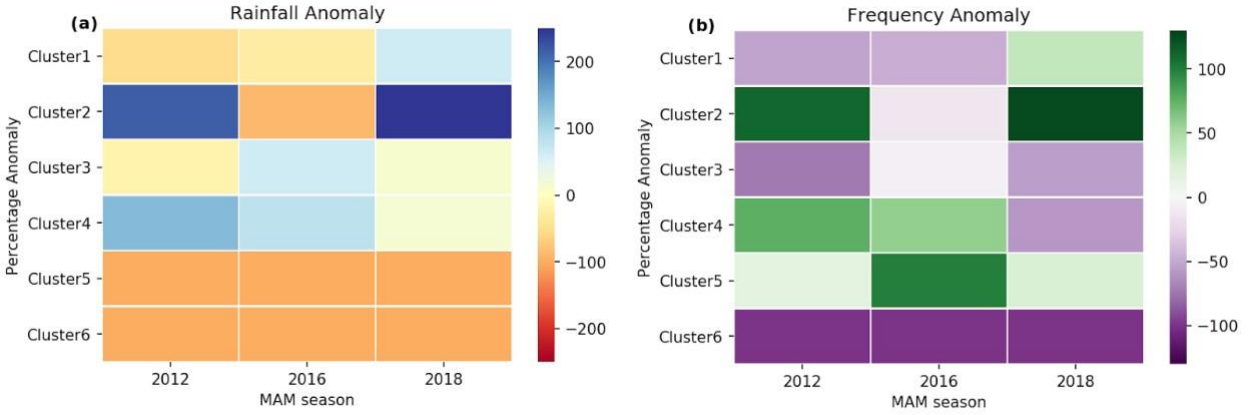

Figure 5.7 Anomalies of rainfall (a) and node frequency (b) for node clusters in 2012, 2016 and 2018, relative to 1981-2018 climatological period, over the SOM domain on days characterised by states identified by SOM of qtuv at 850hPa.

From Figures 5.6 and 5.7, wetter-than-normal nodes were more prevalent and drier-than-normal less so in MAM 2012, 2016 and 2018. In other words, nodes that produced more than normal rainfall were more frequent in the season (regardless of whether they are climatologically wet or dry) and those that produced below normal rainfall were less frequent. More than half of the nodes that are associated with above normal rainfall increased in frequency while more than half of those that produced below rainfall were less

prevalent. In MAM 2012, of eight wetter-than-normal nodes (1, 4, 5, 9, 11, 15, 16, 20) six (1, 4, 5, 9, 16, 20) increased in frequency. In nine drier-than-normal nodes (7, 8, 10, 12, 13, 14, 17, 18, 19), eight (7, 8, 10, 12, 14, 17, 18, 19) were less frequent in the season. In MAM 2016, in 9 nodes (2, 5, 7, 10, 11, 15, 16, 20) that produced above-normal rainfall, 7 (2, 5, 10, 11, 12, 16, 20) were more prevalent while all but two that produced below normal rainfall (1, 3, 4, 6, 8, 9, 13, 14, 17, 18, 19) reduced in frequency during the season. For MAM 2018, 5 (1, 2, 4, 5, 15) out of 8 (1, 2, 4, 5, 7, 8, 10, 15) wetter-than-normal nodes increased in frequency while 7 (6, 9, 12, 14, 18, 19, 20) 11 (3, 6, 9, 11, 12, 13, 14, 17, 18, 19, 20) drier-than-normal nodes were less frequent during the season.

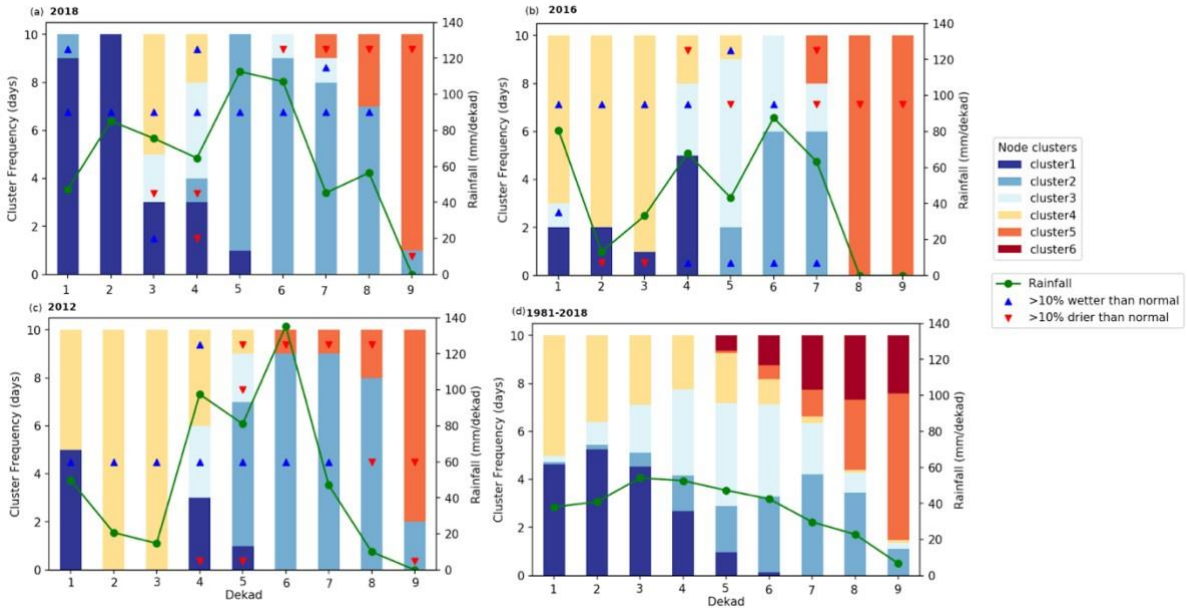

Figure 5.8 Dekadal analysis of node clusters showing total rainfall and node frequencies for MAM 2012(a), 2016(b), 2018(c) based on SOM archetypes of qtuv at 850hPa, and evolution of rainfall through the seasons over the rainfall region. Climatological analysis (1981-2018; d) is provided for ease of comparison. The clusters are ordered from wettest (1) to driest (6). The triangles represent the direction of change in rainfall, blue for positive and red for negative anomalies.

Cluster 1: Nodes 3, 4, 8, 12

During MAM 2012, cluster 1 nodes were present in dekads 1, 4, and 5. The nodes were wetter than-normal in dekad 1 but drier than normal in dekads 4 & 5. No days were characterised by node 3 in the season. For node 4, a divergent flow is seen at the surface on the western strip of the study area as a north-westerly flow sweeps across the rest of the rainfall region (Figure 5.9a). For nodes 8 & 12, low-level convergence is only confined to the western strip of the study area as the rest of the study region experiences low-level divergence. For node 8, weak low-level westerlies allowed the incursion of warm Congo air supplying moisture to the rainfall region. These conditions resulted in enhanced rainfall in the 1st dekad (likely by

nodes 8 & 12) and suppression of rainfall in the 4th & 5th dekads (likely by nodes 4). Generally, cluster 1 nodes were less prevalent in 2012 and their contribution to the total season rainfall was minimal.
In MAM 2016, days characterised by cluster 1 nodes marked the first four dekads of the season. Of this, those in the 1st and 4th dekad were wetter-than-normal and drier-than-normal in the 2nd & 3rd dekads. Those that occurred during the 4th dekad were more prevalent than usual.

In 2016, the presence of relatively higher pressure over the western strip of the study region (around Lake Victoria basin - node 3 in 5.9b) compared to the surrounding areas resulted in low level divergence over this region. Strong easterlies at low and high levels did not favour convective activities in node 4. These conditions can be attributed to the reduced rainfall in the 2nd and 3rd dekads. For nodes 8 and 12, low-level convergence to the west of the study area accompanied by weak low-level easterlies favoured the influx of moisture from the Indian Ocean and the Congo basin. These conditions are likely responsible for the above-normal rainfall delivered by cluster 1 nodes in the 4th dekad.

In MAM 2018, cluster 1 nodes prevailed during the first five dekads of the season with nearly all the days in the 1st and 2nd dekads. From Figure 5.9c, the nodes are characterised by anomalous surface pressure extended over the rainfall region compared to the surrounding areas. This triggers widespread low-level convergence and favours the advection of warm moist Congo air into the region through an anomalous westerly flow (Figure 5.10c). The concomitant easterly flow at upper levels enhanced vertical wind shear and attenuated low-level convergence and upper-level divergence over the rainfall region. These conditions favour instability and enhance convective activities. In MAM 2018, anomalous rainfall was recorded during the 1st and 2nd dekads (Kilavi et al. 2018; Kimutai, et al. 2022). It resulted in widespread floods that displaced more than 244,400 people and killed 80 (OCHA, 2018) in several parts of the rainfall region. At least 21,741 acres of farmland were destroyed, and an estimated 19,223 livestock losses were reported (Kenya Red Cross Society, 2018).

Cluster 2: Nodes 1,2,5,9,
In MAM 2012, cluster 2 nodes were more prevalent than climatology and generally wetter-than normal. These nodes dominated the 5th, 6th, 7th & 8th dekads of the season. This coincides with the period (late April to early May 2012) when most parts of the rainfall region experienced extreme rainfall that caused flash floods and landslides, killing at least 84 people and displacing around 30,000 (OCHA, 2012). By mid-May, more than a quarter million people had been affected by floods in Kenya (KRCS, 2012), the majority from the rainfall region. On these days, there was an anomalous surface low-pressure over the rainfall region

that favoured low-level convergence due to inflows from the surrounding areas of relatively higher pressure (Figure 5.9a). The presence of weak easterlies to weak westerlies in the lower troposphere allowed an incursion of warm Congo air mass into the region (Figure 5.9a). Southwesterly moisture flux at mid-levels, presumably from the Atlantic, increased the availability of moisture in the study region (Figure 5.9a).

In MAM 2016, cluster 2 nodes were also more frequent and wetter-than-normal. No days were characterised by nodes 1 & 9. The additional rainfall from nodes 2 & 5 to already saturated soils from the flooding event in 4th dekad (contribution from cluster 1) led to severe floods reported in dekad 6 that affected 34,129 people in Nairobi County. On 29 April 2016, for instance, heavy rains led to the collapse of a residential building in the city. As of 3 May 2016, 16 deaths had been confirmed (IFRC, 2016). In 2016, nodes 2 & 5 experienced relatively lower pressure anomalies over the study region compared to the Congo basin resulting in westerly flow that enabled advection of warm moist air and favoured low-level convergence over the study area (Figures 5.9b; 5.10b).

In MAM 2018, cluster 2 nodes characterised nearly all days of dekads 5, 6, 7 & 8. On all these days, the nodes produced above-normal rainfall. As of mid-May, at least 311,164 had been displaced by floods across the country. The death toll had risen to at least 186 people, 47 deaths due to a dam collapse in Nakuru County (located in the rainfall region) on 9 May 2018, and a further 33 people have been injured (NDMA, 2018; OCHA, 2018). The nodes were characterised by large-scale low-level convergence over the rainfall region as a result of anomalous low pressure over the study region compared to the Congo basin and the surrounding regions (especially nodes 1, 2, and 5). The anomalous low-level westerly/south-westerly (Figure 5.9c; 5.10c) allowed an influx of moisture flux from the Congo basin and the Atlantic Ocean into the study region. Well defined tropospheric wind patterns of upper easterlies and lower westerlies favoured vertical wind shear which enhanced unstable conditions and convective activities.

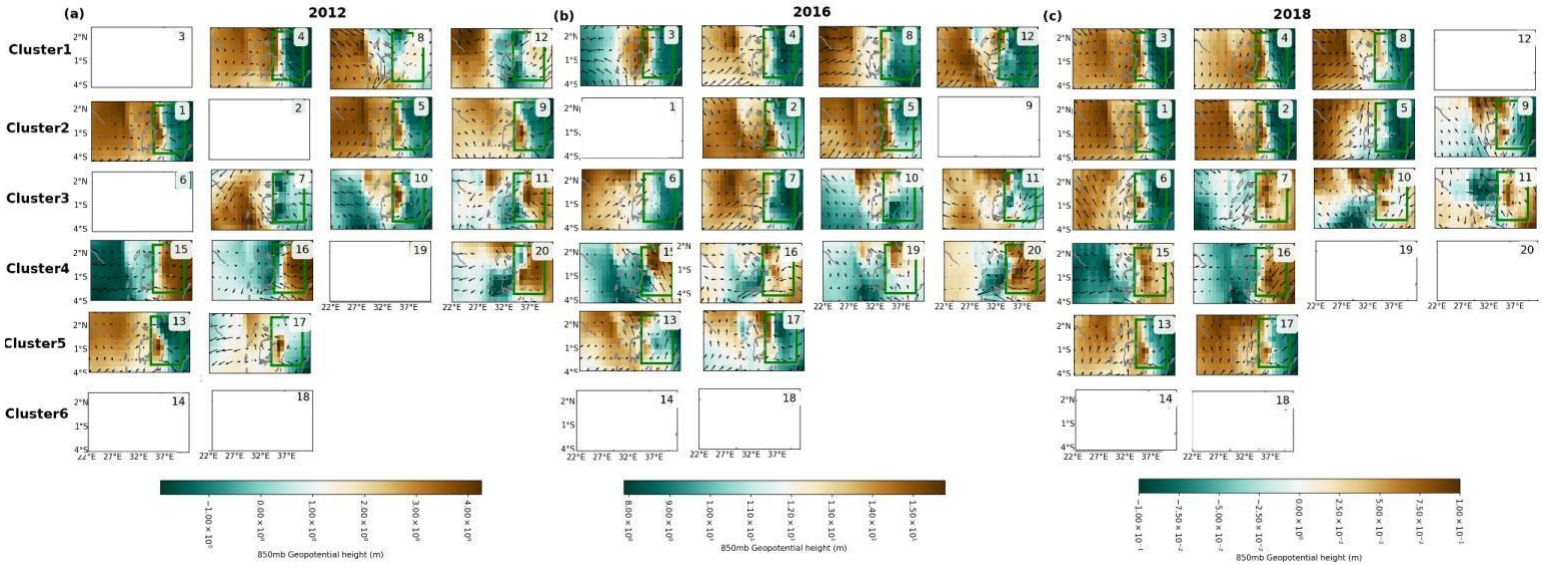

Figure 5.9 Anomalies of Geopotential height with moisture flux for node clusters in 2012(a), 2016(b) and 2018 (c), relative to 1981-2018 climatological period for each node, over the SOM domain on days characterised by states identified by SOM of qtuv at 850hPa. The box shows the rainfall region. The nodes that were absent during the season are left blank.

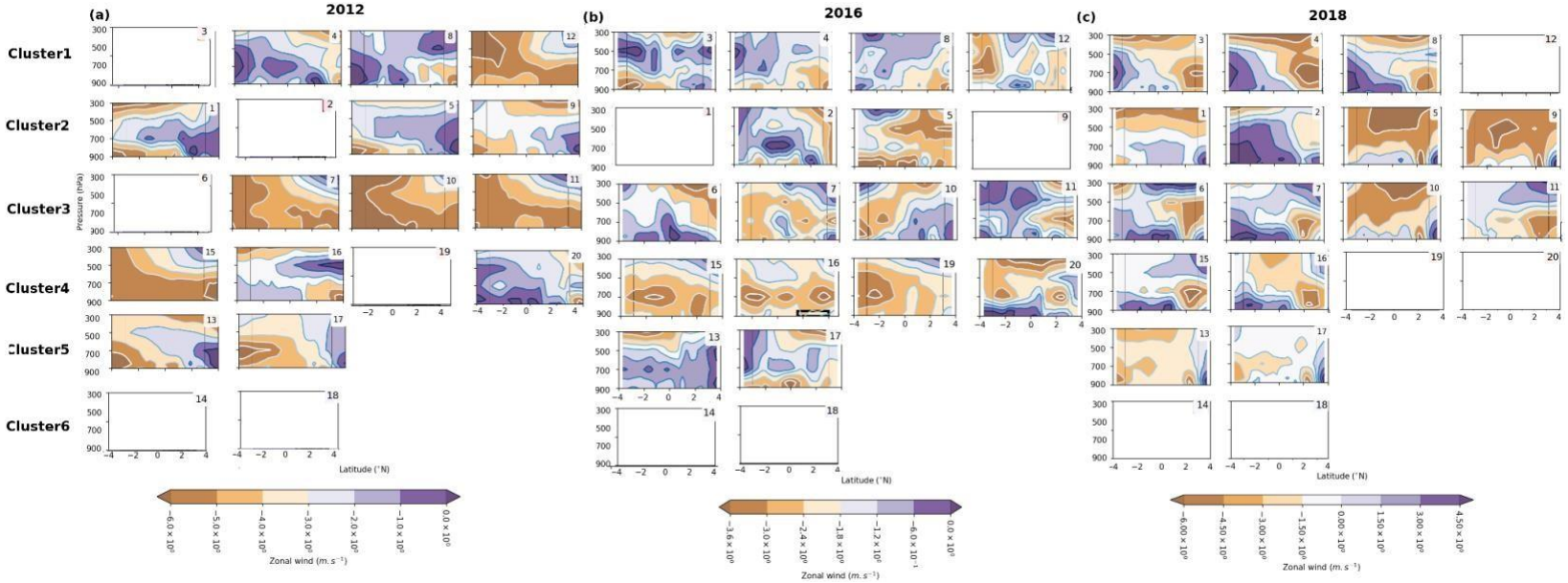

Figure 5.10 Anomalies of zonal wind for node clusters in 2012(a), 2016(b) and 2018 (c), relative to 1981-2018 climatological period for each, over the SOM domain on days characterised by SOM archetypes of qtuv at 850hPa. The box shows the rainfall region. The unshaded nodes are those that were absent during the event-year seasons.

Cluster 3: Nodes 6, 7, 10, 11

In MAM 2012, cluster 3 nodes were only present for a few days in the 4th & 5th dekads. Synoptic conditions show that neutral to anomalous high pressure over the study region and the Indian Ocean compared to the surrounding areas resulted in low-level easterly flow (Figures 5.9a, 5.10a). For nodes 7 & 10, zones of localised low-level divergence are seen in the rainfall region. However, easterly flow at all tropospheric levels appears to have depressed rainfall activities over the region. In MAM 2016, cluster 3 nodes were relatively more prevalent. These nodes contributed to increased wet weather conditions in the 1st, 4th & 6th dekads and reduction in the 5th & 7th. The increase in dekad 6 contributed to the flooding event of April 29 (IFRC, 2016), in addition to the amounts produced by cluster 2. During this period there was anomalous low pressure over the rainfall region compared to the surrounding areas triggering low-level convergence and an anomalous low-level westerly moisture flux from the Congo basin (Figure 5.10b). Furthermore, the presence of mid to high-level easterly flow (Figure 5.10b) enhanced vertical wind shear and attenuated low-level divergence and upper-level subsidence. During MAM 2018, cluster 3 nodes were less common and their contribution to total rainfall was minimal. On these days neutral pressure conditions prevailed over the rainfall region. However, there was a weak anomalous westerly flow at a low level with a subsequent weak flux of moisture from the Congo basin in node 6 which might have contributed to rainfall received in dekad 4 & 7.

Cluster 4: Nodes 15, 16, 19, 20

Cluster 4 nodes were more prevalent in MAM 2012 and 2016 (nearly all days of the 1st, 2nd, and 3rd dekads) compared to 2018 (few days of 3rd and 5th dekads). A reduction in rainfall was experienced in the dekads that these nodes occurred across the three seasons (Figure 5.8). In the three seasons, days characterised by cluster 3 nodes experienced neutral to anomalous high pressure conditions over the rainfall with weak to no low-level convergence on the western strip of the rainfall region around L. Victoria. The dominant flow is easterly at all levels, albeit weak at the surface in some nodes (e.g. Node 12 in 2012, 20 in 2016 and 15 & 16 in 2018; Figure 5.10) which allowed incursion of warm moist Congo airmass into areas around Lake Victoria.

Cluster 5: Nodes 13, 17

Cluster 5 nodes are climatologically drier than cluster 4 nodes (Table 5.1; Figure 5.5). Cluster 5 nodes dominated all the days of the 8th and 9th dekads in MAM 2016 and 9th in 2012 and 2018. The nodes were drier-than-normal across the three seasons resulting in little to no rainfall in the last two dekads. The nodes are characterised by a divergent flow at the surface due to relatively high-pressure conditions over the

rainfall region (Figure 5.9., row 5) and dominance of easterly flow at all levels of the atmosphere (Figure 5.10, row 5). These conditions inhibit convective activities and favour dry weather conditions.

Cluster 6: Nodes 14, 18

Cluster 6 nodes did not occur in MAM 2012, 2016 and 2018.

5.3 Summary of findings

From the analysis, the following summary points are made. The days characterised by synoptic conditions that favour above-normal rainfall were more frequent compared to those with drier than-normal rainfall across the season. The atmospheric patterns which typically lead to rainfall that's higher than average occurred more often than the patterns leading to below-average rainfall. The fact that these were more frequent during the season suggests a heavier contribution of rainfall. In contrast, the climatologically dry nodes, which are conditions that would usually lead to drier periods, were less frequent. This means that their impact in reducing the overall rainfall for the season was minimal.

The three extreme rainfall events of the March-April-May season over the rainfall region were caused by anomalous localised and widespread low-level convergence of anomalous low-level westerly and weak easterly flow over the rainfall region. This was triggered by anomalous low-pressure conditions at the surface. These synoptic conditions favour the influx of moisture from both the Congo basin and the Indian Ocean increasing moisture availability for formations of convective storms. The concomitant presence of easterlies in the mid to upper troposphere creates vertical wind shear which enhances atmospheric instability. These conditions were dominant on dekads in which flood-inducing rainfall was recorded (4th, 5th, 6th in 2012; 4th, 6th, 7th in 2016 and 1st, 2nd, 5th, 6th, 7th, and 8th dekads in 2018). On the other hand, the presence of strong low to mid-level easterlies and southerlies over the rainfall region favour divergent flow at the surface and tend to deposit moisture deep into the African interior. Depressed rainfall was experienced on dekads characterised by clusters 4 & 5 nodes (e.g., 1st and 2nd in 2012; 2nd and 3rd in 2016, and 8th and 9th across the three seasons). The driest nodes (cluster 6) were absent across the extreme rainfall seasons.

Synoptic conditions over equatorial East Africa in MAM seem to be largely governed by the interplay of pressure differences in the sub-tropical high-pressure systems. Changes in sea level pressure over the Indian and Atlantic oceans control the zonal advection of moisture across the region. In MAM 2018, for instance, the anomalous cyclonic circulation observed over the southwest Indian Ocean with a corresponding strengthened St. Helena High was a significant feature of the widespread lower tropospheric westerlies across East Africa (Kilavi et al. 2018; Finney et al. 2019). Zonal propagation of convective cells during MJO activity coincides with zonal wind anomalies, consistent with eastward propagation of the MJO signal (e.g Sandjon et al. 2014; Hogan et al. 2015) and weakened sea level pressure over the Indian Ocean. MJO phases 2–4 (the main centre of enhanced convection is concentrated over the western Indian Ocean) are associated with the anomalous westerly flow and wet spells over Kenyan highlands. Some studies have established evidence of a link between surface westerly anomalies and stationary or transient troughs extending from the subtropics to the equator, e.g Johnson and Morth, (1960); Habtemichael and Pedgley (1974); Okoola, (1999). The dry dekads of 7th, 8th & 9th dekads i.e May, coincide with the start of the southeast monsoon season (Okoola, 1999; Camberlin and Philippon, 2001) and the strengthening of East African low-level jet (Indeje, 2001; Nicholson, 2016; Munday et al., 2020) both associated with thermal stability. These conditions result from a change in pressure pattern associated with abnormally warm temperatures over the African continent and South Atlantic, weakened trade winds, a weakened St. Helena High, and strong easterlies in the low-mid troposphere (e.g Camberlin and Okoola, 2003).

6 Results: Attribution of Human Influence on Magnitude of Rainfall

This chapter presents and discusses the results of the quantification of the role and contribution of human influence on the intensity of heavy rainfall events of MAM 2012, 2016 and 2018 seasons based on the three approaches used (see objective 2, section 1.2; step 3, section 3.3). Sections 6.1, 6.2 and 6.3 present the results of the attribution analysis based on observations, AGCMs and CGCMs respectively. A synthesis of results from the three experiments is provided in section 6.4 while a summary of findings is presented at the end of the chapter.

6.1 Observational analysis

Table 6.1 shows changes in the magnitude of Rx5d, Rx10d, and Rx20d with their corresponding return time periods between the event-years and preindustrial period based on observational data. The values in red (blue) show increase (decrease) in the magnitude of the rainfall maxima. Bolded values show a statistically significant change. Attribution analysis of CHIRPS data shows an increase in the attributable magnitude (MR > 1.0) of all three extreme rainfall metrics, in each of the three event-years. For KMD data, increases in magnitude are seen for Rx10d and Rx20d in all three event years, but the magnitude of Rx5d decreases in all three years. The highest return periods are seen for 2018 events based on CHIRPS analysis, while KMD analysis shows the highest in 2012. The fraction of attributable magnitude (FAM) ranges from -2 to 22% with highest shown by CHIRPS for 2016 across all the indices. Despite an overall increase in the magnitude of rainfall maxima, the increases are statistically non-significant (lower bound on the uncertainty range less than or equal to 1.0) and thus no attributable human influence on heavy rainfall magnitude is discerned with this approach.

Table 6.1 Summary of estimated magnitude ratios and fraction of attributable magnitude using observational data. The values in red (blue) show increase (decrease) in the magnitude of the rainfall maxima.

		2012				**2016**				**2018**			
Dataset	Metric	Return period	MR	95%CIs	FAM	Return period	MR	95%CIs	FAM	Return period	MR	95%CIs	FAM
CHIRPs	Rx5d	3.67	1.11	0.90,1.44	11%	1.45	1.20	0.85,1.65	20%	11.5	1.17	0.88,1.64	17%
	Rx10d	10.8	1.12	0.80,1.46	12%	1.58	1.22	0.76,1.82	22%	50.3	1.04	0.73,1.55	4%
	Rx20d	23.8	1.16	0.78,1.54	16%	2.38	1.21	0.73,2.01	21%	32.75	1.06	0.70,1.66	6%
KMD	Rx5d	8.1	0.97	0.74,1.31	-3%	2.87	0.97	0.68,1.43	-3%	1.82	0.98	0.74,1.43	-2%
	Rx10d	11.02	1.04	0.81,1.36	4%	2.10	1.06	0.76,1.47	6%	2.81	1.06	0.73,1.56	6%
	Rx20d	11.69	1.05	0.75,1.42	5%	2.31	1.08	0.69,1.60	8%	9.53	1.07	0.66,1.63	7%

6.2 AGCM analysis

Table 6.2 shows the results of the atmospheric model analysis. The values in red (blue) show increase (decrease) in the magnitude of the rainfall maxima. Bolded values show a statistically significant change. Results from ECHAM5.4 and weather@home show an intensification of rainfall across all the years whereas CAM5.1 shows an increase in 2012 and 2018, but a reduction in magnitude in 2016. Overall, the largest proportion of human influence attributable magnitude is seen in MAM 2018, although ECHAM5.4 depicts equally high values in 2012. Correspondingly, the lowest proportions of attributable magnitude are seen in 2016 across all RxNds. Statistically significant increases (95% CI of the MR does not encompass 1) in intensity are shown by weather@home in all RxNds; ECHAM5.4 for Rx20d in 2012, Rx5d and Rx10d in 2016 and Rx5d in 2018, and CAM5.1 for Rx10d and Rx20d in 2012 and RxNds in 2018. ECHAM5.4 shows higher values of fraction of attributable magnitude across the years in all indices compared to weather@home and CAM5.1. While there are still several instances where the result is not statistically significant, the result is much stronger than for the observations (lower CI close to 1.0 when it is below 1.0).

Table 6.2 Summary of estimated magnitude ratios and fraction of attributable magnitude using atmosphere-only attribution runs. The values in red (blue) show increase (decrease) in the magnitude of the rainfall maxima. Bolded values show a statistically significant change

		2012			**2016**			**2018**		
Model	Metric	MR	95%CIs	FAM	MR	95%CIs	FAM	MR	95%CIs	FAM
weather@home2	Rx5d	1.046	1.028,1.063	4.6%	1.033	1.015,1.051	3.3%	1.073	1.052,1.096	7.3%
	Rx10	1.051	1.31,1.071	5.1%	1.036	1.018,1.055	3.6%	1.085	1.061,1.108	8.5%
	Rx20d	1.068	1.048,1.088	6.8%	1.030	1.011,1.049	3.0%	1.099	1.072,1.13	9.9%
ECHAM5.4	Rx5d	1.138	0.962,1.346	13.8%	1.109	1.009,1.226	10.9%	1.120	1.006,1.262	12%
	Rx10	1.143	0.977,1.341	14.7%	1.098	1.015,1.190	9.8%	1.111	0.994,1.239	11.1%
	Rx20d	1.186	1.000,1.387	18.6%	1.074	0.984,1.165	7.4%	1.060	0.945,1.189	6%
CAM5.1	Rx5d	1.028	0.989,1.065	2.8%	0.983	0.951,1.018	-1.7%	1.040	1.000,1.079	4%
	Rx10	1.043	1.002,1.084	4.3%	0.988	0.954,1.022	-1.2%	1.053	1.014,1.094	5.3%
	Rx20d	1.064	1.023,1.106	6.4%	0.965	0.930,1.000	-3.5%	1.045	1.009,1.081	4.5%

6.3 CGCM analysis

There is less agreement on the change of magnitude of RxNds in analyses based on CMIP6 data compared to the other two experiments (Table 6.3). The values in red (blue) show increase (decrease) in the magnitude of the rainfall maxima. Bolded values show a statistically significant change. IPSL-CM6A-LR, INM-CM5, and NorESM2-MM show a general increase while MRI-ESM20 shows reduction in intensity, across all the event years. UKESM1-0-LL shows a general reduction except for Rx10d and Rx20d in 2018 which depict a substantial statistically significant increase. Analysis of CNRM-CM6-1-HR shows an increase in the intensity of all RxNds in 2018 and Rx5d and Rx20d in 2012 but a reduction in 2016 and Rx20d in 2012. For NESM3, the magnitude of Rx5d increased in 2012 and 2018 while the magnitude of Rx10d and Rx20d for 2012 and 2018 decreased. Of these, NorESM2-MM for all RxNds in 2018 and UKESM1-0-LL for Rx5d in 2012, and Rx5d and Rx20d in 2016 show a significant positive influence of anthropogenic climate change.

Table 6.3 Summary of estimated magnitude ratios and fraction of attributable magnitude using the coupled model runs. The values in red (blue) show increase (decrease) in the magnitude of the rainfall maxima. Bolded values show a statistically significant change.

		2012			**2016**			**2018**		
Model	Metric	MR	95% CIs	FAM	MR	95% CIs	FAM	MR	95% CIs	FAM
CNRM-CM6-1-HR	Rx5d	1.025	0.831,1.272	2.5%	0.98	0.69,1.293	-2%	1.08	0.86,1.33	8%
	Rx10	0.979	0.785,1.152	-2.1%	0.86	0.61,1.15	-14%	1.01	0.70,1.29	1%
	Rx20d	1.028	0.856,1.181	2.8%	0.88	0.68,1.09	-12%	1.21	0.96,1.54	21%
IPSL-CM6A-LR	Rx5d	1.025	0.831,1.272	2.5%	0.98	0.69,1.293	-2%	1.08	0.86,1.33	8%
	Rx10	0.979	0.785,1.152	-2.1%	0.86	0.61,1.15	-14%	1.01	0.70,1.29	1%
	Rx20d	1.028	0.856,1.181	2.8%	0.88	0.68,1.09	-12%	1.21	0.96,1.54	21%
INM-CM5	Rx5d	1.27	1.09,1.58	27%	1.21	1.089,1.35	21%	1.22	0.92,1.44	22%
	Rx10	1.35	0.91,1.84	35%	1.23	0.096,1.34	23%	1.11	0.82,1.54	11%
	Rx20d	1.23	0.96,1.69	23%	1.28	1.16,1.40	28%	1.15	0.83,1.57	15%
NorESM2-MM	Rx5d	1.27	1.09,1.58	27%	1.21	1.089,1.35	21%	1.22	0.92,1.44	22%
	Rx10	1.08	0.98,1.28	8%	1.08	0.93,1.37	8%	1.34	1.13,1.57	34%
	Rx20d	1.11	0.93,1.32	11%	1.04	0.89,1.22	4%	1.44	1.16,1.75	44%
UKESM1-0-LL	Rx5d	0.68	0.51,0.90	-32%	0.78	0.50,1.36	-22%	0.83	0.33,1.19	-17%
	Rx10	0.89	0.54,1.30	-11%	0.63	0.40,1.17	-37%	1.69	1.31,3.82	69%
	Rx20d	1.10	1.01,1.78	10%	0.64	0.47,1.05	-36%	1.33	0.46,3.39	33%
NESM3	Rx5d	1.02	0.92,1.11	2%	1.05	0.92,1.18	5%	1.01	0.92,1.06	1%
	Rx10d	0.99	0.89,1.07	-1%	1.06	0.92,1.21	6%	0.96	0.88,1.11	-4%

	Rx20d	0.98	0.89,1.07	-2%	1.07	0.97,1.26	7%	0.97	0.84,1.12	-3%
MRI-ESM2-0	Rx5d	0.85	0.75,0.94	-15%	0.80	0.74,0.93	-20%	0.82	0.75,0.94	-18%
	Rx10d	0.86	0.74,0.98	-14%	0.77	0.67,0.89	-23%	0.83	0.56,1.27	-17%
	Rx20d	0.94	0.79,1.23	-6%	0.82	0.71,0.96	-18%	0.88	0.77,1.01	-12%

6.4 Synthesis results

Figure 6.1 gives a synthesis of the results, where outcomes from each experiment type are first synthesised independently after which an overall synthesis result is shown, for each of the rainfall indices, and for each year. For observations, Rx5d shows an increase of 8%, 5% for Rx10d, and 7% for Rx20d in 2018. In 2016, an increase of 9% is seen in Rx5d, 14%, in Rx10d and 15% in Rx20d, while in 2012 Rx5d increase by 4%, Rx10d by 8% and Rx20d by 11%. For atmospheric models, Rx5d increased by 7%, Rx10d by 8% and Rx20d by 7% in 2018, while in 2016 increases of 4% in Rx5d, and 2% in both Rx10d and in Rx20d are seen. In 2012, Rx5d increased by7%, Rx10d by 8%, and Rx20d by 11%. For coupled models, Rx5d shows an increase of 3%, 13% for Rx10d, and 14% for Rx20d in 2018. In 2016, a decrease of 1%, 5%, 4% is seen in Rx5d, Rx10d and Rx20d, respectively. Also, the magnitude of Rx5d decreased by 1% while those of Rx10d and Rx20d increased by 2% and 6%, respectively.

In general, it is only atmospheric models that show a significant positive influence of anthropogenic climate change in the rainfall events. Results of individual experiment synthesis indicate that the intensity of MAM 2018 extreme rainfall has increased across all experiments. Highest values of FAM are found in Rx20d in the synthesis of coupled models (14%). However, changes in observational data and coupled models' analysis show non-significant change in intensity. For 2016, the analysis of observations and atmospheric models shows intensification of extreme rainfall while that of coupled models shows reduction in intensity. Overall synthesis results show intensification of extreme rainfall in all the event years relative to a preindustrial climate across all the experiments, but without statistical significance (the 95% CI encompasses a MR of 1.0). MAM 2018 shows higher levels of intensification compared to 2012 and 2016. In 2018, intensity of Rx5d, Rx10d and Rx20d is seen to increase by 6%, 9% and 9% respectively relative to preindustrial period. For 2016, the multi-experiment mean change in magnitude is found to be 3% in Rx5d, 4% in Rx10d and Rx20d, while in 2012 the intensity of Rx5d increased by 3%, and 6% in Rx10d and Rx20d.

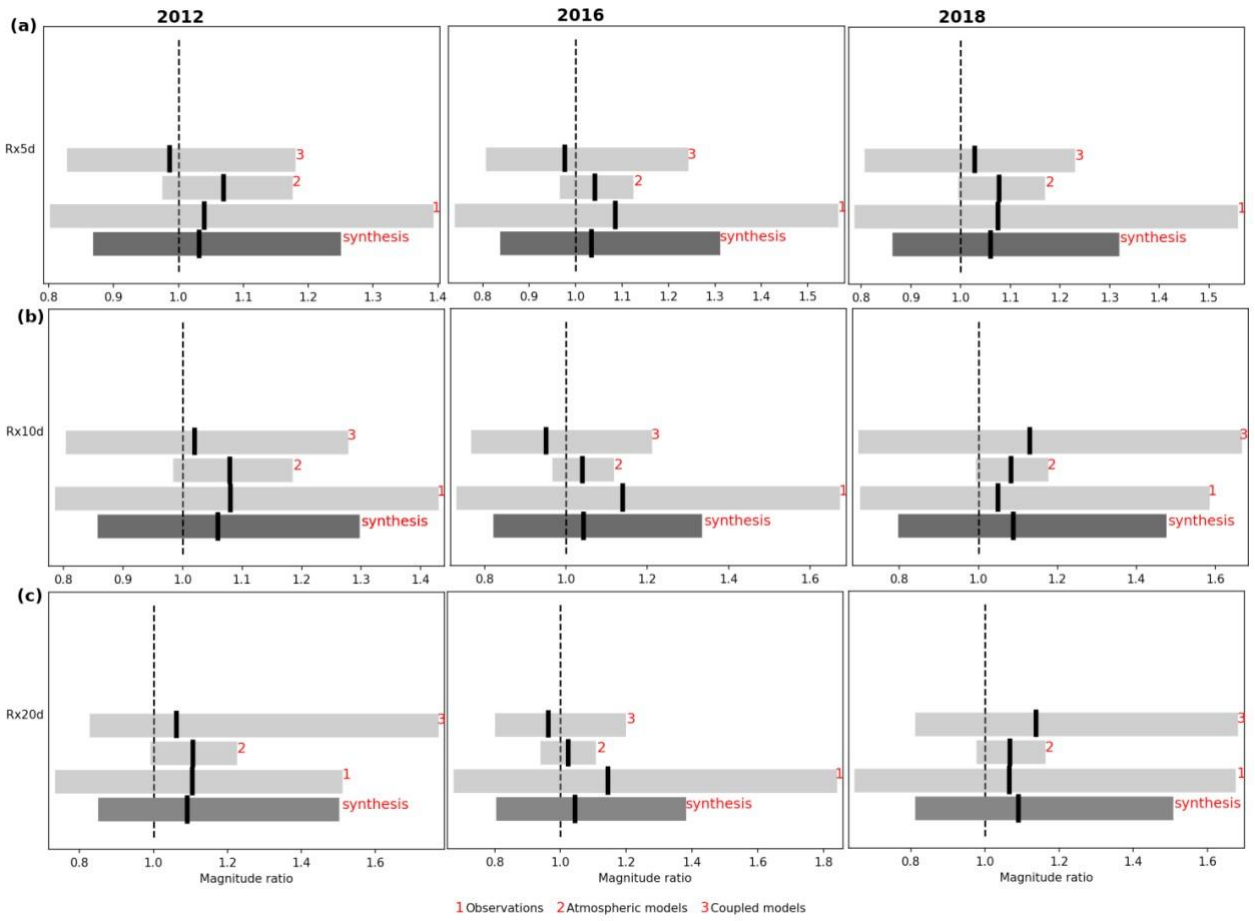

Figure 6.1 Synthesis results for attribution analysis of observations, atmospheric models, and coupled models for change in magnitude of Rx5d, Rx10d and Rx20d between preindustrial period and event-year 2012, 2016, and 2018. The overall synthesis result for the three experiments is shown by the thicker bar marked 'synthesis' below the individual experiment results. The thick black marking represents the mean while the bar spans the 95% confidence interval.

6.5 Summary of findings

Looking across all the three event years, there is a general shift towards positive FAM, although this is not statistically significant. Therefore, while there might be an emerging signal of human influence on climate causing heavier rainfall events, this is not yet formally attributable to human influence on the climate system. This is an interesting finding in the context of the 'East African climate paradox' where a contradiction exists in model projections and observed trends in MAM total rainfall — an observed overall decline in rainfall since the early 1990s while model projections show a wetting trend. It remains unclear whether a changing balance in anthropogenic forcing exists whereby past trends may have been influenced by anthropogenic aerosols while the future trends are driven by increasing concentrations of greenhouse gases (e.g., Rowell et

al., 2015). Over the past decade, extreme wet conditions in the MAM season e.g., 2012 (OCHA, 2012), 2016 (KMD, 2016; IFRC, 2016), 2018 (Kilavi et al. 2018; OCHA, 2018), 2020 (OCHA, 2020) have punctuated the dominant drier conditions. However, there is still limited knowledge of past and present trends of rainfall extremes over the MAM season in Kenya as reported by various studies including Omondi et al. (2014) and Schmocker et al. (2016), mainly attributed to inadequate long and quality observations (Anyah & Qiu, 2012b; Otto et al., 2020). Variation in results of historical trend analysis also exist (Phillipon et al., 2015; Nicholson, 2016b; Thiery et al., 2016) whereby some studies show increase (e.g., Gebrechorkos et al., 2019; Ongoma et al. 2018) with some decrease e.g., Schmocker et al. (2016), depicting the high variability in space and time of precipitation extremes in Kenya.

7 Results: Attribution of Human Influence on Synoptic Conditions

This chapter presents the results and discussion of the assessment of the role and contribution of human influence on the atmospheric conditions associated with MAM extreme rainfall of the 2012, 2016 and 2018 seasons (see objective 3, section 2.1; step 4, section 3.3). Section 7.1 provides and discusses results of the conditions and characteristics of SOM atmospheric patterns as simulated by the CGCMs and AGCMs in comparison with those identified by the reanalysis data and observed rainfall. Section 7.2 provides a discussion on changes in simulated synoptic conditions between the current and the pre-industrial climates. Section 7.3 presents and discusses the results on changes in SOM atmospheric states i.e., change in node frequency and associated rainfall in the current climate relative to pre-industrial climate. A summary of findings is presented at the end of the chapter.

7.1 Climate Model Replicability of Observed Characteristics of SOM Atmospheric Patterns

From chapter 5, findings show that, when compared to climatology, the MAM seasons of 2012, 2016 and 2018 where characterised by more frequent synoptic conditions that favoured above-normal rainfall over the study region and less frequent "dry" synoptic conditions. The extreme rainfall was primarily driven by anomalous localised and widespread low-level convergence of low-level westerly and weak easterly flow over the rainfall region. These synoptic conditions favour enhanced influx of moisture from the Congo basin and the Indian Ocean which increase moisture availability for formation of convective storms, especially on highland regions. These conditions were dominant on dekads in which flood events were experienced across the three seasons. This section presents the assessment findings of the models' ability to simulate the observed atmospheric conditions defined by SOM analysis in comparison to the SOM results for reanalysis data (ERAINT) (see also Figure 5.1, Chapter 5).

Figures 7.1 shows the geopotential heights (shaded) and moisture flux (arrows) for each SOM node in the current climate for CGCMs (CanESM, INM-CM5-0, MPI-ESM-2-HR and IPSL-CM6ALR) based on SOM classification of MAM qtuv at 850hPa. Generally, CanESM and MPI-ESM-2HR reliably reproduced the main features of the SOM nodes in the observational analysis while INM-CM5-0 and IPSL-CM6A-LR exhibit limited ability. These include (i) easterly to southeasterly zonal moisture flux, and (ii) the atmospheric low-level pressure gradient over the SOM domain with relatively high pressure to east compared to the western half of the domain. CanESM5 exhibits remarkable ability to simulate the two features, particularly the zonal moisture flow. However, for nodes 3, 4, 8, it shows limited ability to simulate the east-west pressure

gradient (underestimation) and nodes 1, 5, 9, 13, 17 (overestimation — particularly in the current climate). For INM-CM5-0, the zonal flow is relatively well simulated but with a general underestimation of the low-level pressure over most part of the SOM domain, particularly the eastern region. The weak pressure gradient created by the somewhat neutral pressure conditions at the surface is highlighted by absence of low-level convergence zones. Like CanESM5, MPIESM-2-HR reliably simulates the main features. The east-west pressure gradient is adequately reproduced except for nodes 1, 5, 9, 13 and 17 which show some overestimation of the surface pressure across the SOM domain. Additionally, the model is reproduced zones of localised and widespread convergence for cluster 1 nodes (3, 4, 8, 12) both in current and pre-industrial climates. Like INM-CM5-0, IPSL-CM6A-LR simulates the zonal flux of moisture relatively well but underestimates the surface pressure, notably nodes 3, 4, 7, 8 .11, 12, 15, 16, 19 and 20. Hardly any zones of low-level convergence are seen for the wet clusters. Of the four CGCMs, CanESM and MPI-ESM-2-HR reproduce, albeit imperfectly, the atmospheric states as identified by ERAINT relatively well.

Figure 7.2 shows the current synoptic atmospheric conditions for the atmosphere-only model used in this part of the research, HadGEM3-A, over MAM 2012, 2016 and 2018. For 2012, the study utilised 15 simulations for both current and pre-industrial climates to simulate the synoptic conditions for the season. The model exhibits good performance in reproducing the main features of the SOM nodes as identified using ERAINT. Notably, the moisture flux is easterly to south westerly with localised zones of convergence seen for wet clusters — cluster 1 (nodes 3, 4, 8, 12) and cluster 2 (nodes 1, 2, 5, 9) (see cluster classification; Section 5.1, Chapter 5), particularly in the current climate. High surface pressure and unidirectional flow (low-level divergence) is seen for dry clusters (cluster 5; nodes 13, 17, and cluster 6; node 18). However, the model overestimates the east-west pressure gradient for nodes 3, 4, 8, 12, 16 and 20, notably in the natural climate. Characterised states identified by the reanalysis data show that nodes 2, 3, 6, 14, 18, 19, were absent in the MAM 2012, however, this is not replicated by the model. For MAM 2016, 140 ensemble runs in the current climate and 210 in the pre-industrial climate were used to calculate the synoptic conditions. The model remarkably simulates the general synoptic features over the SOM domain except nodes 13, 17 and 18 in which the model tends to overestimate the surface pressure. Zones of low-level convergence within the rainfall region are also replicated by the model particularly for wet clusters — cluster 1 (3, 4, 8) and cluster 2 (1, 2, 5, 9) nodes. As identified by ERAINT, nodes 1, 9, 14, 18 were absent during the season. But according to the model, nodes 12 and 20 were absent the in current climate, while nodes 12, 16, 17, and 20 were absent in the pre-industrial climate. For MAM 2018, 61 runs in the current climate and 66 in the pre-industrial climate were used to simulate the atmospheric states. Like MAM 2012 and 2016, the model exhibits remarkable performance in simulating the atmospheric states for MAM 2018 season.

Notably, the east-west pressure gradient over the domain and zones of convergence for cluster 2 (1, 2, 5, 9) nodes. From ERAINT, nodes 12, 14, 18, 19, 20 were absent in the season while in the model nodes 12, 16, 17, 18 and 20 in the current climate and nodes 12, 16, 17, 18 and 20 were absent. In this section, it is important to note that comparing the ERAINT conditions from 1981 to 2018 with those of HadGEM3-A for 2012, 2016, and 2018 is only indicative of assessing the model's performance and not to validate the individual years for the model with the climatological conditions.

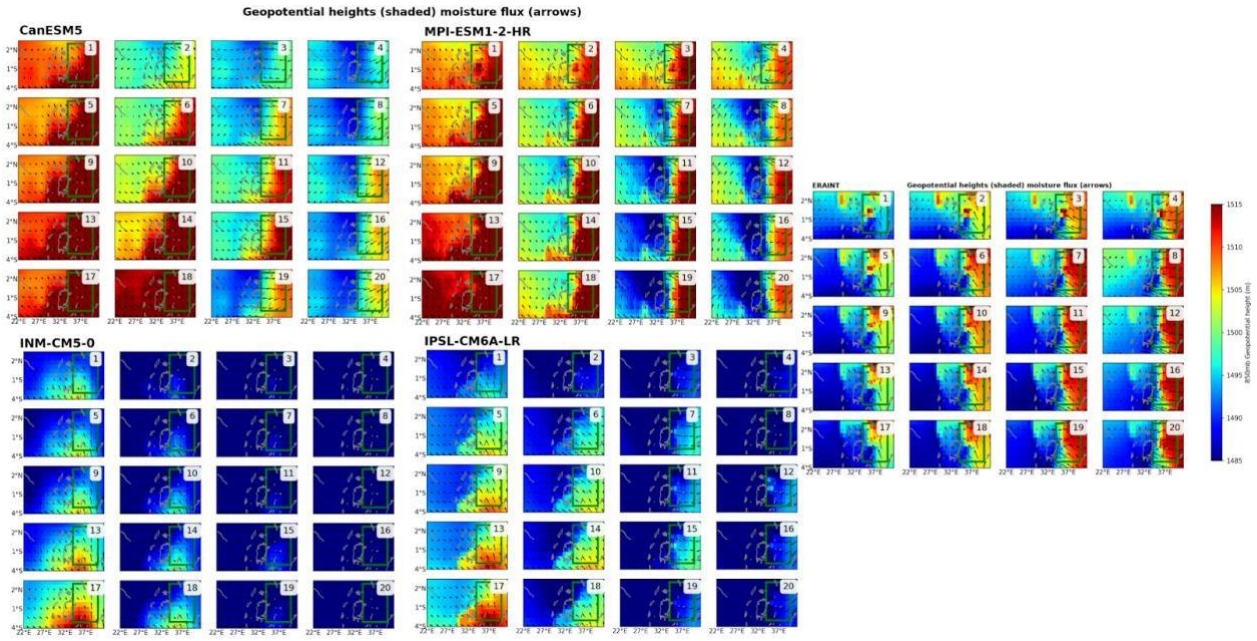

Figure 7.1 Mean MAM geopotential heights (shaded) and moisture flux (arrows) at 850hPa over the SOM domain on days in the current (1981-2018) climate conditions for CanESM, INM-CM5-0, MPIESM-2-HR and IPSL-CM6A-LR and climatological conditions (1981-2018) for ERAINT characterised by synoptic atmospheric conditions identified by SOM classification of MAM qtuv at 850 hPa. The box shows the rainfall region analysed (see Figure 3.2; section 3.3.2).

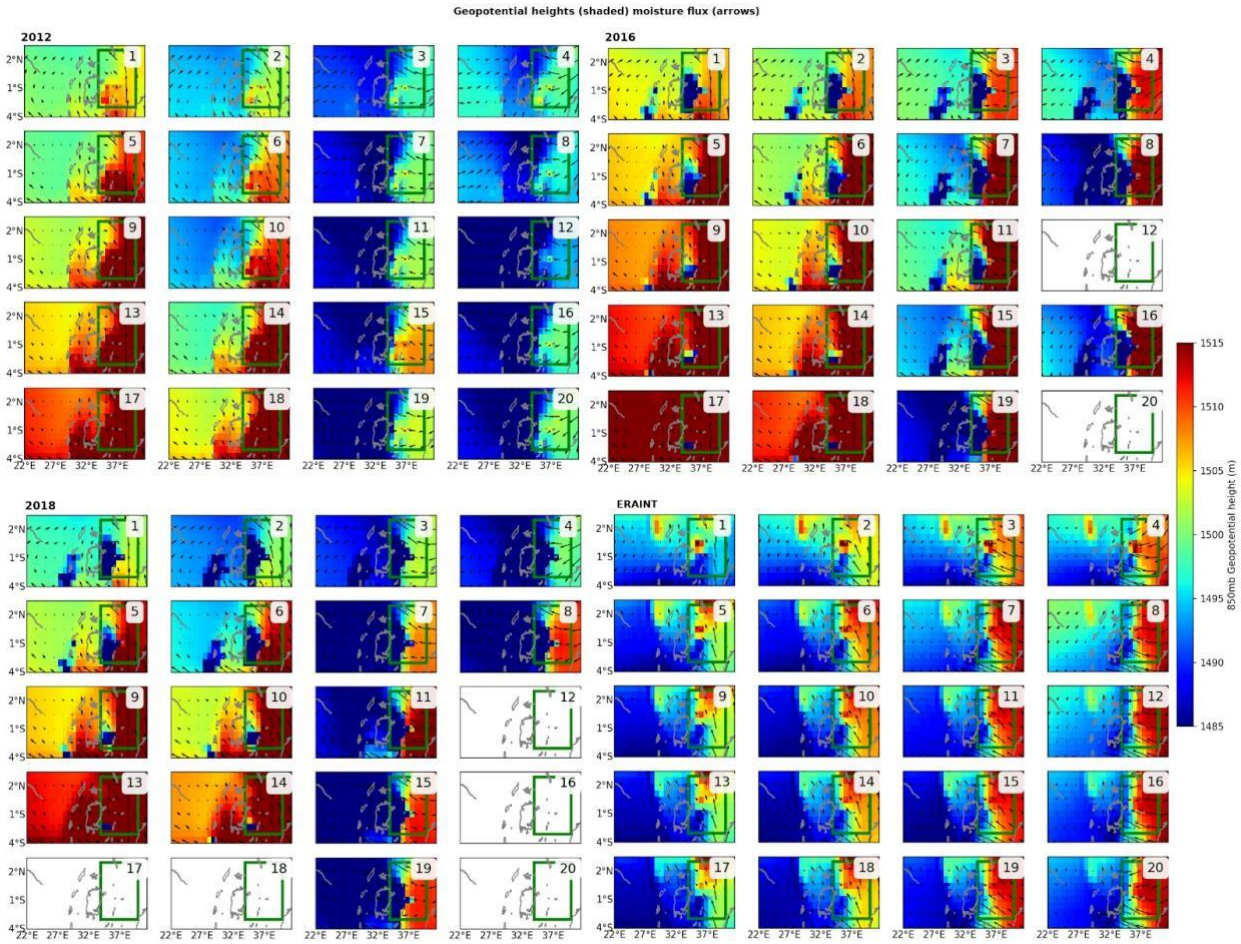

Figure 7.2 Mean MAM geopotential heights (shaded) and moisture flux (arrows) at 850hPa over the SOM domain on days in the current (2012, 2016 & 2018) climate conditions for HadGEM3-A and climatological conditions (1981-2018) for ERAINT characterised by synoptic at atmospheric conditions identified by SOM classification of MAM qtuv at 850 hPa. The box shows the rainfall region analysed (see Figure 3.2; section 3.3.2). The nodes that were absent during the season are left blank.

Figure 7.3 for shows the actual simulated characteristics of SOM atmospheric states i.e., node frequency and total rainfall for the coupled models. The observed rainfall (orange bars; CHIRPS (a)) and node frequency based on reanalysis (orange bars; ERAINT (b)) are included to aid in the assessment of how well the models simulate the observed characteristics. All the coupled models reliably delineate the wet and dry nodes. Also, the observed amount of rainfall associated with dry nodes is in the range of those simulated by the models for similar nodes. Similarly, the models replicate the amounts associated with wet nodes despite few instances of overestimation, e.g., nodes 2 and 3. The ability of the models to simulate the node frequencies is somewhat inconsistent; higher than ERAINT in some nodes and low in others. Nodes 7, 11, 13, 14 and 15 are however within the range of the reanalysis. MPI-ESM-2-HR and INM-CM5-0 are the best performing models as both rainfall and frequency associated with each node are generally in the range of with the

observed, albeit not equal. IPSL-CM6A-LR is the lowest performing — exhibits highest overestimation of rainfall and frequencies.

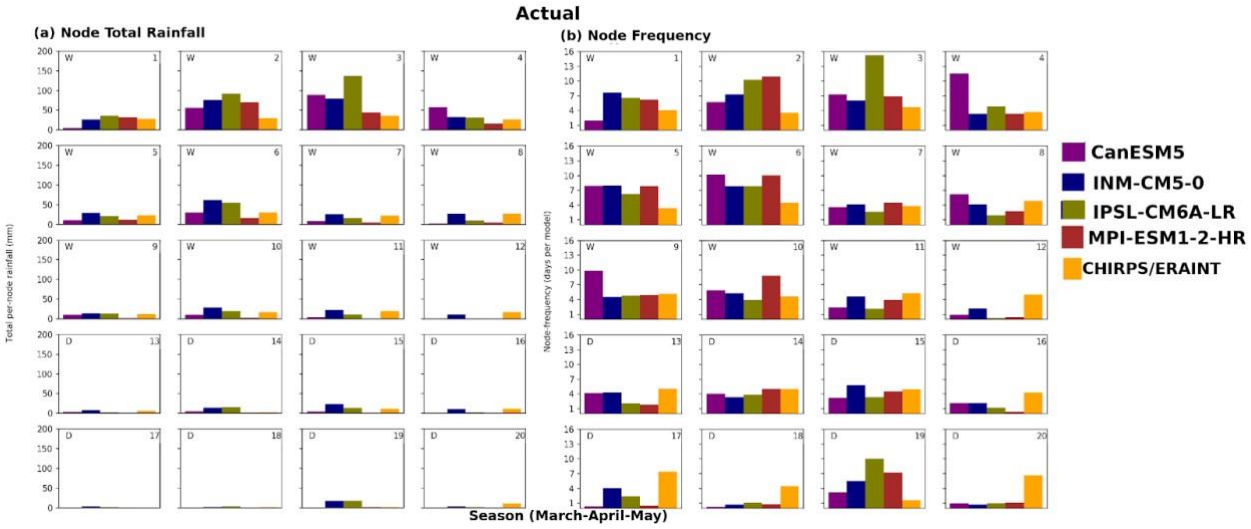

Figure 7.3 Total seasonal rainfall and (b) Frequency per-node for CanESM, INM-CM5-0, MPI-ESM2-HR and IPSL-CM6A-LR in the current (actual) climate conditions on days characterised by circulation types of SOM classification of MAM qtuv at 850 hPa. The orange bars represent the total observed seasonal rainfall (CHIRPS; a) and node frequency (ERAINT; b).

Figure 7.4 shows the total seasonal rainfall and node frequencies associated with the actual simulated SOM atmospheric patterns for the HadGEM3-A model. For rainfall, the model reliably delineates the wet and dry nodes. However, it tends to underestimate rainfall associated with nodes 1, 5, 7, 10, 15 and 11 and overestimate those associated with node 3 across the three seasons. Contrary to observations, the model is completely dry on days characterised by nodes 11, 12, 15, 16 and 20 in 2016 and 2018. Compared to coupled models, HadGEM3-A reliably reproduced node frequencies as represented by the reanalysis. Most of the node frequencies are in the range for those of ERAINT. Inadequacies in simulation of frequencies are, however, seen in nodes 3, 17 and 20. In general, node frequencies in 2018 are, however, relatively adequately reproduced by the model compared to those of 2012 and 2016. For instance, in 2018, 3 (12 18, 20) out of 5 (12, 14, 18 19 20) nodes absent in the reanalysis are also absent in the model; with the two having the least occurrence. For 2016, nodes identified as absent in reanalysis (1, 9, 14) are different from those identified in the model — current 12, 20 and natural 12, 16 and 20. For 2012, all nodes are present in the model despite 2, 3, 14, 18 and 19 missing in ERAINT.

Generally, two CGCMs (CanESM and MPI-ESM-2-HR) and HadGEM3-A reproduce the SOM synoptic atmospheric patterns and characteristics, albeit imperfectly, as identified by ERAINT and CHIRPS.

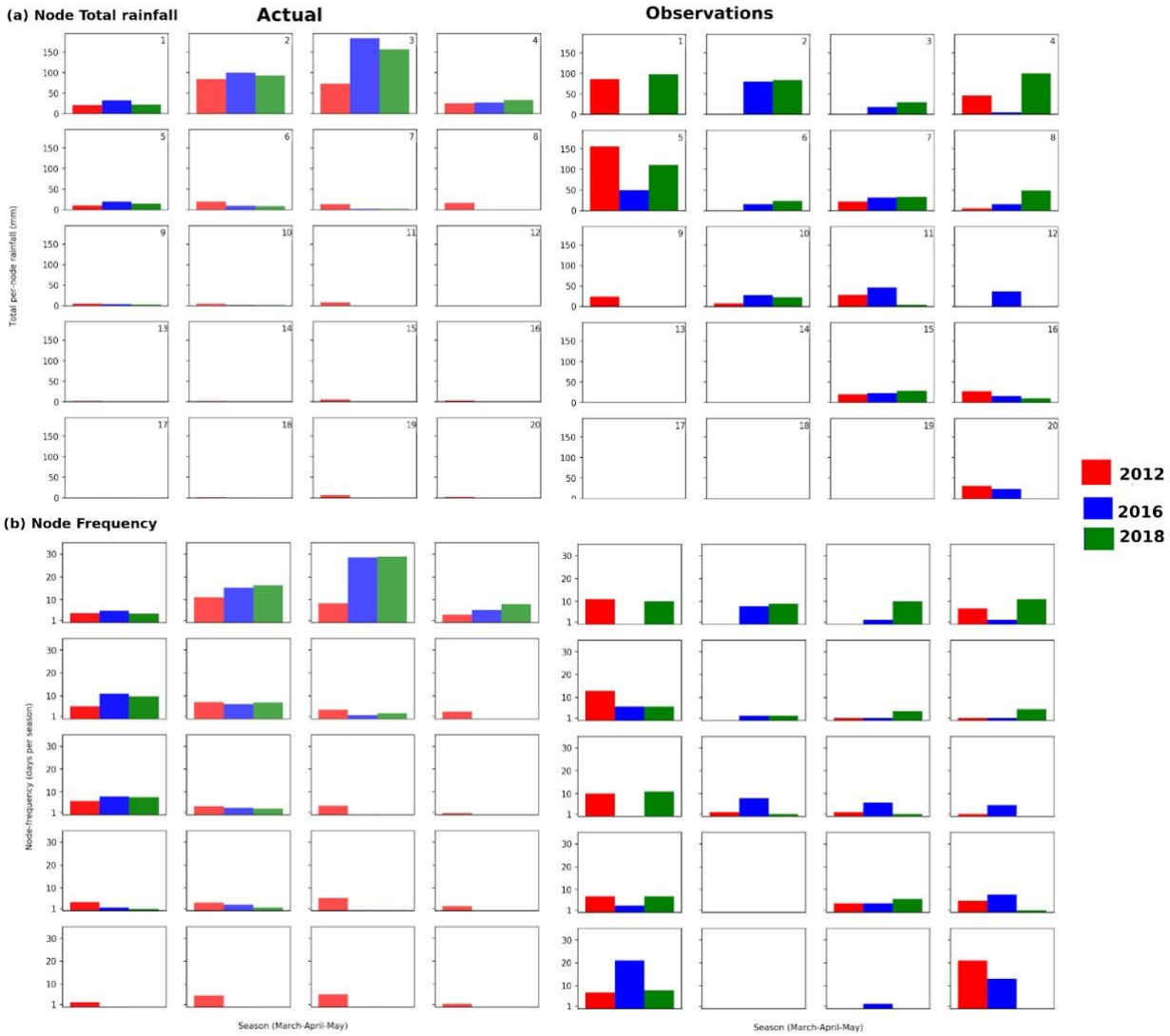

Figure 7.4 Total seasonal rainfall and (b) Frequency per-node for HadGEM3-A in the current (actual) climate conditions and observations on days characterised by circulation types of SOM classification of MAM qtuv at 850 hPa. The observations are based on CHIRPS (rainfall; a) and ERAINT (frequency; b) datasets.

7.2 Changes in the simulated SOM atmospheric conditions

This section discusses the changes in simulated synoptic conditions between the current and the pre-industrial climates for the cluster nodes. Figure 7.5 shows the current (actual) and the pre-industrial (natural) atmospheric synoptic conditions for CGCMs. For cluster 1 (3, 4, 8, 12) nodes in CanESM5, the east-west pressure gradient is rather weak in the natural climate compared to the current climate. In the current climate, zones of surface convergence are confined in the rainfall region due to relatively low pressure over the region compared to the surrounding areas. For cluster 2 (1, 2, 5, 9), 5 (13, 17) and 6 (14, 18) nodes, the current climate exhibits relatively high-pressure conditions over the entire SOM domain compared to the natural climate. For these nodes, the flow is predominantly unidirectional and divergent in the current climate with few to no zones of convergence seen while the relatively well-defined east-west pressure gradient with lower pressure over the rainfall region in the natural climate is evidenced by regions of convergent flow. Cluster 3 (6, 7, 10, 11) and 4 (15, 16, 19, 20) nodes depict somewhat similar synoptic patterns in both climates, however, the natural climate show relatively lower pressure conditions over the Congo basin. For INM-CM5-0, there is no clear distinctive change in the synoptic conditions between the current and the pre-industrial climates. The model simulates similar patterns of zonal wind flow and surface pressure conditions in both climates. Like CanESM5, the pressure conditions over the western side (Congo Basin) of the domain as simulated by MPI-ESM1-2-HR are relatively low in the natural compared to the current climate. For wind flow, however, both climates show similar patterns across the nodes. However, convergent flow in cluster 1 (3, 4, 8, 12) nodes tends to be confined to the rainfall region in the current climate but spread out to include the Congo basin in the natural climate. For cluster 2 nodes, similar atmospheric conditions prevailed in both climates except for the heightened pressure over the western side of the domain in the current climate. This pattern is replicated in the other clusters. Like INM_CM5-0, there is no clear distinctive change in synoptic conditions as simulated by IPSL-CM6A-LR in the current compared to those in the pre-industrial climate. However, the east-west pressure gradient is relatively strong in the current climate particularly for nodes 2, 3, 6, 7, 10, 11 and 15.

Figure 7.6 shows the current (actual) and pre-industrial (natural) simulated synoptic atmospheric climate conditions at 850hPa over the SOM domain for HadGEM3-A. Generally, the model tends to simulate lower atmospheric surface pressure for nodes in the natural climate particularly those on the right side of the SOM array (nodes 3, 4, 7, 8, 11, 12, 15, 16, 19 and 20) compared to those in the current climate in all seasons. For 2012, all nodes are present in both climates. Cluster 1 and 2 nodes exhibit similar atmospheric conditions although the divergent flow is more widespread within and around the rainfall region in the current climate. The zonal flow is more divergent for cluster 3 and 4 nodes due to relatively strong east-west pressure gradient

in the current climate compared to the natural climate. In contrast, the flow is convergent for cluster 5 and 6 nodes but confined in the rainfall region in the current climate and outside in the natural climate. In MAM 2016, two (12 & 20) and four (12, 16, 17 & 20) nodes were absent in the current and pre-industrial climates, respectively. Despite a relatively lower surface pressure over the western side of the SOM domain in the natural climate, the model simulates similar flow patterns for cluster 1 & 2 nodes in both climates. For cluster 3, 4, 5 & 6 nodes, the convergent flow tend to be confined within the rainfall in the current climate unlike the lower pressure region to the west in the natural climate. In 2018, five (12, 16, 17, 18 & 19) node were absent in each climate world. For all the nodes, a consistent pattern in the current and pre-industrial climates exist — stronger east-west pressure gradient for nodes in the current climate and relatively lower pressure conditions to the west of the SOM domain for those in the natural climate.

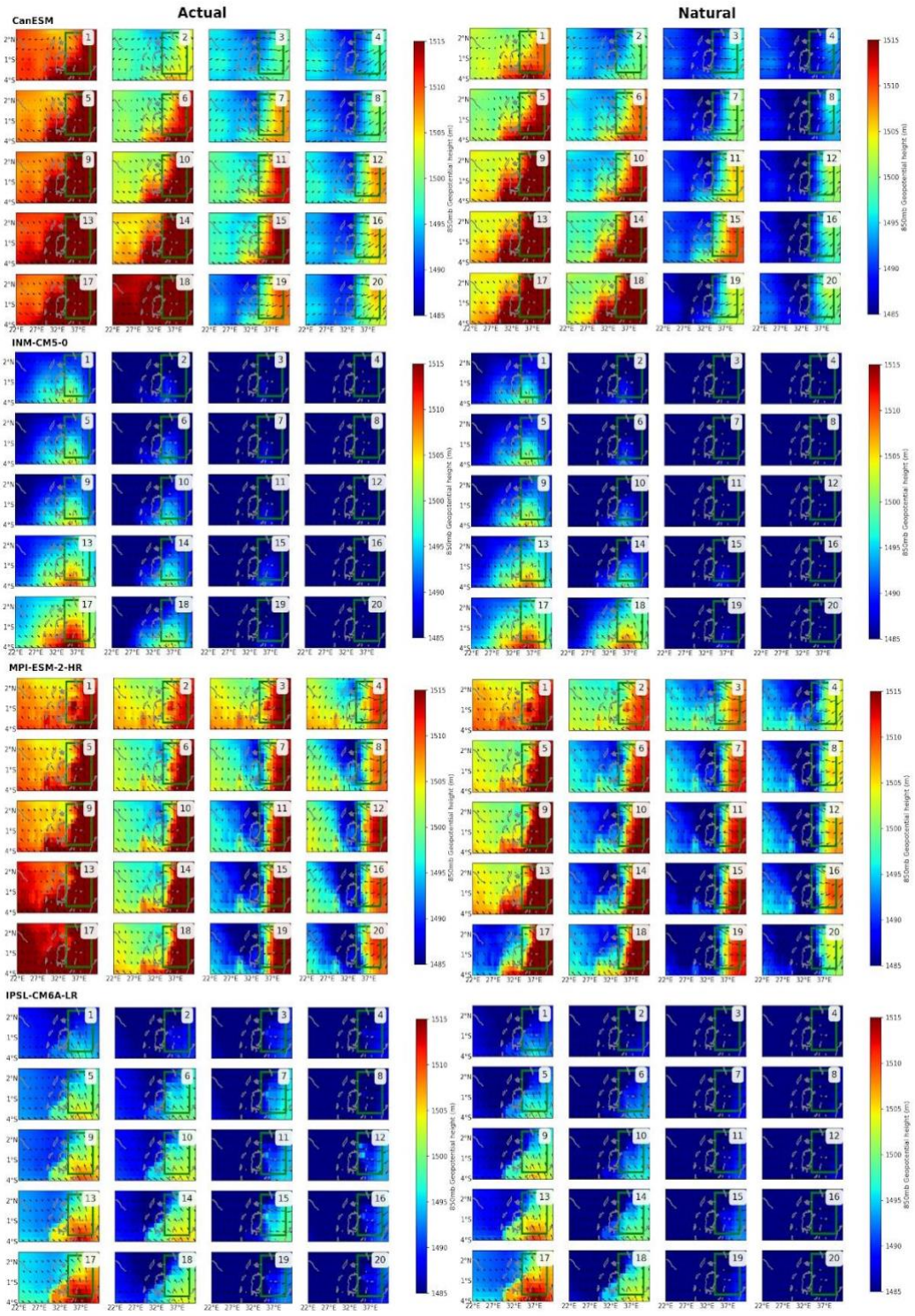

Figure 7.5 Mean MAM geopotential heights (shaded) and moisture flux (arrows) at 850hPa over the SOM domain on days in the actual/ current (2000-2030) and natural/ pre-industrial (1850-1900) climate conditions for CanESM, INM-CM5-0, MPI-ESM-2-HR and IPSL-CM6A-LR characterised by synoptic atmospheric conditions identified by SOM classification of MAM qtuv at 850 hPa. The box shows the rainfall region analysed (see Figure 3.2; section 3.3.2).

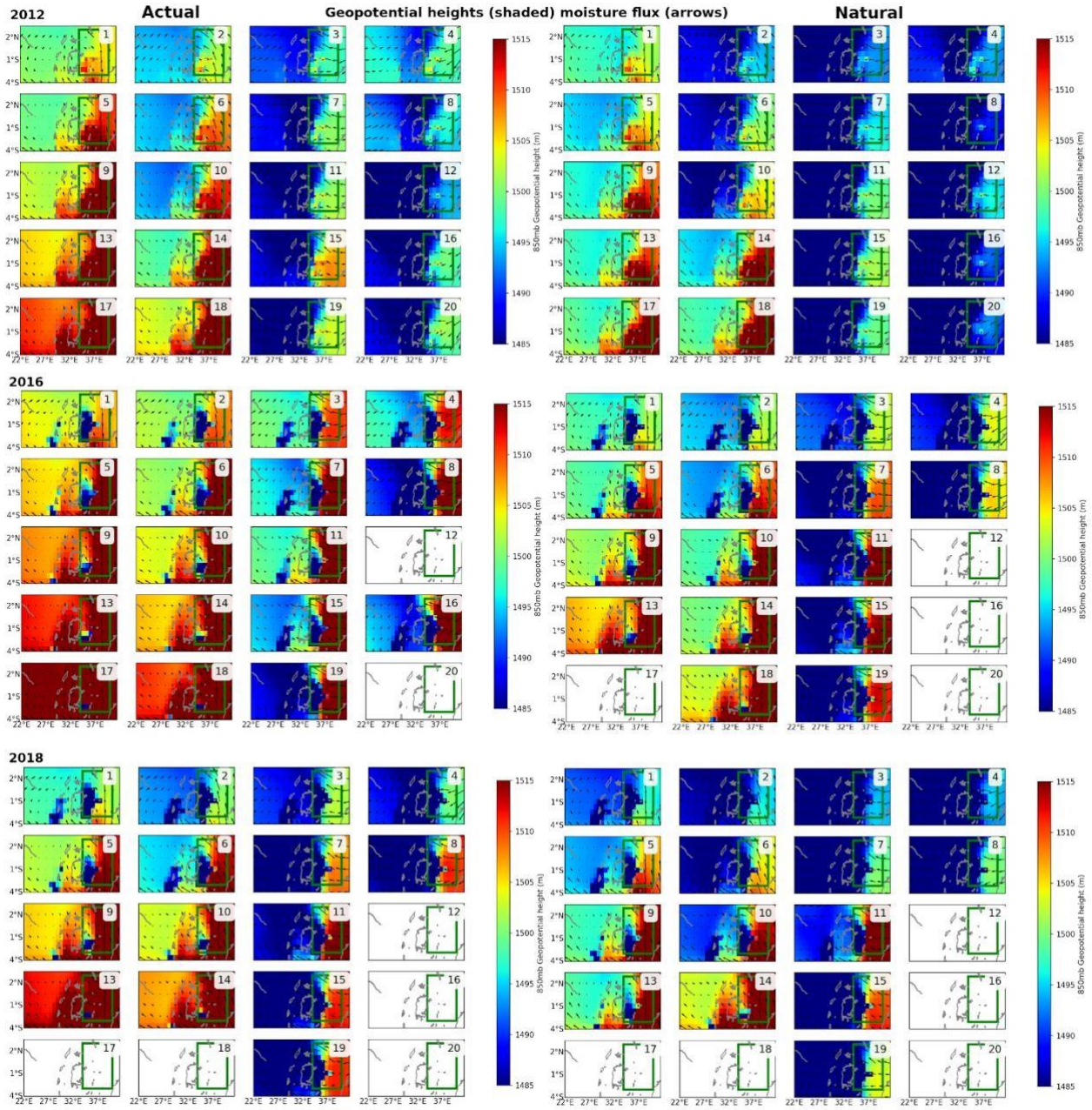

Figure 7.6 Mean MAM geopotential heights(shaded) and moisture flux (arrows) at 850hPa over the SOM domain on days in the current (actual) and pre-industrial (natural) climate conditions for HadGEM3-A characterised by synoptic atmospheric conditions identified by SOM classification of MAM qtuv at 850 hPa. The box shows the rainfall region analysed (see Figure 3.2; section 3.3.2). The nodes that were absent during the season are left blank.

7.3 Attribution of changes in SOM cluster frequency and associated rainfall

This section presents the results for attribution of changes in total rainfall and node occurrence between the current and pre-industrial climates for the two model experiments. Figures 7.7 and 7.9 show total seasonal rainfall and frequency per-node in both climate conditions for CGCMs and HadGEM3-A, respectively. Figures 7.8 and 7.10 show changes (actual - natural) in total seasonal rainfall and the frequency of SOM nodes in the six clusters for the CGCMs and HadGEM3-A, respectively. The significance of the changes is tested using Chi-square (χ^2) test for node frequencies and Mann-Whitey U (Wilcoxon Rank Sum test) test for rainfall, both at 90% significance level. Tables 7.1 and 7.2 present the test statistics and p-values for χ^2 and U for the CGCMs and HadGEM3-A, respectively. The assessment of changes is carried out on the clustered nodes (see Chapter 5). Results in Chapter 5 show that wet cluster nodes (cluster 1 & 2) were more prevalent (relative to climatology) during 2018 and 2012 MAM seasons, particularly on dekads when flooding was experienced. For coupled models, generally, the rainfall associated with wet nodes (cluster 1 & 2) has increased while that of dry nodes (cluster 5 & 6) has decreased. INMCM5-0 and MPI-ESM-2-HR, however, show increases in rainfall associated with cluster 6. Rainfall associated with cluster 4 nodes, which are relatively dry, has also increased across all the models (highest increases exhibited by CanESM5). Changes in cluster 3 nodes are mixed across the models; decrease in CanESM5 and IPSL-CM6A-LR and increase in INM-CM5-0 and MPI-ESM-2-HR. The models do not seem to agree on the sign of change in the frequency of the SOM nodes. There is however a general tendency towards a change in node occurrence, but not in a consistent way for all models — 3 out of 5 models show increase in nodes for cluster 1, 2, 4, and 2 for cluster 3, 5 and 6. It is worth noting that wet nodes (cluster 1 and 2) that show increases in node occurrence also show corresponding increase in rainfall i.e., wetter, and more prevalent in the current climate relative to preindustrial. Cluster 4 nodes depict a similar pattern, notably by CanESM5, INM-CM5-0 and IPSL-CM6A-LR. Even so, the changes in rainfall are not statistically significant across all the models (Tables 7.1 & 7.2). For node frequency, however, INM-CM5-0 and MPI-ESM-2-HR show increases in clusters 2, 4 and 6 in the current climate relative to pre-industrial. Generally, there is an increased node contribution to rainfall in the current climate compared to the pre-industrial climate as well as prevalence.

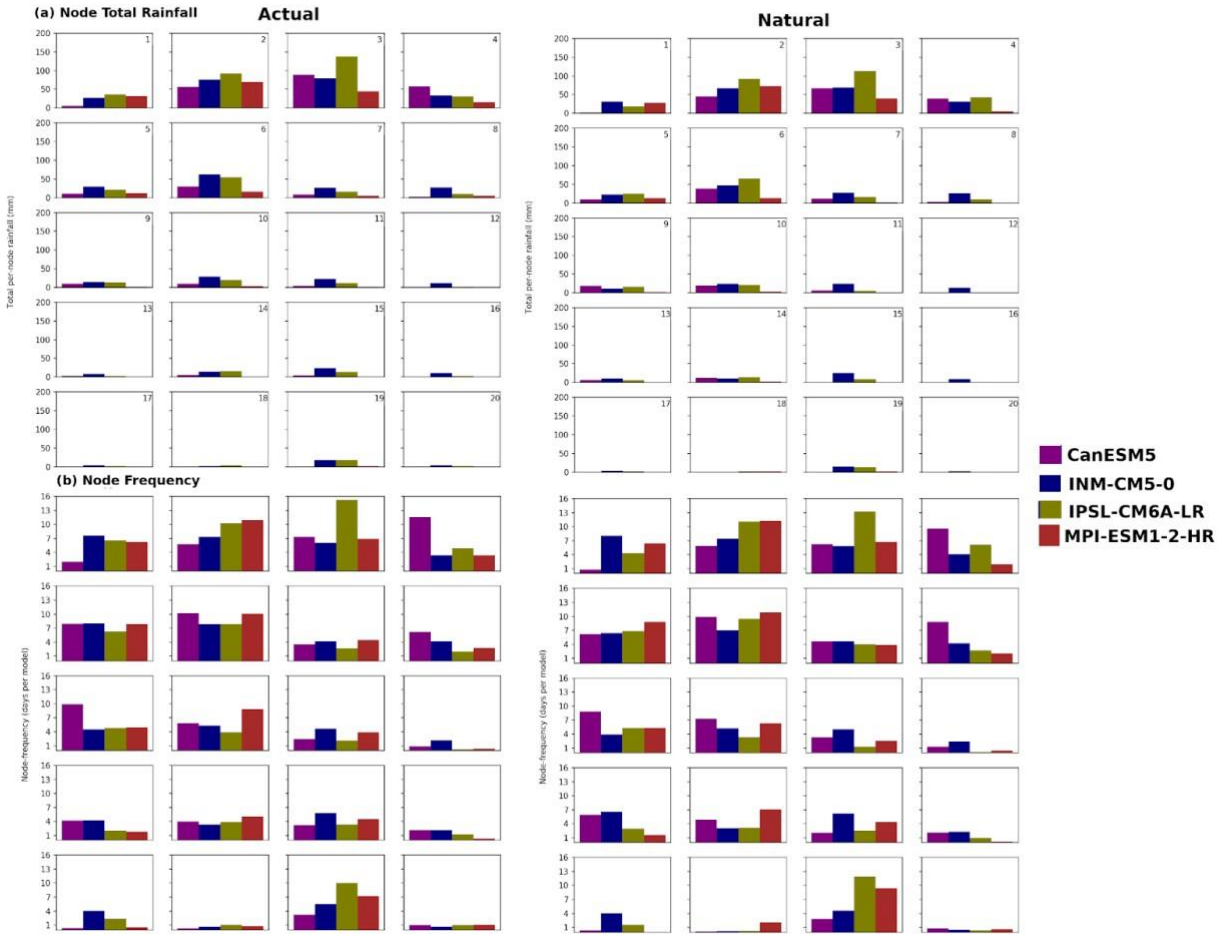

Figure 7.7 (a) Total seasonal rainfall and (b) Frequency per-node for CanESM, INM-CM5-0, MPI-ESM2-HR and IPSL-CM6A-LR in the current (actual) and pre-industrial (natural) climate conditions on days characterised by circulation types of SOM classification of MAM qtuv at 850 hPa.

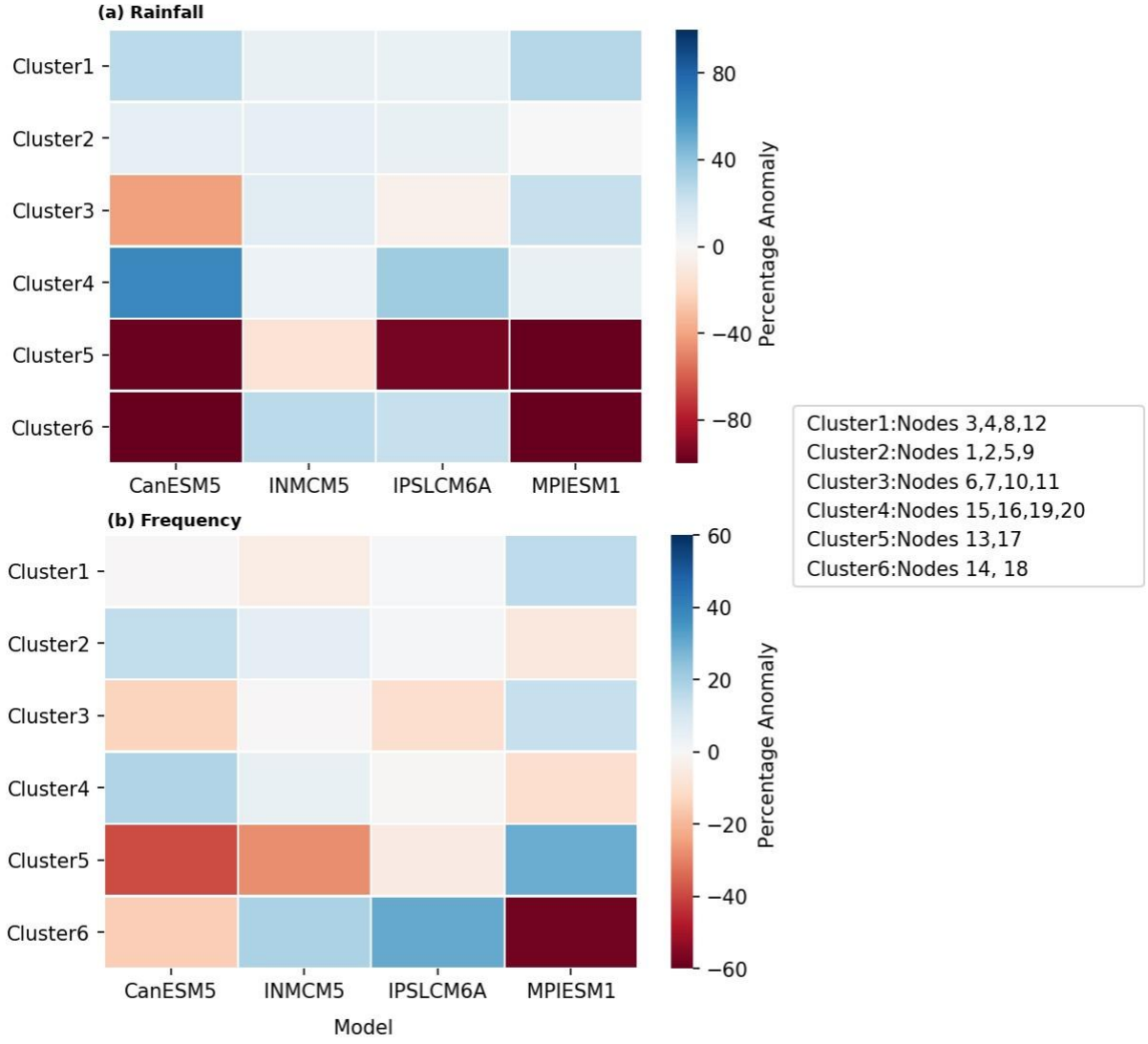

Figure 7.8 Changes (expressed in percentage anomalies) in MAM node-cluster (a) total seasonal rainfall and (b) frequency for coupled models in the current (historical) climate relative to the preindustrial (natural) climate for SOM analysis of qtuv at 850hPa.

Table 7.1 Values for test statistic and p-value for significance test of cluster rainfall between current and the pre-industrial climate for coupled models using Mann-Whitney U test

Model	**U**	**p-value**
CanESM	17	0.47
INM-CM5-0	13	0.24
MPI-ESM-2-HR	18	0.47
IPSL-CM6A-LR	17	0.47

Table 7.2 Values for test statistic and p-value for significance test of cluster frequency between current and the pre-industrial climate for coupled models using Chi-square test

Model	χ^2	**P-value**
CanESM	1.94	0.85
INM-CM5-0	0.84	0.97
MPI-ESM-2-HR	0.84	0.97
IPSL-CM6A-LR	2.74	0.73

For HadGEM3-A, there is a general increase in rainfall across the three seasons in the current climate. All clusters except for 4 in 2012 and 2018, and 3 in 2012, show increase in rainfall. Minimal increases are however found for wet nodes compared to dry, especially for 2016. Recognizing that evaluating percentage changes can lead to overestimations in values close to zero, it is important to note that our simulated preindustrial frequencies and rainfall amounts are significantly above zero. For cluster frequency, reduction is seen across the three seasons for cluster 1. For cluster 2, frequency of the nodes decreased in 2018 and 2016 but increased in 2012. Conversely, the frequency increased in 2018 and 2016 and decreased in 2012 for cluster 3 and 4. For cluster 5 and 6, the frequency has increased across the three seasons. To note is that the substantial rainfall contribution by dry clusters (notably 5 & 6) across the three seasons corresponds to increase in node frequency. Wet clusters, however, show decreasing frequencies. Cluster 3 and 4 nodes were more prevalent in 2016 and 2018 and less prevalent in 2012. The changes in rainfall are not statistically significant across the three seasons while those of node frequencies are significant in 2018 and 2012 (Table 7.2).

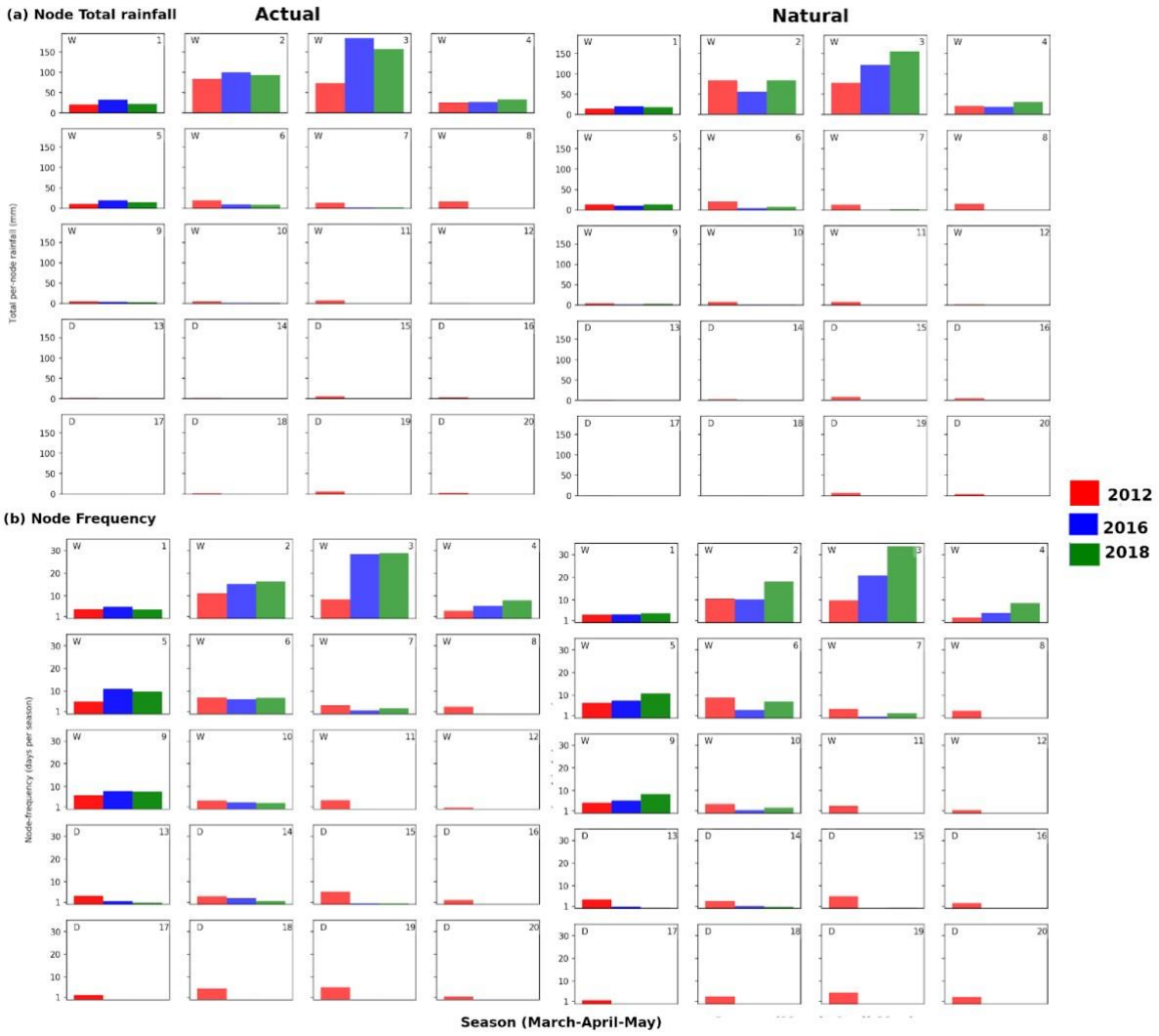

Figure 7.9 (a) Total seasonal rainfall and (b) Frequency per-node for HadGEM3-A in the current (actual) and pre-industrial climate conditions on days characterised by circulation types of SOM classification of MAM qtuv at 850 hPa.

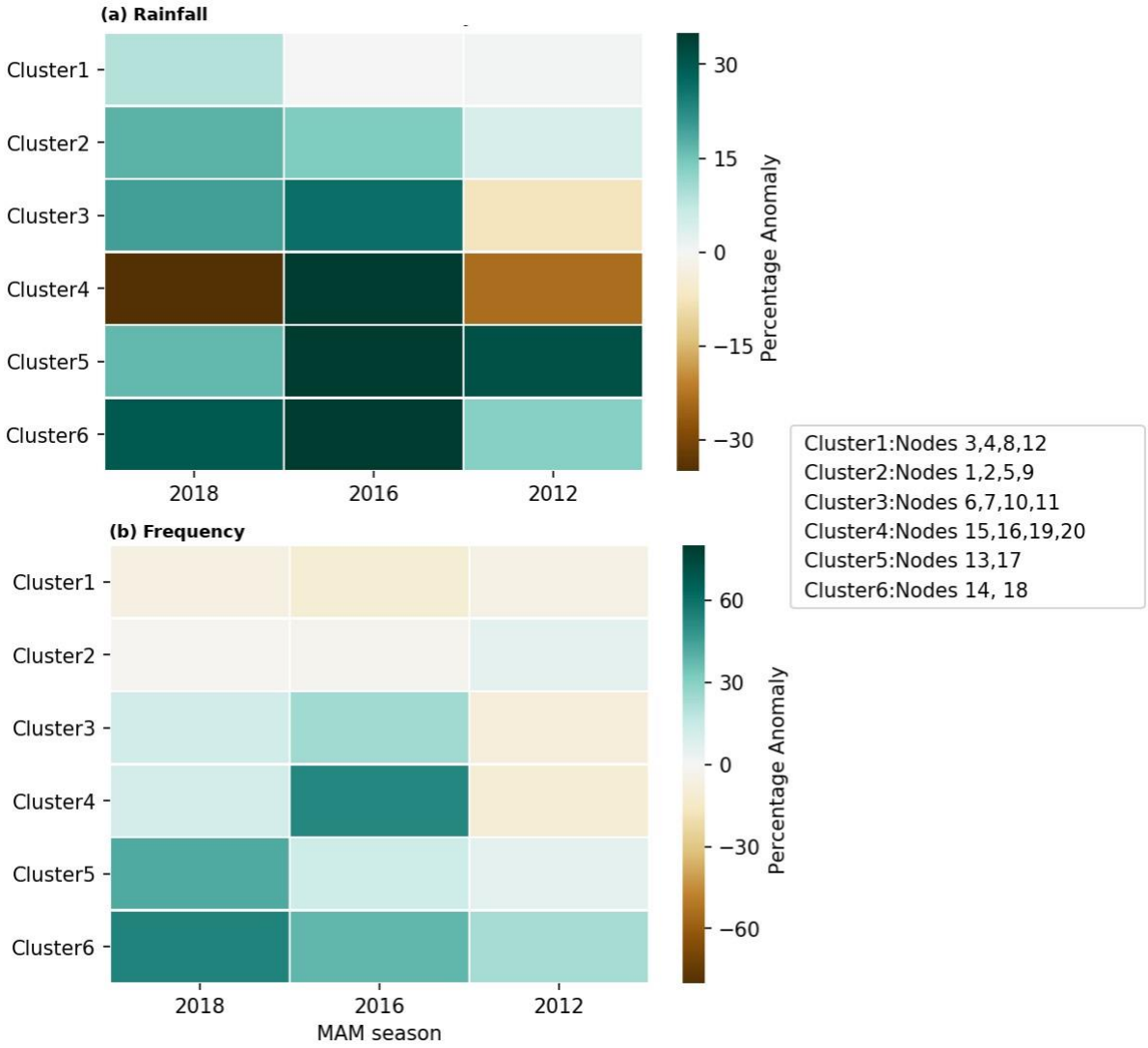

Figure 7.10 Changes (expressed in percentage anomalies) in MAM node-cluster (a) total seasonal rainfall and (b) frequency for HadGEM3-A model in the current (actual) climate relative to the preindustrial (natural) climate for SOM analysis of qtuv at 850hPa.

Table 7.3 Values for test statistic and p-value for significance test of node cluster rainfall between current and pre-industrial climates for HadGEM3-A using Mann-Whitney U test

Event-year	U	p-value
2012	16	0.40
2016	14	0.29
2018	16	0.40

Table 7.4 Values for test statistic and p-value for significance test of cluster frequency between current and pre-industrial climates for HadGEM3-A using Chi-square test

Year	χ^2	p-value
2012	1.026	0.96
2016	2.226	0.81
2018	1.46	0.92

7.4 Summary of findings

While the contribution of human influence on synoptic conditions of MAM 2012, 2016 and 2018 are not statistically significant in any if the model experiments, results show that for nodes found to increase in frequency most exhibit a corresponding increase in rainfall. INM-CM5-0 shows a corresponding increase in rainfall for every instance of increased node frequency shown by clusters 2, 3, 4, 6. For HadGEM3-A, significant increase in node frequencies is seen for clusters 2, 3, 4, 5 and 6 in 2018. Of these, all but cluster 4 show increases in rainfall. For 2012, significant prevalence of nodes in cluster 2, 5 and 6 also correspond to a significant increase in rainfall. From analysis of observation (chapter 5), the study detects increased prevalence of wet cluster nodes in the three wet MAM seasons assessed in this study. However, the results here are unable to clearly attribute whether human influence on climate contributes to the detected changes. Given the overall increase in rainfall where node frequencies increase, even if not statistically significant, results could be indicative of an emerging anthropogenic signal that is not yet above natural variability to be attributable.

8 Conclusions and Recommendations

This thesis sought to investigate the role and contributions of anthropogenic climate change on the magnitude of rainfall anomalies and large-scale driving atmospheric conditions on three specific flood-inducing heavy rainfall periods in the 2012, 2016 and 2018 MAM seasons in Kenya over a region defined by grid boxes (3ºS, 1.7ºN, 34.7ºE, 37ºE), (3ºS, 2.0ºN, 34ºE, 36.7ºE) and (3ºS, 1.7ºN, 34.7ºE, 39ºE). The regions cover the central highlands, western highlands and parts of the arid and semi-arid central regions of Kenya. This was the first study to attempt an attribution analysis of human influence on both thermodynamic and dynamic factors in understanding changes in the intensity of extreme rainfall in East Africa. The approach aimed to improve the ability to quantify multiple facets of climate risk by characterizing physical mechanisms behind extreme rainfall events in assessing their sensitivity to a changing climate. First, the rainfall magnitude and associated synoptic atmospheric conditions were defined and characterised and then the role of human influence on these was assessed. Atmospheric states over a 38-year period (1981-2018) were identified and characterised, and then an assessment on whether the conditions conducive to heavy rainfall were more prevalent during the periods when the flood-inducing heavy rainfall events occurred in MAM 2012, 2016 and 2018 was carried out. To do this, the study utilised Self-Organizing Maps, an unsupervised machine learning technique that identifies frequently occurring spatial patterns in higher-dimensional datasets by clustering and reducing their initial dimensions to a lower representation (in our case, two-dimensional), while preserving the topological structure of the data. And since there was no clear definition of what aspects of the observed rainfall caused the floods, three heavy-rainfall maxima were investigated: maximum consecutive 5-day, 10-day and 20-day (Rx5d, Rx10d and Rx20d) rainfall. Assessment of the three indices across three different MAM seasons allowed for a more inclusive analysis of candidate rainfall extremes under anthropogenic forcing and natural variability. The role of human-induced climate change on the magnitude of the heavy precipitation events and associated synoptic atmospheric conditions were evaluated based on three different experiments applying independent event-attribution approaches. Two observational (station and gridded) and one reanalysis datasets, and climate model ensembles representing the preindustrial or past (period prior to the onset of large-scale industrialization and human influence on the climate) and current (MAM 2012, 2016 and 2018) climates, were utilised in the study. The climate models were evaluated to determine their suitability for use in the study. Seven of fifteen coupled and three of five atmospheric models were found to adequately simulate MAM spatio-temporal characteristics of seasonal and heavy precipitation over the study region. This multi-method multi-model methodology allowed attribution results to be relatively independent of assumptions within specific methods and idiosyncrasies of data, and thus enhancing robustness in the assessment of human-induced changes in the extreme rainfall events. This is

particularly important for attribution studies in East Africa where models generally perform poorly, in addition to limited availability of long historical observations.

From this study, the following conclusions are drawn:

- A strong relationship between air mass flow, as a key contributor to moisture transport and availability, and MAM seasonal and intra-seasonal rainfall variability is established and confirmed in accordance with other previous work. Findings show that the dominant synoptic mechanisms that drive heavy precipitation over the rainfall region involve an interaction between reduced surface pressure over the region, anomalous low-level westerly/southwesterly flow into the region, weak low-level easterly flow into the region, and strong upper-level easterlies over the region. This is consistent with previous studies (e.g., Johnson and Morth, 1960; Ayamba, 1983; Camberlin and Wairoto, 1997; Pohl and Camberlin (2006b); Ngarukiyimana et al., 2017; Kilavi et al., 2018; Finney et al., 2019).
- Anomalous low pressure at the surface triggers an anomalous westerly/southwesterly flow that advects warm moist air from the Congo Basin/Atlantic Ocean and a weak easterly flow which advects moisture from the Indian Ocean. This creates both large-scale and localised low-level convergence zones. A simultaneous presence of well-defined strong upper tropospheric easterlies favours vertical wind shear which enhances atmospheric instability.
- Dry days in the MAM season over the rainfall/study region are marked by strong easterlies at low to mid-levels. These easterlies tend to transport water vapour further beyond Kenya into the continental interior accompanied by strong divergent conditions at the surface over Kenya. This inhibits convective rainfall activities due to reduced moisture content/availability and increased atmospheric stability.
- Reduced surface pressure, anomalous low-level westerly/southwesterly flow, weak low-level easterly flow, and strong upper-level easterlies characterised the dekads in which flood events occurred in MAM 2018, 2012 and 2016 seasons. Furthermore, days characterised by these conditions prevailed more often in the MAM seasons, especially in MAM 2018 and 2012, compared to climatology. Days characterised by strong low-level easterly flow, which are associated with drier conditions, were less frequent and completely absent during the period when impactful flooding occurred.
- A synthesis of results from the three approaches used in attribution of rainfall intensity show intensification of extreme rainfall in the current climate (MAM 2012, 2012, 2018) compared to the pre-industrial period climate (1850-1900), but without statistical significance. MAM 2018

shows higher levels of intensification compared to 2012 and 2016. These results could suggest that it is more likely than not that anthropogenic climate change increased the magnitude of heavy rainfall in these years, but this influence is yet not formally (not statistically significant) attributable to human influence on the climate system.

- Analysis of differences in synoptic atmospheric conditions in climate model simulations between today's climate and a preindustrial climate did not find consistent differences across models. Further, for all models, differences in rainfall associated with atmospheric states (SOM node clusters) and frequencies of atmospheric states are statistically significant. Therefore, the current analysis was unable to attribute a human influence on the driving synoptic conditions associated with heavy rainfall over the study area.

These findings provide new insights on drivers of extreme MAM rainfall in Kenya and the potential influence of anthropogenic climate change. Over the last two decades, a drying trend in the MAM season has been observed (Rowel et al. 2015; Williams and Funk, 2011) with prolonged droughts greatly impacting agricultural productivity (food security) and water resources in the region. This work shows that even in the drying trend, flood-inducing extreme rainfall can and does occur, and is associated with a higher frequency of certain synoptic conditions. While a clear attribution conclusion of human influence on the magnitude and atmospheric drivers of heavy rainfall in the three study years was not possible, there is tentative evidence that a human influence might be emerging. Most of the attribution studies on the drying trend in the MAM season found an attributable anthropogenic influence (Hoell et al. 2017; Funk et al. 2018), although a few unable to do so (and therefore assuming the trend is due to natural interdecadal variability (Lyon, 2014). It is important to note that precipitation change signals have been found to emerge more slowly in regions experiencing high climate variability, such as East Africa, especially for analysis at smaller scales where models do not capture all necessary processes to realistically simulate regional details and regionally important forcings, and with high observational uncertainties (Bindoff et al., 2013; Collins et al., 2013). Also, since rainfall in East Africa is driven by both dynamic and thermodynamic processes (Finney et al., 2020), it is unclear whether these processes acted in opposite directions during the events, attenuating the anthropogenic signal (Finney et al., 2020). Whereas the current global models do not realistically simulate all necessary processes, key limitations especially exist in simulating intense rainfall associated with deep convection. There is potential to use convective permitting models in attribution analyses in East Africa, however this is not feasible at present. At the time of this analysis, no convection permitting simulations of sufficient length and ensemble size exist that would allow for their use in attribution of trends in extremes.
Results here show tentative evidence of intensification of extreme rainfall in today's climate. A shift towards higher precipitation is consistent with what is expected under an enhanced greenhouse gas climate world via

Clausius-Clapeyron relationship (Boer, 1993; Allen and Ingram, 2002; Trenberth 2011; O'Gorman 2015). Intense rainfall events amid an overall drying MAM rainfall season, leave the already vulnerable Kenyan society with uncertainties of how to prepare adequately for changing climate risks. Societal adaptation to climate change in areas with high climate variability is more challenging, since extreme weather and climate events have a higher impact than the mean climate (Parmesan et al., 2000). Also, exposure to vagaries of extremes increases vulnerability and lowers the adaptive capacity of both the environmental and human systems. This study, therefore, provides a first step for in-depth assessment of a county in East Africa of recent rainfall extremes from an attribution perspective, with the ultimate aim of supporting society to anticipate weather and climate risks. Extreme event attribution studies are particularly important in vulnerable regions of the world, such as East Africa, where the impacts of these events can be severe and far-reaching. Many communities rely on rain-fed agriculture, and most are employed in climate-sensitive sectors. Studies such as this one help support climate-resilient development (see, section 2.8 for detailed role and importance of attribution studies). Notwithstanding, attributing extreme events to anthropogenic climate change in such regions is a complex task that faces multiple challenges (Otto et al., 2021). Major issues include lack of long-term, high-quality observational data, poor model performance and lack of local expertise. Presently, most attribution studies are conducted by scholars in the global north with a sole focus on events in high-income countries. Framing and contextualising of attribution studies (such as during event definition) can be improved by drawing on local expertise. Local experts also help to integrate findings into decision-making e.g., by tailoring the studies to support the policy processes — which often are country-specific. Highlighting the documented dire need for capacity development in low-income regions, the field of attribution science must grow in Africa following similar principles outlined in the Paris Agreement for capacity-building.

EEA can is important for quantifying how the hazard in changing, and how much of this change is attributable to human influence. Climate risks from extreme events are a function of both hazard, alongside vulnerability and adaptive capacity. Therefore, recognising the hazard is increasing can and should be used to focus on reducing vulnerability and increasing adaptive capacity. Following the challenges of attributing extreme events in regions like East Africa, there is need for a comprehensive attribution approach that integrates components of vulnerability and exposure. By any means, focusing solely on the physical component (quantitative assessment) of the hazard somehow creates a discourse that deflects responsibility for human actions that cause disasters (Raju et al., 2022). For many high-impact events that often result in disasters in vulnerable regions, such as the ongoing drought in the Greater Horn of Africa, qualitative assessments can be very beneficial, especially when a quantitative assessment cannot provide a definite

answer. They provide an opportunity for targeted interventions i.e., by identifying the most vulnerable populations/communities and/or regions, resources and efforts can be targeted to where they are most needed, leading to more effective and efficient adaptation efforts. Essentially, disentanglement of key drivers of disasters enhances the understanding of disaster impacts which help improve early warning systems and overall disaster management.

Climate change science relies heavily on physical understanding, and the concept of causality is a key aspect in physical science, as well as to decision-making. However, there is a disconnect between physical reasoning and statistical practice in the current climate change science discourse (Amrhein et al., 2019; McShane et al., 2019; Wasserstein et al., 2019; Wasserstein & Lazar, 2016; Shepherd, 2021). Climate model simulations are central to attribution studies. These simulations may or often differ from the real world and could yield conflicting results. On a global scale, where the signal-to-noise ratio is high, it is possible to make scientific statements with high confidence. However, at the local and regional level, where natural variability is high, it is harder to discern the signals of change and models often provide inconsistent results. According to Wasserstein et al, (2019), statistical significance is not the same as scientific significance, although it is often mistaken as such. The common practice of categorizing p-values as "statistically significant" or "not statistically significant" gives an illusion of certainty by ignoring the extensive physical knowledge of the climate system and the mechanisms involved (Shepherd, 2021). Additionally, the observed record only provides a limited sample of what is possible and is subject to non-stationary factors, many of which may be unknown. The disconnect between physical reasoning and statistical practice highlights the importance of considering both the physical understanding and uncertainties in the findings, as well as clearly communicating these elements for the climate information to be usable. Findings from attribution studies that are not statistically significant, like those here, do not necessarily indicate absence of evidence. With the frequent extremes raving the Greater Horn of Africa, where signals of change are not unambiguously evident in the observed record as the interaction of local factors with mesoscale and large-scale atmospheric conditions strongly determines climatic conditions, and climate models provide conflicting results, it is pertinent to raise risk awareness and tailor information at the space and time scales relevant for climate adaptation Some limitations of this research are identified as follows.

- The focus on season-long attribution may not have provided a comprehensive understanding of the specific dekads during which the flooding occurred. Primarily for detection, the focus could be on the dekads in which flooding was experienced. Additionally, linking the climate models to hydrological models to perform impact attribution modelling on floods could enhance the understanding of the underlying physical mechanisms and the vulnerability and exposure factors

that cause disasters. Vulnerability and exposure factors turn hazards into disasters and cause disproportionate impacts on many vulnerable communities across the world. Impact modelling recognizes the need for location and context-specific adaptation measures depending on levels of vulnerability, actors involved, and resources available.

- The study primarily focussed on the regional circulation patterns affecting rainfall in the region, without delving into mesoscale convective systems which have substantial control of the equatorial tropical climate. Yet, it is noted that attribution analysis of mesoscale systems in regions like the Rift Valley and the highlands, and around Lake Victoria would necessitate models' adept at addressing convective processes.
- The evaluation of climate models for magnitude attribution did not have a well-defined metric for good, moderate, and poor performance, but was rather heuristic. It is imperative to develop a rigorous model evaluation procedure for use in East Africa since models are currently underperforming. The validation of the synoptic conditions for the HadGEM-3A model using an equivalent period as the reanalysis data would enable a stronger evaluation of the model. The number of climate models used attribution of synoptic conditions was limited (4 GCMs and 1 AGCM) to daily data suitable for atmospheric state analysis. To minimise idiosyncrasies of data, a wider range of model simulations would be beneficial for the analysis. Despite no such simulations suitable for attribution studies at present, the use of convective-permitting climate models could provide a more accurate representation of deep convection in regions of high topographic heterogeneity like East Africa, for studies of attribution rainfall in both attribution and forecasting.
- Relying on a single reanalysis data may not provide a comprehensive understanding of the synoptic conditions driving extreme rainfall and the evaluation of models. Using multiple reanalysis datasets to characterise the synoptic conditions could provide a stronger understanding of the detected changes in node frequencies and the changes in he identified circulation states. Additionally, the self-organizing map (SOM) analysis of the models should have been conducted independently of the reanalysis data to ensure the robustness of the results.

The field of attribution of extreme of rainfall In East Africa provides numerous opportunities for future research, few outlined as follows.

- Improving the ability of models to simulate climate extremes over the region, particularly focussing on convective-permitting models will provide a more accurate representation of the impact of climate change on the region, and more robust inputs to extreme rainfall attribution studies. This has the potential to support attribution studies at the local level, especially in

highland areas and around Lake Victoria, where models are required to simulate mesoscale weather systems. Efforts to produce such simulations are already underway at global modelling centres like UK Met Office, now providing avenues for collaboration.

- Integration of machine learning techniques in attribution studies. Machine learning has the potential to provide complementary tools that enhance our understanding of the climate systems (and changes thereof) e.g., through complex pattern recognition, uncertainty quantification and downscaling etc.
- Development of a comprehensive attribution framework that integrates components of exposure and vulnerability is crucial to fully understand how an attributable change in rainfall propagates through to an attributable impact on the ground. This will inform the loss and damage debate.
- Improvement of the observation network and access to quality long historical data will enable researchers to conduct robust analysis in identifying trends and changes in the frequency and intensity of extreme rainfall events. More effort is required in archiving atmospheric variables so that dynamical attribution can be more easily undertaken.
- Funding research in this field will enable researchers to carry out detailed studies and explore new avenues for understanding human influence on the climate.
- Training and capacity building for researchers to carry out attribution studies will enhance the research output and provide a better understanding of the contribution and impact of climate change on East African society.

9 References

Allen, M. R., & Ingram, W. J. (2002). Constraints on future changes in climate and the hydrologic cycle. In *Nature* (Vol. 419, Issue 6903, p. 642). Cambridge Univ. Press. https://doi.org/10.1038/nature01092

Andrews, M. B., Ridley, J. K., Wood, R. A., Andrews, T., Blockley, E. W., Booth, B., Burke, E., Dittus,A.J., Florek, P., Gray, L. J., Haddad, S., Hardiman, S. C., Hermanson, L., Hodson, D.,Hogan, E., Jones,G.S.,Knight, J. R., Kuhlbrodt, T., Misios, S., … Sutton, R. T. (2020). Historical Simulations With HadGEM3GC3.1 for CMIP6. *Journal of Advances in Modeling Earth Systems*, *12*(6), 2019MS001995.https://doi.org/10.1029/2019MS001995

Anyah, R. O., & Qiu, W. (2012a). Characteristic 20th and 21st century precipitation and temperature patterns and changes over the Greater Horn of Africa. *International Journal of Climatology*, *32*(3), 347–363. https://doi.org/10.1002/joc.2270

Anyah, R. O., & Qiu, W. (2012b). Characteristic 20th and 21st century precipitation and temperature patterns and changes over the Greater Horn of Africa. *International Journal of Climatology*, *32*(3), 347–363. https://doi.org/10.1002/joc.2270

Ayugi, B., Zhidong, J., Zhu, H., Ngoma, H., Babaousmail, H., Rizwan, K., & Dike, V. (2021). *Comparison of CMIP6 and CMIP5 Models in Simulating Mean and Extreme Precipitation over East Africa*. *February*. https://doi.org/10.20944/preprints202102.0111.v1

Anyah, R. O., Semazzi, F. H. M., & Xie, L. (2006). Simulated physical mechanisms associated with climate variability over Lake Victoria basin in East Africa. *Monthly Weather Review*, *134*(12), 3588–3609. https://doi.org/10.1175/MWR3266.1

Bindoff, N. L., Stott, P. A., AchutaRao, K. M., Allen, M. R., Gillett, N., Gutzler, D., Hansingo, K., Hegerl, G., Hu, Y., Jain, S., Mokhov, I. I., Overland, J., Perlwitz, J., Sebbari, R., & Zhang, X. (2013). Detection and Attribution of Climate Change: from Global to Regional. *Climate Change 2013: The Physical Science Basis. Contribution of Working Group I to the Fifth Assessment Report of the Intergovernmental Panel on Climate Change [Stocker, T.F., D. Qin, G.-K. Plattner, M. Tignor, S.K. Allen, J. Boschung, A. Nauels, Y. Xia,* 1217–1308. https://doi.org/10.1017/CBO9781107415324.028

Boer, G. J. (1993). Climate change and the regulation of the surface moisture and energy budgets. *Climate Dynamics*, *8*(5), 225–239. https://doi.org/10.1007/BF00198617

Boucher, O., Servonnat, J., Albright, A. L., Aumont, O., Balkanski, Y., Bastrikov, V., Bekki, S., Bonnet, R., Bony, S., Bopp, L., Braconnot, P., Brockmann, P., Cadule, P., Caubel, A., Cheruy, F., Codron, F., Cozic, A., Cugnet, D., D'Andrea, F., … Vuichard, N. (2020). Presentation and Evaluation of the IPSL-CM6A-LR Climate Model. *Journal of Advances in Modeling Earth Systems*, *12*(7), 1–52. https://doi.org/10.1029/2019MS002010

Camberlin, P., & Okoola, R. E. (2003). The onset and cessation of the "long rains" in eastern Africa and their interannual variability. *Theoretical and Applied Climatology*, *75*(1–2), 43–54. https://doi.org/10.1007/s00704-002-0721-5

Carbon Brief (2023). https://www.carbonbrief.org/mapped-how-climate-change-affects-extreme-weather-around-the-world/

Cao, J., Wang, B., Yang, Y. M., Ma, L., Li, J., Sun, B., Bao, Y., He, J., Zhou, X., & Wu, L. (2018). The NUIST Earth System Model (NESM) version 3: Description and preliminary evaluation. *Geoscientific Model Development*, *11*(7), 2975–2993. https://doi.org/10.5194/gmd-11-2975-2018

Cheng, L., Hoerling, M., Smith, L., & Eischeid, J. (2018). Diagnosing human-induced dynamic and thermodynamic drivers of extreme rainfall. *Journal of Climate*, *31*(3), 1029–1051. https://doi.org/10.1175/JCLI-D-16-0919.1

Christopher H. Trisos, Ibidun O. Adelekan, E. T. (2022). *Africa*. 2022.https://www.ipcc.ch/report/ar6/wg2/downloads/report/IPCC_AR6_WGII_Chapter09.pdf

CRED. (n.d.). *CRED Crunch 56 - Disasters in Africa: 20 Year Review (2000-2019) | EM-DAT*. Retrieved

June 29, 2022, from https://www.emdat.be/cred-crunch-56-disasters-africa-20-year-review-2000-2019
Conway, D. (2011). Adapting climate research for development in Africa. *Wiley Interdisciplinary Reviews: Climate Change*, *2*(3), 428–450. https://doi.org/10.1002/wcc.115
Danabasoglu, G., Lamarque, J. F., Bacmeister, J., Bailey, D. A., DuVivier, A. K., Edwards, J., Emmons, L. K., Fasullo, J., Garcia, R., Gettelman, A., Hannay, C., Holland, M. M., Large, W. G., Lauritzen, P. H., Lawrence, D. M., Lenaerts, J. T. M., Lindsay, K., Lipscomb, W. H., Mills, M. J., … Strand, W. G. (2020). The Community Earth System Model Version 2 (CESM2). *Journal of Advances in Modeling Earth Systems*, *12*(2), e2019MS001916. https://doi.org/10.1029/2019MS001916
Döscher, R., Acosta, M., Alessandri, A., Anthoni, P., Arneth, A., Arsouze, T., Bergmann, T., Bernadello, R., Bousetta, S., Caron, L.-P., Carver, G., Castrillo, M., Catalano, F., Cvijanovic, I., Davini, P., Dekker, E., Doblas-Reyes, F., Docquier, D., Echevarria, P., … Zhang, Q. (2021). The EC-Earth3 Earth System Model for the Climate Model Intercomparison Project 6. *Geoscientific Model Development Discussions*, 1–90. https://doi.org/10.5194/gmd-2020-446
Dyn, C., & Moron, N. P. P. C. V. (2015). *Anomalously wet and dry rainy seasons in Equatorial East Africa and associated differences in intra - seasonal characteristics*. https://doi.org/10.1007/s00382-014-2460-6
Enenkel, M., Brown, M. E., Vogt, J. v., McCarty, J. L., Reid Bell, A., Guha-Sapir, D., Dorigo, W., Vasilaky, K., Svoboda, M., Bonifacio, R., Anderson, M., Funk, C., Osgood, D., Hain, C., & Vinck, P. (2020). Why predict climate hazards if we need to understand impacts? Putting humans back into the drought equation. *Climatic Change*, *162*(3), 1161–1176. https://doi.org/10.1007/S10584-020-02878-0/TABLES/1
E. Roeckner • G. Bäuml • L. Bonaventura • R. Brokopf • M. Esch M. Giorgetta • S. Hagemann • I. Kirchner • L., & E. Manzini • A. Rhodin • U. Schlese • U. Schulzweida • A. Tompkins Hamburg. (2003). The atmospheric general circulation model ECHAM5. *Journal of Geophysical Research Atmospheres*, *115*(18). https://doi.org/10.1029/2010JD014036
Eyring, V., Bony, S., Meehl, G. A., Senior, C. A., Stevens, B., Stouffer, R. J., & Taylor, K. E. (2016). Overview of the Coupled Model Intercomparison Project Phase 6 (CMIP6) experimental design and organization. *Geoscientific Model Development*, *9*(5), 1937–1958. https://doi.org/10.5194/gmd-9-1937-2016
Finney, D. L., Marsham, J. H., Walker, D. P., Birch, C. E., Woodhams, B. J., Jackson, L. S., & Hardy, S. (2020). The effect of westerlies on East African rainfall and the associated role of tropical cyclones and the Madden–Julian Oscillation. *Quarterly Journal of the Royal Meteorological Society*, *146*(727), 647– 664. https://doi.org/10.1002/qj.3698
Funk, C. C., & Hoell, A. (2015). The leading mode of observed and CMIP5 ENSO-residual sea surface temperatures and associated changes in indo-pacific climate. *Journal of Climate*, *28*(11), 4309–4329. https://doi.org/10.1175/JCLI-D-14-00334.1
Funk, C., Dettinger, M. D., Michaelsen, J. C., Verdin, J. P., Brown, M. E., Barlow, M., & Hoell, A. (2008). Warming of the Indian Ocean threatens eastern and southern African food security but could be mitigated by agricultural development. *Proceedings of the National Academy of Sciences of the United States of America*, *105*(32), 11081–11086. https://doi.org/10.1073/pnas.0708196105
Funk, C., Harrison, L., Shukla, S., Pomposi, C., Galu, G., Korecha, D., Husak, G., Magadzire, T., Davenport, F., Hillbruner, C., Eilerts, G., Zaitchik, B., & Verdin, J. (2018). Examining the role of unusually warm Indo-Pacific sea-surface temperatures in recent African droughts. *Quarterly Journal of the Royal Meteorological Society*, *144*(June 2017), 360–383. https://doi.org/10.1002/qj.3266
Funk, C., Husak, G., Michaelsen, J., Shukla, S., Hoell, A., Lyon, B., Hoerling, M. P., Liebmann, B., Zhang, T., Verdin, J., Galu, G., Eilerts, G., & Rowland, J. (2013). Attribution of 2012 and 2003-12 rainfall deficits in Eastern Kenya and Southern Somalia. *Bulletin of the American Meteorological Society*, *94*(9), S45–S48. https://doi.org/10.1175/BAMS-D-13-00085.1

Funk, C., Peterson, P., Landsfeld, M., Pedreros, D., Verdin, J., Shukla, S., Husak, G., Rowland, J., Harrison, L., Hoell, A., & Michaelsen, J. (2015). *The climate hazards infrared precipitation with stations — a new environmental record for monitoring extremes*. 1–21. https://doi.org/10.1038/sdata.2015.66

Funk, C., Harrison, L., Shukla, S., Hoell, A., Korecha, D., Magadzire, T., … Galu, G. (2016). 15. Assessing the contributions of local and East Pacific warming to the 2015 droughts in Ethiopia and Southern Africa. *Bulletin of the American Meteorological Society*, *97*(12), S75–S80. https://doi.org/10.1175/BAMS-D-16-0167.1

Hanel, M., Buishand, T. A., & Ferro, C. A. T. (2009). A nonstationary index flood model for precipitation extremes in transient regional climate model simulations. *Journal of Geophysical Research Atmospheres*, *114*(15), 1–16. https://doi.org/10.1029/2009JD011712

Hannart, A., Pearl, J., Otto, F. E. L., Naveau, P., & Ghil, M. (2016). Causal counterfactual theory for the attribution of weather and climate-related events. *Bulletin of the American Meteorological Society*, *97*(1), 99–110. https://doi.org/10.1175/BAMS-D-14-00034.1

Hastenrath, S., Polzin, D., & Mutai, C. (2010). Circulation mechanisms of kenya rainfall anomalies. *Journal of Climate*, *24*(2), 404–412. https://doi.org/10.1175/2010JCLI3599.1

Haustein, K., Otto, F. E. L., Uhe, P., Schaller, N., Allen, M. R., Hermanson, L., Christidis, N., McLean, P., & Cullen, H. (2016). Real-time extreme weather event attribution with forecast seasonal SSTs. *Environmental Research Letters*, *11*(6). https://doi.org/10.1088/1748-9326/11/6/064006

Hegerl, G., & Zwiers, F. (2011). Use of models in detection and attribution of climate change. *Wiley Interdisciplinary Reviews: Climate Change*, *2*(4), 570–591. https://doi.org/10.1002/wcc.121

Herring, S. C., Christidis, N., Hoell, A., Kossin, J. P., Schreck Iii, C. J., Stott, P. A., Quan, X. W., Hoerling, M., Smith, L., Perlwitz, J., Zhang, T., Hoell, A., Wolter, K., & Eischeid, J. (2018). EXPLAINING EXTREME EVENTS OF 2016 From A Climate Perspective EXPLAINING EXTREME EVENTS OF 2016 FROM A CLIMATE PERSPECTIVE AmericAn meteorologicAl Society. *Bulletin of the American Meteorological Society Bulletin of the American Meteorological Society Bull. Amer. Meteor. Soc*, *99*(991), 54–59. https://doi.org/10.1175/BAMS-D-17-0118.1

Hersbach, H., Bell, B., Berrisford, P., Hirahara, S., Horányi, A., Muñoz-Sabater, J., Nicolas, J., Peubey, C., Radu, R., Schepers, D., Simmons, A., Soci, C., Abdalla, S., Abellan, X., Balsamo, G., Bechtold, P., Biavati, G., Bidlot, J., Bonavita, M., … Thépaut, J. N. (2020). The ERA5 global reanalysis. *Quarterly Journal of the Royal Meteorological Society*, *146*(730), 1999–2049. https://doi.org/10.1002/qj.3803

Hoell, A., Hoerling, M., Eischeid, J., Quan, X. W., & Liebmann, B. (2017). Reconciling theories for human and natural attribution of recent East Africa drying. *Journal of Climate*, *30*(6), 1939–1957. https://doi.org/10.1175/JCLI-D-16-0558.1

Hogan, E., Shelly, A., & Xavier, P. (2015). The observed and modelled influence of the Madden-Julian Oscillation on East African rainfall. *Meteorological Applications*, *22*(3), 459–469. https://doi.org/10.1002/met.1475

Humanitarian Bulletin Eastern Africa No. 6, 11 – 25 May 2012 - Somalia | ReliefWeb. (2012). https://reliefweb.int/report/somalia/humanitarian-bulletin-eastern-africa-no-6-11-%E2%80%93-25-may-2012

Harrison, L., Funk, C., McNally, A., Shukla, S., & Husak, G. (2019). Pacific sea surface temperature linkages with Tanzania's multi-season drying trends. *International Journal of Climatology*, *39*(6), 3057–3075. https://doi.org/10.1002/joc.6003

Herring, S. C., Christidis, N., Hoell, A., Hoerling, M., & Stott, P. A. (2019). Introduction to explaining extreme events of 2017 from a climate perspective. *Bulletin of the American Meteorological Society*. https://doi.org/10.1175/BAMS-D-18-0307.1

Hoell, A., & Funk, C. (2014). Indo-Pacific Sea surface temperature influences on the failed consecutive rainy seasons over eastern Africa. *Climate Dynamics*, *43*(5–6), 1645–1660. https://doi.org/10.1007/s00382-

013-1991-6
Hope, P., Lim, E. P., Hendon, H., & Wang, G. (2018). 26. The effect of increasing CO2 on the extreme September 2016 rainfall across southeastern Australia. *Bulletin of the American Meteorological Society*, *99*(1), S133–S138. https://doi.org/10.1175/BAMS-D-17-0094.1
IPCC. (2021). *Assessment Report 6 Climate Change 2021: The Physical Science Basis*. https://www.ipcc.ch/report/ar6/wg1/
IPCC. (2018). Summary for Policymakers. In Global Warming of 1.5°C: IPCC Special Report on Impacts of Global Warming of 1.5°C above Pre-industrial Levels in Context of Strengthening Response to Climate Change, Sustainable Development, and Efforts to Eradicate Poverty (. *Global Warming of 1.5°C*, 1–24. https://www.cambridge.org/core/product/identifier/9781009157940%23prf2/type/book_part
Kew, S. F., Philip, S. Y., Hauser, M., Hobbins, M., Wanders, N., Jan Van Oldenborgh, G., Van Der Wiel, K.,Veldkamp, T. I. E., Kimutai, J., Funk, C., & Otto, F. E. L. (2021). Impact of precipitation and increasing temperatures on drought trends in eastern Africa. *Earth System Dynamics*, *12*(1), 17–35. https://doi.org/10.5194/esd-12-17-2021
Kilavi, M., MacLeod, D., Ambani, M., Robbins, J., Dankers, R., Graham, R., Helen, T., Salih, A. A. M., & Todd, M. C. (2018). Extreme rainfall and flooding over Central Kenya Including Nairobi City during the long-rains season 2018: Causes, predictability, and potential for early warning and actions. *Atmosphere*, *9*(12). https://doi.org/10.3390/atmos9120472
Kenya: The 2018 Long Rains Season Assessment Report - Kenya | ReliefWeb. (2018). https://reliefweb.int/report/kenya/kenya-2018-long-rains-season-assessment-report
Kenya - Floods - Emergency Plan of Action DREF n° MDRKE037 - Kenya | ReliefWeb. (2016). https://reliefweb.int/report/kenya/kenya-floods-emergency-plan-action-dref-n-mdrke037
King, J. A., Washington, R., & Engelstaedter, S. (2020). Representation of the Indian Ocean Walker circulation in climate models and links to Kenyan rainfall. *International Journal of Climatology*, *December 2019*, 1–28. https://doi.org/10.1002/joc.6714
Kimutai, J., New, M., Wolski, P., & Otto, F. (2022). Attribution of the Human Influence on Heavy Rainfall Associated with Flooding Events during the 2012, 2016, and 2018 March-April-May Seasons in Kenya. May. https://doi.org/10.1016/j.wace.2022.100529
Lee, W. L., Wang, Y. C., Shiu, C. J., Tsai, I. C., Tu, C. Y., Lan, Y. Y., Chen, J. P., Pan, H. L., & Hsu, H. H. (2020). Taiwan Earth System Model Version 1: Description and evaluation of mean state. *Geoscientific Model Development*, *13*(9), 3887–3904. https://doi.org/10.5194/gmd-13-3887-2020
Liebmann, B., Hoerling, M. P., Funk, C., Bladé, I., Dole, R. M., Allured, D., Quan, X., Pegion, P., & Eischeid, J. K. (2014). Understanding recent eastern Horn of Africa rainfall variability and change. *Journal of Climate*, *27*(23), 8630–8645. https://doi.org/10.1175/JCLI-D-13-00714.1
Lott, F. C., Christidis, N., & Stott, P. A. (2013). Can the 2011 East African drought be attributed to human-induced climate change? *Geophysical Research Letters*, *40*(6), 1177–1181. https://doi.org/10.1002/grl.50235
Lurton, T., Balkanski, Y., Bastrikov, V., Bekki, S., Bopp, L., Braconnot, P., Brockmann, P., Cadule, P., Contoux, C., Cozic, A., Cugnet, D., Dufresne, J. L., Éthé, C., Foujols, M. A., Ghattas, J., Hauglustaine, D., Hu, R. M., Kageyama, M., Khodri, M., … Boucher, O. (2020). Implementation of the CMIP6 Forcing Data in the IPSL-CM6A-LR Model. *Journal of Advances in Modeling Earth Systems*, *12*(4), 1– 22. https://doi.org/10.1029/2019MS001940
Lawal, K. A., Abatan, A. A., Angélil, O., Olaniyan, E., Olusoji, V. H., Oguntunde, P. G., … Stone, D. A. (2016). 13. The late onset of the 2015 wet season in Nigeria. *Bulletin of the American Meteorological Society*, *97*(12), S63–S69. https://doi.org/10.1175/BAMS-D-16-0131.1
Lintner, B. R., Biasutti, M., Diffenbaugh, N. S., Lee, J.-E., Niznik, M. J., & Findell, K. L. (2012). Amplification of wet and dry month occurrence over tropical land regions in response to global warming. *Journal of Geophysical Research: Atmospheres*, *117*(D11), n/a-n/a.

https://doi.org/10.1029/2012JD017499
Marthews, T. R., Otto, F. E. L., Mitchell, D., Dadson, S. J., & Jones, R. G. (2015). The 2014 drought in the horn of Africa: Attribution of meteorological drivers. *Bulletin of the American Meteorological Society*, *96*(12), S83–S88. https://doi.org/10.1175/BAMS-D-15-00115.1
Matthew Collins, Krinner, G., Germany, F., Shongwe, M., Africa, S., France, S. B., Uk, B. B. B. B., Germany, V. B., Uk, O. B., France, C. B., Uk, R. C., Canada, M. E., Erich, M., Uk, R. W. L., Uk, S. L., & Lucas, C. (2013). Long-term climate change: Projections, commitments and irreversibility. *Climate Change 2013 the Physical Science Basis: Working Group I Contribution to the Fifth Assessment Report of the Intergovernmental Panel on Climate Change*, *9781107057*, 1029–1136. https://doi.org/10.1017/CBO9781107415324.024
Meehl, G. A., Stocker, T. F., Collins, W. D., Friedlingstein, P., Gaye, A. T., Gregory, J. M., Kitoh, A., Knutti, R., Murphy, J. M., Noda, A., Raper, S. C. B., Watterson, I. G., Weaver, A. J., & Zhao, Z.-C. (2007). Global Climate Projections. *Climate Change 2007: The Physical Science Basis. Contribution of Working Group I to the Fourth Assessment Report of the Intergovernmental Panel on Climate Change*.
Mondal, A., & Mujumdar, P. P. (2015). Modeling non-stationarity in intensity, duration and frequency of extreme rainfall over India. *Journal of Hydrology*, *521*, 217–231. https://doi.org/10.1016/j.jhydrol.2014.11.071
NAS. (2016). Attribution of Extreme Weather Events in the Context of Climate Change. In *Attribution of Extreme Weather Events in the Context of Climate Change*. https://doi.org/10.17226/21852
Nicholson, S. E. (2016a). An analysis of recent rainfall conditions in eastern Africa. *International Journal of Climatology*, *36*(1), 526–532. https://doi.org/10.1002/joc.4358
Nicholson, S. E. (2016b). An analysis of recent rainfall conditions in eastern Africa. *International Journal of Climatology*, *36*(1), 526–532. https://doi.org/10.1002/joc.4358
Nicholson, S. E. (2017). Climate and climatic variability of rainfall over eastern Africa. *Reviews of Geophysics*, *55*(3), 590–635. https://doi.org/10.1002/2016rg000544
OCHA. (2020.). *Eastern Africa Region: Floods and Locust Outbreak Snapshot (May 2020) - Ethiopia | ReliefWeb*. Retrieved May 12, 2021, from https://reliefweb.int/report/ethiopia/eastern-africa-region-floods-and-locust-outbreak-snapshot-may-2020
OCHA. (2012). *Eastern Africa Region: Floods and Locust Outbreak Snapshot (May 2020) - Ethiopia | ReliefWeb*. https://reliefweb.int/report/ethiopia/eastern-africa-region-floods-and-locust-outbreak-snapshot-may-2020
OCHA Flash Update #5: Floods in Kenya | 10 May 2018 - Kenya | ReliefWeb. (n.d.).
Omondi, P. A. o., Awange, J. L., Forootan, E., Ogallo, L. A., Barakiza, R., Girmaw, G. B., Fesseha, I., Kululetera, V., Kilembe, C., Mbati, M. M., Kilavi, M., King'uyu, S. M., Omeny, P. A., Njogu, A., Badr, E. M., Musa, T. A., Muchiri, P., Bamanya, D., & Komutunga, E. (2014). Changes in temperature and precipitation extremes over the Greater Horn of Africa region from 1961 to 2010. *International Journal of Climatology*, *34*(4), 1262–1277. https://doi.org/10.1002/joc.3763
Omondi, P., Ogallo, L. A., Anyah, R., Muthama, J. M., & Ininda, J. (2012). Linkages between global sea surface temperatures and decadal rainfall variability over Eastern Africa region. *International Journal of Climatology*, *33*(8), 2082–2104. https://doi.org/10.1002/joc.3578
Ongoma, V., Chen, H., & Gao, C. (2018). Evaluation of CMIP5 twentieth century rainfall simulation over the equatorial East Africa. *Theoretical and Applied Climatology*, *Ipcc 2013*, 1–18. https://doi.org/10.1007/s00704-018-2392
Ongoma, V., Chen, H., & Omony, G. W. (2018). Variability of extreme weather events over the equatorial East Africa, a case study of rainfall in Kenya and Uganda. *Theoretical and Applied Climatology*, *131*(1–2), 295–308. https://doi.org/10.1007/s00704-016-1973-9

Otieno, V. O., & Anyah, R. O. (2012). CMIP5 simulated climate conditions of the Greater Horn of Africa (GHA). Part II: Projected climate. *Climate Dynamics*, *41*(7–8), 2099–2113. https://doi.org/10.1007/s00382-013-1694-z

Otto, F. E. L., Boyd, E., Jones, R. G., Cornforth, R. J., James, R., Parker, H. R., & Allen, M. R. (2015). Attribution of extreme weather events in Africa: a preliminary exploration of the science and policy implications. *Climatic Change*, *132*(4), 531–543. https://doi.org/10.1007/s10584-015-1432-0

Otto, F. E. L., Harrington, L., Schmitt, K., Philip, S., Kew, S., van Oldenborgh, G. J., Singh, R., Kimutai, J., & Wolski, P. (2020). Challenges to understanding extreme weather changes in lower income countries. *Bulletin of the American Meteorological Society*, *101*(10), E1851–E1860. https://doi.org/10.1175/BAMS-D-19-0317.1

Otto, F. E. L., Van Oldenborgh, G. J., Eden, J., Stott, P. A., Karoly, D. J., & Allen, M. R. (2016a). The attribution question. *Nature Climate Change*, *6*(9), 813–816. https://doi.org/10.1038/nclimate3089

Otto, F. E. L., Van Oldenborgh, G. J., Eden, J., Stott, P. A., Karoly, D. J., & Allen, M. R. (2016b). The attribution question. *Nature Climate Change*, *6*(9), 813–816. https://doi.org/10.1038/nclimate3089

Otto, F. E. L. (2016). Extreme events: The art of attribution. *Nature Climate Change*, *6*(4), 342–343. https://doi.org/10.1038/nclimate2971

Otto, F. E. L. (2017). Attribution of Weather and Climate Events. *Annual Review of Environment and Resources*, *42*(1), 627–646. https://doi.org/10.1146/annurev-environ-102016-060847

O'Gorman, P. A. (2015). Precipitation Extremes Under Climate Change. *Current Climate Change Reports*, *1*(2), 49–59. https://doi.org/10.1007/s40641-015-0009-3

Ogwang, B. A., Chen, H., Li, X., & Gao, C. (2014). The Influence of Topography on East African October to December Climate: Sensitivity Experiments with RegCM4. *Advances in Meteorology*, *2014*, 1–14. https://doi.org/10.1155/2014/143917

Oldenborgh., V. (2015). Climate change increases the probability of heavy rains like those of storm Desmond in the UK – an event attribution study in near-real time. *Hydrology and Earth System Sciences Discussions*, *12*(12), 13197–13216. https://doi.org/10.5194/hessd-12-13197-2015

Oldenborgh, G. J. van, Urk, A. van, & Allen, M. (2012). The absence of a role of climate change in the 2011 Thailand floods. *Bulletin of the American Meteorological Society*, *93*(july), 1047–1049.

Otto, F., James, R., & Allen, M. (n.d.). *The science of attributing extreme weather events and its potential contribution to assessing loss and damage associated with climate change impacts*

Owiti, Z., Ogallo, L. a., & Mutemi, J. (2008). Linkages between the Indian Ocean Dipole and east African seasonal rainfall anomalies. *Journal of Kenya Meteorological Society*, *2*(1), 3–17. Retrieved from http://kms.or.ke/phocadownload/VOl.2 Paper 1.pdf

Paciorek, C. J., Stone, D. A., & Wehner, M. F. (2018). Quantifying statistical uncertainty in the attribution of human influence on severe weather. *Weather and Climate Extremes*, *20*(December 2017), 69–80. https://doi.org/10.1016/j.wace.2018.01.002

Park, Sungsu; Shin, J. (n.d.). *NCC NorESM2-MM model output prepared for CMIP6 CMIP historical*. Retrieved June 4, 2021, from https://cera-www.dkrz.de/WDCC/ui/cerasearch/cmip6?input=CMIP6.CMIP.SNU.SAM0-UNICON.piControl

Parmesan, C., Root, T. L., & Willig, M. R. (2000). Impacts of extreme weather and climate on terrestrial biota. *Bulletin of the American Meteorological Society*, *81*(3), 443–450. https://doi.org/10.1175/1520-0477(2000)081<0443:IOEWAC>2.3.CO;2

Philip, S., Kew, S., van Oldenborgh, G. J., Otto, F., Vautard, R., van der Wiel, K., King, A., Lott, F., Arrighi, J., Singh, R., & van Aalst, M. (2020). A protocol for probabilistic extreme event attribution analyses. *Advances in Statistical Climatology, Meteorology and Oceanography*, *6*(2), 177–203. https://doi.org/10.5194/ascmo-6-177-2020

Philip, S., Sparrow, S., Kew, S. F., Van Der Wiel, K., Wanders, N., Singh, R., Hassan, A., Mohammed, K., Javid, H., Haustein, K., Otto, F. E. L., Hirpa, F., Rimi, R. H., Saiful Islam, A. K. M., Wallom, D. C. H., & Jan Van Oldenborgh, G. (2019). Attributing the 2017 Bangladesh floods from meteorological and hydrological perspectives. *Hydrology and Earth System Sciences*, *23*(3), 1409–1429. https://doi.org/10.5194/hess-23-1409-2019

Philippon, N., Camberlin, P., Moron, V., & Boyard-Micheau, J. (2015). Anomalously wet and dry rainy seasons in Equatorial East Africa and associated differences in intra-seasonal characteristics. *Climate Dynamics*, *45*(7–8), 1819–1840. https://doi.org/10.1007/s00382-014-2436-6

Pohl, B., & Camberlin, P. (2006). Influence of the Madden-Julian Oscillation on East African rainfall. II. March-May season extremes and interannual variability. *Quarterly Journal of the Royal Meteorological Society*, *132*(621), 2541–2558. https://doi.org/10.1256/qj.05.223

Pohl, B., & Camberlin, P. (2011). Intraseasonal and interannual zonal circulations over the Equatorial Indian Ocean. *Theoretical and Applied Climatology*, *104*(1–2), 175–191. https://doi.org/10.1007/s00704-010-0336-1

Polson, D., Hegerl, G. C., Allan, R. P., & Sarojini, B. B. (2013). Have greenhouse gases intensified the contrast between wet and dry regions? *Geophysical Research Letters*, *40*(17), 4783–4787. https://doi.org/10.1002/grl.50923

Richard B. Neale, C.-C. C., Lauritzen, A. G. P. H., Sungsu Park David L. Williamson, A. J. C. R. G., Lamarque, D. K. J.-F., Mills, D. M. M., Tilmes, A. K. S. S., Francis Vitt, Hugh Morrison, Philip Cameron-Smith, William D. Collins, Michael J. Iacono, Richard C. Easter, S. J. G., & Rasch, Xiaohong Liu Philip J., M. A. T. (2012). Description of the NCAR Community Atmosphere Model (CAM 5.0). *Theory of Hindi Syntax*. https://doi.org/10.1515/9783111358611-006

Roeckner, E., Brokopf, R., Esch, M., Giorgetta, M., Hagemann, S., Kornblueh, L., Manzini, E., Schlese, U., & Schulzweida, U. (2006). Sensitivity of Simulated Climate to Horizontal and Vertical Resolution in the ECHAM5 Atmosphere Model. *Journal of Climate*, *19*(16), 3771–3791. https://doi.org/10.1175/JCLI3824.1

Rowell, D. P., Booth, B. B. B., Nicholson, S. E., & Good, P. (2015). Reconciling past and future rainfall trends over East Africa. *Journal of Climate*, *28*(24), 9768–9788. https://doi.org/10.1175/JCLI-D-15-0140.1

Rowell, D. P., Senior, C. A., Vellinga, M., & Graham, R. J. (2016). Can climate projection uncertainty be constrained over Africa using metrics of contemporary performance? *Climatic Change*, *134*(4), 621–633. https://doi.org/10.1007/s10584-015-1554-4

Richard W a s h i n g t o n , Mike Ha r r i s o n , De c l a n Conway , Emily Black, An d r e w c hHa l l i n o r , David Grimes, Ri c h a r d Jones, Andy Morse, g i l l i a n kay, a n d m a r t i n t o d d. (2006). Taking the Shorter Route ONTEXT : CLIMATE AND DEVELOP-. *American Meteorological Society*, (May), 1355–1366. https://doi.org/10.1175/BAMS-87-10-1355

Schmocker, J., Liniger, H. P., Ngeru, J. N., Brugnara, Y., Auchmann, R., & Brönnimann, S. (2016). Trends in mean and extreme precipitation in the Mount Kenya region from observations and reanalyses. *International Journal of Climatology*, *36*(3), 1500–1514. https://doi.org/10.1002/joc.4438

Seland, Ø., Bentsen, M., Seland Graff, L., Olivié, D., Toniazzo, T., Gjermundsen, A., Debernard, J. B., Gupta, A. K., He, Y., Kirkevåg, A., Schwinger, J., Tjiputra, J., Schancke Aas, K., Bethke, I., Fan, Y., Griesfeller, J., Grini, A., Guo, C., Ilicak, M., … Schulz, M. (2020). The Norwegian Earth System Model, NorESM2 – Evaluation of theCMIP6 DECK and historical simulations. *Geoscientific Model Development Discussions*, *February*, 1–68. https://doi.org/10.5194/gmd-2019-378

Sellar, A. A., Jones, C. G., Mulcahy, J. P., Tang, Y., Yool, A., Wiltshire, A., O'Connor, F. M., Stringer, M., Hill, R., Palmieri, J., Woodward, S., de Mora, L., Kuhlbrodt, T., Rumbold, S. T., Kelley, D. I., Ellis, R., Johnson, C. E., Walton, J., Abraham, N. L., … Zerroukat, M. (2019). UKESM1: Description and Evaluation of the U.K. Earth System Model. *Journal of Advances in Modeling Earth Systems*, *11*(12), 4513–4558. https://doi.org/10.1029/2019MS001739

Seneviratne, S. I., Zhang, X., Adnan, M., Badi, W., Dereczynski, C., Luca, A. di, Ghosh, S., Iskandar, I., Kossin, J., Lewis, S., Otto, F., Pinto, I., Satoh, M., Vicente-Serrano, S. M., Wehner, M., & Zhou, B. (2021). Weather and Climate Extreme Events in a Changing Climate. *Climate Change 2021: The Physical Science Basis. Contribution of Working Group I to the Sixth Assessment Report of the Intergovernmental Panel on Climate Change*, *46*, 2573–2582.

Shepherd, T. G. (2016). A Common Framework for Approaches to Extreme Event Attribution. *Current Climate Change Reports*, *2*(1), 28–38. https://doi.org/10.1007/s40641-016-0033-y

Sillmann, J., Kharin, V. V., Zhang, X., Zwiers, F. W., & Bronaugh, D. (2013). Climate extremes indices in the CMIP5 multimodel ensemble: Part 1. Model evaluation in the present climate. *Journal of Geophysical Research Atmospheres*, *118*(4), 1716–1733. https://doi.org/10.1002/jgrd.50203

Stone, D. A., & Allen, M. R. (2005). The end-to-end attribution problem: From emissions to impacts. *Climatic Change*, *71*(3), 303–318. https://doi.org/10.1007/s10584-005-6778-2

Stone, D. A., Christidis, N., Folland, C., & Perkins-kirkpatrick, S. (2019). *Authors Experiment design of the International CLIVAR C20C + Detection and Attribution project*. https://doi.org/10.1016/j.wace.2019.100206

Stone, D. A., Risser, M. D., Angélil, O. M., Wehner, M. F., Cholia, S., Keen, N., Krishnan, H., O'Brien, T. A., & Collins, W. D. (2018). A basis set for exploration of sensitivity to prescribed ocean conditions for estimating human contributions to extreme weather in CAM5.1-1degree. *Weather and Climate Extremes*, *19*(August 2017), 10–19. https://doi.org/10.1016/j.wace.2017.12.003

Stott, P. A., Christidis, N., Otto, F. E. L., Sun, Y., Vanderlinden, J. P., van Oldenborgh, G. J., Vautard, R., von Storch, H., Walton, P., Yiou, P., & Zwiers, F. W. (2016). Attribution of extreme weather and climate-related events. *Wiley Interdisciplinary Reviews: Climate Change*, *7*(1), 23–41. https://doi.org/10.1002/wcc.380

Stuart Coles. (2001). An Introduction to Statistical Modeling of Extreme Values, Springer Series in Statistics. *Questiio*, *25*(2), 375.

Sun, Q., & Miao, C. (2018). 20. Extreme rainfall (R20MM, RX5day) in Yangtze–Huai, China, in June–July 2016: The role of ENSO and anthropogenic climate change. *Bulletin of the American Meteorological Society*, *99*(1), S102–S106. https://doi.org/10.1175/BAMS-D-17-0091.1

Swart, N. C., Cole, J. N. S., Kharin, V. V., Lazare, M., Scinocca, J. F., Gillett, N. P., Anstey, J., Arora, V., Christian, J. R., Hanna, S., Jiao, Y., Lee, W. G., Majaess, F., Saenko, O. A., Seiler, C., Seinen, C., Shao, A., Sigmond, M., Solheim, L., … Winter, B. (2019). The Canadian Earth System Model version 5 (CanESM5.0.3). *Geoscientific Model Development*, *12*(11), 4823–4873. https://doi.org/10.5194/gmd-12-4823-2019

Singh, D., Horton, D. E., Tsiang, M., Haugen, M., Ashfaq, M., Mei, R., … Diffenbaugh, N. S. (2014). 17. Severe precipitation in Northern India in June 2013: Causes, historical context, and changes in probability. *Bulletin of the American Meteorological Society*, *95*(9), 558–561.

Tatebe, H., Ogura, T., Nitta, T., Komuro, Y., Ogochi, K., Takemura, T., Sudo, K., Sekiguchi, M., Abe, M., Saito, F., Chikira, M., Watanabe, S., Mori, M., Hirota, N., Kawatani, Y., Mochizuki, T., Yoshimura, K., Takata, K., O'Ishi, R., … Kimoto, M. (2019). Description and basic evaluation of simulated mean state, internal variability, and climate sensitivity in MIROC6. *Geoscientific Model Development*, *12*(7), 2727– 2765. https://doi.org/10.5194/gmd-12-2727-2019

Thiery, W., Davin, E. L., Seneviratne, S. I., Bedka, K., Lhermitte, S., & Van Lipzig, N. P. M. (2016). Hazardous thunderstorm intensification over Lake Victoria. *Nature Communications*, *7*, 1–7. https://doi.org/10.1038/ncomms12786

Thiessen, A. H. (1911). PRECIPITATION AVERAGES FOR LARGE AREAS. *Monthly Weather Review*, *39*(7), 1082–1089. https://doi.org/10.1175/1520-0493(1911)39<1082b:pafla>2.0.co;2

Tierney, J. E., Ummenhofer, C. C., & DeMenocal, P. B. (2015). Past and future rainfall in the Horn of Africa. *Science Advances*, *1*(9), 1–8. https://doi.org/10.1126/sciadv.1500682

Trenberth, K. E. (2011). Changes in precipitation with climate change. *Climate Research*, *47*(1–2), 123–138. https://doi.org/10.3354/cr00953

Trenberth, K. E., Dai, A., Rasmussen, R. M., & Parsons, D. B. (2003). The changing character of precipitation. *Bulletin of the American Meteorological Society*, *84*(9), 1205-1217+1161. https://doi.org/10.1175/BAMS-84-9-1205

Taylor, K. E., Stouffer, R. J., & Meehl, G. A. (2012). An overview of CMIP5 and the experiment design. *Bulletin of the American Meteorological Society*, *93*(4), 485–498. https://doi.org/10.1175/BAMS-D-11-00094.1

Uhe, P., Philip, S., Kew, S., Shah, K., Kimutai, J., Mwangi, E., … Otto, F. (2018). Attributing drivers of the 2016 Kenyan drought. *International Journal of Climatology*, *38*, e554–e568. https://doi.org/10.1002/joc.5389

UN CRED. (2020). Human cost of disasters (2000-2019). *Human Cost of Disasters*, *61*, 1–2. https://doi.org/10.1186/s12889

Van Der Wiel, K., Kapnick, S. B., Jan Van Oldenborgh, G., Whan, K., Philip, S., Vecchi, G. A., Singh, R. K., Arrighi, J., & Cullen, H. (2017). Rapid attribution of the August 2016 flood-inducing extreme precipitation in south Louisiana to climate change. *Hydrology and Earth System Sciences*, *21*(2), 897–921. https://doi.org/10.5194/hess-21-897-2017

Van Oldenborgh, G. J., Otto, F. E. L., Haustein, K., & Achutarao, K. (2016). 17. The heavy precipitation event of December 2015 in Chennai, India. *Bulletin of the American Meteorological Society*, *97*(12), S87–S91. https://doi.org/10.1175/BAMS-D-16-0129.1

van Oldenborgh, G. J., Philip, S., Aalbers, E., Vautard, R., Otto, F., Haustein, K., Habets, F., Singh, R., & Cullen, H. (2016). Rapid attribution of the May/June 2016 flood-inducing precipitation in France and Germany to climate change. *Hydrology and Earth System Sciences Discussions*, *June*, 1–23. https://doi.org/10.5194/hess-2016-308

Vellinga, M., & Milton, S. F. (2018). Drivers of interannual variability of the East African "Long Rains."*Quarterly Journal of the Royal Meteorological Society*, *144*(712), 861–876. https://doi.org/10.1002/qj.3263

Vigaud, N., Lyon, B., & Giannini, A. (2016). Sub-seasonal teleconnections between convection over the Indian Ocean, the East African long rains and tropical Pacific surface temperatures. *International Journal of Climatology*, *37*(3), 1167–1180. https://doi.org/10.1002/joc.4765

Voldoire, A., Saint-Martin, D., Sénési, S., Decharme, B., Alias, A., Chevallier, M., Colin, J., Guérémy, J. F., Michou, M., Moine, M. P., Nabat, P., Roehrig, R., Salas y Mélia, D., Séférian, R., Valcke, S., Beau, I., Belamari, S., Berthet, S., Cassou, C., … Waldman, R. (2019). Evaluation of CMIP6 DECK Experiments With CNRM-CM6-1. *Journal of Advances in Modeling Earth Systems*, *11*(7), 2177–2213. https://doi.org/10.1029/2019MS001683

Volodin, E., & Gritsun, A. (2018). Simulation of observed climate changes in 1850-2014 with climate model INM-CM5. *Earth System Dynamics*, *9*(4), 1235–1242. https://doi.org/10.5194/esd-9-1235-2018

Volodin, E. M., Mortikov, E. V., Kostrykin, S. V., Galin, V. Y., Lykossov, V. N., Gritsun, A. S., Diansky, N. A., Gusev, A. V., & Iakovlev, N. G. (2017). Simulation of the present-day climate with the climate model INMCM5. *Climate Dynamics*, *49*(11–12), 3715–3734. https://doi.org/10.1007/s00382-017-3539-7

Wolter, K., Hoerling, M., Eischeid, J. K., & Cheng, L. (2016). 3. What history tells US about 2015 U.S. Daily rainfall extremes. *Bulletin of the American Meteorological Society*, *97*(12), S9–S13. https://doi.org/10.1175/BAMS-D-16-0166.1

Y ukiko I mada , M asahiro W atanabe , M asato M ori , M asahide K imoto, H. ideo S. hiogama, & Shii, and M. asayoshi I. (n.d.). Contribution of atmospheric circulation change to the 2012 heavy Rainfall in Southwestern Japan | Request PDF. Retrieved August 30, 2019, from https://www.researchgate.net/publication/291296829_Contribution_of_atmospheric_circulation_change_to_the_2012_heavy_Rainfall_in_Southwestern_Japan

Yiou, P., & Cattiaux, J. (2013). Contribution of atmospheric circulation to wet North European summer precipitation of 2012. *Bulletin of the American Meteorological Society*, *94*(9), S39–S41

Zhang, X., Alexander, L., Hegerl, G. C., Jones, P., Tank, A. K., Peterson, T. C., Trewin, B., & Zwiers, F. W. (2011). Indices for monitoring changes in extremes based on daily temperature and precipitation data. *Wiley Interdisciplinary Reviews: Climate Change*, *2*(6), 851–870. https://doi.org/10.1002/wcc.147

Zorita, E., Stocker, T. F., & von Storch, H. (2008). How unusual is the recent series of warm years? *Geophysical Research Letters*, *35*(24). https://doi.org/10.1029/2008GL036228

.....